

Ingeniería e Investigación
Journal
Abbreviated Journal Title: **Ing. Investig.**

Editor-in-chief
Andrés Pavas, Ph.D.

Editorial Assistants
Fabián Hernando Ríos, B. Eng.
Ingri Gisela Camacho

Editorial Board
Paulo César Narváez Rincón, Ph.D.
Universidad Nacional de Colombia - Bogotá
Julio Esteban Colmenares, Ph.D.
Universidad Nacional de Colombia - Bogotá
Luis Fernando Niño, Ph.D.
Universidad Nacional de Colombia - Bogotá
Óscar Germán Duarte, Ph.D.
Universidad Nacional de Colombia - Bogotá
Jaime Salazar Contreras, M.U.
Universidad Nacional de Colombia - Bogotá
Ignacio Pérez, Ph.D.
Escuela Colombiana de Ingeniería - Colombia
Nelly Cecilia Alba, Ph.D.
Universidad Autónoma de Occidente - Colombia
Heberto Tapias García, Ph.D.
Universidad de Antioquia - Colombia
Ricardo Llamasa Villalba, Ph.D.
UIS - Bucaramanga - Colombia
Gustavo Bolaños, Ph.D.
Universidad del Valle - Colombia
Dora Ángela Hoyos Ayala, Ph.D.
Universidad de Antioquia - Colombia
Lourdes Zumalacárregui, Ph.D.
Ciudad Universitaria José Antonio Echeverría -
Cujae, Cuba
Federico Méndez Lavielle, Ph.D.
Universidad Nacional Autónoma de México -
México
Mauricio Camargo, Ph.D.
Université de Lorraine - France
Laure Morel, Ph.D.
Université de Lorraine - France
Andrés Romero Quete, Ph.D.
Universidad Nacional de San Juan
San Juan - Argentina
Víctor Berrera Núñez, Ph.D.
Data Analytics Senior Manager - PwC
México D.F. - México

Frequency
Quarterly, 3 issues per year
April, August and December

Cover Layout
Carlos Andrés Ortiz Valle

Proofreader
José Daniel Martínez

Layout Artist
Patricia Chávez R.

For additional information contact
revii_bog@unal.edu.co
Bogotá - Colombia
April - 2022

Table of Contents

Chemical Engineering / Food Engineering / Environmental Engineering

Effect of Diesel Oil and Mixture of Alcohol-Glycol Ether on Colombian Ultrafine Coal
Cleaning Using a Test-Rig Closed-Loop Flotation Column
Jorge L. Piñeres-Mendoza, Juan M. Barraza-Burgos, and Silvia P. Bellich-Fernandez

Civil Engineering / Sanitary Engineering

A Structural Design Comparison Between Two Reinforced Concrete Regular 6-Level
Buildings using Soil-Structure Interaction in Linear Range
*Nelson A. López M., Gabriela E. Pérez M., Christian F. Castro P., Juan C. Vielma P.,
Leonardo J. López M., José D. Alviar M., Carlos A. Romero R., David P. Guerrero C.,
and Vanessa V. Montesinos M.*

Overview of the Constitutive Model and Numerical Calibration by FEM to Compute
Bearing Capacity and Embankment-Core Deformability
*Milena Mesa-Lavista, Francisco Lamas-Fernández, Eduardo Tejeda-Piusseaut, Rafael
Bravo-Pareja, Carolina Cabrera-González, and José Álvarez-Pérez*

Empirical Models to Predict Compaction Parameters for Soils in the State of Ceará,
Northeastern Brazil
*Amanda V. Hohn, Rosiel F. Leme, Francisco C. da Silva Filho, Thales E. Moura, and
Grover R. Llanque A.*

Embedded Discrete Fracture Networks to Analyze Groundwater Inflows during Tunnel
Drilling
Adriana Piña, Diego Cortés, Leonardo David Donado, and Daniela Blessent

Mechanical Engineering / Materials Engineering / Mechatronics Engineering

Electrochemical Behavior of a Stainless Steel Superficially Modified with Nitrogen by
Three-dimensional Ion Implantation
*Felipe Sanabria-Martínez, Ely D. Valbuena-Niño, Leidy S. Chacón-Velasco, and Hugo
A. Estupiñán-Durán*

Comparison of Treatments by Mercerization and Plasma Glow Discharge on Residues of
the Amazon Chestnut Shell (*Bertholletia excelsa*)
*Ximena Zapata-Londoño, James Janderson Rosero-Romo, Hugo Armando
Estupiñán-Durán*

Systems Engineering / Computer Engineering

COVID-19 Diagnosis with Deep Learning
Hatice Catal Reis

Detection of COVID-19 and Other Pneumonia Cases using Convolutional Neural
Networks and X-ray Images
Carlos Eduardo Belman-López

Design and Implementation of Network Monitoring System for Campus Infrastructure
Using Software Agents
*Rodrigo I. Espinel-Villalobos, Erick Ardila-Triana, Henry Zarate-Ceballos, and Jorge
E. Ortiz-Triviño*

**Facultad de Ingeniería
Universidad Nacional de Colombia**

María Alejandra Guzmán
Dean
Camilo Andrés Cortés Guerrero
Vice Dean of Research and Extension
Jesús Hernán Camacho Tamayo
Vice Dean of Academic Affairs
Sandra Liliana Rojas Martínez
Director of the Students Welfare Service

Scientific Committee

Fabio González, Ph.D.
Universidad Nacional de Colombia, Bogotá
Miguel J. Bagajewicz, Ph.D.
University of Oklahoma, USA
Jayant Rajgopal, Ph.D.
University of Pittsburgh, USA

Ethical Committee

Óscar Fernando Castellanos, Ph.D.
Universidad Nacional de Colombia - Bogotá
Julio César Cañón, Ph.D.
Universidad Nacional de Colombia - Bogotá

**Papers published in *Ingeniería e Investigación*
journal are abstracted/indexed in**

- Science Citation Index Expanded (SciSearch®), Clarivate Analytics
- Scopus - Elsevier
- Scientific Electronic Library Online - SciELO, Colombia
- Chemical Abstract
- Índice de Revistas Latinoamericanas en Ciencias Periódica
- Dialnet
- Sistema Regional de Información en Línea para Revistas Científicas de América Latina, El Caribe, España y Portugal - Latindex
- Ebsco Publishing
- DOAJ - Directory of Open Access Journals
- Redib - Red Iberoamericana de Innovación y Conocimiento Científico

Ingeniería e Investigación journal was created in 1981. This is an entity in charge of spreading the teaching, scientific and technical research developed in the Universidad Nacional de Colombia's Engineering Faculty and other national and international institutions. *Ingeniería e Investigación* journal deals with original, unedited scientific research and technological developments in the various disciplines related to engineering. *Ingeniería e Investigación* journal contributes towards the development of knowledge, generating a global impact on academia, industry and society at large, through an exchange of knowledge and ideas maintaining a set of serious and recognized quality standards.

The content of the articles published in this journal does not necessarily reflect the opinions of the Editorial Team. These texts can be totally or partially reproduced provided a correct citation of the source.

Ingeniería e Investigación journal publications are developed for the academic community who is interested in research and engineering knowledge development. We invite readers to be part of this journal and participate either as authors, peer reviewers or subscribers.

For additional information contact:
www.revistas.unal.edu.co/index.php/ingenv
E-mail: revi_bog@unal.edu.co
Tel: 57(1) 3 16 5000 Ext. 13674

Tabla de Contenido

Ingeniería Química, de Alimentos y Ambiental

Efecto del *diésel oil* y la mezcla de alcohol-glicol-éter en la limpieza de carbón ultrafino colombiano utilizando una columna de flotación de prueba en bucle cerrado
Jorge L. Piñeres-Mendoza, Juan M. Barraza-Burgos y Silvia P. Bellich-Fernandez

Ingeniería Civil y Sanitaria

Comparación de diseño estructural entre dos edificaciones de concreto armado de seis niveles utilizando interacción suelo-estructura en el rango lineal
Nelson A. López M., Gabriela E. Pérez M., Christian F. Castro P., Juan C. Vielma P., Leonardo J. López M., José D. Alviar M., Carlos A. Romero R., David P. Guerrero C. y Vanessa V. Montesinos M.

Una mirada a los modelos constitutivos y la calibración numérica mediante MEF para calcular la capacidad de carga y la deformabilidad del núcleo del terraplén
Milena Mesa-Lavista, Francisco Lamas-Fernández, Eduardo Tejeda-Piusseaut, Rafael Bravo-Pareja, Carolina Cabrera-González y José Álvarez-Pérez

Modelos empíricos para predecir parámetros de compactación para suelos en el Estado de Ceará, Noreste de Brasil
Amanda V. Hohn, Rosiel F. Leme, Francisco C. da Silva Filho, Thales E. Moura y Grover R. Llanque A.

Redes de fracturas discretas embebidas para el análisis de infiltraciones de agua subterránea durante la excavación de túneles
Adriana Piña, Diego Cortés, Leonardo David Donado y Daniela Blessent

Ingeniería Mecánica, Mecatrónica y Ciencia de los Materiales

Comportamiento electroquímico de un acero inoxidable modificado superficialmente con nitrógeno por medio de implantación iónica tridimensional
Felipe Sanabria-Martínez, Ely D. Valbuena-Niño, Leidy S. Chacón-Velasco y Hugo A. Estupiñán-Durán

Comparación de tratamientos por mercerización y descarga intensa de plasma sobre residuos de la cáscara de castaña amazónica (*Bertholletia excelsa*)
Ximena Zapata-Londoño, James Janderson Rosero-Romo, Hugo Armando Estupiñán-Durán

Ingeniería de Sistemas e Informática

Diagnóstico de COVID-19 con *Deep Learning*
Hatice Catal Reis

Detección de COVID-19 y otros casos de neumonía utilizando redes neuronales convolucionales e imágenes de rayos-X
Carlos Eduardo Belman-López

Diseño e implementación de un sistema de monitoreo de red para infraestructura de campus usando agentes de software
Rodrigo I. Espinel-Villalobos, Erick Ardila-Triana, Henry Zarate-Ceballos y Jorge E. Ortiz-Triviño

Effect of Diesel Oil and Mixture of Alcohol-Glycol Ether on Colombian Ultrafine Coal Cleaning Using a Test-Rig Closed-Loop Flotation Column

Efecto del *diésel oil* y la mezcla de alcohol-glicol-éter en la limpieza de carbón ultrafino colombiano utilizando una columna de flotación de prueba en bucle cerrado

Jorge L. Piñeres-Mendoza¹, Juan M. Barraza-Burgos², and Silvia P. Bellich-Fernandez³

ABSTRACT

A test-rig closed-loop flotation column was used to observe the effect of diesel oil (collector) and Flomin F-425 (frother) on mass yield and ash content for two Colombian coals: Caypa (northern zone) and Guachinte (southwestern zone). The coal samples of less than 38 μm (-400 M) were processed in a collector concentration range of 0,32 to 1,60 kg/ton of coal, as well as a frother concentration range of 10 to 50 ppm. The response surface methodology was used for the experimental test runs. The results showed that the maximum mass yield obtained by Caypa coal was 98,39% at 1,28 kg of collector/ton of coal and 40 ppm of frother concentration, whereas Guachinte coal obtained a maximum mass yield of 94,71% at 0,96 kg of collector/ton of coal and 30 ppm of frother concentration. In general, for Caypa coal, the mass yield tends to increase (low ash removal) with the collector and frother concentration increase; while the mass yield tends to decrease (high ash removal) for Guachinte coal when the collector concentration increases (low ash removal) at high frother concentrations. It is worth highlighting that the ash content of 0,65% obtained for Caypa coal is the lowest value reported in the literature while employing a test-rig loop flotation column in a single stage, which is considered to be an ultra-clean coal obtained by a physical cleaning process.

Keywords: flotation column, Colombian coals, closed loop, experimental design

RESUMEN

Se usó una columna de flotación de prueba en bucle cerrado para observar el efecto del *diesel oil* (colector) y *Flomin F-425* (espumante) sobre el rendimiento másico y el contenido de cenizas de dos carbones colombianos: Caypa (zona norte) y Guachinte (zona suroeste). Las muestras de carbón de menos de 38 μm (-400 M) se procesaron en un rango de concentración de colector de 0,32 a 1,60 kg/tonelada de carbón y un rango de concentración de espumante de 10 a 50 ppm. Se utilizó la metodología de superficie de respuesta para las de pruebas experimentales. De los resultados obtenidos, se observó que el rendimiento másico máximo para el carbón de Caypa fue del 98,39 % a 1,28 kg de colector/tonelada de carbón y 40 ppm de concentración de espumante, mientras que el carbón Guachinte presentó un rendimiento másico máximo del 94,71 % a 0,96 kg de colector/tonelada de carbón y 30 ppm de concentración de espumante. En general, para el carbón Caypa, el rendimiento másico tiende a aumentar (baja remoción de cenizas) con el incremento en la concentración de colector y espumante; mientras que el rendimiento másico tiende a disminuir (alta remoción de cenizas) con el carbón Guachinte cuando la concentración del colector aumenta (baja remoción de cenizas) a altas concentraciones de espumante. Es de destacar que el contenido de cenizas de 0,65 % obtenido para el carbón de Caypa es el valor más bajo reportado en la literatura usando una columna de flotación de prueba en bucle cerrado en una sola etapa, que se considera como un carbón ultra limpio obtenido por un proceso de limpieza física.

Palabras clave: columna de flotación, carbones colombianos, bucle cerrado, diseño experimental

Received: June 13th, 2020

Accepted: June 16th, 2021

¹Chemical Engineer, Universidad del Atlántico, Barranquilla Colombia. Ph.D. in Engineering, Universidad del Valle, Cali, Colombia. Affiliation: Full Professor, Universidad del Atlántico, Barranquilla, Colombia.
E-mail: jorgepineres@uniatlantico.edu.co

²Chemical Engineer, Universidad del Atlántico, Barranquilla, Colombia. Ph.D. in Chemical Engineer, University of Nottingham, United Kingdom. Affiliation: Full Professor, Universidad del Valle, Cali, Colombia.
E-mail: juan.barraza@correounivalle.edu.co

³Chemical Engineer, Universidad del Atlántico, Barranquilla, Colombia. Affiliation: Master's Student, Universidad del Atlántico, Barranquilla, Colombia.
E-mail: sbellichfernandez@gmail.com

Introduction

Coal is a heterogeneous mixture of residual plants and associated minerals that have undergone physical and chemical changes that stem from biological and geological processes.

How to cite: Piñeres, J., Barraza, J., and Bellich, S. (2022). Effect of Diesel Oil and Mixture of Alcohol-Glycol Ether on Colombian Ultrafine Coal Cleaning Using a Test-Rig Closed-Loop Flotation Column. *Ingeniería e Investigación*, 42(1), e88273. [10.15446/ing.investig.v42n1.88273](https://doi.org/10.15446/ing.investig.v42n1.88273)



Attribution 4.0 International (CC BY 4.0) Share - Adapt

They are chemically composed of oxygen, hydrogen, carbon, and mineral matter, among others. In order to use coal efficiently, it is necessary to implement appropriate cleaning processes to reduce mineral matter. To clean fine coal particles, beneficiation processes focused on the use of flotation columns have been used due to their performance (efficiency) and wide range of operating conditions (Wieslaw, 1994; Polat and Chander, 2003).

One of the most important achievements in fine mineral processing has been the introduction of the flotation column concept in the early 1960s as an alternative solution to the difficulties encountered in mechanical flotation cells. However, it was not until the 1980s that its popularity and commercialization increased, given the growing development of operation and design procedures for mineral beneficiation. The mechanism used by the flotation columns eliminates the entrainment problem (due of the addition of wash water at the top), which is common in conventional flotation machines and generates small bubbles that improve the particle-bubble adhesion process, which contributes to fine particle recovery (Dobby and Finch 1986; Yoon 1993).

Nowadays, flotation columns are highly preferred for the beneficiation of ultra-fine coal. Froth flotation is a solid-solid separation process based on the differences of hydrophobicity between particles. During the flotation process, hydrophobic particles adhere to air bubbles, while hydrophilic particles remaining in the slurry. The successfulness of the mineral matter reduction present in coal is related to the difference in the grade of intrinsic hydrophobicity between the organic matter and the mineral matter present in the coal (Honaker *et al.*, 1996; Polat and Chander, 2003; Piñeres and Barraza, 2012).

Some authors determined the effects of frother mixture on froth flotation performance. Three mixed frother systems are designed based on combinations of alcohol, ketone, aldehyde, and polyglycol ether frothing molecules. Frother *x* is composed of alcohol and ketone, frother *y* is based on alcohol and aldehyde group chemicals, and frother *z* is a mixed product of alcohol and polyglycol ether. The results show that frother *z* is better than *x* and *y* in terms of selectivity. In terms of ash reduction and recovery, frother *z* is effective for coarse and ultrafine particle size fractions. This can be explained by the presence of short chain alcohol molecules (selective for ultrafine fraction) and polyglycol ether molecules (stronger frother for coarse size fraction) in frother *z* (Gupta *et al.*, 2009).

Peng *et al.* (2015) studied the effect of flotation reagent adsorption by different fine coal particles on coal flotation. The authors found that low ash fine coal particles have a very strong adsorption to both collector and frother, while high ash fine coal particles have a strong adsorption to collector but weak adsorption to frother, which indicates that frother may play a very important role in the recovery of coarse coal particles (Peng *et al.*, 2015). Other authors studied the effect of methyl cyclohexane methanol and cyclic frothers, as well as comparing coal flotation performance with methyl isobutyl carbinol using two coking coals with different floatability. The

results showed that it was an effective alternative to methyl isobutyl carbinol (Hangil *et al.*, 2016).

Without chemical agents (such as collectors and frothers), flotation would not be possible, and, without froth flotation, the mineral processing industry would not have developed as we currently know it. Thus, it is important to understand the effect of the collector and the frother, as well as their role in the performance of the process (recovery and selectivity), especially when Colombian coals are used. The objective of this work was to obtain the highest ash content reduction with the highest mass yield production of two Colombian coal samples using diesel oil (collector) and Flomin F-425 (frother) (information on the use of this frother agent is scarce with regard to cleaning Colombian coals) using a test-rig loop flotation column. One coal sample with high ash content and one with low ash content were selected to evaluate the effectiveness of the reagents (effect) on the selectivity and performance of the process. It should be noted that, theoretically, when a sample has low ash contents, it is more difficult to reduce this value through a cleaning process, because the mineral matter associated with this type of coal (low ash) is normally part of its molecular structure, thus making it very difficult to remove through a physical cleaning process.

Experimentation

Materials and equipment: Two Colombian coal samples, Caypa (North zone) and Guachinte (South western zone), were selected in this research, one with low ash content (Caypa) and another with high ash content (Guachinte) to evaluate the selectivity and performance of the flotation system. The coal particle size used in the flotation column runs was -400 mesh (38 μm), according to the liberation study results. Diesel oil (with a density of 832 kg/m^3) and Flomin F-425 (a mixture of alcohol-glycol ether with a density of 1009 kg/m^3) were used as collector and frother, respectively.

In this project, a 0,05 m diameter, 2 m high flotation column was used. The feed flow rate was 1,25 m, measured from the bottom of the column, while the static mixer for bubble generation and air flow rate was 0,2 m from the bottom of the column. To measure pressure drops, two pressure transmitters were installed along the flotation column (PT1 and PT2). A Danfoss solenoid proportional valve was selected along with a PLC (programmable logic controller). Finally, for communication between control valve and controller, the NB Omron Designer interface was used (Piñeres *et al.*, 2019). The test-rig loop flotation column diagram is presented in Figure 1.

In this work, for the contact angle measurements, a goniometer (Rame-Hard) was used using the sessile-drop technique. For the preparation of the polished section specimens, the coal samples were introduced into a hardener solution. Subsequently, the specimens were subjected to a polishing process with sandpaper and, finally, with a solution of aluminum oxide. For each specimen, ten contact angle measurements were made at different sites on the surface of the coal and

then averaged. Measurements were made with methylene iodide and double distilled water. These experiments were reproducible within $\pm 2^\circ$. Further description of the experimental development is provided in the referenced literature (Brady and Gauger, 1940; Gutiérrez *et al.*, 1984; Piñeres and Barraza, 2011). For FTIR analysis, Shimadzu IRAffinity-1 equipment was used to account for the identification of functional groups on the coal samples.

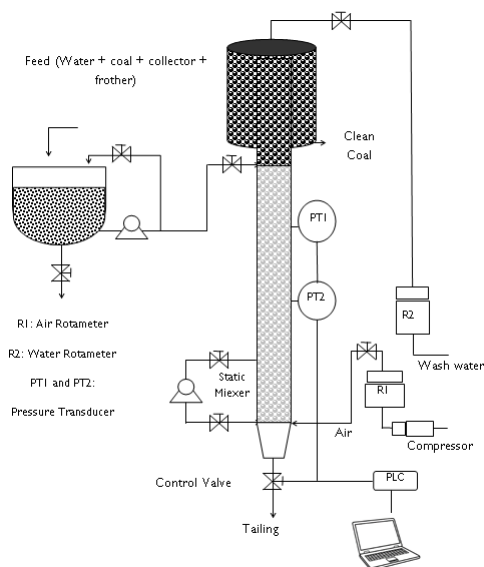


Figure 1. Schematic representation of the test-rig loop flotation column.
Source: Authors

Flotation test: Initially, water was added to the preparation tank. Then, the collector was added to the desired concentration, and the specific quantity of coal and frother was added, which produced a slurry concentration of 2,5% w/w used in all experimental tests. This slurry was mixed for 10 min until a homogeneous mixture was obtained. Finally, the feed valve was opened until the desired level height (interface) was obtained inside the flotation column. Table 1 shows a summary of the operating conditions used in the flotation column. The tuning process of the level control loop depends on pressure drop data obtained by the transducers. A set point was selected for the pressure transducers (1,01 psi), in which a froth depth of $58 \text{ cm} \pm 3\%$ and a tail velocity (Jsl) of $0,76 \text{ cm/s} \pm 6\%$ were maintained inside the flotation column in accordance with the design (Bellich, 2016). The float and tailing streams were collected in containers and subsequently filtered, dried, and prepared for the necessary analyses.

Table 1. Operation parameters

Parameter	Values (cm^3/s)
Feed flow rate	13,6
Tailing flow rate	14,9
Wash water flow rate	2,2
Bias flow rate	1,3

Source: Authors

Experimental design: In this research, a response surface methodology was used (Hicks, 1982; Montgomery, 2013),

where the effect of diesel oil (collector) and a mixture of alcohol-glycol ether (frother) on mass yield and ash content of two coal samples was evaluated. Table 2 shows the coding used during the experimental development (A: collector concentration, B: frother concentration). Collector concentration was selected because of its influence on coal hydrophobicity, while frother concentration was selected because of its influence on bubble diameter.

Table 2. Data and nomenclature

Nomenclature	code	Values
A (Collector)	-1	Low level: 0,64 kg/ton of coal
	1	High level: 1,28 kg/ton of coal
	0	Mid level: 0,96 kg/ton of coal
	*1	Low axial level: 0,32 kg/ton of coal
	*2	High axial level: 1,60 kg/ton of coal
B (Frother)	-1	Low level: 20 ppm
	1	High level: 40 ppm
	0	Mid level: 30 ppm
	*1	Low axial level: 10 ppm
	2	High axial level: 50 ppm

Source: Authors

The experimental error was 5%. Initially, experimental tests that make up factorial design and its center points were performed. Later, the correlation between the response variables and the input variables was determined using a second-order model. If the quadratic terms (curvature) were not significant, the experimental test stopped and the data were fixed to a first-order correlation. Otherwise, it was necessary to perform the axial points and propose a new model (Hicks, 1982; Montgomery, 2013). The ash analysis was performed in duplicate, and the deviations from the average value of the response were a mass yield of 5% and an ash content of 0,5%.

Results and discussion

Coals: Tables 3 and 4 show the proximate analysis and contact angle values of raw coal.

Table 3. Properties of coal samples (raw)

Analysis (db)	Caypa coal	Guachinte coal
Volatile matter (%)	40,89	29,80
Ash (%)	3,97	31,40
Sulphur (%)	0,65	0,80
Heat value (KJ/Kg)	32 003	21 174

Source: Authors

Table 4. Contact angle values of coal samples (raw)

Contact angle	Caypa coal	Guachinte coal
Distilled water $\pm 2^\circ$	63,1	60,9
Methylene iodide $\pm 2^\circ$	27,2	31,0

Source: Authors

The results indicate that Caypa coal and Guachinte coal are bituminous (Leonard and Hardinge, 1991). Caypa coal exhibits higher values in volatile matter than Guachinte coal. It was observed that the ash content for Guachinte coal (31,4%) exhibits a higher value than Caypa coal (3,97%). Caypa coal and Guachinte coal had relatively close sulfur contents (0,65 and 0,8%, respectively). Ash content, heat value, and contact angle are correlated with each other, as can be seen in Tables 3 and 4, where Caypa coal has a low ash content (3,97%) with a higher heat value (32003 KJ/kg) and contact angle ($63,1^\circ$), compared to Guachinte coal, which has higher ash content (31,40%), with low heat value (21174 KJ/kg) and contact angle ($60,9^\circ$). These results may be attributed to the difference in hydrophobic sites on the coal surface of each sample, indicating that the Caypa coal could have a higher degree of hydrophobicity than Guachinte coal. This result may be due to the chemical (quantity and types of functional groups on the surface of the coal) and geological nature of each sample. The contact angle values in methylene iodide are lower than those measured with water (Table 4), which could be due to the increase in the dispersion component on coal surface. (Gutiérrez *et al.*, 1984; Piñeres and Barraza, 2011, 2012). Figures 2 and 3, which do not have the same scale, show the spectra obtained using Fourier Transform Infrared Spectroscopy (FTIR) on both coal samples, with which it was possible to qualitatively identify the functional chemical groups present. Qualitatively, the intensity of each peak at a given wavelength is considered to be directly related to the group concentration. The spectrum shows a vibration variety corresponding to groups such as: $-\text{NH}-\text{NH}_2-\text{OH}-$ ($3\ 400-3\ 700\ \text{cm}^{-1}$), CH_2 , CH_3 ($2\ 850-2\ 920\ \text{cm}^{-1}$), $-\text{C}=\text{O}-\text{O}-\text{CO}$, $\text{C}=\text{C}-\text{OH}$ (aromatic), $\text{C}=\text{O}$, $\text{C}=\text{C}$, aromatic $-\text{OH}$ ($1\ 580-1\ 800\ \text{cm}^{-1}$), minerals ($460-540$ and $1\ 000-1\ 050\ \text{cm}^{-1}$), aromatic ($600-920\ \text{cm}^{-1}$), $\text{C}=\text{O}$, aromatic $-\text{O}-\text{aromatic}$ ($1\ 100-1\ 380\ \text{cm}^{-1}$), nitrite groups attached to alkenes and aromatic structures ($1\ 330-1\ 530\ \text{cm}^{-1}$), short aliphatic chains ($2850\ \text{cm}^{-1}$), and long aliphatic chains (2920 and $3920\ \text{cm}^{-1}$).

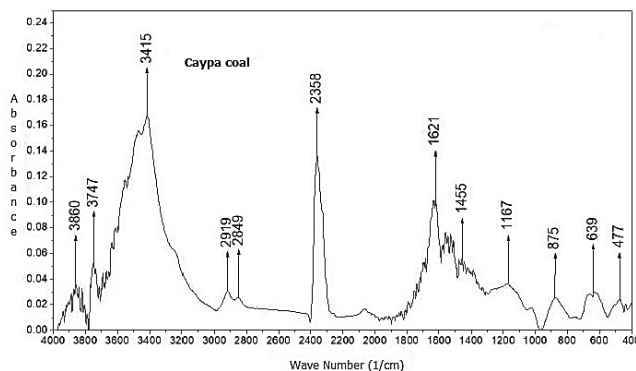


Figure 2. FTIR Analysis for Caypa coal.

Source: Authors

It is worth highlighting that these bands represent characteristic groups, and a specific structure cannot be specified, which may be attributed to the complex chemical structure of coal. For example, the $\text{C}=\text{C}$ group can be attached to simple or complex aromatic structures. The characteristic wavelengths

of these groups were taken from other works carried out with bituminous coals (Sobkowiak *et al.*, 1984; Cooke *et al.*, 1986; Solomon and Carangelo, 1988; Shu *et al.*, 2002). Based on the reported wavelengths, Figure 3 shows that Guachinte coal presents a large number of functional groups that contain oxygen, $-\text{C}=\text{O}-\text{O}-\text{CO}$, $\text{C}=\text{C}-\text{OH}$ (aromatic), $\text{C}=\text{O}$, $\text{C}=\text{C}$, and aromatic $-\text{OH}$ in comparison with Caypa coal (Figure 2). Caypa coal has less minerals than Guachinte coal, which can be corroborated through proximate analysis (Table 3), with Guachinte coal having the highest mineral quantity (Table 3) and the highest intensity of the corresponding band. Caypa coal has a lower concentration of the aromatic $-\text{O}-\text{aromatic}$ group compared with Guachinte coal. It was also observed that the two coal samples show close values regarding the CH_2 , CH_3 and $-\text{NH}-\text{NH}_2-\text{OH}-$ groups.

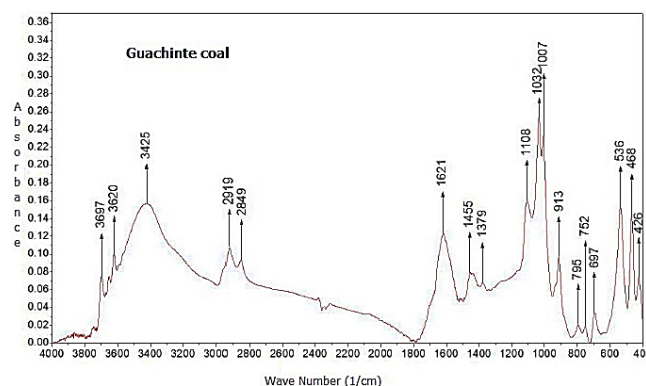


Figure 3. FTIR Analysis for Guachinte coal.

Source: Authors

Effect of Flomin F-425 and diesel oil on mass yield and ash percentage of the clean coal: The effect of collector and frother concentration on mass yield, ash content, and ash removal of floats on a dry basis is shown in Table 5. It was observed that Caypa coal reported a yield higher than 80% (84,63-98,39%). The highest value was obtained by adding 1,28 kg/ton of coal and 40 ppm of collector and frother concentration, respectively; while, for the Guachinte coal, a yield range between 74,63 and 94,71% was obtained. Its highest value (94,71%) was reached at 0,96 kg/ton of coal of collector concentration and 30 ppm frother concentration. It is also shown in Table 5 that, for all the conditions used in the experimental procedure, the coal samples generally showed a significant decrease in the ash content with respect to their initial value (3,97 and 31,4%, Table 3). The largest value in the ash removal for Caypa coal was 83,75% (0,65% of ash content), obtained at a collector and frother concentration of 0,64 kg/ton of coal and 20 ppm, respectively; whereas, for Guachinte coal, the greatest ash removal value was 71,46% (8,96% of ash content), which was reached at 0,96 kg/ton of coal of collector concentration and 10 ppm of frother concentration.

It is worth highlighting that the obtained ash content of 0,65% is the lowest value reported in the literature using a single-stage test-rig loop flotation column (without chemical reagent addition such as HF and HCl, among others), which is considered to be an ultra-clean coal obtained through a physical

cleaning process. The sample had an initial ash content of 3,97%, which is considered relatively low. Theoretically, the lower the ash content in a coal sample, the greater the degree of difficulty in reducing this value through a physical cleaning process, because the mineral matter associated with this coal type (low in ash) is normally part of its molecular structure, thus making it very difficult to eliminate. This indicates that the coal sample used had a high degree of mineral matter release. Likewise, the flotation column had a bubble size distribution that promoted a good bubble-coal particle adhesion, thus proving the effectiveness and selectivity of test-rig loop flotation columns (Piñeres and Barraza, 2012).

Table 5. Results of float samples

CC(kg/ton)/ FC(ppm)	Mass yield (wt %)		Ash (wt %) db		Ash removal (wt %) db	
	Caypa	Guachinte	Caypa	Guachinte	Caypa	Guachinte
0,64/20	84,63	84,65	0,65	11,71	83,75	62,71
0,64/40	90,97	89,94	1,12	13,98	72,00	55,48
1,28/20	91,34	82,04	0,76	11,84	81,00	62,29
1,28/40	98,39	91,20	1,33	17,83	66,75	43,22
0,96/30	96,67	90,02	0,94	14,95	76,50	52,39
0,96/30	97,59	94,71	0,85	15,88	78,75	49,43
0,96/30	95,62	90,90	0,96	15,10	76,00	51,91
0,96/30	97,46	92,49	1,13	14,93	71,75	52,45
0,96/30	96,00	94,51	1,22	15,22	69,50	51,53
0,96/50	97,74	86,18	1,61	15,42	59,75	50,89
1,60/30	97,32	84,80	1,24	12,28	69,00	60,89
0,96/10	90,98	74,63	0,68	8,96	83,00	71,46
0,32/30	91,34	88,94	0,74	16,99	81,50	45,89

Source: Authors

The results show that the mass yield tends to increase with the frother concentration increase for the two coal samples (Table 5). The maximum mass yield values for Caypa coal (98,39%) and for Guachinte coal (94,71%) were obtained by adding 40 and 30 ppm of frother concentration, respectively; whereas, for ash removal, an opposite effect was observed: with the frother concentration increase, the ash removal tends to decrease (the ash content increases when the frother concentration increases) for both samples. The maximum value of the ash removal for Caypa coal was 83,75% (the lowest value for ash content was 0,65%), and, for Guachinte coal, it was 71,46% (ash content of 8,96%). They were obtained when 20 and 10 ppm of frother concentration were added, respectively.

The high mass yield obtained at high frother concentrations is due to the decrease in bubble diameter obtained under these conditions (increase in the frother concentration) as a consequence of water surface tension decrease (Fuerstenau and Pradip, 1982; Finch *et al.*, 2008; Piñeres and Barraza, 2012). This effect may be attributed to mass transfer at the water-frother interface, which produces a surface tension gradient, thus generating spherical, small-sized air bubbles with a rigid surface (increase in available surface area of air bubbles) and, likewise, increasing air bubble hydrophobicity, favoring particle-bubble adhesion and increasing the mass

yield. According to the results in Table 5 we can see that the test-rig loop flotation column used reported a good performance for coal beneficiation (Fuerstenau and Pradip, 1982; Finch *et al.*, 2008).

The frother used was Flomin F-425, a non-ionic, completely water miscible reagent that has a hydrophilic polar group (mixture of alcohol) at one end and a hydrophobic non-polar group (glycol ether) at the other. Its molecular structure can be represented as: $\text{CH}_3\text{--}[\text{O--C}_3\text{H}_6]_n\text{--OH}$. Due to its amphiphilic nature, Flomin F-425 orients its hydrophilic group (polar) towards water, while its hydrophobic group (non-polar) is oriented towards the air bubble. The action of Flomin F-425 at the air bubble-water interface seems to be halfway between being completely lying down and fully standing, which suggests the formation of loops and coiling up at the interface with the frother molecule. The addition of Flomin F-425 to the slurry (coal-water) breaks the hydrogen bridges that form the water molecule (the hydrogen bridges create high surface tension in the water) and decreases its surface tension, causing the molecules to tend to lie at the surface, possibly increasing the viscosity of the froth and, therefore, their stability. The action of this frother can be attributed to the interaction of the Flomin F-425 oxygenated polar group (Flomin F-425 has several oxygenated groups in the molecular chain), which acts strongly with the oxygen-containing functional groups on the surface of the coal through hydrogen bridges (decreasing hydrophilic sites on coal surface), thus generating a stable coal particle-bubble adhesion (Fuerstenau and Pradip, 1982; Finch *et al.*, 2008; Gupta *et al.*, 2009).

Table 5 shows that the mass yield tends to increase lightly with the collector concentration increase for Caypa coal, the maximum mass yield value (98,39%) was reached when 1,28 kg of collector/ton of coal was added. On the other hand, the opposite effect occurred with ash removal; when the collector concentration increases, ash removal tends to decrease slightly (ash contents increase with the collector concentration increases). The maximum value of the ash removal for Caypa coal was 83,75% (ash content of 0,65%), which was obtained at 0,64 kg of collector/ton of coal. Similarly, for Guachinte coal, the mass yield tends to decrease when the collector concentration increases. The maximum value obtained for mass yield (94,71%) was reached when 0,96 kg of collector/ton of coal were added. The opposite effect occurred once more with ash removal; with the increase in collector concentration, ash removal tends to increase slightly (ash contents decrease when the collector concentration increases). The maximum ash removal value for Guachinte coal was 71,46% (ash content of 8,96%), which was obtained at 0,96 kg of collector/ton of coal.

Diesel oil, a non-polar type of hydrocarbon (insoluble in water), was used as collector. It is approximately 75% aliphatic and 25% aromatic with the following molecular structure: $\text{C}_{12}\text{H}_{26}$. It adheres to the coal surface in order to increase hydrophobicity and improve particle-bubble adhesion. The action mechanism of diesel oil may be due to the interaction of the non-polar chain with the carbonaceous (hydrophobic) sites on the surface, displacing the water molecules and

facilitating their adhesion. The action of this collector can be attributed to hydrophobic bonding of the aliphatic chain and π bonding of the aromatic rings with the hydrophobic and aromatic sites on the coal surface (Jia *et al.*, 2002).

The differences in the behavior of the two coal samples with respect to the employed frother and collector concentrations mainly depend on the mineral types, occurrence mode, and ion concentration (valence) of the coal structure. Nevertheless, the liberation grade of the mineral matter during the grinding process and the interaction between flotation reagents (collector and frother) and coal surface affects floatability and the selectivity of the test-rig loop flotation column (Fuerstenau *et al.*, 1983; Arnold and Aplan, 1986a, 1986b).

Statistical analysis: The data for mass yield and ash content were statistically analyzed using the Design Expert software. Table 2 presents the nomenclature used, and Table 6 shows the results of the statistical analysis of the variables and their interactions. The regression models for each coal are described using Equations (1) to (4):

Caypa coal:

$$\begin{aligned} 1/\text{Mass yield} = & 0,01034535 - 2,38E^{-4}A - 2,69E^{-4}B \\ & + 2,04E^{-4}AB + 1,77E^{-4}A^2 \\ & + 1,77E^{-4}B^2 - 3,28E^{-4}A^2B \\ & + 8,12E^{-6}AB^2 \end{aligned} \quad (1)$$

$$\begin{aligned} 1/\text{Ash}(db) = & 0,99731899 - 0,19265115A \\ & - 0,30033308B + 0,02042366AB \\ & + 0,05638366A^2 + 0,03985948B^2 \\ & - 2,05E^{-3}A^2B + 0,10173877AB^2 \end{aligned} \quad (2)$$

Guachinte coal:

$$\begin{aligned} \text{Mass yield} = & 95,53 - 0,8381A + 3,79B \\ & + 1,09AB - 2,03B^2 - 5,26B^2 \end{aligned} \quad (3)$$

$$\begin{aligned} \sqrt{\text{Ash}(db)} = & 3,9 - 0,2184A + 0,33B + 0,1162AB \\ & - 0,0263A^2 - 0,2028B^2 \\ & - 0,0554A^2B + 0,344AB^2 \end{aligned} \quad (4)$$

For both studied coals, Table 6 shows that these model equations have a significant effect ($F > F_c$), whereas the lack of fit shows no significant effect ($F < F_c$), thus indicating that the expression found is a reasonable approximation for the surface in the region considered in the experiment (Hicks, 1982; Montgomery, 2013).

Table 6 shows that collector and frother concentrations present a significant effect on mass yield for Caypa coal ($F > F_c$), while, for Guachinte coal only frother concentration presents a significant effect ($F > F_c$). Meanwhile, collector concentration does not report any significant effect ($F < F_c$). Likewise, curvature effects were found for the different

variables used, showing that, in the case of mass yield, the collector and frother concentrations are significant for the quadratic terms (A^2 , B^2) on Caypa coal ($F > F_c$), while Guachinte coal only reports a significant effect in the quadratic term of the frother concentration (B^2) ($F > F_c$). It is also possible to notice that the interaction between AB and A^2B is only significant ($F > F_c$) for Caypa coal (Hicks, 1982; Montgomery, 2013).

The significance of the frother concentration on the Caypa and Guachinte coals indicates an effective interaction between frother agent and coal surface, which increased floatability. Nevertheless, bubble hydrophobicity can be increased as a consequence of the association of water molecules with the frother's non-polar group on the surface of the bubbles, thus promoting coal particle-bubble adhesion. The significance of collector concentration ($F > F_c$) on the Caypa coal shows the interaction between the collector and the coal's surface. The opposite effect was observed for the Guachinte coal, where collector concentration was not significant ($F < F_c$). This may be attributed to the lack of affinity between the collector used and coal surface, due to the differences in their chemical and mineralogical structures (mineral specie and valence), surface properties, and the functional groups of the samples. Therefore, the collector agent shows a different behavior for each coal sample (Jia *et al.*, 2002).

Table 6 shows that collector and frother concentrations have a significant effect on ash content for the two coal samples ($F > F_c$), while the frother concentration of Guachinte coal ($F > F_c$) has a significant curvature effect (B^2 , AB^2). It is also possible to notice that the interaction AB and AB^2 is significant ($F > F_c$) only for Guachinte coal, which shows that the flotation reagents (collector and frother) interact with mineral matter on the surface of the coal, thus affecting the selectivity of the flotation process (Hicks, 1982; Montgomery, 2013).

Table 6. Result of the statistical analysis of the variables and their interactions

	Mass yield Caypa			Mass yield Guachinte			Ash (db) (%) Caypa			Ash (db) (%) Guachinte		
	df	F	F_c	df	F	F_c	df	F	F_c	df	F	F_c
Model	7	20,3	2,9	5	11,0	3,1	7	8,0	2,9	7	48,8	2,9
A	1	11,9	6,6	1	0,9	5,6	1	8,9	6,6	1	48,9	6,6
B	1	15,2	6,6	1	19,2	5,6	1	21,6	6,1	1	111,7	6,6
AB	1	8,8	6,6	1	0,8	5,6	1	0,1	6,6	1	13,8	6,6
A^2	1	11,4	6,6	1	4,8	5,6	1	1,3	6,6	1	1,2	6,6
B^2	1	11,4	6,6	1	32,2	5,6	1	0,6	6,6	1	73,3	6,6
A^2B	1	11,3	6,6				1	0,0	6,6	1	1,6	6,6
AB^2	1	0,0	6,6				1	1,2	6,6	1	60,7	6,6
Residual	5			7			5			5		
Lack of fit	1	7,0	7,7	3	1,8	6,6	1	0,4	7,7	1	3,9	7,7
Pure error	4			4			4			4		
Total	12			12			12	2,9		12	48,8	2,91

Source: Authors

The differences in the values of the mass yield and ash content may be attributed to the differences in the hydrophobicity of each coal, as a consequence of the different degrees of carbonization, petrographic composition, mineralogical distribution, and chemical nature.

Conclusions

Caypa and Guachinte coals presented high mass yield values and low ash content values for all flotation column operation conditions. Caypa coal reported a yield higher than 80%, (84,63-98,39%), and the highest value was reached by adding 1,28 kg/ton of coal and 40 ppm of collector and frother concentration, respectively; while Guachinte coal obtained a yield range between 74,63 and 94,71%. Its highest value was obtained at 0,96 kg/ton of coal of collector concentration and 30 ppm frother concentration. The lowest ash content value for Caypa coal was 0,65%, obtained at collector and frother concentrations of 0,64 kg/ton of coal and 20 ppm, respectively; whereas, for Guachinte coal, the lowest ash content value of ash content was 8,96%, obtained at 0,96 kg/ton of coal of collector concentration and 10 ppm of frother concentration. For Caypa coal, the mass yield tends to increase (low ash removal) when the collector and frother concentrations increase, while the mass yield of Guachinte coal tends to decrease (high ash removal) when the collector concentration increases (low ash removal) at high frother concentrations. The ash content of 0,65% obtained is the lowest value reported in the literature using a single-stage test-rig loop flotation column.

Acknowledgements

The authors are grateful to Universidad del Atlántico for their financial support within the framework of project Caribbean Impact: "Production of activated coals to remove heavy metals starting at coal mining waste benefited by flotation processes" (ING03.CIC2014).







References

- Arnold, B. and Aplan, F. (1986a). The effects of clays slimes on coal flotation, part 1: the nature of the clay. *International Journal of Mineral Processing*, 17(3-4), 225-242. 10.1016/0301-7516(86)90058-X
- Arnold, B. and Aplan, F. (1986b). The effects of clays slimes on coal flotation, part 2: The role of water quality. *International Journal of Mineral Processing*, 17(3-4), 243-260. 10.1016/0301-7516(86)90059-1
- Bellich, S. (2016). *Diseño y montaje de una columna de flotación a escala de laboratorio para la remoción de la materia mineral presente en carbones térmicos* [Undergraduate thesis, Universidad del Atlántico, Barranquilla, Colombia]. <http://biblioteca.uniatlantico.edu.co/cgi-bin/koha/opac-detail.pl?biblionumber=78734>
- Brady, G., Gauger, A. (1940). Properties of coal surface. *Industrial and Engineering Chemistry*, 32(12), 1599-1604. 10.1021/ie50372a019
- Cooke, N., Maynard, F., and Gaikwad, R. (1986). FT-i.r spectroscopic analysis of coals and coals extracts. *Fuel*, 65(9), 1254-1260. 10.1016/0016-2361(86)90238-3
- Dobby, G. and Finch, J. (1986). Flotation column scale-up and modelling. *CIM Bulletin*, 79(891), 89-96. <https://store.cim.org/en/flotation-column-scale-up-and-modelling>
- Finch, J., Nasset, J., Acuña, C. (2008). Role of frother on bubble production and behaviour in flotation. *Minerals Engineering*, 21(12-14), 949-957. 10.1016/j.mineng.2008.04.006
- Fuerstenau, D. W. (1982). Adsorption of frother at coal/water interfaces. *Colloid and Surface*, 4(3), 213-227. 10.1016/0166-6622(82)80019-X
- Fuerstenau, D. W., Rosenbaum, J., and Laskowski, J. (1983). Effect of surface functional groups on the flotation of coal. *Colloid and Surface*, 8(2), 153-173. 10.1016/0166-6622(83)80082-1
- Gupta, A., Banerjee, P., and Mishra, A. (2009). Influence of chemical parameters on selectivity and recovery of fine coal through flotation. *International Journal of Mineral Processing*, 92(1-2), 1-6. 10.1016/j.minpro.2009.02.001
- Gutiérrez, J., Purcell, J., and Aplan F. (1984). Estimating the hydrophobicity of coal. *Colloids and Surface*, 12, 1-25. 10.1016/0166-6622(84)80086-4
- Hangil, P., Junyu, W., and Liguang, W. (2016). A comparative study of methyl cyclohexanemethanol and methyl isobutyl carbinol as frother for coal flotation. *International Journal of Mineral Processing*, 155, 32-44. 10.1016/j.minpro.2016.08.006
- Hicks, D. (1982). *Fundamental concepts in the design of experiments*. Saunders Collage Publishing.
- Honaker, R., Monhanty, M., and Crelling J. (1996). Coal maceral separation using column flotation. *Minerals Engineering*, 9(4), 449-464. 10.1016/0892-6875(96)00030-1
- Jia, R., Harris, G., and Fuerstenau, D. W. (2002). Chemical reagents for enhanced coal flotation. *International Journal of Coal Preparation and Utilization*, 22(3), 123-149. 10.1080/07349340213847
- Leonard, J. and Hardinge, B. (1991). *Coal Preparation*. Society for Mining, Metallurgy and Exploration, Inc.
- Montgomery, D. (2013). *Design and Analysis of Experiments*. John Wiley & Sons.
- Peng, Y., Liang, L., Tan, J., Sha, J., and Xie, G. (2015). Effect of flotation reagent adsorption by different ultra-fine coal particles on coal flotation. *International Journal Mineral Processing*, 142, 17-21. 10.1016/j.minpro.2014.12.005
- Piñeres, J. and Barraza, J. (2011). Energy barrier of aggregates coal particle-bubble through the extended DLVO theory. *International Journal of Mineral Processing*, 100(1-2), 14-20. 10.1016/j.minpro.2011.04.007
- Piñeres, J. and Barraza, J. (2012). Effect of pH, air velocity and frother concentration on combustible recovery, ash and sulphur rejection using column flotation. *Fuel Processing Technology*, 97, 30-37. 10.1016/j.fuproc.2012.01.004

- Piñeres, J., Mendoza, M., Téllez, M., and Jiménez, F. (2019). Level control loop design for a test-rig flotation column. *Journal of Physics: Conference Series*, 1219, 012014. 10.1088/1742-6596/1219/1/012014
- Polat, M., Polat, H., and Chander, S. (2003). Physical and chemical interactions in coal flotation. *International Journal of Mineral Processing*, 72(1-4), 199-213. 10.1016/S0301-7516(03)00099-1
- Sobkowiak, M., Reisser, E., Given, P., and Painter, P. (1984). Determination of aromatic and aliphatic CH groups in coal by FT-i.r. 1. Studies of coal extracts. *Fuel*, 63(9), 1245-1252. 10.1016/0016-2361(84)90433-2
- Solomon, P. and Carangelo, R. (1988). FT-i.r analysis of coal 2. Aliphatic and aromatic hydrogen concentration. *Fuel*, 67(7), 949-959. 10.1016/0016-2361(8)90095-6
- Shu, X., Wang, Z., and Xu, J. (2002). Separation and preparation of macerals in Shenfu coals by flotation. *Fuel*, 81(4), 495-501. 10.1016/S0016-2361(01)00106-5
- Wieslaw, S. (1994). *New trends in coal preparation technologies and equipment*. Gordon and Breach Publishers.
- Yoon, R. (1993). Microbubble flotation. *Minerals Engineering*, 6(6), 619-630. 10.1016/0892-6875(93)90116-5

A Structural Design Comparison Between Two Reinforced Concrete Regular 6-Level Buildings using Soil-Structure Interaction in Linear Range

Comparación de diseño estructural entre dos edificaciones de concreto armado de seis niveles utilizando interacción suelo-estructura en el rango lineal

Nelson A. López M. ¹, Gabriela E. Pérez M. ², Christian F. Castro P. ³, Juan C. Vielma P. ⁴, Leonardo J. López M. ⁵, José D. Alviar M. ⁶, Carlos A. Romero R. ⁷, David P. Guerrero C. ⁸, and Vanessa V. Montesinos M. ⁹

ABSTRACT

Structural engineers commonly design superstructures as fixed at the base and transmit the reactions to the infrastructure in order to design the foundation system and estimate the displacement of the soil while disregarding the change in seismic response that this induces. In this article, the foundation system was transformed into equivalent springs, and the seismic response in the linear range was compared and quantified, obtaining results such as increased periods, increased amounts of steel reinforcement in beams (between 7% and 25%) and columns (between 29% and 39%), an increase in the number of stirrups per linear meter (between 3% and 11% in columns and between 5% and 45% in beams) and drifts (between 1% and 14%), and a decrease in basal shear (up to 20%), which directly affects the design of the structure. This study concludes that the inclusion of the soil-structure interaction is necessary for structural design in the linear range.

Keywords: seismic response, foundation system, soil-structure interaction, linear range

RESUMEN

Comúnmente, los ingenieros estructurales diseñan superestructuras como empotradas en la base y transmiten las reacciones a la infraestructura para diseñar el sistema de cimientos y estimar los desplazamientos del suelo, obviando el cambio en la respuesta sísmica que esto induce. En este artículo se transformó el sistema de cimientos en resortes equivalentes y se comparó y cuantificó la respuesta sísmica en el rango lineal, obteniendo resultados como aumento de los períodos, aumento de las cuantías de acero de refuerzo en vigas (entre 7% y 25%) y columnas (entre 29% y 39%) un aumento de la cantidad de estribos por metro lineal (entre 3% y 11% en columnas y entre 5% y 45% en vigas) y las derivas (entre 1% y 14%), y una disminución de cortantes basales (hasta 20%), lo que afecta de forma directa el diseño de la estructura. Este estudio concluye que es necesaria la inclusión de la interacción suelo estructura en el diseño estructural en el rango lineal.

Palabras clave: respuesta sísmica, sistema de cimientos, interacción suelo-estructura, rango lineal

Received: April 30th, 2020

Accepted: May 25th, 2021

¹Civil engineer, Universidad Centroccidental Lisandro Alvarado, Venezuela. MSc. in Mechanics Applied to Construction, Universidad Centroccidental Lisandro Alvarado, Venezuela. Affiliation: PhD. Candidate, Pontificia Universidad Católica de Chile, Chile. E-mail: nalopez4@uc.cl

²Civil engineer, Universidad Politécnica Salesiana, Ecuador. E-mail: gabype33@outlook.es

³Civil engineer, Universidad Politécnica Salesiana, Ecuador. E-mail: christian20castro21@hotmail.com

⁴Civil engineer, Universidad Centroccidental Lisandro Alvarado, Venezuela. PhD. from Universidad Politécnica de Cataluña. Affiliation: University professor, Pontificia Universidad Católica de Valparaíso. E-mail: juan.vielma@pucv.cl

⁵Civil engineer, Universidad Centroccidental Lisandro Alvarado, Venezuela. MSc. in Mechanics Applied to Construction, Universidad Centroccidental Lisandro Alvarado, Venezuela. Affiliation: PhD. Candidate, Pontificia Universidad Católica de Chile, Chile. E-mail: ljlopez@uc.cl

⁶Civil engineer, Universidad Central de Venezuela, Venezuela. PhD. in Structures and Geotechnics, Universidad Central de Venezuela, Venezuela. Affiliation: University professor, Universidad Politécnica Salesiana, Ecuador. E-mail: jalviar@ups.edu.ec

⁷Civil engineer, Universidad del Zulia. Venezuela. MSc. in Structures, Universidad del Zulia. Venezuela. Affiliation: Professor, Universidad Politécnica Salesiana,

Ecuador. E-mail: cromero@ups.edu.ec

⁸Civil engineer, Universidad Central del Ecuador, Ecuador. MSc. in Structures, Escuela Politécnica Nacional, Ecuador. Affiliation: University professor, Universidad Politécnica Salesiana, Ecuador. E-mail: dguerrero@ups.edu.ec

⁹Civil engineer, Universidad Centroccidental Lisandro Alvarado, Venezuela. Specialist in Structures, Universidad Católica Andres Bello, Venezuela. E-mail: vanessamontesinos22@gmail.com

How to cite: López, N., Pérez, G., Castro, C., Vielma, J., López, N., Romero, C., Alviar, J., Guerrero, D., and Montesinos, V. (2021). A Structural Design Comparison Between Two Reinforced Concrete Regular 6-Level Buildings using Soil-Structure Interaction in Linear Range. *Ingeniería e Investigación*, 42(1), e86819. <https://doi.org/10.15446/ing.investig.v42n1.86819>



Attribution 4.0 International (CC BY 4.0) Share - Adapt

Introduction

Structural engineering always aims for the best way to represent a real structure in a mathematical model in order to obtain the best approach to the reality. Soil-structure interaction is one of many ways to get closer to the behavior of a real structure. There are many ways to represent this relationship: it could be static or dynamic, linear or non-linear, and the possible combinations among them (Zeevaert, 1980; Mejía-Bermejo, 2017; Hernández-Velasco, 2013; Galicia and León, 2007; Villareal, G. 2009). To represent soil and substructure displacements, it is necessary to calculate the foundation system, in order to substitute it with equivalent springs using the concepts of rotational and translational stiffness (Uribe-Escamilla, 2000; Weaver and Gere, 1990; López *et al.*, 2019), which express that a structural element can be represented through its rotational and translational stiffness coefficients, as shown in Equations (1) and (2).

$$F = K_T d \quad (1)$$

$$F = K_R \theta \quad (2)$$

where F is the force applied on a structural element; K_T is the element's translational stiffness constant; d is the displacement in the force's direction; M is the torsional or bending moment applied on the structural element; K_R is the element's rotational stiffness constant; and θ is the rotation in the moment's direction. To make soil-structure interaction possible, it is necessary to obtain the values of F , d , M , and θ . Thus, the values of K_T and K_R , can be calculated for each direction, representing the equivalent spring constants for the foundation system, as shown in Figure 1. It is worth noting that that K_T and $F = K_R$ remain linear, with a single value for each direction (Wu and Pantelides, 2019).

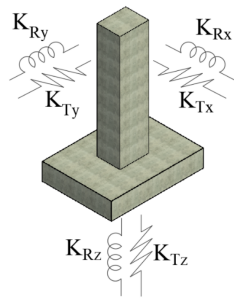


Figure 1. Equivalent springs for foundation system.
Source: (Castro-Pilco and Pérez-Martínez, 2020)

After calculating the equivalent springs, the initial structural model fixed at the base is submitted to a new structural analysis using springs (Figure 2), thus allowing changes in global stiffness and, hence, a variation in the results.

Methodology

This research was based on basic structural concepts for soil-structure interaction in linear range. The structure used for this research was residential and consisted of six levels, one elevator, one stair module, with 3 types of foundation soil and

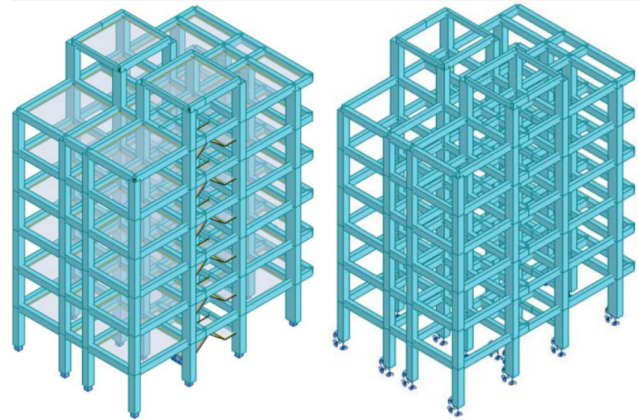


Figure 2. Structural model with fixed supports (left) and equivalent springs (right) at the base.
Source: (Authors)

spectral parameters typical from Quito, Ecuador. The main objective of this research was to quantify the differences in seismic response and structural members design of the same regular reinforced concrete structure using soil-structure interaction in linear range. Basic structural dynamics applied to building analysis and design explains how to obtain the main structural criteria in order to accept or reject the structural member cross section, with the vibrational modes, periods, and drifts being the most important, including the force diagrams for structural member design. Based on the basic concepts of structural dynamics, the modal matrix and the structure's frequencies can be calculated from Equations (3), (4), and (5).

$$[M] \{\ddot{x}\} + [C] \{\dot{x}\} + [Ke] \{x\} = 0 \quad (3)$$

$$\phi = \text{eigenvectors} \{[Ke], [M]\} \quad (4)$$

$$w^2 = \text{eigenvalues} \{[Ke], [M]\} \quad (5)$$

where $[Ke]$ is the structure's equivalent stiffness matrix, which depends on the cross section, inertia, length, supports, and material of each structural member for 2D planar analysis; $[M]$ is the mass matrix of the structure; $[C]$ is the matrix of damping factor, which is considered to be constant in this research; \ddot{x} is the structure acceleration vector; \dot{x} is the structure velocity vector; x is the structure displacement vector; ϕ is the modal matrix; and w is the angular velocity for each vibrational mode.

In this research, three different inelastic spectra were considered, and the general solution was obtained by performing modal-spectral analysis, with modal truncation for three vibration modes per floor, and then obtaining the response of each degree of freedom (DOF) by applying Equations (6) and (7).

$$\ddot{D}_n + 2\zeta_n w_n \dot{D}_n + w_n^2 D_n = \ddot{u}_g \quad (6)$$

$$u_n = \frac{\phi_n^T M l}{m_n} \phi_n D_n \quad (7)$$

where ζ_n is the damping value per mode; w_n is the angular velocity per mode; D_n is the modal displacement value per

mode; \ddot{u}_g is the spectral acceleration; ι is the directional vector for the spectral acceleration (x, y, z); u_n is the displacement for each DOF and each vibrational mode; m is the modal mass; and n is the number of each vibrational mode. The total response is estimated through the CQC method. These calculations were made with Autodesk Robot Structural 2020, academic version (547L1, 900-95470127).

The $[Ke]$ factor is the key for the structural changes in results using soil-structure interaction due to the change in stiffness in the first level, which directly affects global stiffness. If a structure is assumed to be fixed at the base or uses equivalent springs, stiffness changes according to the case. The fixed element has translational and rotational restrictions at the base, whereas the non-fixed element has no restrictions, thus allowing displacements and rotations at the base and increasing displacements. According to the literature (Falconí, 2008; Chopra, 1980; Reyes, 1998; Paz, 1992), stiffness decreases are in accordance with equivalent stiffness theory, which expresses an equivalence with the configuration through Equation (8), for springs in parallel arrangement, and Equation (9), for springs in continuous arrangement.

$$Ke = \sum_{i=1}^n K \quad (8)$$

$$\frac{1}{Ke} = \sum_{i=1}^n \frac{1}{K_n} \quad (9)$$

The stiffness modification at the base directly affects the $[Ke]$ structure matrix, modifying the periods, frequency, modal response, and modal displacements. Some studies express that damping is another important factor (Lutes and Sarkani, 1995; Cruz, and Miranda, 2017). However, this value has remained constant, imposing a 5,00% damping value corresponding to structures provided with reinforced concrete.

Analysis and discussion

Inelastic design spectrum

This research was based on three typical soil types from the city of Quito, Ecuador, with an acceleration value on rock according to a seismic hazard of 0,40 g. The three soil types were A, C, and E, based on the scale from A to E, with A being the best soil type, with a shear wave velocity greater than 1500,00 m/s; C, an intermediate soil, with shear wave velocities between 360 m/s and 760 m/s; and E, the worst soil type, with a shear wave velocity of less than 180 m/s. The inelastic spectrum by soil type used for the analysis are shown in Figure 3, as a fraction of gravity according to the Ecuadorian building regulations for seismic hazard (NEC, 2014).

Fixed superstructure analysis and design

The first step in the analysis is the correct design of the structure, in accordance with the regulations (ACI, 2014 2019; NEC, 2015; ASCE/FEMA, 2000), aiming to guarantee a

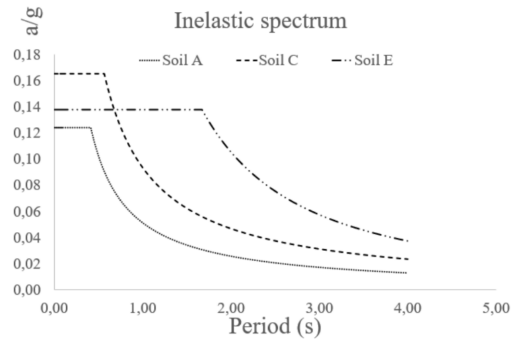


Figure 3. Inelastic seismic design spectrum for each soil type.
Source: Authors

good capacity, stiffness, and seismic response. Vibrational modes and displacements (mm) for the three main periods are shown in Figures 4, 5, and 6 for modal analysis with fixed structure. Note that these displacements are the result of the application of Equations (6) and (7) for each DOF and for each vibrational mode.

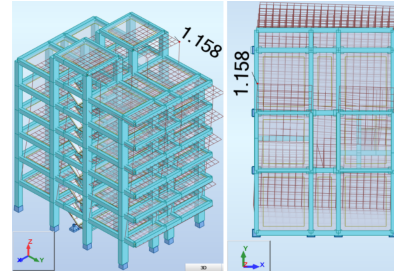


Figure 4. First vibrational mode (period 0,78 s).
Source: Authors

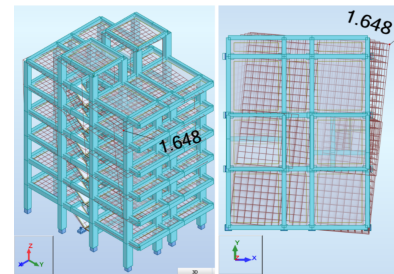


Figure 5. Second vibrational mode (period 0,65 s).
Source: Authors

Substructure analysis and design

Following the traditional procedure, reactions from the superstructure are turned into actions on the substructure, in order to analyze and design the foundation system for the three soil types. The sizes of the foundations have been selected so as not to exceed the allowable stresses at the foundation level, which are represented in Figures 10 and 11 by soil type. The influence of the foundation system was checked, concluding that there was no considerable difference in stress and displacements. The foundation system was analyzed

using equivalent springs for vertical displacements at the base to simulate soil elasticity (Figure 7), based on Ballast coefficient (Meli Piralla, 1986). The equivalent soil stiffness is shown in Table 1, using a finite element node spacing of 25 cm (de Macedo Wahrhaftig, 2020) (Figures 8 and 9).

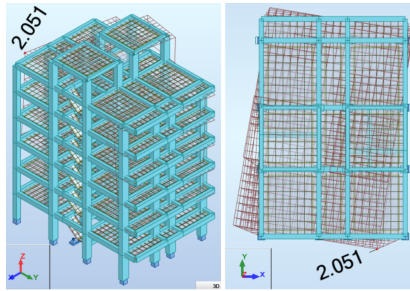


Figure 6. Third vibrational mode (period 0,58 s).

Source: Authors

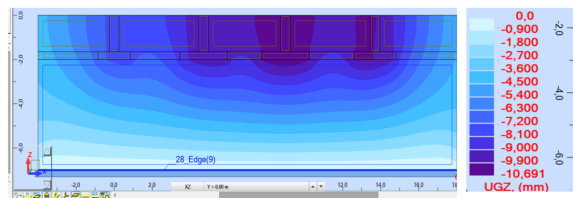


Figure 7. Isolines for displacements.

Source: Authors

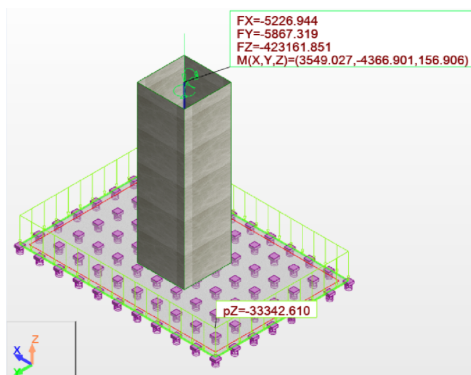


Figure 8. Foundation system using equivalent springs at the isolated foundation base (kN, kN.m).

Source: Authors

Table 1. Ballast coefficient for each soil type

Soil type	Ballast Coefficient (N/cm ³)	Equivalent stiffness (N/cm)
A	470,88	294 300,00
B	196,20	122 625,00
C	78,48	49 050,00

Source: Authors

The definitive dimensions for each foundation system and for each soil type are shown in Figures 10 and 11, according to (Pérez-Valcárcel, J., 2013; Garza-Vásquez, 2000; Paz, 1992).

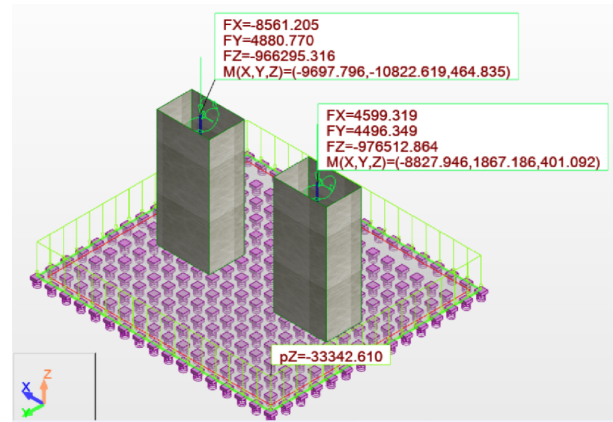


Figure 9. Foundation system using equivalent springs at the combined foundation base (kN, kN.m).

Source: Authors

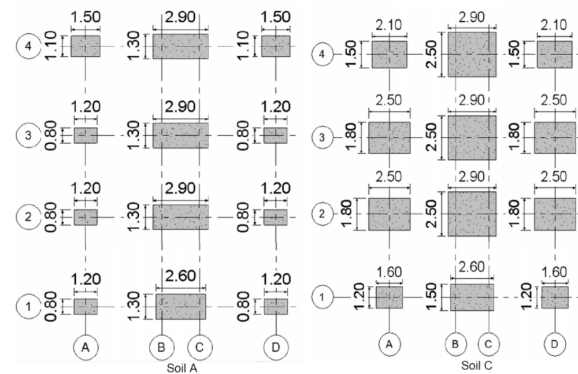


Figure 10. Foundation system for soils A and C (m).

Source: Authors

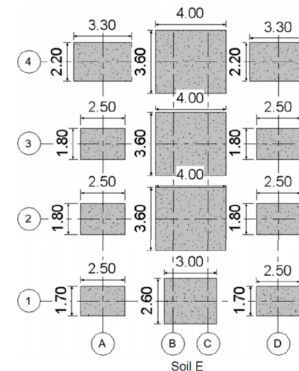


Figure 11. Foundation system for soil E (m).

Source: Authors

According to Equations (1) and (2), stiffness constants for each soil type are shown in Tables 2 to 7. After calculating the equivalent spring constants, the fixed supports were replaced, thus changing structure stiffness. Please note that, on average, stiffness decreases for soils A to E, with soil A being the best, and E the worst in terms of behavior.

Table 2. Equivalent translational springs constant for soil A

		Translational stiffness (MN/m)			
Axis		4	3	2	1
A	kx	164,41	127,78	126,47	56,81
A	ky	50,99	21,72	59,45	63,80
A	kz	1 030,00	1442,00	1 442,00	765,19
B	kx	242,20	122,52	131,38	49,58
B	ky	56,22	30,46	59,48	62,03
B	kz	1 177,00	1 177,00	1 177,00	1 000,00
C	kx	158,67	124,10	126,78	62,73
C	ky	55,48	58,61	52,50	63,09
C	kz	1 177,00	1 177,00	1 177,00	1 000,00
D	kx	202,59	134,92	125,81	50,78
D	ky	54,24	72,36	41,95	84,62
D	kz	1 030,00	1 442,00	1 442,00	765,15

Source: Authors

Table 3. Equivalent rotational springs constant for soil A

		Rotational stiffness (MN.m/rad)			
Axis		4	3	2	1
A	kx	393,65	243,77	247,05	94,97
A	ky	233,22	267,74	169,1	77,18
A	kz	5,40E ⁻⁴	6,40E ⁻⁴	8,30E ⁻⁵	1,50E ⁻⁴
B	kx	196,61	254,29	247,51	113,36
B	ky	220,77	250,66	169,24	81,66
B	kz	9,50E-05	2,70E ⁻⁴	2,40E ⁻⁵	7,80E ⁻⁵
C	kx	400,97	260,23	245,77	76,69
C	ky	220,48	173,36	189,31	77,78
C	kz	2,80E-04	5,60E ⁻⁴	1,60E ⁻⁴	3,80E ⁻⁵
D	kx	287,98	224,1	248,88	111,68
D	ky	224,77	134,98	216,23	18,68
D	kz	2,20E ⁻⁴	1,80E ⁻³	8,80E ⁻⁴	5,00E ⁻⁴

Source: Authors

Table 4. Equivalent rotational springs constant for soil C

		Rotational stiffness (MN.m/rad)			
Axis		4	3	2	1
A	kx	462,38	243,77	247,05	94,97
A	ky	247,21	267,74	169,1	77,18
A	kz	4,90E ⁻⁴	6,40E ⁻⁴	8,30E ⁻⁵	1,50E ⁻⁴
B	kx	196,61	254,29	247,51	113,36
B	ky	220,77	250,66	169,24	81,66
B	kz	9,50E ⁻⁵	2,70E ⁻⁴	2,40E ⁻⁵	7,80E ⁻⁵
C	kx	400,97	260,23	245,77	76,69
C	ky	220,48	173,36	189,31	77,78
C	kz	2,80E ⁻⁴	5,60E ⁻⁴	1,60E ⁻⁴	3,80E ⁻⁴
D	kx	341,03	224,1	248,88	111,68
D	ky	237,49	134,98	216,23	18,68
D	kz	1,90E ⁻⁴	1,80E ⁻³	8,80E ⁻⁴	5,00E ⁻⁴

Source: Authors

Analysis and design of the superstructure using equivalent springs

As shown in Figure 2, the fixed supports were replaced, and a new modal analysis including the new global stiffness was made. The first main comparison takes place on displacements and periods, as shown in Figures 12 to 14. Periods and displacements remained closer with the use of equivalent springs, and they were located at different points of the

Table 5. Equivalent translational springs constant for soil C

		Translational stiffness (MN/m)			
Axis		4	3	2	1
A	kx	193,12	127,78	126,47	56,81
A	ky	54,05	21,72	59,45	63,8
A	kz	772,52	1.079,13	1.078	527,32
B	kx	242,2	122,52	131,38	49,58
B	ky	56,22	30,46	59,48	62,03
B	kz	876,72	876,77	876,81	472,11
C	kx	158,67	124,1	126,78	62,73
C	ky	55,48	58,61	52,5	63,09
C	kz	876,72	876,77	876,81	472,11
D	kx	239,91	134,92	125,81	50,78
D	ky	57,31	72,36	41,95	84,62
D	kz	772,54	1 079,10	1 079,00	527,34

Source: Authors

Table 6. Equivalent translational springs constant for soil E

		Translational stiffness (MN/m)			
Axis		4	3	2	1
A	kx	164,41	127,78	126,47	56,81
A	ky	50,99	21,72	59,45	63,8
A	kz	1 030,00	1 442,00	1 442,00	765,19
B	kx	242,2	122,52	131,38	49,58
B	ky	56,22	30,46	59,48	62,03
B	kz	1 177,00	1 177,00	1 177,00	1 000,00
C	kx	158,67	124,1	126,78	62,73
C	ky	55,48	58,61	52,5	63,09
C	kz	1 177,00	1 177,00	1 177,00	1 000,00
D	kx	202,59	134,92	125,81	50,78
D	ky	54,24	72,36	41,95	84,62
D	kz	1 030,00	1 442,00	1 442,00	765,15

Source: Authors

Table 7. Equivalent rotational springs constant for soil E

		Rotational stiffness (MN.m/rad)			
Axis		4	3	2	1
A	kx	393,65	243,77	247,05	94,97
A	ky	233,22	267,74	169,1	77,18
A	kz	5,40E ⁻⁴	6,40E ⁻⁴	8,30E ⁻⁵	1,50E ⁻⁴
B	kx	196,61	254,29	247,51	113,36
B	ky	220,77	250,66	169,24	81,66
B	kz	9,50E ⁻⁵	2,70E ⁻⁴	2,40E ⁻⁵	7,80E ⁻⁵
C	kx	400,97	260,23	245,77	76,69
C	ky	220,48	173,36	189,31	77,78
C	kz	2,80E ⁻⁴	5,60E ⁻⁴	1,60E ⁻⁴	3,80E ⁻⁵
D	kx	287,98	224,1	248,88	111,68
D	ky	224,77	134,98	216,23	18,68
D	kz	2,20E ⁻⁴	1,80E ⁻³	8,80E ⁻⁴	5,00E ⁻⁴

Source: Authors

structure, in comparison with Figures 4 to 6, which means that foundation equivalent system reflects a similar response. On the other hand, results for frequencies and periods are shown in Tables 8 and 9, and the maximum displacements are shown in table 10 for each soil type and the first three vibrational modes. The frequencies decrease while the periods increase, as well as the maximum displacements. Additionally, the global stiffness estimate is shown in Table 11, which

decreases from soil E to soil A, meaning that the stiffness is not related only to the size of the foundation system, but also to the Ballast coefficient and the type of foundation (isolated or combined).

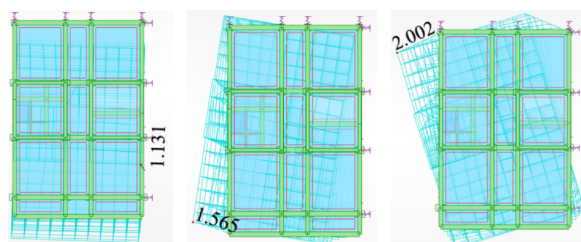


Figure 12. Maximum displacements for soil A (cm): 1st mode on the left, 2nd mode in the middle, and 3rd mode on the right.

Source: Authors

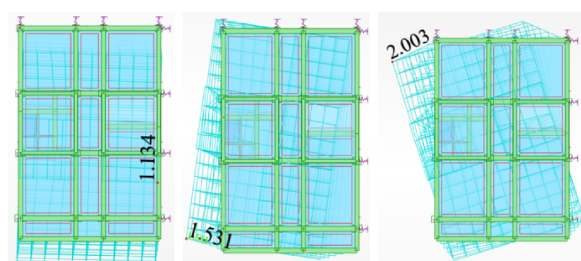


Figure 13. Maximum displacements for soil C (cm): the 1st mode on the left, the 2nd mode in the middle, and the 3rd mode on the right.

Source: Authors

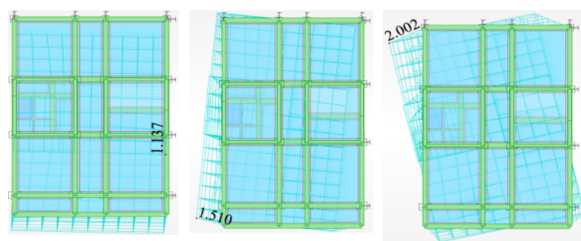


Figure 14. Maximum displacements for soil E (cm): 1st mode on the left, the 2nd mode in the middle, and the 3rd mode on the right.

Source: Authors

Table 8. Frequencies

Mode	Frequencies w (rad/s)			
	Fixed	Springs (A)	Springs (C)	Springs (E)
1	1,27	1,19	1,18	1,17
2	1,54	1,44	1,42	1,41
3	1,73	1,60	1,59	1,58

Source: Authors

Comparisson between fixed models and with springs models

To compare the structural response among the fixed and non-fixed models, a complete design for each soil type was made. The final dimensions for the fixed structure remained the same for the non-fixed structure, in order to compare them against

Table 9. Periods

Mode	Periods T (s)			
	Fixed	Springs (A)	Springs (C)	Springs (E)
1	0,78	0,84	0,85	0,85
2	0,65	0,70	0,70	0,71
3	0,58	0,62	0,63	0,63

Source: Authors

Table 10. Maximum displacements

Maximum displacements (cm)			
Fixed	Springs (A)	Springs (C)	Springs (E)
1,158	1,131	1,134	1,137
1,648	1,565	1,531	1,510
2,051	2,002	2,003	2,002

Source: Authors

Table 11. Global stiffness

	Kx (kN/mm)	Ky (kN/mm)	K average (kN/mm)
Fixed	166,69	126,38	146,53
A	129,06	123,17	126,12
C	137,56	100,11	118,83
E	133,79	98,65	116,22

Source: Authors

the reinforcement steel areas and drifts. Reinforcement steel areas for beams and columns for each model are shown in Tables 12 to 16. It can be observed that, for soil A, the required reinforcement increase is related to the stiffness, which is the highest among the three soil types, approaching to fixed model (Wahrhaftig and Brasil, 2017).

Table 12. Average required reinforcement

Soil type	Average required reinforcement (cm ²)				Average required reinforcement (%)	
	Fixed		Equivalent springs		Difference	
	As-	As+	As-	As+	As-	As+
A	3,98	2,61	4,37	3,24	9,89	24,04
C	4,74	2,90	4,97	3,18	4,75	9,97
E	4,78	2,87	5,12	3,15	7,05	9,79

Source: Authors

Table 13. Total required reinforcement for beams (entire structure)

Soil type	Total required reinforcement for beams (cm ²)			
	Fixed		Equivalent springs	
	As-	As+	As-	As+
A	3 128,23	2 050,05	3 437,65	2 542,90
C	3 725,82	2 275,83	3 902,86	2 502,73
E	3 759,05	2 256,32	4 024,00	2 477,18

Source: Authors

The increase in positive and negative reinforcement areas implies an increase in the maximum deflection of beams, as shown in Table 17. Please note that these increases were negligible, but, if a structural design is susceptible

Table 14. Differences on total required reinforcement for beams (entire structure)

Soil type	Difference (cm ²)		Difference (%)	
	As-	As+	As-	As+
A	309,42	492,85	9,89	24,04
C	177,04	226,90	4,75	9,97
E	264,95	220,86	7,05	9,79

Source: Authors

Table 15. Total reinforcement required for columns (entire structure)

Soil type	Average required reinforcement (cm ²)		Total required reinforcement for columns (cm ²)	
	Fixed	Equivalent springs	Fixed	Equivalent springs
A	16,92	23,54	1 760,00	2 448,51
C	18,12	23,54	1 884,86	2 448,50
E	17,30	23,54	1 799,25	2 448,37

Source: Authors

Table 16. Differences on total reinforcement required for columns (entire structure)

Soil type	Difference (cm ²)	Difference (%)
A	688,51	39,12
C	563,64	29,90
E	649,12	36,08

Source: Authors

to deflections, the amplification must be considered, even though the increases for positive bending moments are being countered by the increase in negative bending moments, thus compensating the deflection increase. For columns, the quantities of reinforcement areas remain almost equal for each soil type, but, for all cases, there was a considerable increase associated with the new bending moments of the beams.

Table 17. Average maximum deflection for beams

Level	Average deflection (mm)			
	Fixed	A	C	E
1	-4,12	-4,20	-4,16	-4,21
2	-4,08	-4,05	-4,06	-4,12
3	-4,10	-4,08	-4,10	-4,13
4	-4,11	-4,10	-4,11	-4,14
5	-4,19	-4,16	-4,16	-4,19
6	-3,37	-3,37	-3,37	-3,46

Source: Authors

The direct relationship between bending moment and shear force implies an increase in shear effects; hence, a measurement of quantities of stirrups per length was established, as shown in Tables 19 and 20. Please note that stirrups quantities increase in average for beams and columns, and this is related to the increase bending moments due to gravitational effects and the reduction of the stiffness. Tables 21 and 22 show the base shear, and, for soil E, there is an amplification

Table 18. Average ratios for maximum deflection for beams

Level	Average ratios (spring/fixed)		
	A	C	E
1	1,0196	1,0103	1,0218
2	0,9919	0,9940	1,0087
3	0,9946	0,9998	1,0062
4	0,9991	1,0004	1,0066
5	0,9936	0,9943	1,0009
6	1,0002	1,0009	1,0272
Average	0,9998	0,9999	1,0119

Source: Authors

consistent with these results, whereas, for soils A and C, a reduction is observed while gravitational forces still increase.

Table 19. Stirrups per length in columns (16 mm)

Soil type	Fixed	Equivalent springs	Difference (%)
A	4,51	4,67	3,55
C	4,71	5,01	6,45
E	4,55	5,03	10,56

Source: Authors

Table 20. Stirrups per length in beams (10 mm)

Soil type	Fixed	Equivalent springs	Difference (%)
A	7,50	7,86	4,8
C	8,88	9,44	6,31
E	7,55	11,00	45,7

Source: Authors

As an example, the calculation of drifts for soil E are shown in Tables 21 and 22, while the total drifts and ratios for each soil type are shown in Table 23. Ratios were calculated using Equation (10). Elastic drifts were calculated according to (NEC, 2014), which specifies that, if $ratio > 1$, then drifts using equivalent springs are greater than drifts using fixed supports, and vice-versa.

$$ratio = \frac{\text{Equivalent springs drifts}}{\text{Fixed drifts}} \quad (10)$$

The procedure shown in Tables 21 and 22 was applied to all frames in both directions to obtain a global average for each structure (Table 23).

The results for drifts were as expected, which means that they were greater in models based on equivalent springs than in the fixed models. Although drifts for models with equivalent springs are greater, all models still remained within admissible values, which did not exceed the value of 0,02. Ratios increased from soil A to soil E, which is related to the global stiffness, modified due to the change from fixed supports to spring supports. Torsional irregularity was checked according to regulations and standards (FEMA, 2006, 2018; NEC, 2014), by applying Equation (8). If $r \geq 1,4$, then the torsional irregularity is extreme. If $1,2 \leq r \leq 1,4$, then the torsional

Table 21. Example for calculation of inelastic drifts for spectral Y displacements (soil E, one frame)

Level	Spectral (Y)				
	Fixed (mm)	Drifts	Equivalent springs (mm)	Drifts	Ratio
6	29,195	0,004	34,847	0,005	1,15
5	26,665	0,006	31,946	0,007	1,10
4	22,613	0,009	27,499	0,009	1,08
3	17,146	0,010	21,593	0,011	1,07
2	10,671	0,010	14,639	0,011	1,09
1	4,052	0,006	7,432	0,008	1,28
0	0,000	0,000	2,251	0,004	-
Average ratio Y					1,13

Source: Authors

Table 22. Example for calculation of inelastic drifts for spectral X displacements (soil E, one frame)

Level	Spectral (X)				
	Fixed (mm)	Drifts	Equivalent springs (mm)	Drifts	Ratio
6	15,662	0,002	17,594	0,003	1,19
5	14,177	0,004	15,825	0,004	1,09
4	11,923	0,005	13,369	0,005	1,04
3	9,006	0,005	10,324	0,005	1,02
2	5,617	0,005	6,855	0,005	1,01
1	2,170	0,003	3,365	0,003	1,02
0	0,000	0,000	1,159	0,002	-
Average ratio X					1,06

Source: Authors

Table 23. Average ratios for each soil type (all frames)

Soil type	Average ratios		
	Spectral X	Spectral Y	Average
A	1,04	0,98	1,01
C	1,04	1,01	1,02
E	1,16	1,12	1,14

Source: Authors

irregularity must be considered in the structural analysis and design by reinforcing columns or changing their configuration or orientation. If $r \leq 1,2$, then the torsional irregularity can be dismissed from the analysis. The results for torsional irregularity are shown in Tables 24 to 26.

Table 24. Average ratios for soil A (all frames)

Condition	Fixed		Equivalent springs	
	X	Y	X	Y
Displacements (mm)	14,17	13,25	14,58	14,96
	9,65	15,31	10,62	12,81
Average (mm)	11,91	14,28	12,60	13,88
r(mm/mm)	1,19	1,07	1,16	1,08

Source: Authors

Tables 24 to 26, show that torsional irregularity values remain admissible, and that the difference between fixed and equivalent

Table 25. Average ratios for soil C (all frames)

Condition	Fixed		Equivalent springs	
	X	Y	X	Y
Displacements (mm)	21,71	21,07	26,89	23,75
	17,94	24,96	18,81	27,70
Average (mm)	22,83	23,01	22,85	25,73
r (mm/mm)	1,21	1,08	1,18	1,08

Source: Authors

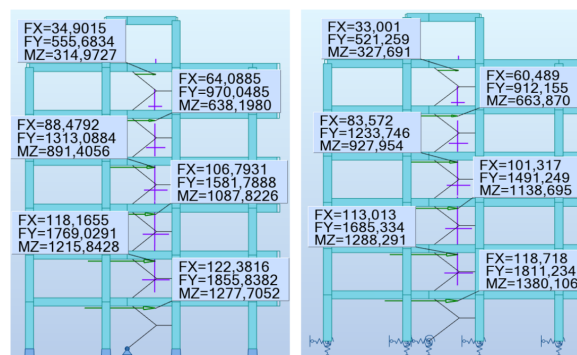
Table 26. Average ratios for soil E (all frames)

Condition	Fixed		Equivalent springs	
	X	Y	X	Y
Displacements (mm)	22,58	24,93	28,51	34,87
	14,22	28,92	18,13	29,88
Average (mm)	18,40	26,92	23,32	32,37
r(mm/mm)	1,23	1,07	1,22	1,08

Source: Authors

lent springs models remain closer. Despite using equivalent springs, the structure still has admissible values. Additionally, the ratios for torsional moments were evaluated. Therefore, if $ratio \geq 1$, then the torsional moment increases using equivalent springs and vice versa. The same equation was used to calculate ratio for base shear forces; Figure 15 shows the results for base shear forces and torsional moments for soil C.

Tables 27 to 29 show a decrease in shear forces in directions X and Y for soil A and C, although, for soil E, an increment is visible in the direction of the applied spectral forces. These results reflect that the displacements and rotations at the base using equivalent springs not only imply that the behavior of the structure changes for bad (in the form of drifts, reinforcement, or increasing torsional moments), but the spectral forces can also be reduced for each spectral load state. Table 30 shows similar results for torsional moments, decreasing for soils A and C, and increasing for soil E. These results can be attributed to the stiffness, given the fact that it decreased from soil A to E.

**Figure 15.** Base shear for soil C (kN, kN.m).

Source: Authors

Table 27. Soil A (spectral)

	X		Y	
Level	Base shear ratio			
	Fx	Fy	Fx	Fy
6	0,91	0,88	0,87	0,96
5	0,89	0,88	0,88	0,86
4	0,88	0,88	0,88	0,85
3	0,88	0,88	0,89	0,85
2	0,89	0,89	0,90	0,86
1	0,91	0,91	0,91	0,88
Average.	0,89	0,89	0,89	0,88

Source: Authors

Table 28. Soil C (spectral)

	X		Y	
Level	Base shear ratio			
	Fx	Fy	Fx	Fy
6	0,96	0,92	0,93	0,94
5	0,95	0,91	0,93	0,94
4	0,95	0,92	0,93	0,94
3	0,95	0,92	0,93	0,94
2	0,96	0,93	0,94	0,95
1	0,98	0,95	0,95	0,98
Average.	0,96	0,92	0,93	0,95

Source: Authors

Table 29. Soil E (spectral)

	X		Y	
Level	Base shear ratio			
	Fx	Fy	Fx	Fy
6	1,05	1,00	1,01	1,00
5	1,05	0,99	1,01	1,01
4	1,05	1,00	1,01	1,01
3	1,05	1,00	1,02	1,02
2	1,06	1,02	1,02	1,03
1	1,07	1,03	1,03	1,05
Average.	1,05	1,01	1,02	1,02

Source: Authors

Table 30. Ratios for torsional moments for each soil type

Level	Soil A		Soil C		Soil E	
	X	Y	X	Y	X	Y
	Torsional Moment ratio (Mz)					
6	0,81	0,96	0,82	1,02	0,87	1,08
5	0,81	0,95	0,82	1,02	0,88	1,09
4	0,80	0,95	0,82	1,02	0,88	1,09
3	0,80	0,95	0,83	1,03	0,88	1,10
2	0,81	0,85	0,83	1,04	0,89	1,11
1	0,83	0,98	0,85	1,06	0,91	1,13
Av.	0,81	0,94	0,83	1,03	0,88	1,10

Source: Authors

Conclusions

According to the results, for this regular structure, soil-structure interaction in linear range has an impact on the analysis and design. The former is related with reinforcement areas for structural elements which increased for positive and

negative bending moments in all the structural models, while also increasing the quantities of stirrups per length.

Drift values showed an expected increase, being greater for soil E (14%), which was the most critical in terms of stiffness and soil resistance, as well as subjected to gravitational and seismic influences, thus allowing more displacements and rotations at the base. However, it could be enhanced by giving more stiffness to its foundation system by mechanically altering the soil properties to preserve the superstructure's cross section.

A similar response was obtained for torsional irregularity, but, in this case, it remained almost equal in terms of displacement, which is related with stiffness reduction and increasing displacements. Despite this, the torsional risk is the same, and it does not imply a significant change in the superstructure's design, so it could be enhanced by changing the substructure's stiffness.

A structure generally functions as a filter for seismic movement, that is, depending on the structure and its transfer function, it can be susceptible to the frequencies a certain earthquake. The transfer function, in turn, depends directly on the stiffness of the structure; when the structure is fixed at the base, it has more stiffness than it would with springs on it, but even so, this does not mean that the structure with springs at the base will have greater lateral displacements than the fixed structure, given that, when placing translational and rotational springs, vertical and lateral displacements and rotations will occur at the base, which can even reduce lateral displacement.

The shear forces and torsional moments increased and decreased, and so did the drifts, but the stiffness of the structure with springs decreased, which produced a reduction of shear forces in soils A and C, but increased with soil E, which is not the case for torsional moments, (it only increased for soils C and E). The explanation for this lies in the linear stiffness of the structure (translational and rotational). In the case of springs, the stiffness decreased, but the displacements increased, so there is a compensation comparable to the fixed model.

It is highly recommended to apply this study for other soil types and the same structure by optimizing the superstructure and substructure. Additionally, it is recommended to avoid displacements with higher variations at the base, which allows to control additional stresses on the superstructure.

References

- American Concrete Institute, Committee 318 (ACI) (2014). *Building Code Requirements or Structural Concrete (ACI 318-14) and Commentary (ACI 318R-14)*. ACI.
- American Concrete Institute, Committee 318 (ACI) (2019). *Building Code Requirements or Structural Concrete (ACI 318-19) and Commentary (ACI 318R-19)*. ACI.
- ASCE/FEMA (2000). *Prestandard and Commentary for the Seismic Rehabilitation of Buildings (FEMA 356)*. Federal Emergency Management Agency.

- Castro-Pilco, C. F. and Pérez-Martínez, G. E. (2020). *Análisis de la interacción suelo-estructura estática para una edificación regular de hormigón armado y 3 tipos de suelos* [Bachelor's thesis].
- Chopra, A. K. (1980). *Dynamics of structures*. Earthquake Engineering Research Institute.
- Cruz, C. and Miranda, E. (2017). Evaluation of soil-structure interaction effects on the damping ratios of buildings subjected to earthquakes. *Soil Dynamics and Earthquake Engineering*, 100, 183-195. 10.1016/j.soildyn.2017.05.034
- DAS, B. M. (2011). *Principles of Foundation Engineering* (7th ed.). Braja Das.
- Díaz-Guzmán, F. D., Espinoza-Barreras, F., Sánchez-Vergara, R., and Huerta-López, C. I. (2012). *Respuesta dinámica de un edificio considerando el efecto de interacción suelo-estructura*. Centro Internacional de Métodos Numéricos en Ingeniería. <https://core.ac.uk/download/41779960.pdf>
- Falconí, R. A. (2008). *Análisis sísmico de edificios*. Centro de Investigaciones Científicas, Escuela Politécnica del Ejército.
- FEMA (2006). *NEHRP recommended provisions: Design examples (FEMA 451)*. Federal Emergency Management Agency.
- FEMA, P. (2018). *Assessing Seismic Performance of Buildings with Configuration Irregularities*. Calibrating Current Standards and Practices.
- Galicia, W. and León, J. (2007). *Interacción sísmica suelo-estructura en edificaciones de albañilería confinada con plateas de cimentación*. Universidad Privada Antenor Orrego.
- Garza-Vásquez, L. (2000). *Diseño y construcción de cimentaciones*. Escuela de Ingeniería Civil.
- Hernández-Velasco, E. (2013). *Análisis de la interacción dinámica suelo - estructura de un edificio desplantado en la zona de Lago de la Ciudad de México*. Universidad Nacional Autónoma de México.
- López, N., Vielma, J., López, L., and Montesinos, V. (2019). Using Microsoft Excel Macros to Analyze Planar Structures. *Revista internacional de ingeniería de estructuras*, 24(1), 123-139. 10.24133/riie.v24i1.1169
- Lutes, L. D. and Sarkani, S. (1995). Structural damping for soil-structure interaction studies. *Structural Engineering and Mechanics*, 3(2), 107-120. 10.12989/sem.1995.3.2.107
- Mejía-Bermejo, L. A. (2017). *Interacción dinámica suelo-estructura* [Bachelor's Thesis, Universidad Nacional Autónoma de México, México]. <https://repositorio.unam.mx/contenidos/215732>
- Meli Piralla, R. (1986). *Diseño estructural*. LIMUSA.
- Norma Ecuatoriana de la Construcción (NEC) (2015). *Estructuras de hormigón armado*. Cámara de la Industria y la Construcción.
- Paz, M. (1992). *Structural Dynamics, theory and computations*. Van Nostrand Reinhold Company Inc.
- Pérez-Valcárcel, J. (2013). *Métodos de cálculo de cimentaciones superficiales*. <https://www.udc.es/dep/dtcon/estructuras/E-TSAC/Publicaciones/pub-val/Suelos/Zapatas%20EHE.pdf>
- Reyes, L. E. G. (1998). *Dinámica estructural aplicada al diseño sísmico*. Universidad de los Andes, Facultad de Ingeniería, Departamento de Ingeniería Civil.
- Norma Ecuatoriana de la Construcción (NEC) (2014). *Peligro Sísmica*. Cámara de la Industria y la Construcción.
- Uribe-Escamilla, J. (2000). *Análisis de estructuras*. ECOE.
- Villareal, G. (2009). *Interacción sísmica suelo-estructura en edificaciones con zapatas aisladas*. Asamblea Nacional de Rectores. <http://blog.pucp.edu.pe/blog/wp-content/uploads/sites/109/2009/07/Interaccion-suelo-zapata.pdf>
- Wahrhaftig, A. de M. and Brasil, R. M. (2017). Initial undamped resonant frequency of slender structures considering non-linear geometric effects: the case of a 60.8 m-high mobile phone mast. *Journal of the Brazilian Society of Mechanical Sciences and Engineering*, 39(3), 725-735. 10.1007/s40430-016-0547-1
- Wahrhaftig, A. de M. (2020). Time-dependent analysis of slender, tapered reinforced concrete columns. *Steel and Composite Structures*, 36(2), 229-247. 10.12989/scs.2020.36.2.229
- Weaver, W. and Gere, J. M. (1990). Finite-Element Method for Framed Structures. In *Matrix Analysis of Framed Structures* (pp. 447-467). Springer. 10.1007/978-1-4684-7487-9_7
- Wu, R. Y. and Pantelides, C. P. (2019). Seismic evaluation of repaired multi-column bridge bent using static and dynamic analysis. *Construction and Building Materials*, 208, 792-807. 10.1016/j.conbuildmat.2019.03.027
- Zeevaert, L. (1980) *Interacción suelo-estructura, estática y sísmica de cimentaciones monolíticas superficiales* [Conference presentation]. VI Seminario de Mecánica de Suelos Interacción Suelo-Estructura, Caracas, Venezuela. <https://docplayer.es/14218639-Interaccion-suelo-estructura-e-statica-y-sismica-de-cimentaciones-monoliticas-superficiales-1-por-dr-leonardo-zeevaert.html>

Overview of the Constitutive Model and Numerical Calibration by FEM to Compute Bearing Capacity and Embankment-Core Deformability

Una mirada a los modelos constitutivos y la calibración numérica mediante MEF para calcular la capacidad de carga y la deformabilidad del núcleo del terraplén

Milena Mesa-Lavista¹, Francisco Lamas-Fernández², Eduardo Tejeda-Piusseaut³, Rafael Bravo-Pareja⁴, Carolina Cabrera-González⁵, and José Álvarez-Pérez⁶

ABSTRACT

Numerical modeling is a powerful tool to determine the stress-strain relationships of structures. However, for a reliable application, physical and mathematical models must be calibrated and validated. This paper presents an overview of numerical calibration through the finite element method and plate-load tests in an embankment. Additionally, an analysis of the constitutive models used in soils is performed, and the elastic-plastic constitutive model of Mohr-Coulomb was selected since it is the best suited for this study. The results from three test areas within a refinery project that the Cuban government undertook in the province of Cienfuegos are used. The numerical model used in this study was calibrated by means of the error theory and the non-parametric hypothesis tests from Mann-Whitney U. From the practical point of view, this study gives two procedures to calibrate the numerical model with experimental results.

Keywords: constitutive models, load-plate test, finite element method, numerical calibration, embankment stress-strain relationship

RESUMEN

El modelado numérico es una herramienta poderosa para determinar la relación esfuerzo-deformación de las estructuras. Sin embargo, para una aplicación confiable, los modelos físicos y matemáticos deben ser calibrados y validados. Este artículo presenta una mirada a la calibración numérica empleando el método de elementos finitos y ensayos físicos de placa de carga en un terraplén. Se realiza además un análisis de los modelos constitutivos empleados en suelos y se selecciona el modelo constitutivo elástico-plástico de Mohr-Coulomb por ser el que mejor se acomoda a este estudio. Se utilizan los resultados de tres áreas de prueba dentro de un proyecto de refinería que el gobierno cubano llevó a cabo en la provincia de Cienfuegos. El modelo numérico empleado en este estudio se calibró empleando la teoría de errores y la prueba de hipótesis no paramétrica U de Mann-Whitney. Desde un punto de vista práctico, este estudio brinda dos procedimientos para calibrar un modelo numérico con resultados experimentales.

Palabras clave: modelo constitutivo, ensayo de carga con placa, método de elemento finito, calibración numérica, relación esfuerzo-deformación en terraplenes

Received: February 17th, 2021

Accepted: June 28th, 2021

¹Civil Engineer from Instituto Superior Politécnico José Antonio Echeverría (CUJAE), Cuba. Ph.D. from the Central University of Las Villas (UCLV), Cuba. Affiliation: Ph.D. and Professor at Universidad Autónoma de Nuevo León (UANL), Facultad de Ingeniería Civil, San Nicolás de los Garza, México. Email: mmesal@uanl.edu.mx

²Ph.D. from the University of Granada, Spain. Affiliation: Ph.D. and full-time professor at Universidad de Granada, Departamento de Ingeniería Civil, ETSICCP, Granada, España. Email: flamas@ugr.es

³Civil Engineer from Instituto Superior Politécnico José Antonio Echeverría (CUJAE), Cuba. Ph.D. from the University of Madrid, Spain. Affiliation: Ph.D. and full-time professor at Universidad Técnica de Manabí, Facultad de Ciencias Matemáticas, Físicas y Químicas, Ecuador. Email: wardyt2015@gmail.com

⁴Ph.D. from the University of Granada, Spain. Affiliation: Ph.D. and full-time professor at Universidad de Granada, Departamento de Estructuras, ETSICCP, Granada, España. Email: rbravo@ugr.es

⁵Industrial Technical Engineer from the University of Jaen, Spain. Master in Structures from the University of Granada, Spain. Affiliation: Restoration and interior design projects at Universidad de Granada Departamento de Ingeniería Civil, ETSICCP, Granada, España. Email: cabreragonzalezcarolina0@gmail.com

⁶Civil Engineer from Instituto Superior Politécnico José Antonio Echeverría (CUJAE), Cuba. Ph.D. from the Central University of Las Villas (UCLV), Cuba. Affiliation: Ph.D., and full-time professor at Universidad Autónoma de Nuevo León (UANL),

Introduction

To determine the stress-strain states generated within embankments due to applied loads and gravity, researchers have developed analytical and empirical methods (Lamas *et al.*, 2011; Standing *et al.*, 2020) that enable the design and enforcement of the project within the admissible parameters of durability and deformability. Moreover, modelling

Facultad de Ingeniería Civil, San Nicolás de los Garza, México.
Email: jose.alvarezpr@uanl.edu.mx

How to cite: Mesa, M., Lamas, F., Tejeda, E., Bravo, R., Cabrera, C., and Álvarez-Pérez, J. (2022). Overview of the Constitutive Model and Numerical Calibration by FEM to Compute Bearing Capacity and Embankment-Core Deformability. *Ingeniería e Investigación*, 42(1), e93712. 10.15446/ing.investig.v42n1.93712



Attribution 4.0 International (CC BY 4.0) Share - Adapt

techniques have been used to develop constitutive models (Feng *et al.*, 2020; Jiang *et al.*, 2020; Li *et al.*, 2021). So far, in Cuba, there are no available studies, either theoretical or experimental, on construction regulations and standards under different climatic and traffic conditions concerning the performance of slopes, such as the design and construction of the embankments in a highway.

The strength and density levels that must be reached are currently defined through empirical methods by current Cuban standards (NC-11, 2005). This mainly limits the design of embankments of great height because the acting loads exceed the maximum allowed stress. Thus, the need arises for the conception and building of a numerical model to simulate, with admissible error, the stress-strain performance of these embankment fundamentals in highway projects. Additionally, this contributes to improving the current official design and construction standards.

Several numerical methods can be used to calculate the stress-strain state of a structure: boundary elements, finite volumes, finite differences, and the finite-element method, among others (Haftka and Malkus, 1981; Namdar, 2020; Osipov *et al.*, 2018; Otálvaro and Nancrales, 2009). This study uses the finite-element method, which, conceptually, is the breakdown of a continuous physical element into a discrete number of parts or elements that are connected by a number of points called nodes. The movements of these are the main variables to calculate in each problem (Anderson *et al.*, 2021; Zienkiewicz *et al.*, 2015). Within each element, the movements of any point are determined from the movements of the nodes of each element using inverse or semi-inverse formulations (Álvarez, 2014).

One of the fundamental advantages of using the finite-element method in these problems is the reduction of experimental costs once the model is properly represented. However, the numerical model must be calibrated and validated. In this study, two calibration procedures are performed: one by applying the error theory, and the other by using non-parametric hypothesis tests. The results of the plate-load test have been used to validate this procedure.

Overview from embankment construction and design

For a continuous circulation of traffic on highways, with quality and safety during the period of use, embankments must meet certain requirements regarding stability, safety, and strength under the forces exerted by weather and traffic (Mesa, 2017).

Experience in construction embankments has enabled us to prepare firm structures under favorable conditions in terms of topography and materials. However, for problematic conditions, considering the nature of the materials, as well as for geomorphology, many authors have indicated the need to take special safety measures, thus requiring the development of independent projects for each case, given that those are special cases that require further study. For example, Huang *et al.*, (2010) used a two-dimensional finite method

to investigate the stress and strain of embankments built on soft ground, with or without treatment of the foundation. Liu *et al.* (2004) undertook an experimental study on high embankment construction for an expressway. Stuedlein *et al.* (2010) presented a 46 m design for a mechanically stabilized earth wall with a fill slope of 2:1 inclination. Ulloa and Vargas (2007) described a methodology to detect the physical vulnerability of fillings and embankments on mountains and slopes. Shan *et al.* (2009) studied soil compaction, taking into account the performance of an already built high embankment vs. the thaw phenomenon; and Guo-xiong *et al.* (2010) evaluated slope stability through 2D and 3D analysis in high embankments. Murata *et al.* (2020) evaluated pavement and embankments by means of a superficial technique. Although, in recent years, many of the studies for road embankments only focus on pavement and the first layers of the base and subbase (Albarazi, 2020; Hernández-López *et al.*, 2020), others focus on deformational state behavior (Mesa *et al.*, 2020; Pardo de Santayana *et al.*, 2020).

Soil, unlike any other material, has an extremely complex behavior, which is dependent on its type, the *in situ* treatment received, the compaction level, the state of aggregation, etc. Therefore, many countries have developed several criteria for characterizing soils according to their features or the needs of the project (AASHTO, 2021; PG-3, 2017). Approximately 80% of the materials of the embankment constitute the core, in which fine-grained materials can be used, such as clays, silts, and residual soils, if adequate compaction control is carried out, given the potential deformability.

The methods used in practice to estimate settlements are often based on *in situ* tests, such as the Vane cone test, the Standard penetration test (SPT), and the plate-load test.

The plate-load test can be used as part of a soil inspection procedure for foundations design (ASTM, 1994). It was also developed to study the foundation soil of roads and airports. After being developed and improved, it is currently an essential test for the calculation and subsequent monitoring of civil engineering projects. The test is performed *in situ* on the soil to measure the vertical settlement due to the applied load. This test consists of applying a vertical load on a circular metal plate that is firmly seated and levelled on the embankment. When the test preparations are verified, different loads are applied, and the load required for different strain rates is calculated (Figure 1) (Anyang *et al.*, 2018; NC-11, 2005; Patel, 2019).

The aim of this study is to demonstrate the calibration procedure of a finite element model by means of the results of different plate-load tests applied to embankments constructed (physical model) within the project of the refinery plant built in the province of Cienfuegos, Cuba. Data concerning displacements and loads were used to validate the numerical models of the embankment.

Different constitutive models have been used for soil modeling. These models differ from each other in the parameters used for the calculation (e.g. responses such as elastic-plastic, energy dissipation, permanent deformations, etc.) (Zhang *et al.*, 2021). Examples of constitutive models include

elastic models, elastic-plastic models, or those based on the critical state.



Figure 1. Circular plate of charge.

Source: <https://www.fing.edu.uy/en/node/7241>

Elastic models show a linear relationship between applied stresses and deformations, where the instant of applying tension coincides with the moment that the soil deformation ends. These models clearly do not simulate soil performance in an adequate way, since they do not consider residual deformations. However, for the sake of simplicity, they are useful for modeling the initial stress states of embankments. Elastic-plastic models consider the elastic and plastic states of the material. When the remaining deformation is considered, and hence the stress and displacements are reached in soil structures, it is possible to predict their behavior against predetermined load systems. Critical-state models are based on the study of the energy-dissipation mechanisms within the soil skeleton, as well as the observation of the macroscopic behavior of materials.

Incremental hypoelastic models establish a relationship between stress application velocity and strain velocity using a tensorial function. Since this requires a large number of parameters and demanding computer-memory capabilities when integrated into finite-element programs, it has not had significant practical applications. The Kondner-Duncan model, which establishes a hyperbolic function that causes serious continuity problems, was one of the first models adapted to simulate the behavior of large masses of soil such as dam fronts (Mellah *et al.*, 2000).

Hyperbolic models easily represent the stress-strain behavior for the drained-soil response. The model was initially proposed by Kondner and Zelasko (1963) and was subsequently presented on an incremental basis by Duncan and Chan (1970). It assumes that the stress-strain curves of soil can approximate a hyperbola (Lamas *et al.*, 2011).

From all the models mentioned above, the elastic-plastic Mohr-Coulomb model was chosen for this research because the parameters used are readily available, it is best adapted to the behavior of the soil, and it may reach the maximum load break with values between 400 and 500 kPa (Gu *et al.*, 2020; Hai-Sui, 2006; Nieto *et al.*, 2009). The Mohr-Coulomb criterion assumes that failure occurs when the shear stress at any point in a material reaches a value that depends linearly on the normal stress on the same plane. This model is based on Mohr's circle for states of stress at failure on the plane of

the maximum and minimum principal stresses. The break line is the common tangent to all Mohr circles.

Therefore, the Mohr-Coulomb model is defined by Equation (1), where σ is negative in compression, from the average of the maximum and minimum Mohr's circle; c is the cohesion; \emptyset the friction angle; σ_m the principal stresses; and S is half the difference between the maximum and minimum principal stresses.

$$\tau = c - \sigma \tan \emptyset \quad (1)$$

Where $\tau = S \cos \emptyset$; $\sigma = \sigma_m + S \sin \emptyset$ (kPa), c (kPa), σ (kPa), \emptyset (°), S (kPa), σ_m (kPa)

For general states of stress, it is more convenient to write the model in terms of three stress invariants, as shown in Equation (2) (Abaqus/CAE, 2017).

$$F = R_{mc} q - p \tan \emptyset - c_1$$

$$R_{mc}(\Theta, \phi) = \frac{1}{\sqrt{3} \cos \phi} \sin \left(\Theta + \frac{\pi}{3} \right) + \frac{1}{3} \cos \left(\Theta + \frac{\pi}{3} \right) \tan \phi \quad (2)$$

$$\cos(3\Theta) = \left(\frac{r}{q} \right); \quad q = \sqrt{\frac{2}{3}} (S : S); \quad p = -\frac{1}{3} \text{trace } \sigma;$$

$$r = \left(\frac{9}{2} S : S : S \right)^{2/3}; \quad S = \sigma + pI$$

Where θ is the deviatory polar angle defined (°); q is the Mises equivalent stress (kPa); p is the equivalent pressure stress (kPa); r is the third invariant deviatory stress (kPa); and S is the deviatory stress (kPa).

Study area: geotechnical and geological framework

The embankments used for the validation tests are in areas occupied by the facilities of the Camilo Cienfuegos oil refinery. According to the coordinates of the Lambert conical projection system, they are in northern Cuba, from 548450 to 550500 and from 261 000 to 264 300. Its height ranges between 0,00 m to 40,00 m, as reported by the National Altimetry System. They are located in the region of Siboney, Industrial Zone No. 3 ("Carolina") of the city of Cienfuegos in the Republic of Cuba (Figure 2). This refinery is a project of the National Applied Research Company (ENIA) and an Invescons Research Unit construction. In geomorphological terms, the territory was originally a semi-wavy, cumulative-abrasive-denudative marine terrace, and it currently has a slightly rugged topography. It is a product of the human earth movements made for the construction of the refinery between 1995 and 2005.

The area is located within the neo-autochthonous basin of the Palaeocene-Quaternary depression of Cienfuegos, on its north-western flank. The geological structure of the territory consists of pyroclastic-carbonate, terrigenous-carbonate, and carbonate sedimentary rocks from the Upper Cretaceous,

Palaeocene, and Neogene of the Cantabria, Caunao and Paso Real formations, in addition to different Quaternary materials, undifferentiated as formations. Almost all of the faults that complicate the formations in pre-Eocene flanks dissipate towards the inside of the depression, with no seismogenic faults in the environment.

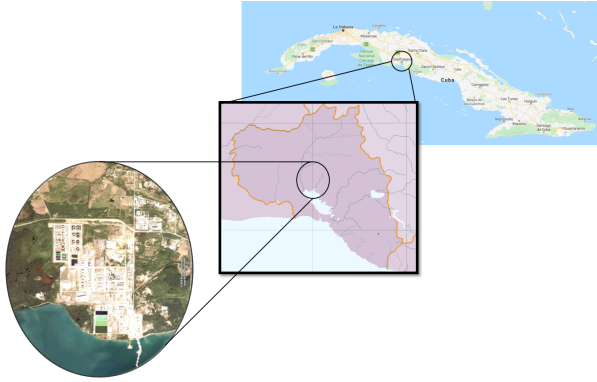


Figure 2. Camilo Cienfuegos oil refinery area.

Source: Authors, based on the report courtesy of Cienfuegos's ENIA.

With the parameters determined from embankment testing conducted in the city of Cienfuegos (Figure 2), it is possible to correctly simulate soil behavior using numerical methods. It is also possible to simulate the plate-load test, which was chosen for validation and subsequent use in determining the deformation and strength of soils.

Materials and tests

In this study, the data calculated from the drilling with UGB-50 bits by ENIA project was used. The methods used in the drilling were percussion and/or rotation due to the soil type. The determination of the index properties was performed according to specifications of international standards group (ASTM, 2000).

The geotechnical profile was characterized to a depth of 29 m. From the samples taken, the parameters of the existing soils in the area were calculated. Tables 1 and 2 show their values.

These tables indicate that the foundation soil, down to 10 m deep, consists of interstratified soils of sandy-clay type with medium to low plasticity and a mean natural density of $19,6 \text{ kN/m}^3$, with a standard deviation of 0,68. Furthermore, the soil has an average natural moisture of 20,7% that has somewhat higher dispersion values (between 13 and 33%).

Regarding the values of the mechanical parameters used in the calculations, the effective cohesion has a mean value of 12,0 kPa, with a maximum of 15,0 kPa and a minimum of 5 kPa; and the angle of effective internal friction averaged 15 degrees (a maximum of 20° and a minimum of 10°).

In the project, three test polygons were executed, each one for 30 plate-load tests. This study was conducted to characterize the zone through a geological engineering investigation on the feasibility of the refinery expansion.

Table 1. Index properties of the soils

Layer waste fill	Natural state			Gs (adm)	e (adm)	S (%)	USCS
	w(%)	γ_f (kN/m ³)	γ_d (kN/m ³)				
1	19,33	19,77	16,68	2,67	-	-	CL
2	13,00	20,30	17,90	2,67	0,49	71,0	SC
3	16,60	20,30	17,40	2,65	0,52	84,6	CL
4	21,30	19,36	15,96	2,68	0,68	83,9	CL
5	20,10	19,43	16,20	2,69	0,66	81,5	CL
6	33,10	18,11	13,60	2,72	1,0	90,0	CH
7	28,20	18,86	14,70	2,69	0,83	91,0	SC
8	12,40	19,78	17,60	-	-	-	GP
9	29,60	17,76	13,70	2,61	0,90	84,1	SC
10 a	14,70	21,10	18,40	-	-	-	GC
10 b	12,40	19,78	17,60	-	-	-	GP

Layer waste fill	Plasticity			% pass; sieve			
	LL (%)	LP (%)	IC	N° 4	N° 10	N° 40	N° 200
1	37,33	16,67	-	-	-	-	-
2	23	10	1,0	86	85	65	40
3	29	14	0,89	91	89	79	63
4	36	8	0,92	98	96	88	69
5	47	28	0,96	88	85	74	58
6	67	37	0,92	97	93	82	62
7	41	19	0,67	74	68	56	44
8	-	-	-	-	-	-	-
9	42	23	0,54	88	87	67	48
10 a	-	-	-	-	-	-	-
10 b	-	-	-	-	-	-	-

Note: Where: w natural humidity; γ_f natural volumetric specific weight; γ_d dry volumetric specific weight; Gs relative specific weight of solids; e void ratio; S saturation; USCS Unified Soil Classification System; LL Liquid limit; LP Plastic limit; IC Consistency Index; N° 4, N° 10, N° 40 and N° 200 sieve size according to ASTM (2000); USCS column Unified Soil Classification System from ASTM (2000); CL Lean clay; SC Clayey sand; CH Fat clay; GP Poorly graded gravel; GC Clayey gravel.

Source: Adapted from technical report, courtesy of Cienfuegos's ENIA.

For the characterization of the landfill of the embankment in the polygons, the index properties were determined, and 24 direct shear tests were performed according to Cuban standards (NC-325, 2004), as well as an Oedometer test (Table 3).

The most representative results from the plate-load tests are shown in Figure 3. The mean value of the most representative tests of the polygons is presented in Table 4. It can be observed that the data of polygon number 2 are not representative of the entire set, which is why this polygon has not been used in the calibration process.

Numerical model

The invariants of the modelling process (geometry, loads, materials, and boundary conditions) were taken into account to elaborate a model that corresponded with the real study.

The geometry of the model was performed in accordance with the existing polygons in terms of height, slope gradient, and crown width. Figure 4 shows the average dimensions of polygons and deep layers of soil.

Table 2. Physical-mechanical properties of the soils

	USCS	GP	GC	SC	CL
Standard Proctor test	γ_{\max} (kN/m ³)	> 17,6	> 18,4	18,2-18,6	16,5-17,5
	Wopt (%)	< 12,4	< 14,7	13,0-15,1	17,0-19,5
Porous Ind.	e	< 0,33	< 0,31	0,33-0,31	0,39-0,35
Permeability	K (cm/s)	> $0,3 \times 10^{-6}$	$1,0 \times 10^{-7}$ $5,0 \times 10^{-7}$	$5,0 \times 10^{-8}$ $2,0 \times 10^{-7}$	$1,0 \times 10^{-8}$ $2,0 \times 10^{-7}$
Oedometer compression	E (%) 1.4 (kPa)	< 30	< 120	100-140	120-160
	E (%) 1.5 (kPa)	-	< 240	190-290	220-300
Shear strength	c' (kPa)	-	5	>5	10-15
	φ' (°)	> 36	> 31	10-20	5-15
Modified Proctor	CBR	35-60	20-40	10-20	5-15
	Reac. Mod.	> 800	500-800	500-800	300-500

Source: Adapted from technical report, courtesy of Cienfuegos's ENIA.

Table 3. Physical-mechanical properties of the soil fill

Zone	Oedometer Module	Shear strength	
	Ed (kPa)	c' (kPa)	φ' (°)
Embankment	5 000	15	13

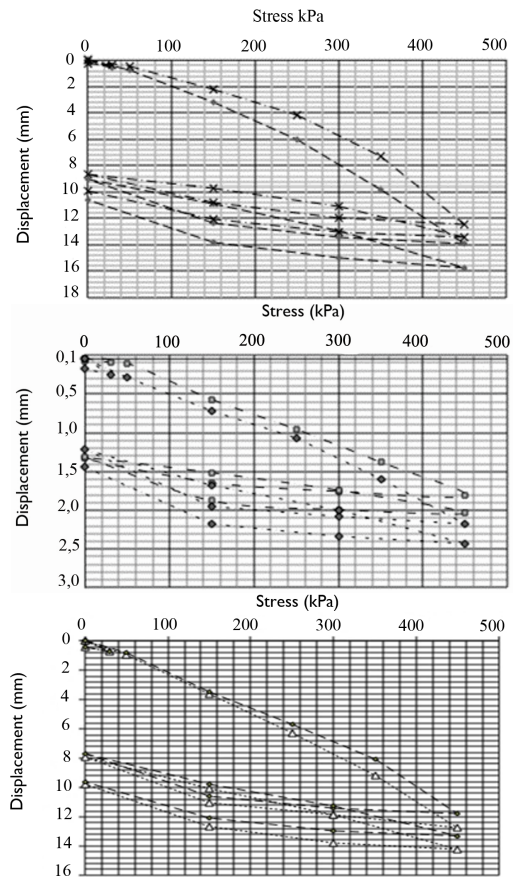
Source: Adapted from technical report Courtesy of Cienfuegos's ENIA.

Table 4. Average values of the load-plate test

Load (kPa)	Displacement, mean values (mm)		
	Polygon 1	Polygon 2	Polygon 3
0	0,00	0,00	0,00
30	0,57	0,16	0,52
0	0,28	0,10	0,32
50	0,96	0,18	0,68
150	2,59	0,80	2,50
250	3,95	1,31	4,34
350	5,35	1,81	6,23
450	6,98	2,39	8,41
300	6,28	2,28	8,04
150	5,68	2,12	7,42
0	4,28	1,70	5,53
150	5,18	2,03	6,78
300	6,06	2,26	7,94
450	7,21	2,56	9,42
300	6,74	2,47	9,09
150	6,22	2,32	8,37
0	4,97	1,88	6,47

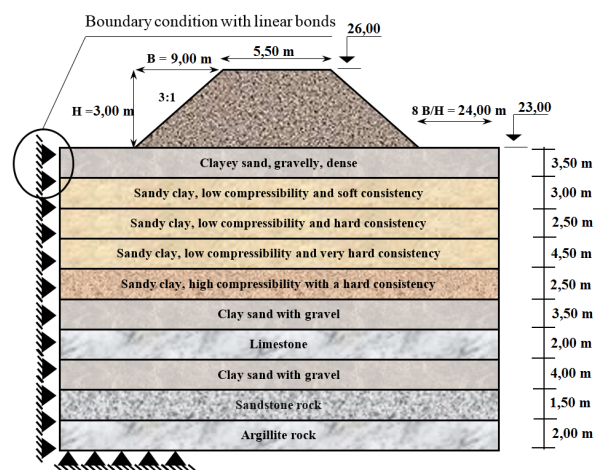
Source: Adapted from technical report, courtesy of Cienfuegos's ENIA.

The distance from the toe of the slope to the boundary condition was established from previous studies to determine the subdomain model (Mesa *et al.*, 2016). The analysis of the influence of stress in the area of crown and core of previous studies determined that the distance most useful for modeling road embankments is eight times the ratio of the base of the slope and height of the embankment,. Linear bonds are used as the boundary condition (Figure 4) (Mesa *et al.*, 2016).

**Figure 3.** Load-plate test results from: a) polygon 1, b) polygon 2, c) polygon 3.

Source: Authors/Adapted from technical report, courtesy of Cienfuegos's ENIA.

The thicknesses of the underlying soil were considered for the depth of the sample perforations performed; the results are in accordance with the physical-mechanical properties found in the laboratory.

**Figure 4.** Model.

Source: Authors

The constitutive model used, Mohr-Coulomb, is well suited for soil behavior at breakage; it stands out over the others because the parameters can be determined from laboratory tests. Regarding the system of loads, stresses applied according to the test at different stages of construction were used (Mesa, *et al.*, 2016). The numerical model of this study is limited to a plane strain model.

Calibration of the mathematical model

From the preparation of the mathematical model of this paper, two important variables were defined: the type of finite element (TFE) and the optimal discretization of domain (DD).

Geo-Studio 2012 was used for this study. This software has different TFE, and only three were used, as shown in Figure 5. For the selection of the mathematical model, a 2^3 test design was defined, varying the two parameters (TFE and DD) at three levels each: 50 cm, 100 cm, and 125 cm; and quadrilateral with four-node, quadrilateral with eight-node and triangular with three-node, respectively (Figure 5) (Mesa, 2017).

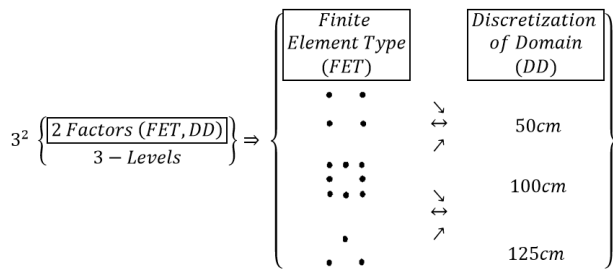


Figure 5. 2^3 test design.

Source: Authors

Nine simulations were performed with the conditions of Figure 4, varying the TFE and DD as shown in Figure 5. After the simulations were completed, an analysis of the results was made. The theory of errors (Table 5) (Kaizhong and Shiyong, 2019) was employed. The errors at several points were applied for each model.

Table 5 shows two expressions used for errors at one point and, three expressions used for several points. All expressions depend on the results of the control pattern ($Q_{e(i)}$), that is, the results obtained from the experimental test and the results from the numerical model ($Q_{n(i)}$).

Figure 6 shows the results from the errors at one point. These are from previous research conducted by the authors (Mesa and Álvarez, 2011). In that study, it was found that the TFE of the quadrilateral 4-node with a discretization of the domain of 50 cm is the mathematical model that best explains the stress-strain results on road embankments, since 8-node elements show greater errors (Figure 6b). Based on these results, the finite element quadrilateral of 4-node and triangular with 3-node were combined in this work (Figure 7).

Table 5. Expressions to compute the errors at one and several points

Errors at one point	
Absolute error (A)	$E_A = Q_{e(i)} - Q_{n(i)} $
Percentage of Absolute error (%AB)	$E_{AP} = \frac{ Q_{e(i)} - Q_{n(i)} }{Q_{e(i)}}$
Errors at several points	
Root Mean Square error (RMSE)	$RMSE = \sqrt{\frac{\sum_{i=1}^n (Q_{e(i)} - Q_{n(i)})^2}{n_p}}$
Mean square error (MSE)	$MSE = \frac{\sum_{i=1}^n (Q_{e(i)} - Q_{n(i)})^2}{n_p}$
Mean Absolute Percentage Error (MAPE)	$MAPE = \frac{\sum_{i=1}^n \left(\frac{ Q_{e(i)} - Q_{n(i)} }{Q_{e(i)}} \right)}{n_p}$

Note: Where: $Q_{e(i)}$ Control pattern results; $Q_{n(i)}$ Results obtained from the numerical model; n_p Analysis points.

Source: Adapted from Mesa and Álvarez (2011).

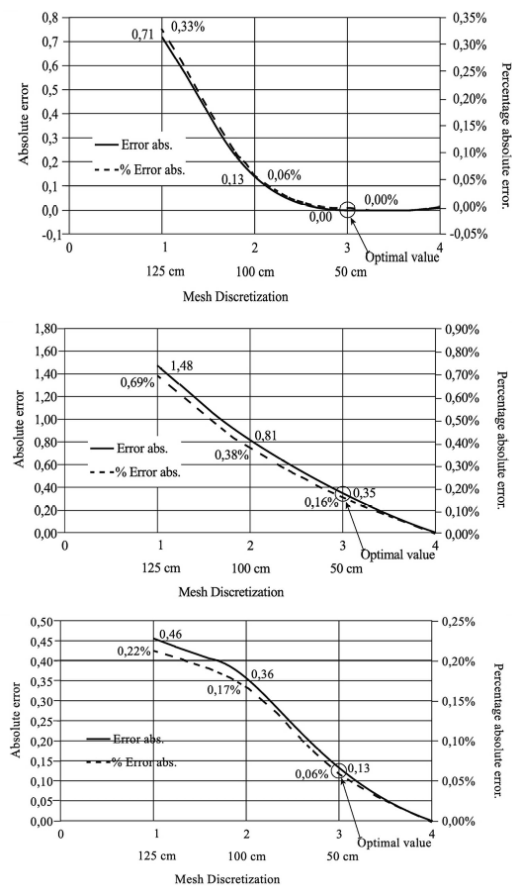


Figure 6. Absolute and percentage of absolute errors in one point with: a) quadrilateral 4-node, b) quadrilateral 8-node, c) triangular 3-node.

Source: Authors, based on the results from Mesa and Álvarez (2011).

Another way to calibrate the model is by using statistics. In order to compare the results from the model and the experimental tests and determine the similarity or difference between results, a parametric or non-parametric test must be carried out.

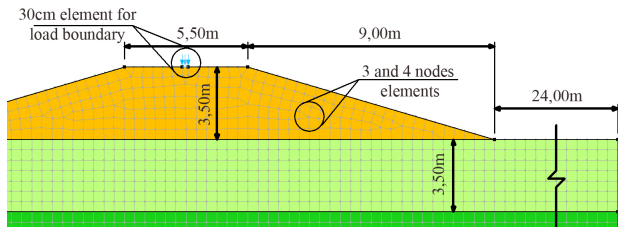


Figure 7. Zoning of area of the slopes with 3-node triangular elements.
Source: Authors

It is known that, for comparing and determining similarities between two independent samples, it is necessary to perform a parametric (t-student) or non-parametric (Mann-Whitney U) test. The parametric test is applicable if the samples fit a normal distribution and their variance is homogeneous. Otherwise, non-parametric tests should be applied for the comparison (Figure 8).

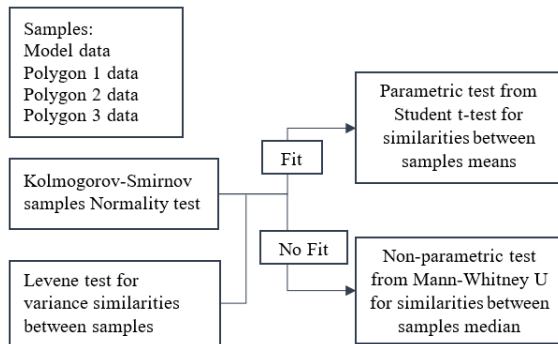


Figure 8. Methodological statistical scheme.
Source: Authors

First, a normality Kolmogorov-Smirnov (K-S) test was applied to determine if the samples fit a normal distribution. The null hypothesis (H_0) assumption was that the samples fit a distribution, and, as an alternative hypothesis (H_1), the negation of H_0 . Additionally, the homogeneity of variance test from Levene was applied.

Results

The problem was simulated with the data shown above, recreating the plate-load test in the process of loading and unloading for a given period of time (Table 6).

Table 6. Values of the loading and unloading process

Stress (kPa)	0	30	0	50	150	250	350	450	300
Time (sec.)	0	15	5	30	30	30	30	30	15
Stress (kPa)	150	0	150	300	450	300	150	0	-
Time (sec.)	15	15	30	30	30	15	15	15	-

Source: Adapted from technical report, courtesy of Cienfuegos's ENIA.

The geometry of the foundation soil was defined considering the stratification and, after simulating the initial stress, the load of the 3 m high embankment was added. Later stages of

implementation regarding the loading and unloading for each of the pressures determined in the test and the application time of the load were defined. For the simulation, the test area with 30 cm elements was zoned to represent the circular plate of 300 mm in diameter and a distributed load on the element equal to the test value (Figure 9).

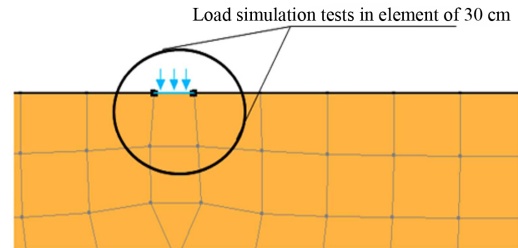


Figure 9. Zoom-in of the simulation of the load-plate test on the finite element size of 30 cm.
Source: Authors

After the test was modeled, the results of the soil strain by the load system were represented graphically as stress-displacement curves for both the model and the test (Figure 10).

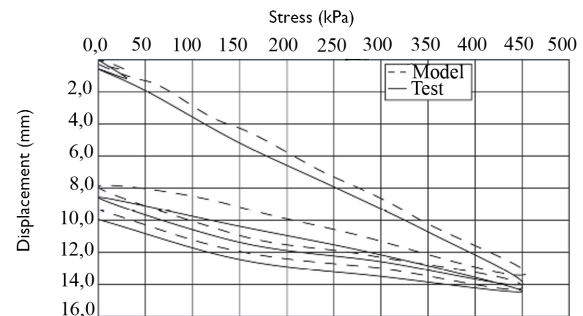


Figure 10. Stress-displacement curves from model and average of results from polygon 3.
Source: Authors

From the results of polygons 1 and 3, the average was obtained and graphically represented as shown in Figure 10. The RMSE, MSE, and MAPE from Table 5 were applied to the results from polygons 1 and 3, since the data of polygon number 2 was not representative.

The MSE and RMSE was 0,49 and 0,70, respectively, for polygon 3; and, for polygon 1, the results were 2,49 and 1,58, respectively. Chai and Draxler (2014) suggest that RMSE is a better metric to present the results than MAE. The error in those cases was 0,70 and 1,58 for polygons 3 and 1, respectively. On the other hand, the value of the MAPE was 9 and 12% for polygons 3 and 1, respectively. It should be noted that, in engineering, acceptable errors are between 5 and 10%. As there are many variables involved in this process and some imprecision in measurements or parameters from the literature, a 12% of error was accepted.

However, this paper presents another way to calibrate the numerical model through the determination of similarities between two independent samples by means of statistical

hypotheses. Table 7 shows the K-S test for polygons and the model, where no data fits the normal distribution, since the p -value was less than 0,05.

Table 7. Kolmogorov-Smirnov tests for one sample

The contrast distribution is Normal					
	Model	Polygon 1	Polygon 2	Polygon 3	
N	1 214	1 124	1 112	1 214	
Mean	10,18	11,16	9,87	10,83	
Measurements of central tendency	Dev.	3,321	4,005	3,528	3,207
Variance	11,031	16,040	12,450	10,282	
COV. (%)	33%	36%	36%	30%	
Z from K-S	3,755	4,423	6,512	4,284	
Sig. Asymptotic (bilateral) P value	0,000	0,000	0,000	0,000	

Source: Authors

On the other hand, the Levene test was applied with the null hypothesis that the population variances are equal. As is shown in Table 8, the p -value was higher than 0,05 when the model was compared with polygons 1 and 3, thus corroborating the similarities in variances. The p -value of polygon 2 was less than 0,05, thus corroborating that those experiments were not representative.

Table 8. Homoscedasticity tests from Levene

Samples	Levene Test for Equality of Variances	
	F	Sig.
Model and Polygon 1	0,439	0,508
Model and Polygon 2	21,962	0,000
Model and Polygon 3	2,469	0,116

Source: Authors

Then, as the data did not fit a normal distribution, a non-parametric Mann-Whitney U test was used, under the assumption of the null hypothesis (H_0) that the samples have statistically similar median, as well as an alternative hypothesis (H_1): the negation of H_0 that the medians of samples are not similar. The test was applied with a confidence level of 95%. This means that, if the p -value is greater than 0,05, the samples have a similar median.

The results in Table 9 show that the significance level was higher than 0,05 for polygons 1 and 3, and thus the null hypothesis was not rejected, which indicates that the samples (model and experimental) can be considered similar. This result matches previously reported results when considering the error theory (9 and 12% for polygons 3 and 1, respectively). Therefore, it is confirmed that the results from the model and those from the load-plate tests (from polygons 1 and 3) were similar.

Table 9. Results of the nonparametric Mann-Whitney U test

Model and Polygon 1	U from Mann-Whitney	646 390,500
	W from Wilcoxon	1 264 106,500
	Z	-1,731
	Sig. Asymptotic (bilateral)	p-value = 0,083
Model and Polygon 3	U from Mann-Whitney	105,000
	W from Wilcoxon	276,000
	Z	-1,805
	Sig. Asymptotic (bilateral)	p-value = 0,071
	Sig. exact [2*(Sig. unilateral)]	0,074 (a)
(a) = Without correction		

Source: Authors

Conclusions

In this paper, the simulation of a load-plate test was performed by using the numerical method of finite elements, based on the project report of the National Applied Research Company (ENIA) of Cuba. An overview of the constitutive models to be applied in soil was carried out. Additionally, to calibrate the numerical model, two procedures were followed: using the error theory and performing the non-parametric hypothesis statistical test of Mann-Whitney U. For both procedures, the results from the model and the experimental data are similar. Moreover, the results show that a load-plate test can be modeled using FEM. To reproduce other load plate tests by using the finite element model, it is necessary to provide the geotechnical characteristics, geometry, and geomorphology of the soils. The procedures shown in this paper can be used in other studies related to soil calibration problems where experimental data are available.

Acknowledgements

The authors want to thank the Cienfuegos's ENIA for providing their studies and data.

References

- AASHTO. (2021). *Road Standard, Section 207: Embankment*.
- AASHTO.Abaqus/CAE. (2017). *Mohr-Coulomb plasticity*. https://abaqus-docs.mit.edu/2017/English/SIMACAEMA_TRefMap/simamat-c-mohrcoulomb.htm#simamat-c-mohrcoulomb-t-MohrCoulombSurface-sma-topic2__simamat-c-cmohrcoulomb-yield
- Albarazi, R. (2020). *Evaluation of Roadway Embankment Under Repetitive Axial Loading Using Finite Element Analysis*. [Master's thesis, Lulea University of Technology]. Lulea University of Technology. <http://urn.kb.se/resolve?urn=urn:nbn:se:ltu:diva-81916>
- Álvarez, J. (2014). *Formulaciones inversas de cáscaras en coordenadas relativas y deformaciones proyectadas*. [Doctoral thesis, UCLV-CUJAE]. https://www.researchgate.net/publication/336349626_Formulaciones_inversas_de_casca

ras_en_coordenadas_relativas_y_deformaciones_proye-
ctadas

- Anderson, R., Andrej, J., Barker, A., Bramwell, J., Camier, J.-S., Cervený, J., Dobrev, V., Dudouit, Y., Fisher, A., Kolev, T., Pazner, W., Stowell, M., Tomov, V., Akkerman, I., Dahm, J., Medina, D., and Zampini, S. (2021). MFEM: A modular finite element methods library. *Computers & Mathematics with Applications*, 81, 42-74. 10.1016/j.camwa.2020.06.009
- Anyang, M. Y., Atarigiya, B. D., Ofori-Addo, R., and Allotey, N. K. (2018). *Plate Load Test: Getting it Right* [Conference presentation]. 9th Ghana Institution of Engineers (GhIE) Annual Conference, Ghana.
- ASTM (1994). *ASTM-D-1194-94 Standard Test Method for Bearing Capacity of Soil for Static Load and Spread*. ASTM. 10.1520/D1194-94
- ASTM (2000). *ASTM D2487-00 Standard Classification of Soils for Engineering Purposes (Unified Soil Classification System)*. 10.1520/D2487-00
- Chai, T. and Draxler, R. R. (2014). Root mean square error (RMSE) or mean absolute error (MAE)? – Arguments against avoiding RMSE in the literature. *Geoscientific Model Development*, 7(3), 1247-1250. 10.5194/gmd-7-1247-2014
- Feng, S., Wang, W., Hu, K., and Höeg, K. (2020). Stress-strain-strength behavior of asphalt core in embankment dams during construction. *Construction and Building Materials*, 259, 119706. 10.1016/j.conbuildmat.2020.119706
- Gu, J., Li, K., and Su, L. (2020). Modified nonlinear Mohr-Coulomb fracture criteria for isotropic materials and transversely isotropic UD composites. *Mechanics of Materials*, 151, 103649. 10.1016/j.mechmat.2020.103649
- Guo-xiong, W., Jing-sheng, D., Min, W., and Xian-yi, L. (2010, August 4-8). *3D Effect Analysis of Geometrically Complicated High-Filled Slope Stability* [Conference presentation]. Transportation Infrastructure Construction and Emerging Technology, ICCTP 2010: Integrated Transportation Systems-Green - Intelligent - Reliable, Beijing, China.
- Haftka, R. T. and Malkus, D. S. (1981). Calculation of sensitivity derivatives in thermal problems by finite differences. *International Journal for Numerical Methods in Engineering*, 17(12), 1811-1821. 10.1002/nme.1620171206
- Hai-Sui, Y. (2006). *Plasticity and geotechnics* (vol. 13). Springer.
- Hernández-López, F. M., Tejeda-Piusseaut, E., Rodríguez-Veliz, E. A., and Recarey-Morfa, C. A. (2020). 3D-FE of jointed plain concrete pavement over continuum elastic foundation to obtain the edge stress. *Revista de la construcción*, 19(1), 5-18. 10.7764/rdlc.19.1.5-18
- Huang, J., Han, J., and Zheng, J. (2010, June 3-5). *Analysis of the Influence of Embankment Widening on Soft Ground with Differential Settlements on Pavement Structure* [Conference presentation]. Ground Improvement and Geosynthetics (GSP 207), Shanghai, China. https://ascelibrary.org/doi/book/10.1061/9780784411087
- Jiang, M., Zhang, A., and Shen, Z. (2020). Granular soils: from DEM simulation to constitutive modeling. *Acta Geotechnica*, 15(7), 1723-1744. 10.1007/s11440-020-00951-7
- Kaizhong, G. and Shiyong, L. (2019). *Fundamentals of Error Theory*. Springer.
- Lamas, F., Oteo, C., and Chacón, J. (2011). Influence of carbonate content on the stress-strength behaviour of neogene marls from the betic cordillera (Spain) in cu triaxial tests using a quasilinear elastic (hyperbolic) model. *Engineering Geology*, 122(3-4), 160-168. 10.1016/j.enggeo.2011.05.013
- Li, W., Yang, Q., Xue, Z., Liu, W., and Hua, Y. (2021). Experimental study and constitutive modeling of volume change behavior in unsaturated soils. *Bulletin of Engineering Geology and the Environment*, 80(1), 679-689. doi:10.1007/s10064-020-01943-3
- Liu, G.-S., Kong, L.-W., Chen S.-X., and Hu, M.-J. (2004). Experimental study on control of high embankment construction on soft foundation in Xiang-jing Expressway. *Yantu Lixue/Rock and Soil Mechanics*, 25, 496-500. https://www.researchgate.net/publication/291173299_Experimental_study_on_control_of_high_embankment_const-
ruction_on_soft_foundation_in_Xiang-jing_expressway
- Mellah, R., Auvinet, G., and Masrouri, F. (2000). Stochastic finite element method applied to non-linear analysis of embankments. *Probabilistic Engineering Mechanics*, 15(3), 251-259.
- Mesa, M. (2017). *Empleo de la modelación para el diseño de terraplenes altos de carretera* [Doctoral thesis, Universidad Central “Marta Abreu” de las Villas]. Editorial Universitaria. https://bd.uveg.edu.mx/opac_css/index.php?lvl=notice_display&id=255153
- Mesa, M. and Álvarez, J. (2011). Calibración numérica de un problema de ingeniería vial. *Revista de la construcción*, 10(3), 52-63. 10.4067/S0718-915X2011000300006
- Mesa, M., Álvarez, J., and Chávez, J. H. (2020). Evaluación del factor de seguridad en taludes de terraplenes carreteros altos ante carga sísmica. *Revista de Ingeniería Sísmica*, 2(103), 1-17. 10.18867/RIS.103.489
- Mesa, M., Álvarez, J., Tejeda, E., and Recarey, C. (2016). Determination of the domain dimensions in embankment numerical modeling. *Dyna*, 83(198), 44-48. 10.15446/dyna.v83n198.49211
- Mesa, M., Lamas, F., Tejeda, E., Álvarez, J., and Recarey, C. (2016, November 21-25). *Simulación de la construcción de terraplenes con técnicas numéricas* [Conference presentation]. 18 Convención Científica de Ingeniería y Arquitectura, Havana, Cuba.
- Murata, Y., Kariya, K., Yashima, A., Okamura, T., Quan, N. H., Yokota, Y., Shuji, I., and Tsuji, S. (2020). Long-life repair method for road based on soundness evaluation of embankment and pavement. *Japanese Geotechnical Society Special Publication*, 8(11), 424-429. doi:10.3208/jgssp.v08.j03
- Namdar, A. (2020). The impact of mesh structural design on non-linear numerical simulation of geo-structure: A seismic

- analysis. *Material Design & Processing Communications*, e195. 10.1002/mdp2.195
- NC-11. (2005). *Geotecnia. Métodos de ensayo de carga sobre placa en suelos* (1 ed., pp. 22). Norma Cubana. NC-325. (2004). Ensayos de corte directo. Norma Cubana.
- Nieto, A., Camacho, J., and Ruiz, E. (2009). Determinación de parámetros para los modelos elastoplásticos Mohr-Coulomb y Handening Soil en suelos arcillosos. *Revista Ingenierías*, 8(15), 75-91. <https://revistas.udem.edu.co/index.php/ingenierias/article/view/63>
- Osipov, Y., Safina, G., and Galaguz, Y. (2018, November 14-16). *Calculation of the filtration problem by finite differences methods* [Conference presentation]. VI International Scientific Conference "Integration, Partnership and Innovation in Construction Science and Education" (IPICSE-2018), Moscow, Russia.
- Otálvaro, I. F. and Nanclares, F. J. (2009). Elements to estimate subgrade reaction coefficients. *Dyna*, 76(157), 81-89. <https://revistas.unal.edu.co/index.php/dyna/article/download/9555/11480>
- Pardo de Santayana, F., Cano Linares, H., Ruiz de Arbuló, M., and Rodríguez Abad, R. (2020). Estudios sobre utilización de residuos en terraplenes de carreteras. *Revista Digital del Cedex*, 196, 26-38. <http://ingenieriacivil.cedex.es/index.php/ingenieria-civil/article/view/2420>
- Patel, A. (2019). Geotechnical investigation. In A. Patel (Ed.), *Geotechnical Investigations and Improvement of Ground Conditions* (pp. 87-155): Woodhead Publishing. PG-3. (2017). Pliego de Prescripciones Técnicas Generales para obras de carreteras y puentes. Gobierno de España.
- Shan, W., Guo, Y., Liu, H., Yang, L., and Yang, L. (2009, July 25-27). *The Compaction for Widening High Embankment and Its Distribution along the Height of Roadbed in Seasonal Frozen Regions* [Conference presentation]. International Conference on Transportation Engineering 2009, Chengdu, China.
- Standing, J. R., Vaughan, P. R., Charles-Jones, S., and McGinnity, B. T. (2020). Observed behaviour of old railway embankments formed of ash and dumped clay fill. *Géotechnique*. Advance online publication. 10.1680/jgeot.19.SiP.045
- Stuedlein, A. W., Bailey, M., Lindquist, D., Sankey, J., and Neely, W. J. (2010). Design and Performance of a 46-m-High MSE Wall. *Journal of Geotechnical and Geoenvironmental Engineering*, 136(6), 10. 10.1061/(ASCE)GT.1943-5606.0000294
- Ulloa, Á. and Vargas, W. (2007). Metodología simplificada para evaluación de vulnerabilidad geotécnica de terraplenes en carreteras de montaña de Costa Rica. *Revista Infraestructura Vial*, 18, 4-14. <https://www.revistas.ucr.ac.cr/index.php/vial/article/view/2051>
- Zhang, P., Yin, Z.-Y., and Jin, Y.-F. (2021). State-of-the-Art Review of Machine Learning Applications in Constitutive Modeling of Soils. *Archives of Computational Methods in Engineering*. 10.1007/s11831-020-09524-z
- Zienkiewicz, O. C., Taylor, R. L., Zhu, J. Z., and Nithiarasu, P. (2015). *El Método de los Elementos Finitos* (6th ed.). CIMNE.

Empirical Models to Predict Compaction Parameters for Soils in the State of Ceará, Northeastern Brazil

Modelos empíricos para predecir parámetros de compactación para suelos en el Estado de Ceará, Noreste de Brasil

Amanda V. Hohn¹, Rosiel F. Leme², Francisco C. da Silva Filho³, Thales E. Moura⁴, and Grover R. Llanque A.⁵

ABSTRACT

This work developed prediction models for maximum dry unit weight ($\gamma_{d,max}$) and optimum moisture content (OMC) for compacted soils in Ceará, Brazil, based on index and physical properties and physical properties. The methodology included data from soils used in the construction of 15 dams in Ceará, with available information regarding laboratory tests of interest. Correlations were developed using non-linear regression, from 169 laboratory results (83 for training and 86 for validating the models), which presented a R^2 of 0,763 for MoPesm (prediction model for $\gamma_{d,max}$) and 0,761 for MoTuo (model for OMC). *A posteriori*, the same physical indexes used to train and validate MoPesm and MoTuo were used as inputs of other prediction models available in the literature, whose outputs differed considerably from laboratory results for the evaluated soils. MoPesm and MoTuo were able to satisfactorily predict compaction parameters, with outputs close to those obtained in laboratory for tested soil samples. Their performance justifies their use for predicting compaction parameters in geotechnical structures that use employ soils when there are financial restraints, short timeframes, or unavailability of test equipment, particularly in early design stages and preliminary studies, before appropriate soil sampling and field investigation can be conducted, thus saving substantial time and financial resources.

Keywords: predicting models, compacted soils, maximum dry unit weight, optimum moisture content

RESUMEN

Este trabajo desarrolló modelos predictivos para el peso específico seco máximo ($\gamma_{d,máx}$) y el contenido de humedad óptima (CHO) para suelos compactados en Ceará, Brasil, basados en índices y propiedades físicas. La metodología incluyó datos de suelos utilizados en la construcción de 15 presas en Ceará, con información disponible sobre las pruebas de laboratorio de interés. Las correlaciones fueron desarrolladas mediante regresión no lineal, a partir de 169 resultados de laboratorio (83 para entrenamiento y 86 para validación de ambos modelos), que presentaron un R^2 de 0,763 para MoPesm (modelo de predicción para $\gamma_{d,máx}$) y 0,761 para MoTuo (modelo para CHO). *A posteriori*, los mismos índices físicos utilizados para entrenar y validar MoPesm y MoTuo fueron utilizados como entradas para otros modelos de predicción disponibles en la literatura, cuyos resultados difirieron considerablemente de los resultados de laboratorio para los suelos evaluados. MoPesm y MoTuo predijeron satisfactoriamente los parámetros de compactación, con resultados cercanos a los obtenidos en laboratorio para las muestras de suelo ensayadas. Su desempeño justifica su uso para predecir parámetros de compactación en estructuras geotécnicas que utilizan suelos compactados cuando existen restricciones financieras, plazos cortos o indisponibilidad de equipos de prueba, particularmente en las primeras etapas de diseño y estudios preliminares, antes de que se pueda realizar muestreos apropiados de los suelos e investigación de campo, ahorrando así tiempo y recursos financieros sustanciales.

Palabras clave: modelos predictivos, suelos compactados, densidad seca máxima, contenido de humedad óptima

Received: April 14th, 2020

Accepted: May 18th, 2021

¹Civil Engineer, Universidade Federal do Ceará, Brazil. M.Sc. Civil Engineering (Geotechnics), Universidade Federal do Ceará, Brazil. Affiliation: D.Sc. Civil Engineering (Water Resources), Universidade Federal do Ceará, Brazil (Bolsista Capes-PDSE 88881.189124/2018-01). E-mail: engenheirista@yahoo.com.br

²Civil Engineer, M.Sc. and D.Sc. Civil Engineering (Water Resources), Universidade Federal do Ceará, Brazil. Affiliation: Associate Professor, Universidade Federal do Ceará, Brazil. E-mail: rosielferreira@gmail.com

³Civil Engineer, Universidade de Fortaleza, Brazil. M.Sc. and D.Sc. Civil Engineering, Universidade Federal do Rio de Janeiro, Brazil. Affiliation: Full Professor, Universidade Federal do Ceará, Brazil. E-mail: fchagas@ufc.br

⁴Civil Engineer, Universidade Federal do Ceará, Brazil. Affiliation: Graduate Student (Specialization in Infrastructure Engineering), Universidade de Fortaleza, Brazil. E-mail: thalesmoura.engcivil@gmail.com

⁵Civil Engineer, Universidad Técnica de Oruro, Bolivia. M.Sc. in Civil Engineering, Universidade Federal do Ceará, Brazil. Affiliation: D.Sc. Geotechnical Engineering, COPPE-Universidade Federal do Rio de Janeiro, Brazil.

Introduction

Every engineering work has its inherent risks, as countless uncertainties are embedded in all phases of its development and execution. For earthworks, the prediction of soil behavior involves several aspects; it is practically impossible to state

E-mail: groverllanque@coc.ufrj.br

How to cite: Hohn, A. V., Leme, R. F., da Silva Filho, F. C., Moura, T. E., and Llanque, G. R. A. (2022). Empirical Models to Predict Compaction Parameters for Soils in the State of Ceará, Northeastern Brazil. *Ingeniería e Investigación*, 42(1), e86328. <https://doi.org/10.15446/ing.investig.v42n1.86328>



Attribution 4.0 International (CC BY 4.0) Share - Adapt

with absolute certainty if it will perform as expected (Vieira, 2005). As for the estimation of parameters, incorrect choices may ultimately result in localized failures or even general collapse of the structure.

In order to make good decisions in the face of so many unavoidable uncertainties, Silva (2015) says it is essential to understand the variables that influence soil behavior in the best possible way, as well as to conceive mathematical models capable of accurately representing and predicting the field performance of geotechnical structures.

When experimental data is limited, the use of simpler, yet responsive methodologies to assess engineering problems and predict soil behavior should be encouraged, especially if they can be performed in shorter computational times (Silva *et al.*, 2016).

Determining soil compaction parameters in a laboratory is a crucial step in controlling the field compaction of earthworks such as dams and embankments (Farooq *et al.*, 2016). However, during the early stages of a project (e.g., in the preliminary assessment of the suitability of borrow materials), considerable time and effort can be saved through the use of empirical correlations (Günaydin, 2009; Di Matteo *et al.*, 2009; Tizpa *et al.*, 2015; Gurtug and Sridharan, 2004), which can be extremely helpful, provided that the engineer knows the index properties of the soil. Index properties are those upon which the identification and classification steps of a soil are based; this includes grain-size distribution, Atterberg limits (liquid limit, plastic limit, shrinkage limit, and plasticity index), density, and specific gravity.

The compaction parameters – optimum moisture content (OMC) and maximum dry unit weight ($\gamma_{d,max}$) – are determined through very time-consuming laboratory tests. This makes prediction models that are based on easily measurable soil properties (such as those described above) highly desirable and remarkably useful (Karimpour-Fard *et al.*, 2019).

Early studies proposing empirical models for estimating compaction parameters based on soil index properties were cited by Wang and Huang (1984), who manually mixed gravel, sand, limestone powder, and bentonite in different proportions, creating 57 samples, compacted with standard Proctor energy. The goal was to develop equations for predicting permeability and compaction parameters based on Atterberg limits and the grain-size distribution curve. The results of the compaction and permeability tests were analyzed along with the classification properties of the samples, which indicated a good response ($R^2 > 0,8$) in predicting compaction and permeability parameters for the mixtures in the analyzed proportions.

Omar *et al.* (2003) collected 311 samples of sandy and sandy-silty soils from the United Arab Emirates and performed laboratory tests. They developed a linear regression model to predict soil compaction parameters for modified Proctor energy using fines percentage, liquid limit (LL), plastic limit (PL), and compaction energy. Their model resulted in nomograms capable of predicting $\gamma_{d,max}$ and OMC for

granular soils within a 95% confidence interval for the analyzed samples.

Gurtug and Sridharan (2002, as cited in Farooq *et al.*, 2016) presented a correlation for clayey soils, where $\gamma_{d,max}$ was 0,98 times the dry unit weight at plastic limit water content, and OMC was 0,92 times PL. In another study (Gurtug and Sridharan, 2004), the same authors evaluated the effect of different compaction energies on fine-grained compacted soils collected in Turkey and Cyprus, as well as data available in the literature. They found a good correlation between PL and OMC, which showed the best results for standard Proctor energy.

Sridharan and Nagaraj (2005) stated that the relationships available at the time between index properties and compaction parameters were unsatisfactory. They analyzed 10 soil samples (natural and commercial kaolinites) plus data available in the literature, finding that PL had a better correlation with compaction parameters than LL and the plasticity index (PI) for standard Proctor compactive effort.

Sivrikaya (2008) presented multiple correlation equations for fine-grained soils at standard Proctor energy by performing multilinear regression (MLR) analyses and using artificial neural networks (ANNs), assessing 113 samples obtained from the literature and collected in different sites in Turkey. His equations had $R^2 > 0,75$ for $\gamma_{d,max}$ and $R^2 > 0,74$ for OMC, respectively. He concluded that $\gamma_{d,max}$ and OMC had a considerably good correlation with PL, better than with LL and PI.

Saikia *et al.* (2017) came to similar conclusions; they analyzed 40 samples of natural fine-grained soils collected in Assam, India. Their results showed that LL had higher correlation rates than PL with $\gamma_{d,max}$ and OMC. The root mean square error (RMSE) for the predicted $\gamma_{d,max}$ was 2,1% when compared to laboratory results, and 7,5% when compared to literature values. For the predicted OMC, RMSE was 7,0% in relation to laboratory results, and 17,5-28,2% to literature values.

Thirty samples of clayey soils ($18 \leq LL \leq 82\%$; $1 \leq IP \leq 51\%$; and $2,47 \leq G_s \leq 3,09$)* were collected in various parts of central Italy by Di Matteo *et al.* (2009) for laboratory determination of index properties and compaction parameters with modified Proctor energy. Considering these results and other 41 reported in the literature, the authors developed multiple regression models that correlated $\gamma_{d,max}$ and OMC with index properties, and they noticed that the most important variable was specific unit weight, followed by LL and PL.

Toms and Philip (2016) performed regression analysis with multiple variables to predict compaction parameters from Atterberg limits and specific unit weight for 30 soil samples from Kuttanad, India, with LL ranging between 70 and 190%, PI between 26 and 127%, and specific unit weight between 2,3 and 2,5 kN/m³. They concluded that there is indeed a direct linear relationship between index properties and compaction

*Gs is the specific gravity, the ratio of the unit weight of the solid particles of a soil to the unit weight of water. Gs is a dimensionless parameter and can be determined according to standard ASTM D854-14.

parameters, and that the most important variables were specific gravity and the index properties.

Farooq *et al.* (2016) analyzed 105 samples of fine soils from Pakistan with various USCS classifications (CH, CL, CL-ML, ML), and, using multiple regression analyses, they proposed prediction curves to estimate compaction parameters from LL and PI for standard and modified Proctor energies, thus eliminating the need for compaction tests in preliminary design stages. The results showed that the variation between experimental and predicted data was within a confidence interval of $\pm 2,5\%$ for $\gamma_{d,max}$ and $\pm 9,5\%$ for OMC.

Wang and Yin (2020) developed a model using multi expression programming (MEP), a method of genetic programming, and data comprising a wide range of soil types from previously published studies. Their model was considered reliable ($R^2 > 0,85$), even for high-plasticity and coarse-grained soils, which did not figure among the soil types analyzed in previous studies; and, although their results were extremely favorable, the required high-end computational tools somewhat lost track of the simplicity present in other models, which yielded as fair predictions and could make a difference in the face of time constraints and the unavailability of a more complex software apparatus.

Regarding soils from Brazil, a study by Karimpour-Fard *et al.* (2019) analyzed data from 728 sets of granular and fine-grained soils, most from 20 literature sources, and 227 of their own, collected in Salvador metropolitan region (State of Bahia, northeastern Brazil). Their approach involved analyses using MLR and ANNs, and the results demonstrated that the ANN model could predict compaction parameters with a zero average error, but it required a lot more of processing time, thus being unsuitable for situations where prompt decision making is mandatory. On the other hand, MLR also yielded fairly precise results at reduced computational and time costs. They noted that the compactive effort level had a low effect on prediction accuracy when compared to other analyzed parameters (LL, PL, fine, sand, gravel content, and specific gravity).

Moura (2019) also analyzed Brazilian soils but from the State of Ceará, which shares the same sedimentary formations present in Bahia, like the Barreiras Formation. Using non-linear regression, he developed models for predicting compaction parameters from index properties, such as Atterberg limits, fines percentage, and void ratio, and finding mean error of 2,3% and R^2 of 0,618 for $\gamma_{d,max}$, and 8,5% and 0,541 for OMC. By comparing laboratory results for $\gamma_{d,max}$ and OMC with outputs of models proposed by Omar *et al.* (2003) and Gurtug and Sridharan (2004), Moura (2019) noticed that their predicted values differed considerably from laboratory results. This divergence was attributed to the singular mineralogical constitution and genesis context of northeastern Brazilian soils, mostly in the semi-arid domain.

Considering this gap, a simplified empirical model to predict compaction parameters ($\gamma_{d,max}$ and OMC) for standard

Proctor energy was developed using results of index tests as its inputs. The goal was to attain a better statistical performance than that of the model proposed by Moura (2019), using a different initial dataset that comprised laboratory results of characterization and compaction tests of soils classified as CL, SC, SM, and SM-SC (USCS), all from the State of Ceará, located in the semi-arid domain of northeastern Brazil.

This simplified model is intended to be used in the preliminary design stages of earth structures (e.g., initial assessment of borrow materials), when more accurate field investigation and laboratory testing may not be available yet. This can save valuable resources when estimating parameters, especially when there are financial constraints, limited time, or unavailability of test equipment. Also, its use will drastically reduce the computational cost of extensive software modeling, which is mandatory for detailed design.

Materials and Methods

Dataset definition

In this research, 169 results of laboratory tests performed on soil samples collected during the construction of 15 dams located in different municipalities in the State of Ceará were used (Figure 1). Out of these samples, 83 were randomly selected to train the empirical models (development dataset), and 86 were used in the validation step.

The analyzed laboratory data comprised compaction parameters ($\gamma_{d,max}$ and OMC) and the results of soil characterization tests (particle size curve, Atterberg limits, and unit weight), all provided by the Laboratory of Soil Mechanics and Paving (LMP) of the Federal University of Ceará.

Table 1 shows information about the earth dams where the soil samples used in this study were collected. Table 2 presents the descriptive statistics for the soil properties used as input variables in the proposed models, including mean, standard deviation, variance, minimum, maximum, and interval.

Table 1. Information about soil samples used in development and validation datasets

	Dam	Location	No. Samples	USCS Classification
Development	Angicos	Coreaú	14	CL, CG
	Catú	Aquiraz	11	SC, CL
	Cauípe	Caucaia	4	SC, SM-SC
	Faé	Quixelô	7	SC, SM-SC
	Farias Brito	Farias Brito	3	CL, SM
	Flor do Campo	Novo Oriente	1	CL
Validation	Itaúna	Granja	15	CL, SC, SM
	Marco	Marco	14	SC, SM
	Missí	Miraima	10	CL
	Paulo Sarasate	Varjota	4	CL, SC
	Rosário	Lavras da Mangabeira	10	CL, SC
	Sítios Novos	Caucaia	28	CL, SC, SM, SM-SC
	Trussu	Iguatu	5	SC
	Ubalzinho	Cedro	29	CL, SC, SM, SM-SC
	Umari	Madalena	14	SC

Source: Authors

[†]USCS is the Unified Soil Classification System, a standard to classify soils for engineering purposes (ASTM D2487-17e1).

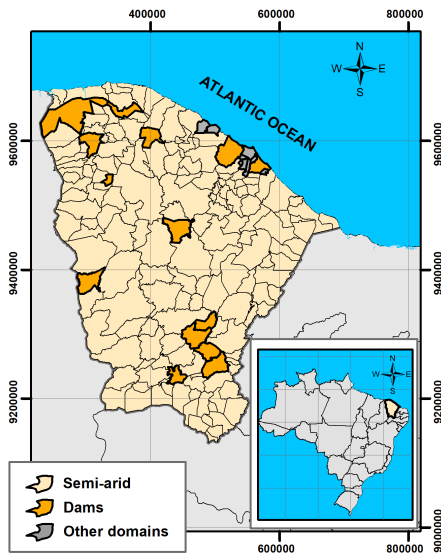


Figure 1. Municipalities in Ceará where analyzed soil samples were collected.

Source: Adapted from IPECE (2018).

Table 2. Descriptive statistics of variables used in development (Dev.) and validation (Val.) datasets

Index	$\gamma_{d,max}$		OMC		LL		PL		Fine %		γ_s	
	Dev.	Val.	Dev.	Val.	Dev.	Val.	Dev.	Val.	Dev.	Val.	Dev.	Val.
Mean	17,94	18,2	14,9	12,73	33,3	30,14	20,4	19,5	47,88	43,98	26,05	26,09
Std dev.	1,00	1,07	2,90	2,99	5,83	7,21	3,32	3,16	17,09	13,1	0,68	0,54
Variance	1,00	1,15	8,4	8,95	33,93	52,05	11,0	10,0	292,1	171,6	0,46	0,29
Minimum	15,1	15,5	9,8	7,0	23,0	16,0	13,0	12,0	5,0	13,0	23,3	24,4
Maximum	20,2	21,0	22,3	23,2	47,0	45,0	25,0	25,0	75,0	79,0	27,4	27,4
Interval	5,1	5,5	12,5	16,2	24,0	29,0	12,0	13,0	70,0	66,0	4,14	3,0

Source: Authors

Among the analyzed samples, there was a casual predominance of clayey soils in the development dataset (52,5%), and of sandy soils in the validation dataset (62,0%). According to Vieira *et al.* (1996), these soil types are widely used in the Brazilian semi-arid region due to their high occurrence and the characteristics they grant to earth structures, such as: high shear strength, low permeability, and low deformability.

In this study, the initial choice of geotechnical properties employed in the development of empirical models was made based on the works of Omar *et al.* (2003), Gurtug and Sridharan (2004), Di Matteo *et al.* (2009), and Farooq *et al.* (2016). Using nonlinear regression, different expressions involving assorted index properties were investigated and subjected to quick statistical analyses. If the results were not satisfactory, new expressions were tested until the final equations were defined.

The laboratory tests used to classify the soil samples and determine their fit as inputs for the proposed equations included the determination of particle-size distribution, specific gravity, and Atterberg limits (LL and PL). Additionally, laboratory results from standard Proctor compaction tests were used to assess the model predictions for $\gamma_{d,max}$ and

OMC. Table 3 shows the technical standards concerning these tests that are valid in Brazil, as well as their equivalent ASTM standards and the befitting soil grain size for each of them.

Table 3. Laboratory tests performed according to ABNT technical standards and their ASTM equivalents

Laboratory Test	Brazilian Technical Standard	ASTM Equivalent	Soil grain size
Particle-Size Distribution of Fine-Grained Soils Using Sedimentation (Hydrometer) Analysis	NBR 7181:2016 (Soil-Grain size analysis)	D7928-17	< 2,0mm
Specific Gravity of Soil Solids (Water Pycnometer)	DNER-ME 093/94 (Determination of specific gravity)	D854-14	< 2,0mm
Determination of Plastic Limit of Soils	NBR 7180:2016 (Soils-Determination of plastic limit)	D4318-17e1	< 0,42mm
Determination of Liquid Limit of Soils	NBR 6459:2016 (Soils-Determination of liquid limit)	D4318-17e1	< 0,42mm
Laboratory Compaction of Soils Using Standard Effort (Proctor)	NBR 7182:2016 (Soils-Compaction test)	D698-12e2	Any

Source: Authors

Predictive model for maximum dry unit weight (MoPesm)

The empirical model to predict the maximum dry unit weight (MoPesm) considered properties that could potentially influence this parameter: liquid limit (LL), plastic limit (PL), percentage of material passing through a No.10 sieve (%P#10), percentage passing through a No. 40 sieve (%P#40), percentage passing through a No. 200 sieve (%P#200), and specific unit weight (γ_s).

Equation (1) displays the original expression used to develop MoPesm. In the nonlinear regression, the value of 1,0 was initially assigned to coefficients a_0 , a_1 , a_2 , a_3 , a_4 , a_5 , and a_6 , as well as to power coefficients α , β , δ , ε , θ , μ , and ω . They were then defined as variables and subjected to an iterative process, aiming to reach the smallest mean error.

$$\gamma_{d,max} = a_0 \left[a_1 \cdot (LL)^\alpha + a_2 (PL)^\beta + a_3 (\%P\#10)^\delta + a_4 (\%P\#40)^\varepsilon + a_5 (\%P\#200)^\theta + a_6 (\gamma_s)^\mu \right]^\omega \quad (1)$$

where:

$\gamma_{d,max}$: maximum dry unit weight [kN/m³];

LL: liquid limit [%];

PL: plastic limit [%];

%P#10: percentage of material passing through a No. 10 sieve [%];

%P#40: percentage of material passing through a No. 40 sieve [%];

%P#200: percentage of material passing through a No. 200 sieve [%]; and

γ_s : specific unit weight [kN/m³].

Predictive model for OMC (MoTuo)

The parameters selected *a priori* to appear in the empirical model for optimum moisture content (OMC) were LL and PL (due to their close relationship with moisture content), those related to particle-size distribution (%P#10, %P#40, and %P#200), and void ratio (e).

Atterberg limits and particle-size distribution variables were chosen because a little over half of the soils analyzed in this study were clays and silts, and, according to Pinto (2006), the fine fraction has a strong influence on moisture content. Void ratio (e) was also assumed to have a potential influence on moisture content, since fine soils have a large specific surface and really small voids, which increase the effect of capillarity and water retention, and, ultimately, moisture content (Leme, 2015; Fredlund *et al.*, 1994).

Equation (2) was the original expression proposed for MoTuo:

$$OMC = a_0 \left[a_1(LL)^\alpha + a_2(PL)^\beta + a_3(\%P\#10)^\delta + a_4(\%P\#40)^\epsilon + a_5(\%P\#200)^\theta + a_6(e)^\mu \right]^\omega \quad (2)$$

where:

OMC: optimum moisture content [%]; and

e : void ratio [dimensionless].

As described for MoPesm, after carrying out the iterative process, model MoTuo was optimized by means of defining the maximum and minimum acceptable values for the chosen parameters, aiming to eliminate values that were not aligned with field reality.

Results and discussion

Predictive model for maximum dry unit weight (MoPesm)

Some of the coefficients in Equation (1) were nullified at the end of the iterative process, which indicates that the corresponding variables had very little to no influence in determining the maximum dry unit weight and could therefore be excluded.

Equation (3) presents the final expression for MoPesm, whose prerequisite is that the soil has $10\% < PL < 25\%$.

$$\gamma_{d,\max} [kN/m^3] = 4,1 \left[2,31(\gamma_s)^{0,5} + 0,27(PL)^{0,73} + 0,025(\%P\#200) \right]^{0,71} \quad (3)$$

As for compacted soils, Pinto (2006) states that $\gamma_{d,\max}$ tends to be higher for sandy and gravelly soils, given that these have a small fine content (pictured in the presented models as variable %P#200) and low PL. The opposite is also true: $\gamma_{d,\max}$ in clayey soils, due to a greater presence of fines (which provides these soils with a higher plasticity), tends to decrease.

Figure 2 shows two curves: MoPesm predictions and laboratory results (regarding the soils in the validation dataset

only). It can be easily seen that MoPesm tends to follow the curve of the laboratory results.

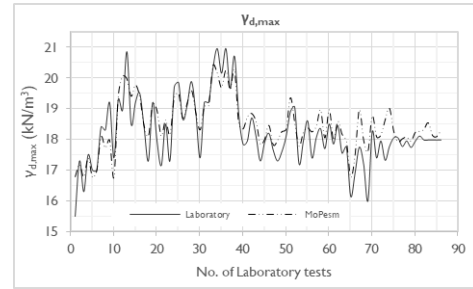


Figure 2. Comparison between results obtained with MoPesm and laboratory tests for $\gamma_{d,\max}$ (validation set).

Source: Authors

Table 4 shows the statistical indexes for laboratory results and MoPesm predictions, considering only the samples in the validation dataset, namely mean, standard deviation, mean absolute percentage error (MAPE), root mean square error (RMSE), and the coefficients of correlation (R) and determination (R^2).

Table 4. Statistics for laboratory results and MoPesm predictions, considering validation dataset only

Index	Laboratory	MoPesm (validation)
Mean	18,227 kN/m ³	18,478 kN/m ³
Standard deviation	1,072 kN/m ³	0,835 kN/m ³
MAPE	–	2,57%
RMSE	–	0,585
R	1,00	0,873
R ²	–	0,763

Source: Authors

Mean and standard deviation for MoPesm and laboratory tests were similar. MoPesm predictions had a MAPE of 2,57%, a RMSE of 0,585, a R of 0,873, and a R^2 of 0,763, a very acceptable performance according to Wang and Yin (2020), to whom a high R^2 and low MAPE and RMSE indicate that a model has a higher precision, and to Karimpour-Fard *et al.* (2019), who considered a R^2 above 0,70 as acceptable, labeling such model as “strong”.

Predictive model for optimum moisture content (MoTuo)

For MoTuo, at the end of the iterative process, some of the coefficients in Equation (2) were nullified and removed from the final expression, shown in Equation (4), also recommended for soils with PL between 10% and 25%.

$$MC (\%) = 0,1 (LL) + 0,07(PL)^{1,44} + 0,09 (\%P\#200) + 2(e)^{0,27} \quad (4)$$

Equation (4) shows that OMC is directly proportional to consistency parameters (LL and PL), fine content, and void

†RMSE, R , and R^2 are dimensionless statistical indexes.

ratio (e). This is in line with the typical behavior of clayey soils described by Pinto (2006), which was mentioned in the previous section.

Figure 3 shows MoTuo results in comparison with the results of laboratory tests for OMC, considering only the samples in the validation dataset. Similar to MoPesm, the curve here also tends to follow laboratory results, although its performance was not as satisfactory, since it yielded some outliers. Table 5 shows the parametric analysis for MoTuo predictions, comprising the validation dataset only.

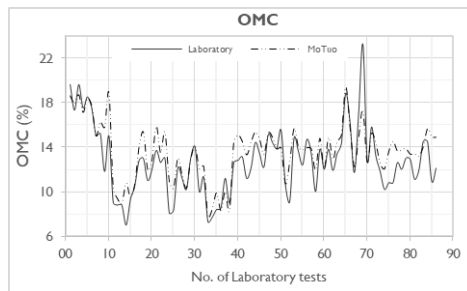


Figure 3. Comparison between results obtained with MoTuo and laboratory tests for OMC (validation set).

Source: Authors

Table 5. Statistics for laboratory results and MoTuo predictions, considering validation dataset only

Index	Laboratory	MoTuo (validation)
Mean	12,733%	13,644%
Standard deviation	2,991%	2,563%
MAPE	–	10,94%
RMSE	–	1,717
R	1,00	0,872
R ²	–	0,761

Source: Authors

MoTuo had a mean of 13,644%, a little above the laboratory dataset, which indicates a slight overprediction. Its standard deviation (2,563%) was smaller than that of the laboratory (2,991%), pointing out that the values were closer to the dataset mean.

MoTuo had a MAPE of almost 11%, a performance that was not as good as MoPesm. However, a R of 0,872 and a R² of 0,761 denoted a reasonable behavior in predicting OMC.

Comparison with other empirical prediction models

Since there are quite a few empirical models to predict compaction parameters based on index properties available in the literature, the initial dataset used to train and validate the proposed empirical models (MoPesm and MoTuo) was used as the input for the prediction models proposed by Sridharan and Nagaraj (2005), Nagaraj *et al.* (2015), Noor *et al.* (2011, as cited in Farooq *et al.*, 2016), Günaydin (2009), and Sivrikaya (2008).

All of these literature models were developed for Standard Proctor compactive effort, and, in Table 6, Equations (5) to

(14) display the expressions proposed by these authors, as well as the prerequisites regarding the inputs.

Table 6. Prediction models for compaction parameters proposed by other authors

Authors	Proposed equations	Preconditions
Sridharan and Nagaraj (2005)	$\gamma_{d, \max} = 0,23(93,3 - PL)$ (5)	Clays, with: LL: 37-73%; PL: 18-51%; PI: 9-37%; Gs: 2,58-2,7
	$OMC = 0,92(PL)$ (6)	
Nagaraj <i>et al.</i> (2015)	$\gamma_{d, \max} = 20,82 - 0,17(PL)$ (7)	SC, SM, CL, MH, CH, with: LL: 24-115%; PL: 17-45%; PI: 3,7-75,6; Gs: 2,6-2,8
	$OMC = 0,76(PL)$ (8)	
Noor <i>et al.</i> (2011)	$\gamma_{d, \max} = 27 - (PL)^{0,60} - (PI)^{0,33} - (Gs)/27$ (9)	Fine-grained soils.
	$OMC = 0,55(PL) + 0,36(PI) - (Gs)/2,7$ (10)	
Günaydin (2009)	$\gamma_{d, \max} = -0,1008(LL) + 21,16$ (11)	CH, CL, SC, GC, with: LL: 25-56; PL: 13-29; PI: 7-33%; Gs: 2,61-2,85
	$OMC = 0,3802(LL) + 2,4513$ (12)	
Sivrikaya (2008)	$\gamma_{d, \max} = 0,22(96,32 - PL)$ (13)	CL, CH, MH, with: LL: 31-74; PL: 12-39; PI: 12-43%; Gs: N/A
	$OMC = 0,94(PL)$ (14)	

Legend: Gs: specific gravity [dimensionless]; PL: plastic limit [%]; LL: liquid limit [%]; PI: plasticity index [%].

Note: Gs was not measured in Sivrikaya (2008).

Source: Authors

Considering the preconditions to apply the five chosen literature models, the data in the development and validation sets were ‘filtered’ to select only the entries which suited the restraints of each model.

The results obtained with MoPesm/MoTuo and the literature models were then compared with laboratory results for these samples. This comparison aimed to evaluate the performance and accuracy of these models when applied to soils from Ceará, since they were developed for soils from other regions of the world, with quite different genesis and lithology.

The statistical analysis carried out when assessing the prediction models proposed by other authors was similar to that described for MoPesm and MoTuo. Table 7 displays the statistical indexes for compaction parameters obtained from laboratory results, literature models, and the proposed model, MoPesm.

It is important to mention that, regarding the parametrical analysis, the number of assessed samples of MoPesm and Motuo corresponded to the validation dataset only ($N = 86$), and, as for the literature models, the number of soil samples used as inputs actually comprised only the ‘filtered’ entries selected from the initial datasets ($N = 169$), that is, those that fell within the range of variability stated in their prerequisites.

As seen in Table 7, MoPesm had a particularly good performance when compared to laboratory results and literature models, with a mean of 18,478 kN/m³, very close to that of the laboratory dataset (18,227 kN/m³), a standard deviation (0,835 kN/m³) a little lower than the laboratory dataset (1,072 kN/m³), and, among the analyzed models, one of the smallest MAPE (2,57%) and highest R² (0,763).

As for the other models, the one proposed by Noor *et al.* (2011) had an excellent performance, and the difference in the performances of all six models might be explained by

the fact that the literature models were developed for soils from different regions of the planet (United Arab Emirates, India, Cyprus, etc.), with quite different characteristics when compared to Brazilian northeastern semi-arid soils.

Table 7. Statistical analysis for evaluated literature models, prediction model MoPesm ($\gamma_{d,max}$), and laboratory results

Statistics	Laboratory	Sridharan and Nagaraj (2005)	Nagaraj et al. (2015)	Noor et al. (2011)	Günaydin Sivrikaya (2009)	(2008)	MoPesm (valid.)
N	169	41	139	169	127	107	86
Mean [kN/m ³]	18,227	16,309	17,254	17,755	16,678	16,560	18,478
Std Dev. [kN/m ³]	1,072	0,572	0,275	0,464	0,497	0,479	0,835
MAPE	–	6,47%	3,77%	2,20%	6,81%	7,12%	2,57%
RMSE	–	1,394	0,432	0,238	0,776	0,886	0,585
R	1,00	0,230	0,570	0,783	0,600	0,603	0,873
R ²	–	0,053	0,325	0,613	0,360	0,364	0,763

Source: Authors

Table 8 displays the statistical indexes for compaction parameters obtained from laboratory results, literature models, and the proposed model, MoTuo.

Table 8. Statistical analysis for evaluated literature models, prediction model MoTuo (OMC), and laboratory results

Statistics	Laboratory	Sridharan and Nagaraj (2005)	Nagaraj et al. (2015)	Noor et al. (2011)	Günaydin Sivrikaya (2009)	(2008)	MoTuo (valid.)
N	169	41	139	169	127	107	86
Mean [%]	12,733	20,599	15,941	14,043	19,281	19,786	13,644
Std Dev. [%]	2,991	2,290	1,231	1,877	2,124	2,048	2,563
MAPE	–	26,48%	24,34%	13,44%	44,46%	48,37%	10,94%
RMSE	–	4,772	1,906	1,114	3,509	4,171	1,717
R	1,00	0,301	0,593	0,795	0,613	0,544	0,872
R ²	–	0,091	0,352	0,633	0,376	0,296	0,761

Source: Authors

Table 8 shows that MoTuo also had a reasonable performance, with a mean (13,644%) close to that of the laboratory result dataset (12,733%), and the smallest MAPE (10,94%) and the highest coefficient R² (0,761) among the analyzed models. Once again, the model proposed by Noor et al. (2011) had a great performance among the evaluated literature models, with indexes quite close to those of MoTuo.

Figure 4 shows a visual comparison between scatter plots for all evaluated literature models for $\gamma_{d,max}$, and Figure 5, for OMC. In these scatter plots, the offset lines above and below the fitted line represent the 95% confidence interval, and the dashed lines correspond to $y = x$.

Based on Figures 4 and 5, it is possible to verify that models MoPesm and MoTuo presented a low data dispersion when compared to the other literature models, and, consequently, a better fit to the regression line. It is worth mentioning also that only the model by Noor et al. (2011) presented a similar statistical performance.

Conclusions

Discerning the properties of a soil is indispensable to anticipate its mechanical peculiarities and field performance (Ortigão, 2007). In this sense, models for predicting soil behavior are essential tools for engineers, as they help rationalize time and costs in preliminary field investigations, which are commonly used to bolster basic design studies (Gurtug and Sridharan, 2004).

This study aimed to evaluate the empirical correlations for different USCS types of soils, correlating basic characterization parameters and index properties with compaction parameters, in order to obtain mathematical models capable of predicting $\gamma_{d,max}$ and OMC for soils compacted with standard Proctor energy.

As seen above, although universal models are highly desirable, empirical correlations developed for a region of the planet do not always correctly portray the attributes of soils from elsewhere. Thus, studies that consider index/physical properties and peculiarities of specific regions are still quite necessary.

About 92% of Ceará's total area is located within the semi-arid domain in northeastern Brazil (BNB, 2005; IPECE, 2018). As shown in Figure 1, most municipalities in Ceará are in this domain, where soil genesis and behavior are very peculiar. This also reinforces the need to develop models which are appropriate for these soils and region.

The modeling process showed that the compaction parameters for the studied soils are mostly influenced by Atterberg limits, fine content (material passing through a No. 200 sieve), and void ratio. The presented results pointed out the advantages of developing specific prediction models for semi-arid soils, like those in the State of Ceará.

Although the performance of empirical models MoPesm and MoTuo was slightly better than that of other literature models, that does not imply that they are the most accurate or reliable. One should always keep in mind that soils are extremely complex materials, and that their physical properties are primarily dictated by the minerals in the constitution of their particles (Das, 2010). Therefore, it is not fully guaranteed that an empirical model trained with soils from one region will have good results for soils from elsewhere, even if they fit the model's prerequisites. Additionally, the outputs of any engineering prediction model – even the most sophisticated and most appropriate for the modeled scenario – should be seen only as good estimates, and not as indisputable ones (Velloso and Lopes, 2011).

Nevertheless, simplified models such as MoPesm and MoTuo are a highly valuable aid for predicting compaction parameters ($\gamma_{d,max}$ and OMC) in situations where there are financial restraints, limited or short timeframes, and/or unavailability of test equipment, especially in early design stages, before appropriate, extensive geotechnical sampling and field investigation can be conducted.

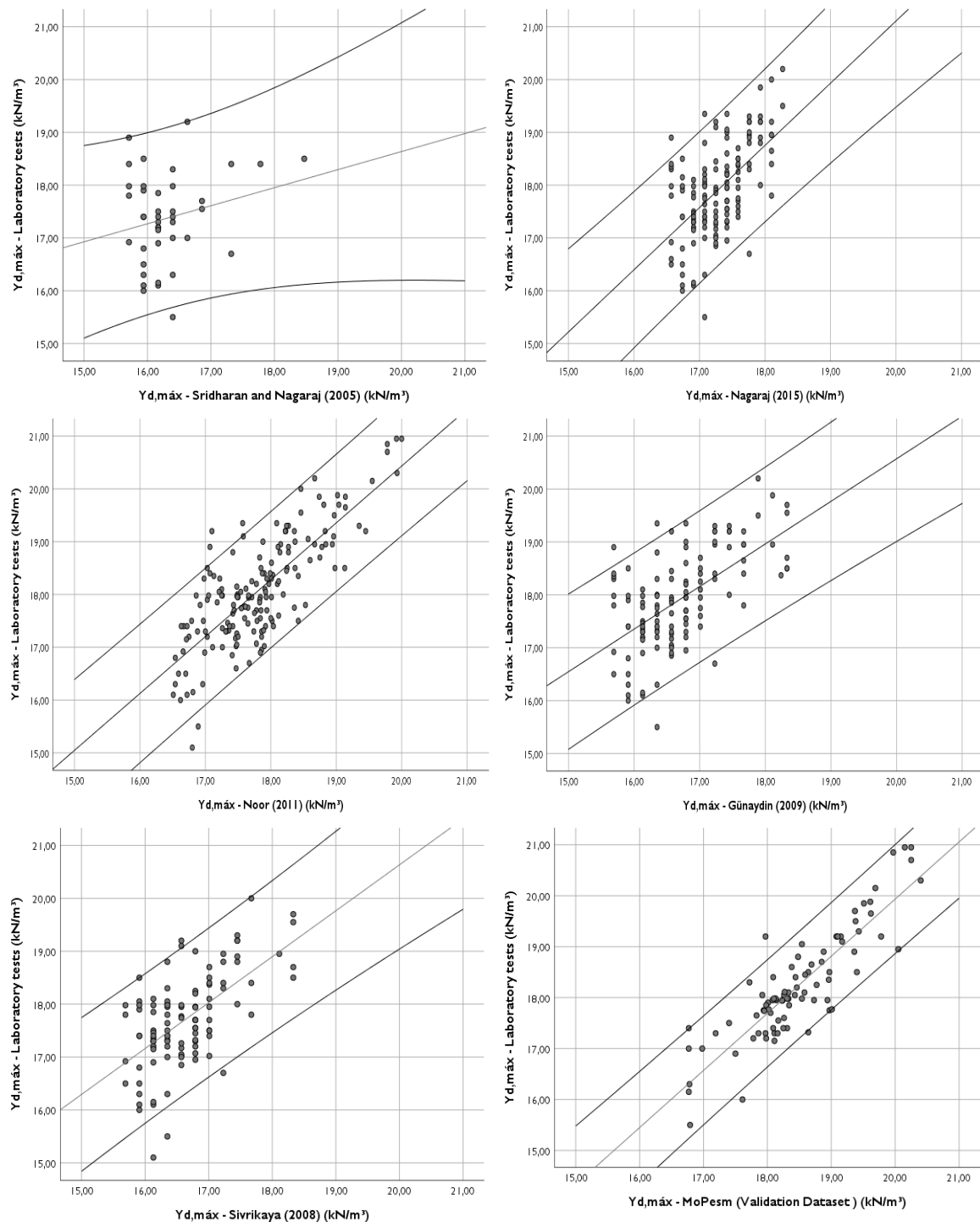


Figure 4. Scatter plots for $\gamma_{d,max}$ obtained with MoPesm and evaluated literature empirical models.

Source: Authors

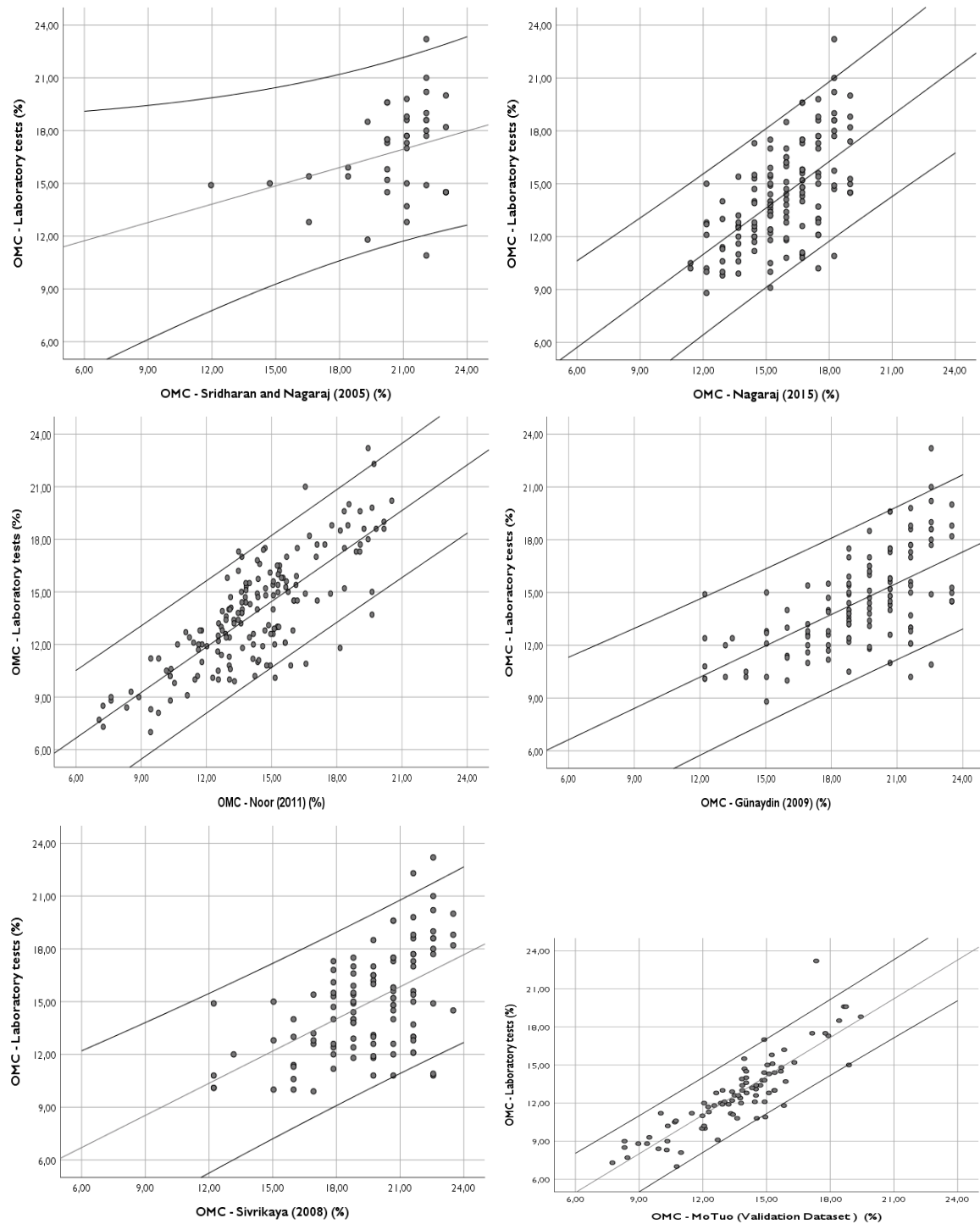


Figure 5. Scatter plots for OMC, obtained with MoTuo and evaluated literature empirical models.
Source: Authors

Acknowledgements

The authors would like to thank CAPES Foundation for the financial aid, as well the Laboratory of Soil Mechanics and Paving (LMP) at the Federal University of Ceará for their operational support to this research.

References

- Banco do Nordeste do Brasil (BNB) (2005). *Proposta de Dimensionamento do Semiárido Brasileiro elaborado pela Área de Meio Ambiente da Funceme*. http://www.funceme.br/wp-content/uploads/2019/02/10-Mapa_CE_Semi%C3%A1rico_BNB-FUNCEME_A2.pdf
- Das, B. M. (2010). *Principles of Geotechnical Engineering* (7th Ed.). Cengage Learning.
- Di Matteo, L., Bigotti, F., and Ricco, R. (2009). Best-Fit Models to Estimate Modified Proctor Properties of Compacted Soil. *Journal of Geotechnical and Geoenvironmental Engineering*, 135(7), 992-996. 10.1061/(ASCE)GT.1943-5606.0000022
- Farooq, K., Khalid, U., and Mujtaba, H. (2016). Prediction of Compaction Characteristics of Fine-Grained Soils Using Consistency Limits. *Arabian Journal for Science and Engineering*, 41, 1319-1328. 10.1007/s13369-015-1918-0
- Fredlund, D. G., Xing, A., and Huang, S. (1994). Predicting the permeability function for unsaturated soils using the soil-water characteristic curve. *Canadian Geotechnical Journal*, 31(4), 533-546. 10.1139/t94-062
- Günaydin, O. (2009). Estimation of soil compaction parameters by using statistical analyses and artificial neural networks. *Environmental Geology*, 57, 203-215. 10.1007/s00254-008-1300-6
- Gurtug, M. S. Y. and Sridharan, A. (2004). Compaction behavior and prediction of its characteristics of fine-grained soils with particular reference to compaction energy. *Soils and Foundations*, 44(5), 1319-1328. 10.1007/s13369-015-1918-0
- Instituto de Pesquisa e Estratégia Econômica do Ceará (IPECE). (2018). *Região Semiárida Cearense – 2017. Ceará em Mapas – Caracterização Territorial – Meio Ambiente*. <http://www2.ipece.ce.gov.br/atlas/capitulo1/12/133x.htm>
- Karimpour-Fard, M., Machado, S. L., Falamaki, A., Carvalho, M. F., and Tizpa, P. (2019). Prediction of Compaction Characteristics of Soils from Index Test's Results. *Iranian Journal of Science and Technology, Transactions of Civil Engineering*, 43(1), 231-248. 10.1007/s40996-018-0161-9
- Leme, R. F. (2015). *Avaliação de uma metodologia para projeto de pequenas barragens de terra no semiárido: construção, ensaios e modelagem numérica* [Doctoral dissertation, Federal University of Ceará]. Repositório Institucional UFC. <http://www.repositorio.ufc.br/handle/riufc/16525>
- Moura, T. E. (2019). *Modelos matemáticos preditivos para estimativa das propriedades de solos compactados* [Undergraduate project, Federal University of Ceará]. Repositório Institucional UFC. <http://www.repositorio.ufc.br/handle/riufc/49557>
- Nagaraj, H. B., Reesha, B., Sravan, M. V., and Suresh, M. R. (2015). Correlation of compaction characteristics of natural soils with modified plastic limit. *Transportation Geotechnics*, 2, 65-77. 10.1016/j.trgeo.2014.09.002
- Noor, S., Chitra, R., and Gupta, M. (2011). Estimation of Proctor properties of compacted fine-grained soils from index and physical properties. *International Journal of Earth Sciences and Engineering*, 4(6), 147-150. 10.1186/s40703-018-0083-1
- Omar, M., Shanableh, A., Basma, A., and Barakat, S. (2003). Compaction characteristics of granular soils in United Arab Emirates. *Geotechnical and Geological Engineering*, 21, 283-295. 10.1023/A:1024927719730
- Ortigão, J. A. R. (2007). *Introdução à Mecânica dos Solos dos Estrados Críticos* (3rd Ed.). Terratek.
- Pinto, C. S. (2006). *Curso Básico de Mecânica dos Solos* (3rd Ed.). Oficina de Textos.
- Saikia, A., Baruah, D., Das, K., Rabha, H. J., Dutta, A., and Saharia, A. (2017). Predicting compaction characteristics of fine-grained soils in terms of Atterberg limits. *International Journal of Geosynthetics and Ground Engineering*, 3(18). /10.1007/s40891-017-0096-4
- Silva, A. V. (2015). *Avaliação do risco de ruptura em análises de estabilidade de taludes de barragens de terra utilizando números fuzzy* [Master's thesis, Federal University of Ceará]. Repositório Institucional UFC. <http://www.repositorio.ufc.br/handle/riufc/16526>
- Silva, A. V., Dantas Neto, S. A., and Souza Filho, F. A. (2016). A Simplified Method for Risk Assessment in Slope Stability Analysis of Earth Dams Using Fuzzy Numbers. *Electronic Journal of Geotechnical Engineering*, 21(10), 3607-3624. <http://www.ejge.com/2016/Ppr2016.0304ma.pdf>
- Sivrikaya, O. (2008). Models of compacted fine-grained soils used as mineral liner for solid waste. *Environmental Geology*, 53, 1585-1595. 10.1007/s00254-007-1142-7
- Sridharan, A. and Nagaraj, H. B. (2005). Plastic limit and compaction characteristics of fine-grained soils. *Ground Improvement*, 9(1), 17-22. 10.1680/grim.2005.9.1.17
- Tizpa, P., Chenari, R. J., Karimpour-Fard, M., and Machado, S. L. (2015). ANN prediction of some geotechnical properties of soil from their index parameters. *Arabian Journal of Geosciences*, 8, 2911-2920. 10.1007/s12517-014-1304-3
- Toms, T. and Philip, J. G. (2016). Prediction of Compaction Characteristics from Atterberg Limits and Specific Gravity for Kuttanad Soil. *International Journal of Science and Research*, 5(8), 1146-1149. https://www.ijsr.net/search_index_results_paperid.php?id=ART20161140
- Velloso, D. A. and Lopes, F. R. (2011). *Fundações. Critérios de projeto, investigação do subsolo, fundações superficiais, fundações profundas. Volume completo*. Oficina de Textos.
- Vieira, V. P. P. B. (2005). *Análise de risco em recursos hídricos: fundamentos e aplicações*. Associação Brasileira de Recursos Hídricos (ABRH).

- Vieira, V. P. P. B., Malveira, V. T. C., Miranda, A. N., and Gouveia Neto, A. (1996). *Roteiro para projeto de pequenos acudes* (4th Ed). Universidade Federal do Ceará.
- Wang, H.-L., and Yin, Z.-Y. (2020). High performance prediction of soil compaction parameters using multi expression programming. *Engineering Geology*, 276, 105758. 10.1016/j.enggeo.2020.105758
- Wang, M. C., and Huang, C. C. (1984). Soil compaction and permeability prediction models. *Journal of Environmental Engineering*, 110(6), 1063-1083. 10.1061/(ASCE)0733-9372(1984)110:6(1063)

Embedded Discrete Fracture Networks to Analyze Groundwater Inflows during Tunnel Drilling

Redes de fracturas discretas embebidas para el análisis de infiltraciones de agua subterránea durante la excavación de túneles

Adriana Piña¹, Diego Cortés², Leonardo David Donado³, and Daniela Blessent⁴

ABSTRACT

Tunnels commonly go through fracture zones, which are analyzed as an equivalent porous medium with homogeneous permeability. However, this is a rough simplification that overlooks the connection triggered by underground works in fractured massifs. This study introduces the use of synthetic discrete fracture networks (DFN) to analyze groundwater inflows through tunnel excavation in a fractured zone while considering the daily advance of the drilling front. First, a hypothetical case with six different settings, varying fracture length and density, as well as aperture distribution, was analyzed. Each setting had about 100 realizations. DFN hydraulic properties were estimated and compared with previous DFN studies, displaying the same behavior even though the magnitude of the estimated parameters differed. As an application example, structural measurements of the Alaska fault zone in the La Línea massif (Colombia) were used to obtain the statistical parameters of fracture length and aperture distributions to generate the DFN. Five settings were built, obtaining measured and simulated groundwater inflows of the same order of magnitude. These results highlight the potential of synthetic discrete fracture networks to analyze the effects of tunnel construction on groundwater flow.

Keywords: discrete fracture networks, groundwater inflows, numerical modeling, tunnel

RESUMEN

Los túneles usualmente atraviesan zonas geológicamente fracturadas, que suelen ser analizadas como medios porosos equivalentes de permeabilidad homogénea. Sin embargo, esta es una simplificación que ignora las conexiones que generan las obras subterráneas en un macizo fracturado. En este trabajo se introduce el uso de redes de fracturas sintéticas (DFN) para analizar los flujos de agua subterránea generados por la perforación de túneles, considerando el avance diario en el frente de excavación. En primer lugar, se analizó un caso hipotético con seis configuraciones diferentes, variando la densidad y longitud de las fracturas, así como la distribución de aperturas. Cada configuración tenía alrededor de 100 realizaciones. Las propiedades hidráulicas de la DFN fueron estimadas y comparadas con estudios previos sobre DFNs, mostrando el mismo comportamiento aún cuando la magnitud de los parámetros estimados difería. Como ejemplo de aplicación, se usó con información estructural de la falla Alaska en el macizo de la Línea (Colombia), con el fin de obtener los parámetros estadísticos de las distribuciones de longitud y apertura de las fracturas para la generación de las DFNs. Se crearon cinco configuraciones, obteniendo caudales de infiltración medidos y simulados del mismo orden de magnitud. Estos resultados resaltan el potencial del uso de redes sintéticas de fracturas para analizar el efecto de la construcción de túneles en el flujo de agua subterránea.

Palabras clave: redes de fracturas discretas, flujo de agua subterránea, modelación numérica, túnel

Received: August 12th, 2020

Accepted: July 2nd, 2021

¹Agricultural Engineer, M.Sc., Ph.D., School of Engineering, Universidad Nacional de Colombia, Colombia. Postdoctoral Researcher and Lecturer at HYDS Research Group, Universidad Nacional de Colombia at Bogotá. E-mail: appinaf@unal.edu.co

²BSc, Civil Engineer, School of Engineering, Universidad Nacional de Colombia at Bogotá. E-mail: diacortesra@unal.edu.co

³Civil Engineer, M.Sc., Ph.D. Affiliation: Full Professor at HYDS Research Group, Universidad Nacional de Colombia at Bogotá. E-mail: lddonadog@unal.edu.co

⁴Environmental Engineer, M.Sc., Ph.D. Affiliation: Ph.D., Assistant Professor, Universidad de Medellín, Colombia, Colombia. E-mail: dblessent@udem.edu.co

How to cite: Piña, A., Cortés, D., Donado, L. D., and Blessent, D. (2022). Embedded Discrete Fracture Networks to Analyze Groundwater Inflows during Tunnel Drilling. *Ingeniería e Investigación*, 42(1), e89889. 10.15446/ing.investig.v42n1.89889



Attribution 4.0 International (CC BY 4.0) Share - Adapt

Introduction

Fractured media refers to lowpermeability matrix rocks that may acquire moderate to good permeability thanks to fractures (Singhal and Gupta, 2010). There, underground projects for groundwater supply, waste disposal, or infrastructures are built up (Evans *et al.*, 2001; Singhal and Gupta, 2010), thus affecting the surrounding surface water sources and groundwater bodies. Some of the reported effects of tunnels are groundwater inflows during and after their construction (Celico *et al.*, 2005; Perrochet and Dematteis, 2007), groundwater and surface water level drawdown, (Molinero *et al.*, 2002; Maréchal and Etcheverry, 2003; Vincenzi *et al.*, 2009; Font-Capóet *et al.*, 2011), the triggering of preferential flow paths (Evans *et al.*, 2001), and rock deformations and instabilities (Preisig *et al.*, 2014; Shen *et al.*, 2014; Loew *et al.*, 2015; Valenzuela *et al.*, 2015).

Different modeling approaches have been implemented to assess the impact of underground projects both in the transient and steady state. In the steady state analysis, long term effects are studied, whereas in the transient state, the effects during the construction process are analyzed until a new steady state condition is reached (Celico *et al.*, 2005). Some analytical formulations based on the equivalent porous media (EPM) approach have been developed for steady state conditions and homogeneous materials (Goodman *et al.*, 1965; Heuer, 1995; Karlsrud, 2001; El Tani, 2003), and some have been extended to the transient-state. Perrochet (2005) evaluates the transient drilling speed-dependent discharge rates using a convolution integral, and extensions to the heterogeneous media have been proposed by Perrochet and Dematteis (2007) and Maréchal *et al.* (2014). Previous approaches do not consider the effect of the excavation-induced drawdown leading to over/underestimated groundwater inflows. For this reason, some authors have proposed analytical or semianalytical approaches to predict the height of lowered water level under the steady (Su *et al.*, 2017) and the transient states (Liu *et al.*, 2017), thus providing a better prediction of tunnel inflows.

Since most groundwater inflows are recorded in fault zones (Attanayake and Waterman, 2006; Perrochet and Dematteis, 2007; Yang *et al.*, 2009; UNAL, 2010; Moon and Fernandez, 2010; Zarei *et al.*, 2011; Loew *et al.*, 2015), fractures have been represented within heterogeneous media as more permeable areas with EPM approaches (Perrochet and Dematteis, 2007; Maréchal *et al.*, 2014; Preisig, 2013). This conceptualization has been extended to numerical modeling in order to predict groundwater inflow into tunnels (Maréchal *et al.*, 1999; Hu and Chen, 2008; Yang *et al.*, 2009; Butscher *et al.*, 2011; Chiu and Chia, 2012; Butscher, 2012; Xia *et al.*, 2018; Golian *et al.*, 2018; Nikvar Hassani *et al.*, 2018).

Even though the EPM approach allows the use of the above-mentioned analyses while the characterization of individual fractures, the complexity of the fractured media could be better represented by discrete fracture networks (DFN), where hydraulic behavior is controlled by their geometry (*i.e.*, aperture, length, density, and orientation distributions) (Adler *et al.*, 2012).

The inclusion of individual fractures or fracture networks in numerical modeling demands higher computational efforts to solve the problem. Nevertheless, some authors have included fractures on their analyses while accounting for the water management in tunnels (Molinero *et al.*, 2002; Lee *et al.*, 2006; Hawkins *et al.*, 2011; Hokr *et al.*, 2012, 2016; Farhadian *et al.*, 2016). Recently, Wang and Cai (2020) proposed a DFN-DEM multi-scale approach for modeling excavation responses in jointed rock masses for settlement purposes. However, the use of synthetic DFNs to estimate groundwater inflows into tunnels or underground works under a transient state has not been reported. In this study, we propose a numerical model to analyze the temporal evolution of groundwater inflows (hydrograph) during the construction of underground works in a fractured massif with a low permeability matrix. The novelty of this work is that

its conceptual model is based on a hybrid model with a DFN embedded on a low-permeability, continuous porous media. The generation of the synthetic DFN was carried out using the probabilistic functions of (i) frequency, (ii) length, (iii) aperture, and (iv) dip of the fractures. The groundwater flow model is bounded with a time-varying atmospheric pressure, which is activated according to a typical drilling speed of 2 m/d (Perrochet and Dematteis, 2007).

To show the capabilities of the proposed model, two types of simulation were performed. The first one is a hypothetical case with a randomly generated fracture network where the numerical model is tested. The second one consists of an embedded synthetic discrete fracture network (DFN) that is generated based on outcrop field data with information from surveys on La Línea massif in the Colombian Andes. The former only gives us information on the numerical performance of the groundwater model, whereas the second model is compared to the groundwater inflows recorded during the drilling of the La Línea tunnel (Colombia).

Methodology

The release of energy above the plastic limit fractures the rock Escobar, 2017, thus generating faulted planes that provide preferential flow paths through the massif rock (Leung and Zimmerman, 2012), which enhances the permeability of the media. Fractures are characterized by their length, surface roughness, aperture, fracture dead-end, and intersections (Adler *et al.*, 2012). These geological measurements are used to estimate hydraulic parameters (Liu *et al.*, 2016) by using frequency distributions such as the power law, lognormal, or exponential functions.

Fracture lengths have shown power-law distributions to have the greatest physical significance (Bonnet *et al.*, 2001) and ubiquitously describe scaling properties (Davy *et al.*, 2010). However, in nature, the frequency of fracture lengths displays *log-normal* (Equation (1)) or *exponential* distributions (Equation (2)) as result of the truncation effect induced by the sampling size, which limits the lower or upper boundary (Bonnet *et al.*, 2001).

$$n(l) = \frac{1}{l \cdot \sigma \sqrt{2\pi}} e^{-\frac{[\ln l - \mu]^2}{2\sigma^2}}, \quad (1)$$

$$n(l) = \frac{1}{\lambda} e^{-l/\lambda}, \quad (2)$$

where μ is the log-mean, σ is the log-standard-deviation, λ is a parameter of the exponential distribution, l is the fracture length, and $n(l)$ is the frequency distribution of fracture lengths.

Meanwhile, aperture distribution cannot be obtained easily from field measurements, which are uncertain because stresses change dramatically at depth (Liu *et al.*, 2016), and the weathering affects fracture appearance at outcrops. DFNs are realistic mappings of fracture geometries based on field observations via a stochastic representation of properties (Somogyvári *et al.*, 2017) such as fractures number, length, aperture, and dip. Their statistical parameters are the inputs

for several codes developed to generate and analyze DFNs, such as ADFNE (Fadakar Alghalandis, 2017), DFN WORKS (Hyman *et al.*, 2015), FracMan (Golder Associates Inc., 2018), and MoFrac (Mirarco, 2018). Nevertheless, these codes do not allow to simulate the advance in tunnel drilling processes, as it could be done using codes such as HydroGosSphere HGS (Aquanty Inc., 2013).

HGS is a 3D, fully integrated surface and subsurface flow simulator that is widely used in the analysis of groundwater issues (Aquanty Inc., 2013). It includes a Random Fracture Generator (RFG) that creates networks with random locations, lengths, and apertures by using any of the available probability distribution functions (PDF): exponential function for the aperture, exponential and lognormal functions for the fracture length, and a double-peaked Gaussian for the orientation. In this research, HGS and RFG were used to generate a synthetic DFN embedded on a very low permeability porous rock matrix.

In the following sections, we present the assumptions of the model components (mesh, DFN generation, definition of hydraulic parameters) and describe the initial and boundary conditions for the numerical simulations. All these components are described for both hypothetical and synthetic cases.

Mesh generation

The accuracy of groundwater models is affected by numerical errors or instabilities that occur in all computational simulations due to aspects such as grid spacing (Woods *et al.*, 2003; Anderson *et al.*, 2015). To ensure numerical stability in the modeling process, multiple preliminary simulations were performed, varying the number of fractures, block size, and grid spacing. Different block sizes were tested according to the width of the fault zones in the La Línea tunnel, which varies approximately from 20 m to 400 m, as well as to the total length of tunnel (8 600 m). Block size and grid spacing were identified as the most important aspects to guarantee a successful run, the availability of computational requirements, and a moderate simulation time. As result, a synthetic block of 400 m in length and height, 200 m in depth (which could be a representative volume for the La Gata, Alaska, or Cristalina fault zones in the La Línea massif), and mesh spacing varying from 1 to 80 m were chosen. In the middle of the block, the mesh was refined to simulate a tunnel with a radius of 2,5 m. That position was chosen to avoid boundary disturbances and aimed for symmetrical conditions. Mesh spacing limits the shortest fractures, while the model size limits the longest fractures. Using this scheme, each groundwater flow simulation took about 60 minutes using an Intel Xeon (@ 3.30GHz) and 32 GB RAM.

Synthetic DFN generation

RFG was used to create a DFN based on the statistical parameters of length, aperture, orientation, and number of fracture distributions. Fractures were randomly distributed in the porous media using a seed that can be changed to

allow the generation of a infinite number of different DFN with the same PDF for each fracture parameter. The resulting three-dimensional model is made of orthogonal blocks, where fractures are superposed as 2D elements to the sides of the 3D blocks, so that the fracture nodes coincide with those of the porous rock. The grid has to be thin enough to allow the creation of the fracture network. Nevertheless, extremely thin grids increase the number of elements and computation times.

A hundred DFN realizations for different configurations or settings were performed by varying density (expressed as the number of fractures generated) and fracture length parameter distributions (Equations (1) and (2)), while length distribution, grid, model dimensions, and hydraulic parameters were kept constant. However, some realizations could not be completed because of numerical instabilities.

DFN hydraulic properties

The hydraulic properties were used as indicators of DFN connectivity. Here, we considered the hydraulic conductivity of each fracture, K_f , the permeability of the fracture network (K_{DFN}), the volumetric fracture density (P_{32}), and the equivalent permeability (K_{EPM}) associated to the DFN mean flow (Q_{DFN}).

HGS estimates K_f by following the cubic law as $K(f) = \frac{gw_f^2}{12\nu}$, where $g[L/T^2]$ is gravity acceleration, $w_f[L]$, is the aperture, and $\nu[M/(L \cdot T)]$ is the kinematic viscosity (Aquanty Inc., 2013). Thus, the permeability of the fracture network, K_{DFN} , was evaluated as the geometric mean of the K_f (de Dreuzy, 2001a). The volumetric fracture density, P_{32} , or the persistence of the fractures area (2D) per unit volume (3D), is expressed as $P_{32} = \frac{1}{V} \sum_f A_f = \frac{1}{V} \sum_f l_f \cdot b$, where V is the volume of model, A_f is the area of the fracture f , l_f is the length, and b the width of the model.

As each setting had as many hydrographs as completed simulations, an equivalent DFN hydrograph (Q_{DFN}) was calculated: $Q_{DFN} = \sum Q_{DFNi}/N$, where N is the number of completed i synthetic generations. Then, an equivalent porous media permeability (K_{EPM}) for each setting was calibrated based on 200 realizations in a homogeneous media configuration (EPM), where K was varied; specific storage, S_s , remained constant as the assigned value of the matrix domain in the DFN approach. In this way, a set of 200 EPM hydrographs Q_{EPM} were obtained, and Q_{DFN} was fitted to the set of Q_{EPM} using the Nash-Sutcliffe coefficient ($NSE = \left[1 - \frac{\sum (Q_{obs} - Q_{sim})^2}{\sum (Q_{obs} - Q_{obs})^2}\right]$; NSE values close to unity indicate good model performance) as the metric to select the K_{EPM} .

Hydraulic properties of the matrix

The matrix was considered as a very low permeable medium with a hydraulic conductivity (K) of 1×10^{-4} m/d, specific storage (S_s) equal to 5×10^{-4} , and porosity (η) equal to 4×10^{-3} (Singhal and Gupta, 2010).

Initial and boundary and conditions

An initial condition of head equal to topography is assigned to the entire domain. No flow conditions are assigned to the bottom and lateral faces of the cubic domain, considering the following assumptions specifically for the La Línea massif : i) preferential radial flow toward the tunnel (Preisig, 2013); ii) there are no significant regional flows, as the tunnel is located in the upper watershed; and iii) very low permeabilities of the crystalline rocks (IRENA, 2010; UNAL, 2015). These assumptions may be rejected due to possible connections with larger faults. However, it is an open issue when working with fractures and the consequent truncation effect due to the scale of the observation window.

A nodal flux of $1 \times 10^{-10} \text{ m}^3/\text{d}$ is assigned to the top face as an arbitrary recharge condition, in order to avoid a constant drawdown. The tunnel is simulated with a mobile boundary condition along the x -axis, in the middle of the $y - z$ plane. The advance of the tunnel drilling is simulated by assigning an atmospheric pressure at an excavation rate of 2 m/d (typical value for tunnel excavation rates (Perrochet and Dematteis, 2007; IRENA, 2007)). Tunnel excavation is completed in 200 days, and the recession flow is observed until 1 000 days.

Test cases

Two example cases were investigated using synthetic DFN in the analysis of groundwater inflows into a tunnel. The first case was a hypothetical block to test the performance of the numerical modeling. The second case was based on outcrop field data from the La Línea massif and the recorded groundwater inflows of the Alaska fault zone during the drilling of the La Línea tunnel.

Hypothetical case

In this case, the behavior of the hydrographs was analyzed by varying the fracture length, aperture, and density distributions. Six settings were built (each one with 100 realizations). The fracture length frequency was assumed to follow a log-normal distribution with $\mu = -4.5 \text{ m}$ and $\sigma = 3.4 \text{ m}$, whereas the exponential distribution was used for the fracture apertures. The fracture density or number of fractures was randomly assigned. Settings S1, S3, and S4 have the same density but their exponent λ varies from 8 000 to 10 000, while, in settings S2, S5, and S6 the exponent λ is kept constant (it is equal to 9 000). The parameters for each setting are displayed in Table 1.

The Alaska fault zone

As an application example, and based on the results from the hypothetical case, the Alaska fault zone was analyzed using five different settings, where fracture density was varied, and fracture length followed the statistical distribution of the La Línea massif.

The Alaska fault is located in the La Línea massif and is crossed by the drilling of two tunnels (Figure 1). These tunnels belong to an important roadway project in the Colombian Andes.

Table 1. Parameters for each configuration and number of completed generations for each setting

Setting	Number of fractures	λ	Completed realizations
S1	700	9 000	64
S2	350	9 000	77
S3	700	8 000	67
S4	700	10 000	48
S5	525	9 000	70
S6	175	9 000	90

Source: Authors

Their mean length is 8 600 m, the elevation at the East entrance is 2 434 m.a.s.l., 2 553 m.a.s.l. in the West, and the maximum depth is 800 m. The massif is formed by the Quebradagrande complex, the Cajamarca complex, and an andesitic porphyry. These geological formations are highly fractured and formed by igneous and metamorphic rocks with a complex structural geology (IRENA, 2007; UNAL, 2010). During the drilling process, important groundwater inflows were recorded, especially in fault zones (IRENA, 2007; UNAL, 2010). The Alaska fault zone is located in shales of the volcanic member of the Quebradagrande complex, Kv, as shown in Figure 1. The mean depth of the tunnel in the zone is 400 m.

When a tunnel is being drilled, there is a flow peak as the drilling front disturbs the rock followed by the recession flow, which diminishes or disappears depending on the hydrogeological conditions. In this way, the total amount of water drained by a tunnel is the convolution of each individual hydrograph. In the La Línea tunnel, the accumulated groundwater inflows were measured daily at each entrance of the tunnel (IRENA, 2007). However, there is no information on the real infiltration rates in specific zones. Hence, based on the average of 100 numerical simulations using an EPM approach, the recession flow of the first 1 000 m of tunnel is obtained and then removed from the accumulated data. Figure 2 displays the inflows recorded at the western entrance and the progression in the drilling front (IRENA, 2007); the hydrograph of the infiltrated water in the Alaska fault zone (inner box in Figure 2) was built subtracting the aforementioned recession or base flow (gray line). There, the drilling process took about 200 days, and about 40 l/s were recorded.

Fracture length distribution: The statistical parameters of the fracture lengths are obtained from structural maps at local and regional scale (10 000 m and 65 000 m, respectively) (Figure 1), considering that just few and small outcrops (less than 30 m) are found as consequence of the dense vegetation in the area.

Finding the best statistical distribution governing a dataset is of critical importance when predicting the tendency of fracture attributes (Rizzo *et al.*, 2017). The information criterion approach is implemented using the Akaike Information Criterion AIC (Akaike, 1974), the corrected AICc (Cavanaugh, 1997), the Bayesian Information Criteria BIC (Schwarz, 1978), and the KIC (Kashyap, 1982). Then, the estimation of the

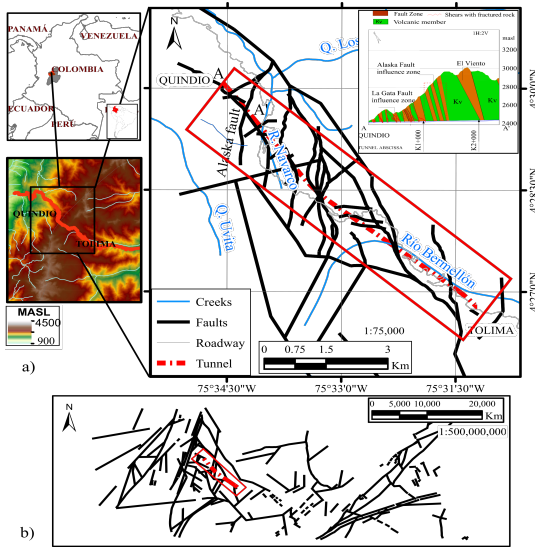


Figure 1. Geographical location of the La Lánea tunnel: a) Location of the Alaska fault and fractures at a local scale (10 000 m); and b) fractures at a regional scale (50 000 m).

Source: Authors

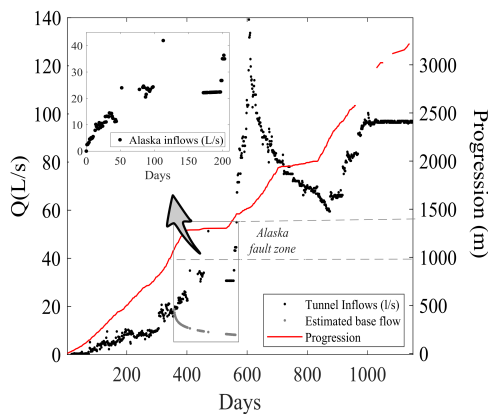


Figure 2. Daily groundwater inflows (black dots) and tunnel progression (red line); base flow (gray dots) was removed from accumulated hydrograph to obtain the Alaska inflows shown in the inner box (2007).

Source: Authors

posterior model weight (for AIC and AICc) or posterior model probability (for BIC and KIC) is implemented, as described in detail by Ye *et al.* (2008) and Siena *et al.* (2017). Fracture length was fitted to five probability density functions (normal, exponential, lognormal, gamma, and General Extreme Value-GEV) using the Maximum Likelihood Estimator approach. The four information criteria indicate the best fit for the exponential distribution with the lowest values. The same result is obtained by the posterior model weight or posterior model probability (showing the higher values) using the AIC, AICc, and BIC (Table 2). However, the KIC posterior probability is better for the GEV distribution, as it discriminates the models on the quality of the model parameter estimates (Siena *et al.*, 2017). Therefore, the exponential distribution is selected for the DFN generations of the Alaska fault zone with $\lambda = 3,16 \times 10^3$ m. The data fit

is shown in Figure 3.

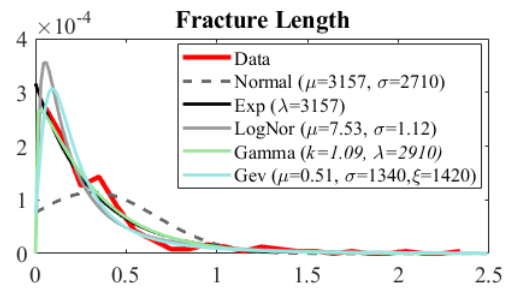


Figure 3. Probability density functions for fracture length in Alaska fault zone in the La Lánea tunnel.

Source: Authors

Table 2. Posterior weights/model probability of the five analytical models evaluated for the model identification criterion

Criteria	Normal	Exponential	Lognormal	Gamma	GEV
AIC	0	34,00	16,99	30,83	18,17
BIC	0	44,24	15,62	28,34	11,80
AICc	0	34,00	16,99	30,83	18,17
KIC	0	29,65	3,14	22,51	44,7

Source: Authors

An example of the synthetic DFN generated using the lognormal (hypothetical case) and the exponential distribution for the fracture length with the same number of fractures is shown in Figure 4.

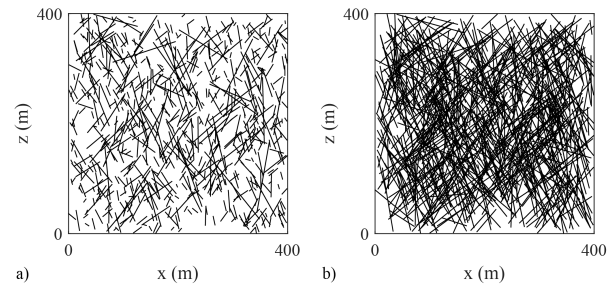


Figure 4. Example of the generated DFN: (a) hypothetical case and (b) application example for the Alaska fault zone.

Source: Authors

Fracture aperture: Regarding the aperture information, it was not possible to obtain aperture measurements within the massif, or any information to estimate a real value. Mean aperture measurements on surface were 1,5 mm, the minimum was 0 mm, and the maximum was 32 mm (Hernandez and Kammer, 2016). These values are extremely high, as result of the weathering of the outcrops. They do not even allow running the model because of numerical convergence issues. However, preliminary tests showed that the default HGS aperture distribution approach worked fine. Consequently, the aperture generation range was kept between $25 \mu\text{m}$ and $3,2 \times 10^2 \mu\text{m}$, and λ equal to $9,0 \times 10^3$ for the exponential distribution (Equation 2).

Results

Hypothetical case

Figure 5a displays the hydrographs for each completed generation in S1, the estimated mean, and the standard deviation (σ). Peak groundwater inflows vary between 28 and 52 L/s, and the recession flows are less spread than those observed for early times. In the estimation of K_{EPM} , it is important to consider that HGS changes the time step to optimize CPU requirements; when the simulated variable shows large variations, time steps are smaller. On the contrary, if no sensible variation is simulated, the time steps increase. After 200 days, when excavation is finished, and hydraulic heads do not vary significantly, the time step increases, and only ten values are generated in the remaining 800 days. For this reason, when the NASH coefficient is calculated, differences between Q_{EPM} and Q_{DFN} in the recession zone of the hydrograph are not so relevant, and the NASH coefficient values are close to one.

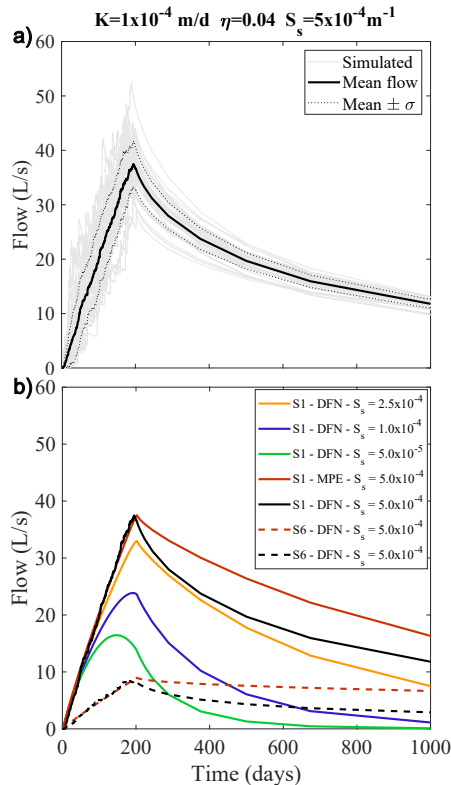


Figure 5. Hydrographs of the simulated groundwater inflows for DFN generations: a) setting 1 (S1); b) mean flow obtained using the DFN and EPM approaches using different fracture densities (settings S1 and S6) and DFN approach for S1, showing the influence of S_s (m⁻¹) in the simulated flows.

Source: Authors

Table 3 contains K_{EPM} , NASH, and K_{DFN} for each setting. K_{EPM} varies between 8×10^{-3} and 4×10^{-2} m/d, while K_{DFN} ranges from 5×10^2 to 6×10^2 m/d. The difference between both approaches (K_{EPM} and K_{DFN}) exceeds 5 orders of magnitude. Therefore, the values are not comparable, and the assumption of an equivalent permeability of the media,

estimated as K_{DFN} and proposed by de Dreuzy *et al.* (2001b), does not work in this study. It may be associated to the matrix of low permeability and P_{32} below 1 used in this research. Consequently, the effects of matrix permeability and fracture density should be taken into account for future modeling and analysis.

Table 3. Equivalent and geometric mean permeability of fractures for each setting

Setting	K_{EPM} (m/d)	NASH	K_{DFN} (m/d)
S1	$4,03 \times 10^{-2}$	0,99	$5,63 \times 10^2$
S2	$1,97 \times 10^{-2}$	0,96	$5,63 \times 10^2$
S3	$4,03 \times 10^{-2}$	0,99	$5,17 \times 10^2$
S4	$4,36 \times 10^{-2}$	0,99	$6,15 \times 10^2$
S5	$3,00 \times 10^{-2}$	0,98	$5,63 \times 10^2$
S6	$8,00 \times 10^{-3}$	0,97	$5,60 \times 10^2$

Source: Authors

Figure 5b displays the calculated Q_{DFN} for different fracture densities in settings S1 and S6, and Q_{EPM} , showing how flow increases as the number of fractures does. The excavation phase shows a good fit between EPM and DFN (until 200 days). However, the tail of the hydrograph is overestimated by the EPM approach, which leads us to perform a sensitivity analysis of the S_s for S1, showing how the peak and the recession flow decrease as a function of S_s .

Based on the obtained results, DFN hydraulic parameters (introduced in the section named after them) were estimated and compared with previous studies (de Dreuzy *et al.*, 2001b; Maillot *et al.*, 2016) in order to validate the behavior of the generated DFN. Figure 6 displays the relationship between permeability and P_{32} for the settings where only the fracture density changes (S1, S2, S5, and S6). A linear relationship between the K_{EPM} and the P_{32} is observed, as found by Maillot *et al.* (2016), but in a lower density range, considering that the estimated P_{32} for the analyzed configuration is below 1.

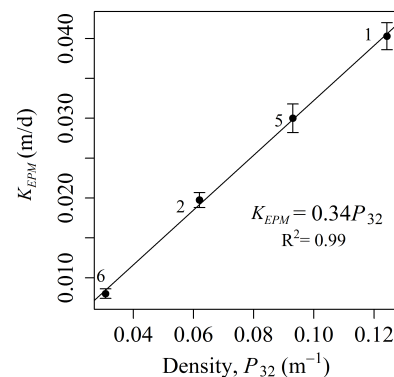


Figure 6. Linear relationship between permeability and fracture density P_{32} , displaying the 95% confidence interval bars of the K_{EPM} (tags indicate the setting number).

Source: Authors

The Alaska fault zone

In this subsection, the results of a more complex fracture network (Figure 1) are presented. The statistical properties for the fracture lengths of the maps (Figure 2) were taken to configure the DFN generation, and the fracture density was varied from 55 to 700 fractures, as indicated in Table 4. As the density changes, connectivity does as well, and, consequently, K_{EPM} (Table 4). However, in this application, the linear relationship observed in the synthetic example (Figure 6) and reported by Maillot *et al.* (2016) is not preserved for the most dense setting (700 fractures), as shown in Figure 7. It is probably a truncation effect caused by the lower number of numerically successful runs (55 of 100 simulations) caused by the difficulty to locate a higher number of fractures in the same domain size and mesh distribution.

Finally, by visual inspection, the synthetic DFN with about 400 fractures generates hydrographs that show a good agreement with the measured inflows in the first 100 days (Figure 8). Unfortunately, there are no records for 60 days, probably as a result of construction problems due to rock quality and the presence of water, which caused the drilling advance to be almost stopped. This would explain the decrease in the flows from 180 to 200 days, followed by a sudden increase as tunnel blasting was resumed. This kind of situation during construction activities is the greatest limitation in the acquisition of information for every geological unit, in addition to the complexity involved in the behavior of the recession flow.

Table 4. Density and K_{EPM} for five settings with different number of fractures implemented for the Alaska fault zone

Number of fractures	P_{32} (m^{-1})	(m/d)	Completed generations
55	$3,20 \times 10^{-2}$	$5,92 \times 10^{-3}$	95
188	$1,10 \times 10^{-1}$	$2,69 \times 10^{-2}$	86
400	$2,37 \times 10^{-1}$	$5,43 \times 10^{-2}$	56
500	$3,01 \times 10^{-1}$	$6,70 \times 10^{-2}$	62
700	$4,10 \times 10^{-1}$	$7,79 \times 10^{-2}$	62

Source: Authors

Discussion

The accurate distribution of fractures in a rock massif is almost impossible to know. Synthetic DFN generations can be used as a tool to model the effects caused by tunnel drilling through fault zones, considering the daily advance in the perforation work.

Figures 6 and 7 show how geological media permeability is heavily dependent on DFN density, P_{32} . However, for the application example of the Alaska fault zone, a perfectly linear relationship is not observed. This may be associated to a truncation effect in the fractures.

The behavior of high-density DFNs in a very low permeability matrix has important characteristics: groundwater must flow through fractures, so that the DFN has to be connected in order to contribute to groundwater circulation. In the porous

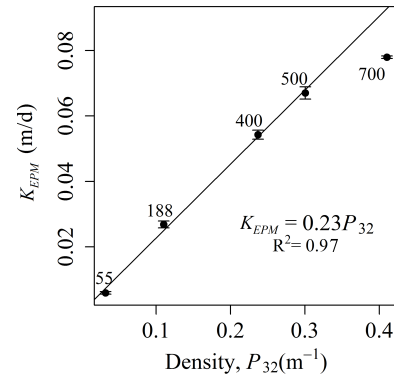


Figure 7. Relationship between permeability and fracture density P_{32} for the Alaska fault zone, displaying the 95% confidence interval bars of the K_{EPM} (tags indicate the number of fractures in each setting).

Source: Authors

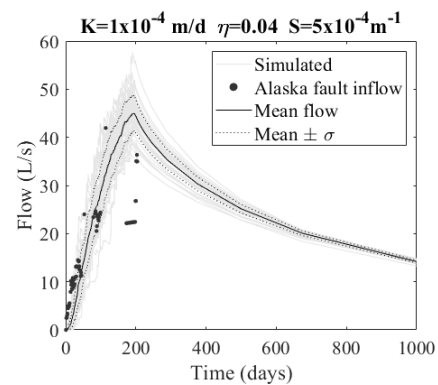


Figure 8. Groundwater inflows simulated for the 400-fracture setting and measured flow in Alaska fault zone (black dots).

Source: Authors

matrix, unconnected fractures take part in groundwater flow through the matrix, and their influence is especially notorious during tunnel excavation. When drilling crosses a fracture, water flows freely as a function of its aperture, and a new connection is generated through the system. Then, a drilled porous matrix gradually releases the water stored in the massif. This explains the fact that EPM overestimates late inflows when permeability is adjusted.

The importance of the S_s in the estimated groundwater inflows for the recession period is evidenced. However, as there are no measured data for this period to fit any parameter, only synthetic data are compared. In this way, the closest behavior between a DFN realization and an EPM was obtained using S_s equal to $2,5 \times 10^{-4} m^{-1}$, which is within the range of the reported specific storage values for crystalline rocks (Hartley and Joyce, 2013).

Conclusions

This work highlights the possibility of implementing synthetic DFNs to analyze the effects of the advance of tunnels excavation in fractured zones. The results show that, based on

the statistical parameters of the structural geology of a massif (i.e., fracture length and aperture measured in geological maps or outcrops), synthetic DFNs can reproduce groundwater inflows of the same order of magnitude than those measured in the Alaska fault zone in the La Línea tunnel, Colombia. This is an outstanding finding of this research, as the results were compared with real data, which has never been reported before. Unfortunately, there are no available measured data of the hydrograph at late times for this specific zone, so Ss estimation is an open issue. As input information of a fracture network is scarce, uncertainty is high. However, it can be established that fracture density, P_{32} , is the parameter that most influences the estimated EPM permeability for the conditions of this study, which is in agreement with Maillot *et al.* (2016). The relationship between P_{32} and equivalent permeability is heavily influenced by the fracture length distribution. Thus, a linear performance cannot be always supposed, probably because of the truncation effect caused by the size of the synthetic model.

Acknowledgements

The authors would like to thank Professor Rene Therrien (Université Laval) for supplying the HGS license, as well as Colciencias-Universidad Nacional de Colombia for the Ph.D. Financing Program 617-2014. This research was also funded by Instituto Nacional de Vías (INVIAS).

References

- Adler, P., Thovert, J.-F., and Mourzenko, V. (2012). *Fractured Porous Media* (1st ed.). Oxford University Press. 10.1061/10.1093/acprof:oso/9780199666515.003.0001
- Akaike, H. (1974). A New Look at the Statistical Model Identification. *IEEE Transactions on Automatic Control*, 19(6), 716-723. 10.1061/10.1109/TAC.1974.1100705
- Anderson, M., Woessner, W., and Hunt, R. (2015). *Applied Groundwater Modeling Simulation of Flow and Advective Transport* (2nd ed.). Elsevier.
- Aquanty Inc. (2013). *HydroGeoSphere user manual*. <https://www.aquanty.com/hydrogeosphere>
- Attanayake, P. M. and Waterman, M. K. (2006). Identifying environmental impacts of underground construction. *Hydrogeology Journal*, 14, 1160-1170. 10.1061/10.1007/s10040-006-0037-0
- Bonnet, E., Bour, O., Odling, N. E., Davy, P., Main, I., Cowie, P., and Berkowitz, B. (2001). Scaling of fracture systems in geological media. *Reviews of Geophysics*, 39(3), 347-383. 10.1061/10.1029/1999RG000074
- Butscher, C., Einstein, H. H., and Huggenberger, P. (2011). Effects of tunneling on groundwater flow and swelling of clay-sulfate rocks. *Water Resources Research*, 47(11), 1-17. 10.1061/10.1029/2011WR011023
- Butscher, C. (2012). Steady-state groundwater inflow into a circular tunnel. *Tunnelling and Underground Space Technology*, 32, 158-167. 10.1061/10.1016/j.tust.2012.06.007
- Cavanaugh, J. E. (1997). Unifying the derivations for the Akaike and corrected Akaike information criteria. *Statistics & Probability Letters*, 33(2), 201-208. 10.1061/10.1016/S0167-7152(96)00128-9
- Chiu, Y.-C. and Chia, Y. (2012). The impact of groundwater discharge to the Hsueh-Shan tunnel on the water resources in northern Taiwan. *Hydrogeology Journal*, 20, 1599-1611. 10.1061/10.1007/s10040-012-0895-6
- Celico, P., Fabbrocino, S., Petitta, M., and Tallini, M. (2005). Hydrogeological impact of the Gran Sasso motor-way tunnels (Central Italy). *Giornale di Geologia Applicata*, 1, 157-165.
- Davy, P., Le Goc, R., Darcel, C., Bour, O., de Dreuz, J.-R., and Munier, R. (2010). A likely universal model of fracture scaling and its consequence for crustal hydromechanics. *Journal of Geophysical Research: Solid Earth*, 115(B10), 1-13. 10.1061/10.1029/2009JB007043
- de Dreuz, J.-R., Davy, P., and Bour, O. (2001a). Hydraulic properties of two-dimensional random fracture networks following a power law length distribution: 1. Effective connectivity. *Water Resources Research*, 37(8), 2065-2078. 10.1061/10.1029/2001WR900011
- de Dreuz, J.-R., Davy, P., and Bour, O. (2001b). Hydraulic properties of two-dimensional random fracture networks following power law distributions of length and aperture. *Water Resources Research*, 38(2), 12-1-12-9. 10.1061/10.1029/2001WR001009
- El Tani, M. (2003). Circular tunnel in a semi-infinite aquifer. *Tunnelling and Underground Space Technology*, 18(1), 49-55. 10.1061/10.1016/S0886-7798(02)00102-5
- Escobar, G. (2017). *Manual de geología para ingenieros*. Universidad Nacional de Colombia, Sede Manizales. <https://repositorio.unal.edu.co/handle/unal/3145>
- Evans, D. D., Nicholson, T. J., and Rasmussen, T. C. (Eds.) (2001). *Flow and Transport Through Unsaturated Fractured Rock*. American Geophysical Union. 10.1061/10.1029/GM042
- Fadakar Alghalandis, Y. (2017). ADFNE: Open source software for discrete fracture network engineering, two and three dimensional applications. *Computers and Geosciences*, 102, 1-11. 10.1061/j.cageo.2017.02.002
- Farhadian, H., Katibeh, H., Huggenberger, P., and Butscher, C. (2016). Optimum model extent for numerical simulation of tunnel inflow in fractured rock. *Tunnelling and Underground Space Technology*, 60, 21-29. 10.1016/j.tust.2016.07.014
- Font-Capó, J., Vázquez-suñé, E., Carrera, J., and Martí, D. (2011). Groundwater in flow prediction in urban tunneling with a tunnel boring machine (TBM). *Engineering Geology*, 121(1-2), 46-54. 10.1016/j.enggeo.2011.04.012
- Golder Associates Inc. (2018) *FracMan*. <https://www.golder.com/fracman/>
- Golian, M., Teshnizi, E. S., and Nakhaei, M. (2018). Prediction of water inflow to mechanized tunnels during tunnel-boring-machine advance using numerical simulation. *Hydrogeology Journal*, 26, 2827-2851. 10.1007/s10040-018-1835-x

- Goodman, R., Moye, D., Schalkwyk, A., and Javandel, I. (1965). Groundwater inflows during tunnel driving. *Bulletin of the International Association of Geologists*, 2, 35-56.
- Hartley, L., and Joyce, S. (2013). Approaches and algorithms for groundwater flow modeling in support of site investigations and safety assessment of the Forsmark site, Sweden. *Journal of Hydrology*, 500, 200-216. 10.1016/j.jhydrol.2013.07.031
- Hawkins, I. R. and Swift, B. T., Hoch, a. R., and Wendling, J. (2011). Comparing flows to a tunnel for single porosity, double porosity and discrete fracture representations of the EDZ. *Physics and Chemistry of the Earth, Parts A/B/C*, 36(17-18), 1990-2002. 10.1016/j.pce.2011.07.029
- Hernández, F. and Kammer, A. (2016). *Caracterización estructural de los complejos Cajamarca y Quebradagrande en la zona del túnel de la línea, con implicaciones hidrogeológicas* [Undergraduate thesis].
- Heuer, R. (1995). Estimating rock-tunnel water inflow. In G. E. Williamson (Ed.) *Proceedings of the Rapid Excavation and Tunneling Conference* (pp. 41-60). SME.
- Hokr, M., Škarydová, I., and Frydrych, D. (2012). Modelling of tunnel inflow with combination of discrete fractures and continuum. *Computing and Visualization in Science*, 15, 21-28. 10.1007/s00791-013-0194-3
- Hokr, M., Shao, H., Gardner, W. P., Balvín, A., Kunz, H., Wang, Y., and Vencel, M. (2016). Real-case benchmark for flow and tracer transport in the fractured rock. *Environmental Earth Sciences*, 75(18), 1273. 10.1007/s12665-016-6061-z
- Hu, L. T. and Chen, C. X. (2008). Analytical methods for transient flow to a well in a confined- unconfined aquifer. *Ground Water*, 46(4), 642-646. 10.1111/j.1745-6584.2008.00436.x
- Hyman, J. D., Karra, S., Makedonska, N., Gable, C. W., Painter, S. L., and Viswanathan, H. S. (2015). DFN WORKS: A discrete fracture network framework for modeling subsurface flow and transport. *Computers and Geosciences*, 84, 10-19. 10.1016/j.cageo.2015.08.001
- IRENA (2007). *Estudios hidrogeológicos e hidrológicos en el área de influencia del túnel piloto de la línea, enmarcado dentro de la gestión ambiental*. IRENA.
- IRENA (2010). *Actualización a 2009 del modelo hidrogeológico del Túnel de la Línea*. INIVIAS - Ministerio del Transporte.
- Karlsrud, K. (2003). Water control when tunneling under urban areas in the Oslo region. *NFF publication*, 12, 27-33.
- Kashyap, R. L. (1982). Optimal Choice of AR and MA Parts in Autoregressive Moving Average Models. *IEEE Transactions on Pattern Analysis and Machine Intelligence, PAMI-4*(2), 99-104. 10.1109/TPAMI.1982.4767213
- Lee, H., Son, B., Kim, Y., and Jeon, S. (2006). Discrete fracture network and equivalent hydraulic conductivity for tunnel seepage analysis in rock mass. *Tunnelling and Underground Space Technology*, 21(3-4), 403. 10.1016/j.tust.2005.12.212
- Leung, C. T. O. and Zimmerman, R. W. (2012). Estimating the Hydraulic Conductivity of Two-Dimensional Fracture Networks Using Network Geometric Properties. *Transport in Porous Media*, 93, 777-797. 10.1007/s11242-012-9982-3
- Liu, R., Li, B., and Jiang, Y. (2016). A fractal model based on a new governing equation of fluid flow in fractures for characterizing hydraulic properties of rock fracture networks. *Computers and Geotechnics*, 75, 57-68. 10.1016/j.compgeo.2016.01.025
- Liu, R., Yu, L., Jiang, Y., Wang, Y., and Li, B. (2017). Recent developments on relationships between the equivalent permeability and fractal dimension of two-dimensional rock fracture networks. *Journal of Natural Gas Science and Engineering*, 45, 771-785. 10.1016/j.jngse.2017.06.013
- Loew, S., Lutzenkirchen, V., Hansmann, J., Ryf, A., and Guntli, P. (2015). Transient surface deformations caused by the Gotthard Base Tunnel. *International Journal of Rock Mechanics and Mining Sciences*, 75, 82-101. 10.1016/j.ijrmms.2014.12.009
- Maillot, J., Davy, P., Le Goc, R., Darcel, C., and de Dreuzy, J.-R. (2016). Connectivity, permeability and channeling in randomly-distributed and kinematically-defined discrete fracture network models. *Water Resources Research*, 52(11), 613-615. 10.1002/2016WR018973
- Maréchal, J.-C., Perrochet, P., and Tacher, L. (1999). Long-term simulations of thermal and hydraulic characteristics in a mountain massif: The Mont Blanc case study, French and Italian Alps. *Hydrogeology Journal*, 7, 341-354. 10.1007/s100400050207
- Maréchal, J.-C. and Etcheverry, J. (2003). The use of 3H and 18O tracers to characterize water inflows in Alpine tunnels. *Applied Geochemistry*, 18(3), 339-351. 10.1016/S0883-2927(02)00101-4
- Maréchal, J.-C., Lanini, S., Aunay, B., and Perrochet, P. (2014). Analytical solution for modeling discharge into a tunnel drilled in a heterogeneous unconfined aquifer, *Ground Water*, 52(4), 597-605. 10.1111/gwat.12087
- Mirarco (2018). *MoFrac: Discrete fracture network modeling*. <https://mofrac.com>
- Molinero, J., Samper, J., and Juanes, R. (2002). Numerical modeling of the transient hydrogeological response produced by tunnel construction in fractured bedrocks. *Engineering Geology*, 64(4), 369-386. 10.1016/S0013-7952(01)00099-0
- Moon, J. and Fernandez, G. (2010) Effect of Excavation-Induced Groundwater Level Drawdown on Tunnel Inflow in a Jointed Rock Mass. *Engineering Geology*, 110(3-4), 33-42. 10.1016/j.enggeo.2009.09.002
- Nikvar Hassani, A., Farhadian, H., and Katibeh, H. (2018). A comparative study on evaluation of steady-state groundwater inflow into a circular shallow tunnel. *Tunnelling and Underground Space Technology*, 73, 15-25. 10.1016/j.tust.2017.11.019
- Perrochet, P. (2005). Confined flow into a tunnel during progressive drilling: An analytical solution. *Ground Water*, 43(6), 943-946. 10.1111/j.1745-6584.2005.00108.x

- Perrochet, P. and Dematteis, A. (2007). Modeling transient discharge into a tunnel drilled in a heterogeneous formation. *Ground Water*, 45(6), 786-790. 10.1111/j.1745-6584.2007.00355.x
- Preisig, G. (2013). Regional simulation of coupled hydromechanical processes in fractured and granular porous aquifer using effective stress-dependent parameters. [Doctoral thesis, University of Neuchâtel].
- Preisig, G., Dematteis, A., Torri, R., Monin, N., Milnes, E., and Perrochet, P. (2014). Modelling discharge rates and ground settlement induced by tunnel excavation. *Rock Mechanics and Rock Engineering*, 47, 869-884. 10.1007/s00603-012-0357-4
- Rizzo, R. E., Healy, D., and de Siena, L. (2017). Benefits of maximum likelihood estimators for fracture attribute analysis: Implications for permeability and up-scaling, *Journal of Structural Geology*, 95, 17-31. 10.1016/j.jsg.2016.12.005
- Schwarz, G. (1978). Estimating the Dimension of a Model. *The Annals of Statistics*, 6(2), 461-464. 10.1214/aos/1176344136
- Shen, S.-L., Wu, H.-N., Cui, Y.-J., and Yin, Z.-Y. (2014). Long-term settlement behaviour of metro tunnels in the soft deposits of Shanghai. *Tunnelling and Underground Space Technology*, 40, 309-323. 10.1016/j.tust.2013.10.013
- Siena, M., Riva, M., Giamberini, M., Gouze, P., and Guadagnini, A. (2017). Statistical modeling of gas-permeability spatial variability along a limestone core. *Spatial Statistics*, 34, 100249. 10.1016/j.spasta.2017.07.007
- Singhal, B. B. S. and Gupta, R. (2010). *Applied Hydrogeology of Fractured Rocks*. Springer. 10.1007/978-90-481-8799-7
- Somogyvári, M., Jalali, M., Jiménez-Parras, S., and Bayer, P. (2017). Synthetic fracture network characterization with transdimensional inversion. *Water Resources Research*, 53(6), 5104-5123. 10.1002/2016WR020293
- Su, K., Zhou, Y., Wu, H., Shi, C., and Zhou L. (2017). An Analytical Method for Groundwater Inflow into a Drained Circular Tunnel. *Ground Water*, 55(5), 1-10. 10.1111/gwat.12513
- Universidad Nacional de Colombia (UNAL) (2010). *Evaluación del impacto de la construcción de los túneles viales del Sumpaz y de La Línea en los hidrosistemas circunvecinos* [Doctoral thesis, Universidad Nacional de Colombia]. Grupo de Investigación en Ingeniería de Recursos Hídricos. <https://repositorio.unal.edu.co/handle/unal/68766>
- Universidad Nacional de Colombia (UNAL) (2015). *Informe Final Ensayos Hidráulicos Especiales en el Macizo Fracturado de La Línea*. Grupo de Investigación en Ingeniería de Recursos Hídricos, 2015.
- Valenzuela, P., Domínguez-Cuesta, M. J., Meléndez-Asensio, M. J., Jiménez-Sánchez, M., and de Santa María, J. A. S. (2015). Active sinkholes: A geomorphological impact of the Pajares Tunnels (Cantabrian Range, NW Spain). *Engineering Geology*, 196, 158-170. 10.1016/j.enggeo.2015.07.007
- Vincenzi, V., Gargini, A., and Goldscheider, N. (2009). Using tracer tests and hydrological observations to evaluate effects of tunnel drainage on groundwater and surface waters in the Northern Apennines (Italy). *Hydrogeology Journal*, 17, 135-150. 10.1007/s10040-008-0371-5
- Wang, X. and Cai, M. (2020). A DFN DEM Multi-scale Modeling Approach for Simulating Tunnel Excavation Response in Jointed Rock Masses. *Rock Mechanics and Rock Engineering*, 53, 1053-1077. 10.1007/s00603-019-01957-8
- Woods, J. A., Teubner, M. D., Simmons, C. T., Narayan, K. A. (2003). Numerical error in groundwater flow and solute transport simulation. *Water Resources Research*, 39(6). 10.1029/2001WR000586
- Xia, Q., Xu, M., Zhang, H., Zhang, Q. and Xiao, X. (2018). A dynamic modeling approach to simulate groundwater discharges into a tunnel from typical heterogeneous geological media during continuing excavation. *KSCCE Journal of Civil Engineering*, 22, 341-350. 10.1007/s12205-017-0668-9
- Yang, F.-R., Lee, C.-H., Kung, W.-J., and Yeh, H.-F. (2009). The impact of tunneling construction on the hydrogeological environment of "Tseng-Wen Reservoir Transbasin Diversion Project" in Taiwan. *Engineering Geology*, 103(1-2), 39-58. /10.1016/j.enggeo.2008.07.012
- Ye, M., Meyer, P. D., and Neuman, S. P. (2008). On model selection criteria in multimodel analysis. *Water Resources Research*, 44(3), 1-12. 10.1029/2008WR006803
- Zarei, H. R., Uromeihy, A., and Sharifzadeh, M. (2011). Evaluation of high local groundwater inflow to a rock tunnel by characterization of geological features. *Tunnelling and Underground Space Technology*, 26(2), 364-373. 10.1016/j.tust.2010.11.007

Electrochemical Behavior of a Stainless Steel Superficially Modified with Nitrogen by Three-dimensional Ion Implantation

Comportamiento electroquímico de un acero inoxidable modificado superficialmente con nitrógeno por medio de implantación iónica tridimensional

Felipe Sanabria-Martínez¹, Ely D. Valbuena-Niño², Leidy S. Chacón-Velasco³, and Hugo A. Estupiñán-Durán⁴

ABSTRACT

Martensitic-grade stainless steels are widely used in diverse industrial and surgical applications, despite their natural tendency to suffer local and uniform corrosion when continuously exposed to aggressive operation conditions. In order to enhance their surface properties, this paper characterized the performance, in saline solutions, of AISI 420 stainless steel, which was surface-modified by three-dimensional ion implantation using electrochemical techniques. The surface of the samples was implanted with ionized nitrogen particles with an energy of 10 keV, varying the implantation time between 30 and 90 minutes. After the surface treatment, the samples were exposed to a NaCl 3% (w/w) aqueous solution for 21 days. Tafel extrapolation, linear polarization resistance, and electrochemical impedance spectroscopy tests were performed, with the purpose of quantifying the effect of the ion implantation technique against electrochemical corrosion. To establish a comparison, the same tests were also performed on non-treated samples. The results indicated an increase in the corrosion potential, polarization resistance, and a decrease in the current density of implanted samples, thus demonstrating that, by delaying corrosive activity, three-dimensional ion implantation offers better protection against electrochemical corrosion in AISI 420 stainless steel samples implanted with nitrogen.

Keywords: martensitic steel, surface, surface modification, corrosion, electrochemical characterization

RESUMEN

Los aceros inoxidables de grado martensítico son ampliamente usados en diversas aplicaciones industriales y quirúrgicas, a pesar de su tendencia natural a presentar corrosión de tipo uniforme y localizada cuando son continuamente expuestos a condiciones de operación agresivas. Con el propósito de mejorar sus propiedades superficiales, este trabajo caracterizó el desempeño en solución salina del acero inoxidable AISI 420 modificado superficialmente por medio de la técnica de implantación iónica tridimensional usando técnicas electroquímicas. La superficie de las probetas fue implantada con partículas ionizadas de nitrógeno a una energía de 10 keV, variando el tiempo de implantación entre 30 y 90 minutos. Posterior al tratamiento superficial, las muestras fueron expuestas a una solución acuosa de NaCl al 3 % wt durante 21 días. Se llevaron a cabo pruebas de extrapolación Tafel, resistencia a la polarización lineal y espectroscopía de impedancia electroquímica, con el objetivo de cuantificar el efecto de la técnica de implantación frente a la corrosión electroquímica. Con motivo de establecer una comparación, los mismos ensayos fueron aplicados a muestras sin tratamiento. Los resultados indicaron un aumento en el potencial de corrosión, resistencia a la polarización y una disminución en la densidad de corriente en probetas implantadas, demostrando así que, retardando la actividad corrosiva, la implantación iónica tridimensional ofrece una mejor protección frente a la corrosión electroquímica en sustratos de acero inoxidable AISI 420 implantados con nitrógeno.

Palabras clave: acero martensítico, superficie, modificación superficial, corrosión, caracterización electroquímica

Received: March 18th, 2020

Accepted: June 25th, 2021

¹Chemical Engineer, Universidad Industrial de Santander, Bucaramanga, Colombia. Affiliation: Foundation of Researchers in Science and Technology of Materials, Colombia. E-mail: felipesanabiamartinez@gmail.com

²Physicist, Universidad Industrial de Santander, Bucaramanga, Colombia. Master in Physics, Universidad Industrial de Santander, Bucaramanga, Colombia. Ph.D. in Mechanical Engineer, Universidad Politécnica de Madrid, Madrid, España. Affiliation: Foundation of Researchers in Science and Technology of Materials, Colombia. E-mail: edvnino@foristom.org

³Metallurgical Engineer, Universidad Industrial de Santander, Bucaramanga, Colombia. Affiliation: Foundation of Researchers in Science and Technology of Materials, Colombia. E-mail: leidyilvanacv@hotmail.com

⁴Metallurgical Engineer, Universidad Industrial de Santander, Bucaramanga,

Colombia. Master in Engineering, Universidad Industrial de Santander, Bucaramanga, Colombia. Ph.D. in Chemical Engineering, Universidad Industrial de Santander, Bucaramanga, Colombia. Affiliation: Associate Professor, Universidad Nacional de Colombia, Medellín, Colombia. Email: haestupinand@unal.edu.co

How to cite: Sanabria-Martínez, F., V-Niño, E. D., Chacón-Velasco, L. S., and Estupiñán-Durán, H. A. (2022). Electrochemical Behavior of a Stainless Steel Superficially Modified with Nitrogen by Three-dimensional Ion Implantation. *Ingeniería e Investigación*, 42(1), e85772. 10.15446/ing.investig.v42n1.85772



Attribution 4.0 International (CC BY 4.0) Share - Adapt

Introduction

Grade 420 martensitic stainless steel (AISI 420 SS) is a high carbon steel with a chromium mass content of up to 14% and other alloying elements such as Mn (1%), Mo (1%), Si (1%), S (0,03%), and P (0,04%). This compositional structure, along with its heat treatment during the manufacturing process, makes it an attractive material for various industrial applications in modern engineering; it has a remarkable operational performance in electrolytic environments and relatively important mechanical properties (hardness and ductility). Despite this, grade 420 SS suffers great damage when exposed to certain conditions, for instance, when operating under annealed conditions or at high temperatures. This type of steel has demonstrated a lower corrosion resistance and pitting tendency in comparison with other martensitic and austenitic alloys (Voort *et al.*, 2004).

Due to cases of this type, the enhancement of the physicochemical properties (particularly in structures of metallic nature), by means of novel, safe, and reliable techniques working with easy-to-operate, inexpensive, and ecofriendly equipment designed specifically to advance in the engineering of solid materials and surface technology, has attracted a growing interest by the scientific community. Numerous experiments have shown that the surface properties of metals, altered by phenomena such as friction, wear, fatigue, and corrosion can be changed with superficial modifications by doping species upon the surface of the solid, and they have also uncovered feasible possibilities for improving the functional capability of several alloys in a variety of applications (Borgioli *et al.*, 2019; Bravo and Vieira, 2015; Walsh *et al.*, 2008). Recently, a number of ion bombardment techniques such as direct ion implantation (or ion beam), ion beam assisted deposition, or plasma source ion implantation, among other variations, have been increasingly implemented for surface treatments, exhibiting a potential for producing, in quantitative terms, enhancements in wear and corrosion applications in metals and alloys at several orders of magnitude.

Initially, ion implantation was commercially presented in the semiconductor industry. Then, it happened to be studied at different laboratories across the world, whose works were aimed at the possibility of improving mechanical and corrosion behavior of steels that are of relevance to the nuclear and metallurgical industry (Was, 1990; Dearnaley, 1969; National Research Council, 1979). In general, the impinging atoms penetrate the target or substrate material at a depth between 0,01 and 1,00 μm , which produces a thin alloyed surface layer on the substrate without altering neither the geometric dimensions nor their internal properties. The implantation range of the atoms depends on the atomic number and the energy at which the atom is accelerated. The process differs from others such as electroplating in that it does not produce a discrete coating, as well as from or carburizing and nitriding, which involve diffusion of species at greater depths into the material at high temperatures. Instead, ion implantation alters the chemical composition near the surface of the base material. Within

the phenomena occurred during the surface modification of the solid surface by ion bombardment, both compositional and microstructural changes can be identified, which lead to the alteration of physicochemical properties such as transport, optical properties, corrosion, strength and wear, and fatigue resistance. The compositional changes associated with ion implantation are classified into recoil implantation, cascade mixing, radiation-enhanced diffusion, radiation-induced segregation, Gibssian adsorption, and sputtering, which, combined, produce complex composition differentials upon the implanted surface. Microstructurally, within the formation of defects expected from thermodynamic equilibrium, it is possible to find phase alterations, metastable (crystalline, amorphous, or quasicrystalline) phase formation and growth, grain growth, texture, and the formation of a high-density dislocation network. It is worth noting that, compared to other surface processes, several advantages have been demonstrated for using ion implantation as a surface modification technique:

- The operation is inherently conducted at low temperatures.
- It yields exceptional adhesion.
- Dimensional changes are not a problem on an engineering tolerance scale (being around the order of a few tenths of nanometers).
- Surface polish is enhanced by the sputtering process.
- The implanted species are dispersed on a microscopic-atomic level, thus producing the most efficient and beneficial effect of the additive.
- Significant compressive surface stresses are produced, which compensate external imposed tensile stresses and protect the components against creep or fatigue failure by surface-initiated cracking.

Notwithstanding the above, an important limitation in metallurgical applications has also been found, where a complete and homogeneous implantation of species upon the surface is required. Certain sections of the surface of complex shapes may be inaccessible to the line-of-sight capability of conventional equipment, thus leading to the expensive and bulky installation of sample manipulation devices (Was, 1990; Dearnaley, 1969; National Research Council, 1979). With the purpose of improving the functionality in corrosive environments of ferrous alloys widely used in engineering applications, this paper presents the results obtained from the electrochemical analysis of a 420-grade stainless steel surface modified by three-dimensional ion implantation (3DII), a particular implantation technique that overcomes the limitations mentioned above. By means of 3DII, nitrogen (N) ions are bombarded upon the surface of AISI 420 SS substrates at previously established energy levels and exposition times (Dougur-Zhabon, 1999, 2002; Valbuena-Niño *et al.*, 2010, 2011, 2020; Sanabria *et al.*, 2019, 2020). Then, the effect of the surface modification and performance of the SS samples

exposed to an aggressive media simulating work operation is evaluated through the following electrochemical techniques: linear polarization resistance (LRP), Tafel extrapolation, and electrochemical impedance spectroscopy (EIS).

Methodology

In general, the experimental methodology in this work was sequentially developed as follows: substrate preparation, definition of parameters prior the ion implantation treatment, and electrochemical characterization.

Substrate material

Disk-shaped AISI 420 SS substrate with a 13 mm diameter and 2 mm thickness were used in this study (see chemical composition in Table 1). Before the surface treatment, the metallographic preparation was carried out in accordance with ASTM standards (2003, 2011a). The samples were ground and then polished with silicon carbide papers from 60 down to 600 grit. Additionally, in order to understand the state and phases of the delivered material, a microstructure analysis was performed with a Carl Zeiss JVC metallographic microscope.

Table 1. Elemental composition of AISI 420 SS

Element	C	Cr	Mn	Si	S	P
Value (wt %)	0,30	13,56	0,50	1,00	0,03	0,04

Source: Authors

Ion implantation

3DII is performed by means of the Joint Universal Plasma and Ion TEchnology Reactor (JUPITER), a prototype of this technique. The process is based on a high voltage pulsed discharge activated within the low-pressure range or 'high vacuum'. For a more detailed description of the properties, phenomena, and other generalities occurred in this type of plasma-ion technology, a review of the referenced literature is encouraged (Parada *et al.*, 2019; Vladimir and Tsygankov, 1997). Once the samples are placed upon the cathode (the region where the applied voltage drops) inside the vacuum chamber of the reactor, a pump system is set up to achieve the required vacuum operations and then ignite the discharge. At this pressure conditions, an ion flux of gaseous nitrogen is fed into the chamber. Once exposed to the applied potential (whose magnitude is of an order from tenths to hundredths of kiloelectronvolts), the gas particles reach an ionization state and then, due to the auto-sustained plasma, which is generated by the effect of this type of discharge at such conditions, the excited particles are attracted towards the cathode, also granting the implantation of ionized species upon the surface of the substrates at a normal angle on the surface. Additionally, prior to the implantation process in this study, there was additional surface preparation by sputtering. That is, before feeding in the ion flux of nitrogen, an Argon (Ar) flux was supplied at certain conditions with

the purpose of eliminating the greatest possible amount of impurities and adapting the roughness across the surface of the substrates. The JUPITER operation conditions for both processes (sputtering and ion implantation) agree with previous experiments and shown in Table 2 (Dougar-Zhabon *et al.*, 1999, 2002; Valbuena-Niño *et al.*, 2010, 2011, 2020; Sanabria *et al.*, 2019, 2020).

Table 2. Operation conditions

Parameter	Sputtering	Treatment (T1)	Treatment 2 (T2)
Gas type	Ar	N	N
Voltage (V)	5	30	30
Frequency (Hz)	30	30	30
Pulse duration (ms)	0,25	0,25	0,25
Pressure (Pa)	1,5 > P > 1,8	1,5 > P > 1,8	1,5 > P > 1,8
Exposition time (min)	20	30	90

Source: Authors

Electrochemical characterization

Implanted and non-implanted substrates were immersed in an electrolyte solution with NaCl (wt. 3%) for 21 days, and electrochemical tests were periodically performed on days 0, 7, 14, and 21. To measure the electrochemical corrosion behavior of AISI 420 SS samples, an electrochemical cell with a KCl salt bridge and Agar-Agar solution was implemented. A typical cell consists of three electrodes, in which AISI 420 SS specimen served as the working electrode with an area of 0,785 cm², a graphite rod as the counter electrode, and Ag/AgCl (saturated calomel electrode) as the reference electrode. This cell is then connected to Gill B1-STAT through a potentiostat plugged into a computer with the ACM v.5 software and a sequencer, as mentioned in the G106-89 standard (ASTM, 2015).

It is worth noting that all electrochemical and corrosion tests were performed according with ASTM standards (2010, 2011b). The Tafel extrapolation test was performed with a scan rate of 1 mV/sec and a potential between -250 mV and +250 mV. LPR analysis was carried out with a linear fit between +25 mV and -25 mV around the previously established corrosion potential (E_{corr}). As for the electrochemical impedance measurements, the spectrums were recorded with an initial and final frequency of 30 000 Hz and 0,05 Hz, respectively. The impedance response was eventually obtained from the applied frequency range and then analyzed by Nyquist plots and Bode representation. An equivalent circuit was proposed to physically interpret the obtained data from EIS measurements. The procedures mentioned above were followed to determine the kinetic parameters (E_{corr}), corrosion current density (i_{corr}), and polarization resistance (R_p). Additionally, the experimental data were simulated by running different types of electrode-electrolyte interfaces with the Zview software (Scribner Associates, Inc.), thus finding the best electric circuit representation, accurately describing each electrochemical

system, and determining the respective values of each component involved.

Results

The characterization results before and after the implantation process are presented in this section in the following way: a metallographic analysis, an electrochemical study with potentiodynamic analysis (Tafel and LPR), and EIS measurements.

Metallographic analysis

The micrograph of the structure is illustrated in Figure 1, which agrees with the typical microstructure of the martensitic stainless steel (AISI 420 SS) supplied in annealed conditions. It consists mainly of ferrite, together with perlite grains dispersed with small colonies of carbides precipitated at the grain boundaries (Nunura and Lecaros, 2015; Voort *et al.*, 2004).

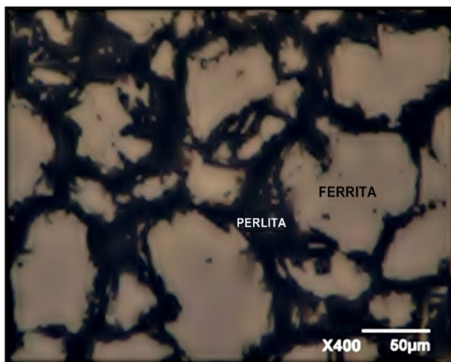


Figure 1. Metallography structure: AISI 420 SS.

Source: Authors

Electrochemical analysis

Extrapolation Tafel: In order to obtain information concerning the corrosion resistance of AISI 420 SS, the quantitative assessment of corrosion was conducted by potentiodynamic polarization tests. Figure 2 illustrates the comparison of the potentiodynamic polarization curves between implanted and non-implanted samples exposed to NaCl (wt. 3%) solution at different exposition times. The relevant parameters are listed in Table 3.

From the Tafel analysis, the E_{corr} value gives an idea of the reactive nature of the surface of AISI 420 SS. In general terms, it can be noticed that, during each stage of the experiment, the blanks, compared with implanted samples, described an active corrosion tendency with a more negative E_{corr} and a rapid increase in the anodic reaction rate. As a result, a more important deterioration of corrosion resistance may be expected. Regarding the implanted samples, the E_{corr} values shifted towards nobler sides, where the samples that stood out were those whose nitrogen ion implantation was carried out for 90 minutes and exposed at 0, 7, and 21 days. Unlike the latter, at 14 days, it was found that the E_{corr} value for

the substrates implanted for 30 minutes was slightly higher, which did not allow establishing a linear correlation between E_{corr} and treatment time during ion implantation with nitrogen on AISI 420 SS. Nevertheless, the analysis of the corrosion potential is only a first approximation of the electrochemical behavior of the material, and other parameters like i_{corr} must be taken into account in order to evaluate corrosion kinetics.

Corrosion current density (i_{corr}) was estimated by means of linear fit and Tafel extrapolation to the cathodic part of the polarization curve. From Table 3, it can be observed that the corrosion current density (i_{corr}) is inversely proportional to the corrosion potential (E_{corr}), which implies the same pattern of corrosion behavior, that is, an increase in i_{corr} implies a degradation of the protective properties of the passive film formed during the implantation process. As mentioned before, the reaction rate in samples without treatment remained the highest throughout the exposition time in saline solutions. Conversely, it can be observed that the E_{corr} and i_{corr} of the implanted samples provided better results compared to non-implanted samples. Since the i_{corr} magnitudes reflect the rate of dissolution through the passive layer, it can be concluded that the samples implanted with nitrogen for 30 minutes possess a better corrosion resistance in comparison with the blanks. Thus, it can be said that the treatment with the same ion implanted for 90 minutes exhibits the highest corrosion resistance. As for the inspection at 14 days of chemical attack, the samples implanted for 90 minutes showed an increase in E_{corr} accompanied by lower i_{corr} than those implanted for 30 minutes, which confirms a more important improvement in the corrosion resistance of AISI implanted with nitrogen under these conditions. Finally, it is worth mentioning the existence of a transpassive region, where the rapid increase in the current value occurs due to a breakdown of the passive films. This tendency is commonly known as pitting corrosion, and it is made evident in Figure 2c for the samples implanted for 30 minutes at a potential of 0,06 V. A more notable tendency of this phenomena is presented in Figure 2d for blanks and samples implanted for 90 minutes at potentials of 0,06 V and 0,12 V, respectively. (Anandan *et al.*, 2007; Maleki-Ghaleh *et al.*, 2014; Muthukumaran *et al.*, 2010; Padhy *et al.*, 2010; Pereira *et al.*, 2017; Osozawa and Okato, 1976).

Table 3. Electrochemical parameters obtained from Tafel analysis

Substrates	Parameter	0 days	7 days	14 days	21 days
Blanks	E_{corr} (V)	-573,90	-543,60	-530,00	-164,00
	i_{corr} (A/cm ²)	3,16E00	2,51E00	2,95E00	3,55E-01
T1 (30 min)	E_{corr} (V)	-524,50	-371,70	-163,70	-128,90
	i_{corr} (A/cm ²)	2,51E00	6,31E-01	3,98E-01	6,31E-02
T2 (90 min)	E_{corr} (V)	-355,80	-348,70	-183,20	-104,00
	i_{corr} (A/cm ²)	1,78E+00	6,31E-01	5,89E-02	2,00E-02

Source: Authors

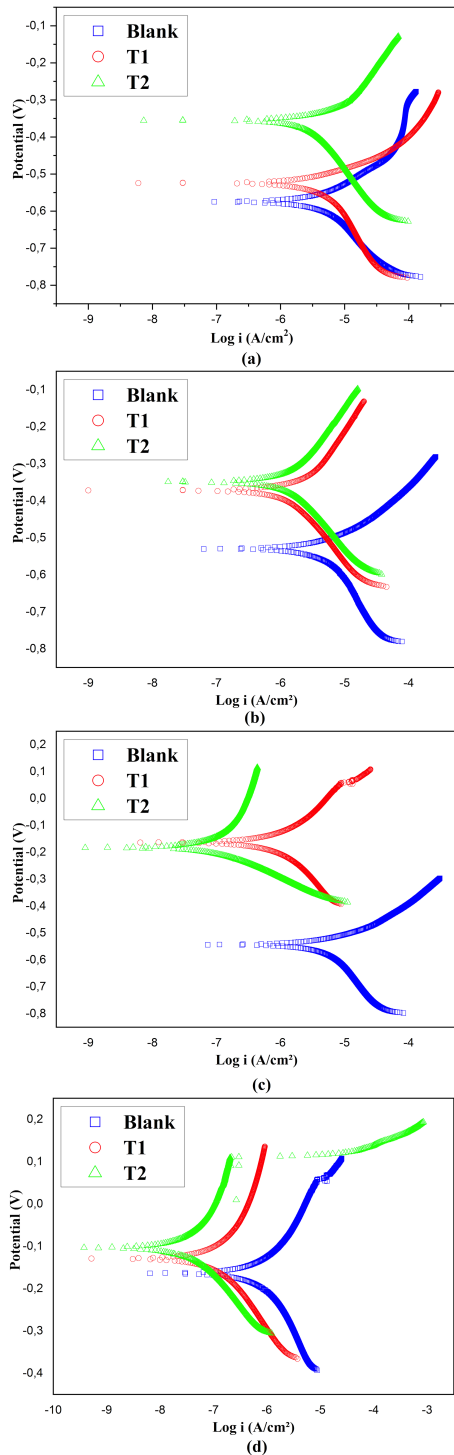


Figure 2. Potentiodynamic curves: Samples exposed to NaCl (wt. 3%) at (a) 0 days, (b) 7 days, (c) 14 days, and (d) 21 days.

Source: Authors

Several works have attributed the beneficial effect of nitrogen ion implantation in ferrous alloys to different physical and chemical phenomena such as the supersaturation of the atomic structure, the generated stresses, and the defect density (Sanabria *et al.*, 2020). Regarding the electrochemical properties of stainless steels, the contribution of both implanted nitrogen and the formation of chromium nitride

on the metal's surface have been confirmed as the main mechanisms in the enhancement of corrosion potential and current density. On one hand, the decrease in i_{corr} is attributed to the formation of stable chromium nitride phases inside the interstitial sites, which act as a kinetic barrier to the dissolution process of the alloy, hence reducing the reaction rate due to a multi-electron transfer process.

Other authors (Anandan *et al.*, 2007; Muthukumaran *et al.*, 2010; Padhy *et al.*, 2010) have proposed a different approach to the effect of implanted nitrogen on electrochemical behavior. Implanted nitrogen favors the formation of ammonium ions (Equation (1)) which eventually increase the local pH at active sites on the surface, such as grain boundaries and kinks, where passive film formation is chiefly unstable. As a result, the production of ammonium, together with further nitrite or nitrate ions through the electrolyte, impedes the reduction of pH, thus shifting the E_{corr} to more positive values (Fossati *et al.*, 2006).



Linear polarization resistance: Linear polarization resistance is inversely related to the corrosion rate and provides useful information on the reactivity of AISI 420 SS in electrolytes. The knowledge of R_p from the cathodic zone enables the direct determination of i_{corr} and, hence, the corrosion rate at any instant (Vasilescu *et al.*, 2015). The results obtained after the exposition to a NaCl (wt. 3%) solution while performing the linear polarization test in non-implanted and implanted samples are presented by the graphs in Figure 3.

The relation between the potential and the current density of non-implanted samples is depicted in Figure 3a. The typical trend of polarization curves was observed, with a relatively similar R_p values at 0 days (3 364,2 $\Omega \cdot \text{cm}^2$), 7 days (3 632,8 $\Omega \cdot \text{cm}^2$), and 14 days (3 937,6 $\Omega \cdot \text{cm}^2$). It then reached the highest value at 21 days (12 810,0 $\Omega \cdot \text{cm}^2$) of exposition due to a possible passivation of the metallic surface by the formation of a chrome oxide film, a natural characteristic of martensitic SS against corrosion. As for the results in the current-potential profile of implanted samples, a remarkable difference between the R_p values was observed; there was a gradual magnitude increase during the immersion time in the saline solution. In the case of the substrates implanted with nitrogen for 30 minutes in Figure 3b, the R_p values were 2 812,1 $\Omega \cdot \text{cm}^2$, 19 562,0 $\Omega \cdot \text{cm}^2$, and 36 455,0 $\Omega \cdot \text{cm}^2$ at 0, 7, and 14 days, respectively. At 21 days, where the R_p reached the highest magnitude or polarization resistance (248 905,0 $\Omega \cdot \text{cm}^2$), the curve presented a vertical trend of quasi-steady current as the potential increased, which indicates the formation of a passive film upon the surface. Similarly, the samples implanted with nitrogen for 90 minutes (Figure 3c) exhibited such tendency, where the R_p values at 0 and 7 days were 6 553,3 $\Omega \cdot \text{cm}^2$ and 28 030,0 $\Omega \cdot \text{cm}^2$, respectively. However, this system achieved the passive behavior at 14 days with an R_p of 269 228,0 $\Omega \cdot \text{cm}^2$, and then at 21 days with the highest polarization resistance at 812 510,0 $\Omega \cdot \text{cm}^2$. An overall R_p behavior of the samples is shown in Figure 3d.

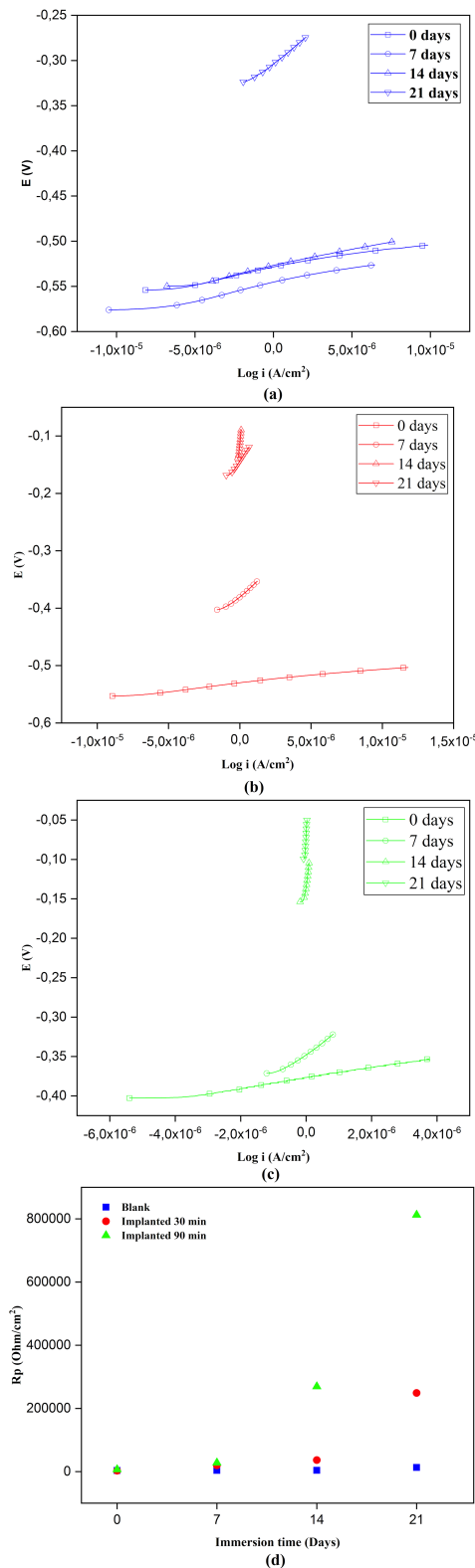


Figure 3. Linear polarization resistance plots: $\log i$ (current density) vs. Potential (v) plots of non-implanted (a) and implanted with nitrogen for (b) 30 minutes, (c) 90 minutes, and (d) R_p vs. exposition time in NaCl.

Source: Authors

By means of this electrochemical measurement, a favorable effect of 3DII technique with nitrogen species upon the surface of martensitic stainless steels was demonstrated; it gradually reduced the current flux across the substrate surface and therefore boosted its corrosion resistance during the immersion time in the electrolyte solution. Additionally, a linear correlation was established between the R_p and treatment time, with a better protection at relatively longer times of nitrogen ion implantation. A reason for this is that the surface of implanted substrates effectively achieves a passive behavior due to the formation of a stable and protective surface oxide layer. This delays the effect of anodic reactions upon the surface of the material once exposed to the chemical attack. Other 3DII studies have found a direct correlation between the treatment time and the implantation dose, reporting better corrosive behavior at higher doses due to the effect of the concentration of the implanted species (Valbuena-Niño *et al.*, 2020; Sanabria *et al.*, 2019). The findings in the LPR measurements agree with other works (Valbuena-Niño *et al.*, 2011; Peña *et al.*, 2009) and reinforce the results obtained in the Tafel analysis regarding the electrochemical behavior of AISI 420 SS against electrochemical corrosion.

Electrochemical Impedance Spectroscopy: Whereas potentiodynamic polarization analysis can give information about the susceptibility of the surface to corrosion, EIS experiments can provide more data concerning to the corrosion mechanisms.

The evolution of the electrochemical behavior of non-implanted AISI 420 SS samples and samples surface-treated by nitrogen ion implantation for 30 and 90 minutes, then exposed to a saline environment for 0, 7, 14, and 21 days, is indicated by the common EIS representations: Nyquist plots and Bode diagrams. Additionally, an appropriate equivalent circuit with its corresponding fitted parameters, such as constant phase elements (CPE), solution resistance (R_s), pore resistance (R_L), and R_p , is also presented in Table 4 and described in a section below.

In Figure 4, the Nyquist plots are illustrated from EIS measurements carried out at different exposition times for both non-implanted (Figure 4a) and implanted samples with nitrogen species at different treatment times (Figure 4b and c). All the Nyquist plots end up with an unfinished semicircular form. A similar electrochemical tendency can be seen in the implanted samples, where the influence of 3DII with nitrogen particles is made evident by comparing the radius of the curves with those described by the blanks. The difference lies in the shifting of the curves for the implanted samples along the real axis, which is due to the series resistances comprising electrolytes and contact resistance. This can be validated from the values obtained in Table 4. Since high R_p values suggest a good corrosion resistance, and low capacitance magnitudes signify the long-term stability of the passive film, the geometric increment in the curve amplitudes is attributed to a direct increase between the polarization resistances of each system with both the exposition time and treatment time in the implantation process. The R_p increased from 990,0 $\Omega \cdot \text{cm}^2$ (0 days) to 22 516,0 $\Omega \cdot \text{cm}^2$ (21 days) in blanks (Figure 4a), from 842,7 $\Omega \cdot \text{cm}^2$ (0 days) to 26 000,0 $\Omega \cdot \text{cm}^2$

(21 days) in samples implanted for 30 minutes (Figure 4b), and from 5 557,0 $\Omega\cdot\text{cm}^2$ (0 days) to 463 780,0 $\Omega\cdot\text{cm}^2$ (21 days) in samples implanted for 90 minutes (Figure 4c).

Conversely, the double layer capacitance for each system globally presented a reduction in its magnitude throughout the electrochemical exposition from 9,38E-03 $\text{F}\cdot\text{cm}^{-2}$ to 9,70E-06 $\text{F}\cdot\text{cm}^{-2}$ in blanks (Figure 4a); from 2,64E-3 $\text{F}\cdot\text{cm}^{-2}$ to 6,59E-06 $\text{F}\cdot\text{cm}^{-2}$ in samples implanted for 30 minutes (Figure 4); and from 3,39E-04 $\text{F}\cdot\text{cm}^{-2}$ to 8,59E-06 $\text{F}\cdot\text{cm}^{-2}$ in samples implanted for 90 minutes (Figure 4c). The increase observed in the R_p values in implanted samples is due to stable and readily passive film formation owing to the interfacial nitrogen and the production of chromium nitride. The similar tendency observed in bare substrates, although at a lower degree, may be attributed to the passive nature of martensitic AISI 420 SS in chloride media. As for the capacitance decrease, it indicates an improvement in the passive film stability, thus validating the positive effect on samples implanted with nitrogen (Leitao *et al.*, 1997; Hannani, and Kermiche, 1998).

Figure 5 shows the Bode diagram representation of EIS measurements for blanks and nitrogen implanted on AISI 420 SS samples after immersion in the same corrosive medium. An ideal capacitive response would result in a (-1) slope and a phase angle of 90° . Although no electrochemical system behaves in such an ideal manner, it is possible to identify the expected capacitive behavior of passive films exposed to electrochemical attack in non-implanted samples, a consequence commonly attributed to the characteristic chromium oxide film AISI 420 SS (Hannani and Kermiche, 1998).

Within the exposition time in saline environments, these curves demonstrated a CPE only. A more complex corrosion mechanism was also detected, with alterations in the responses produced by the 3DII technique in surface-modified substrates. Each variation depends on the treatment time during the implantation process and the immersion time in the electrolyte. At high frequencies, there was a significant increase in the phase angle for implanted samples compared to the blanks at 7 (Figure 5b) and 14 days (Figure 5c). However, these findings were contradictory at 0 (Figure 5a) and 21 days (Figure 5d). At low frequencies, implanted samples achieved higher angle phases throughout the immersion period. As for substrates implanted for 90 minutes, a further CPE could be identified within the same exposition time, a typical response from an electrode with a passive layer (Abreu *et al.*, 2008).

Additionally, while the immersion time increases, an improvement can be seen in the ability to resist the current flow with the impedance modulus for implanted samples at low frequencies with higher resistance values than those of blanks. Despite the improvement in electrochemical properties revealed in previous electrochemical techniques, these EIS results suggested that treatment time variations for 3DII with nitrogen species on AISI 420 SS were not able to reproduce a consistent enhancement against corrosion. They were nevertheless considered to give a satisfactory physical interpretation when modeling the corresponding electric circuit.

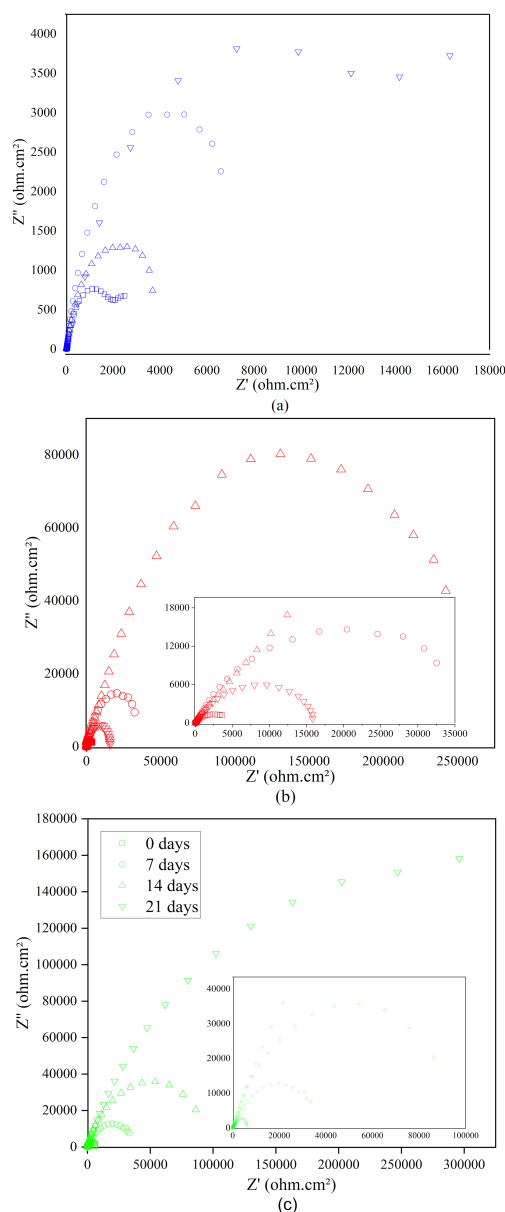


Figure 4. Nyquist diagrams for (a) non-implanted and implanted with nitrogen for (b) 30 minutes and (c) 90 minutes.

Source: Authors

Equivalent circuit: Each system was characterized by using an appropriate equivalent circuit model. The circuit depicted in Figure 6a represents the samples without treatment and can be considered as a simple Randle's cell with only one electroactive interface. The electrical circuit in Figure 6b with two electroactive interfaces is widely used in studies on ion selective membranes (or coated electrode-electrolyte interfaces) when examining metallic corrosion under coatings exposed to corrosive environments (Olaya *et al.*, 2011; Piratoba *et al.*, 2010; Abdi and Savaloni, 2017; Jiménez-Morales *et al.*, 1997).

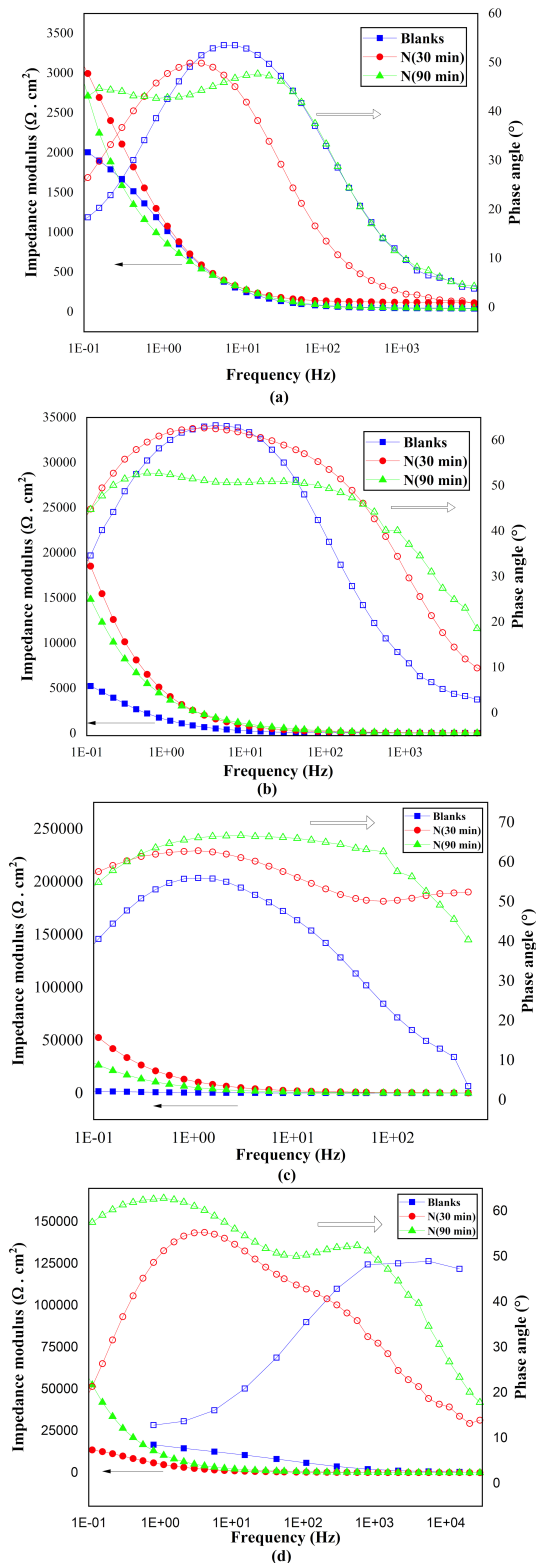


Figure 5. Bode plots for non-implanted and implanted samples after exposition for (a) 0, (b) 7, (c) 14, and (d) 21 days.

Source: Authors

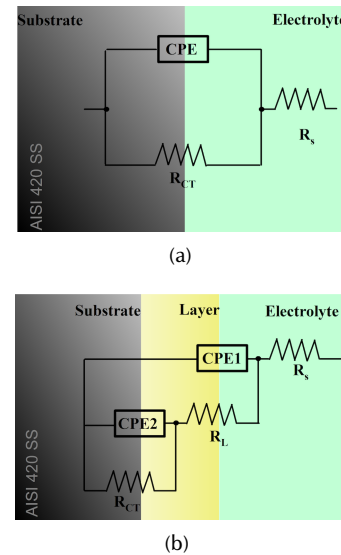


Figure 6. Equivalent circuit representation.

Source: Authors

In general terms, the best electric circuit that fits the experimental data of implanted samples consisted of an arrangement of resistances and pseudo-capacitances or constant phase elements CPE connected in series or parallel. R_s represents the resistance of the solution, for the ion migration describes an ohmic behavior in the electrolyte. The dielectric CPE1 describes the capacitive effect of the interface between the electrolyte and the implanted surface. The following elements correspond to defects or porosities of the passive layer, which ease the transport of the electrolyte, together with oxygen, active ions, and corrosion products, to the metal's surface (Piratoba *et al.*, 2010). The electrolyte precipitated in such an active place is represented by R_L . The electrolyte-substrate interface is represented by the parallel circuit between the dielectric properties of the layer CPE2 (acting as the double layer capacitance), and R_{CT} as the charge transference resistance and the response against polarization resistance. Since CPE accounts for the deviation from an ideal dielectric behavior and is also related to surface heterogeneities, and R_{CT} values give a more approximate interpretation of the corrosion resistance, it is therefore demonstrated that 3DII, applied to this particular material during certain intervals of time, has affected its electrochemical characteristics, and hence its performance in such environments. The fitting parameters were estimated with the Zview software and are shown in Table 4.

Each system increased its R_p and, therefore, the resistance to charge transference at each stage of the chemical exposition. Inversely, a decrease in CPE indicated that the protective layer is either continuous or compact, with the implanted samples being the ones that offered a better improvement in comparison with bare AISI 420 SS substrates. By comparing the performance of implanted samples (with the treatment for 90 minutes standing out) it is possible to conclude that 3DII, for longer periods of time, provides a larger thickness and density of the passive film formed, which, when exposed to chemical attacks, may act as a barrier or blockage of

Table 4. Component values of the equivalent circuit approximation

Substrate	Exposition time in NaCl	R_S ($\Omega \cdot \text{cm}^2$)	R_L ($\Omega \cdot \text{cm}^2$)	R_{CT} ($\Omega \cdot \text{cm}^2$)	CPE1 ($\text{F} \cdot \text{cm}^{-2}$)	n1	CPE2 ($\text{F} \cdot \text{cm}^{-2}$)	n2
Blank	0	42,0	-	990,0	1,86E-04	0,99	-	-
	7	34,3	-	3 986,0	4,31E-04	0,70	-	-
	14	34,3	-	8 764,0	3,86E-05	0,71	-	-
	21	130,6	-	22 516,0	4,97E-07	0,34	-	-
T1 30 min	0	117,1	-	842,7	2,00E-04	0,75	-	-
	7	58,8	-	16 824,0	2,76E-05	0,69	-	-
	14	35,2	2 191,0	40211,0	4,55E-05	0,75	9,19E-06	0,81
	21	33,1	8 448,0	2,6E+05	3,91E-06	0,77	6,59E-06	0,64
T2 90 min	0	45,6	1 407,0	5 557,0	1,74E-04	0,72	3,39E-04	0,89
	7	33,5	6 190,0	36 392,0	5,79E-05	0,64	1,54E-05	0,92
	14	31,3	122,8	104 700,0	6,64E-06	0,77	7,42E-07	0,76
	21	34,8	2 230,0	463 780,0	1,47E-05	0,70	8,59E-06	0,77

Source: Authors

the active sites of such ferrous alloys. Unexpectedly, some discrepancies were obtained in Bode for samples implanted for 30 minutes at 0 and 7 days of exposition (Figure 5a and b). The curve demonstrated an image similar to non-implanted samples, with one CPE only. This particular case is physically interpreted by means of a Randle circuit (order I) (Figure 6a), which compromises the following: the resistance offered by the solution, a capacitance that represents the interface electrolyte-substrate, and the charge transference resistance representing the base material. The identical behavior may be attributed to the fact that, at relatively short periods of implantation time, the layer deposited upon the surface of the substrates will not be as stable as those implanted with higher doses or for longer periods, thus offering little protection against electrochemical corrosion (Valbuena-Niño *et al.*, 2016; Sanabria *et al.*, 2019).

The improvement represented by these values is consistent with the findings in the potentiodynamic polarization experiments. The EIS results also provide an additional support to the effect produced by 3DII as a surface modification technique in metal alloys. However, it is unmistakably difficult to determine which physicochemical mechanism activates in order to reduce the corrosive activity. Some authors have observed that nitrogen ion implantation in stainless steels leads to the formation of chromium nitride layers, thus improving the corrosion-resistant of the metal. Moreover, the neutralizing reaction in Equation (1) occurred upon the AISI 420 SS surface implanted with nitrogen in contact with the electrolyte can minimize reaction rates. Other works reported that the increase in defect density generated by the expansion of the lattice would reduce localized corrosion. Finally, the beneficial response of the radiation damage of certain materials exposed to ion implantation was more evident than the chemical effect itself (Muthukumaran *et al.*, 2010; Anandan *et al.*, 2007; Padhy *et al.*, 2010; Pereira *et al.*, 2017; Maleki-Ghaleh *et al.*, 2014; Fossati *et al.*, 2006).

Conclusions

The effect of 3DII as a surface modification technique on ferrous alloys was demonstrated through potentiodynamic analysis and EIS measurements. The nitrogen ion implantation applied on AISI 420 SS elements for a duration of 30 minutes and 90 minutes, and then exposed to a saline environment, demonstrated the following:

An improvement in the kinetic parameters was obtained from potentiodynamic analysis. It was determined that substrates implanted under such conditions increased the corrosion potential to nobler values and reduced the reaction rates. Remarkably, the corrosion current density values exhibited a direct correlation with the implantation time. Samples implanted for 30 minutes offered better corrosion properties than blanks. Likewise, samples implanted for 90 minutes offered the best protective properties against electrochemical attacks.

Following this comparison, the reactivity of the material in question was also evaluated through linear polarization resistance. These results validated the findings of the Tafel analysis by identifying the same linear tendency between the R_p and the treatment time. Due to a thicker film formed at higher implantation times, it was possible to obtain higher resistance values, thus delaying the charge transference or current density and then increasing corrosion resistance.

Despite the multilevel variation in the Bode diagrams, a better comparison could be observed in the Nyquist representations and the proposed equivalent circuits. A similar tendency was observed for both implanted and non-implanted samples. However, the resistance and capacitance magnitudes of the samples implanted for 90 minutes showed the best performance against electrochemical corrosion.

The general corrosion behavior demonstrated a significant enhancement after 3DII with the increase in treatment duration and/or implanted dose, thus producing thicker interfaces on AISI 420 SS and enhancing its protective properties against electrochemical corrosion.

Acknowledgements

This research work was supported by the laboratory of “Física y Tecnología del Plasma y Corrosión” and “Grupo de Investigaciones en Corrosión” from the “Universidad Industrial de Santander”. This work was partially financed by the Colombian agency Colciencias through doctoral scholarship 617.

References

- Abdi, F. and Savaloni, H. (2017). Surface nanostructure modification of Al substrates by N⁺ ion implantation and their corrosion inhibition. *Transactions of Nonferrous Metals Society of China*, 27(3), 701-710. 10.1016/S1003-6326(17)60078-5
- Abreu C. M., Cristóbal M. J., Merino P., Novoa X. R., Pena G., and Pérez M.C. (2008). Electrochemical behaviour of an AISI 304L stainless steel implanted with nitrogen. *Electrochimica Acta*, 53(20), 6000-6007. 10.1016/j.electacta.2008.03.064
- Anandan, C., William, V. L., Ezhil, S., and Rajam, K. S. (2007). Electrochemical studies of stainless steel implanted with nitrogen and oxygen by plasma immersion ion implantation. *Surface and Coatings Technology*, 201(18), 7873-7879. 10.1016/j.surfcoat.2007.03.034
- ASTM (2003). *G1-03 Standard practice for preparing, cleaning, and evaluating corrosion test specimens*. ASTM. 10.1520/G0001-03
- ASTM (2010). *G102-89 Standard practice for calculation of corrosion rates and related information from electrochemical measurements*. ASTM. 10.1520/G0102-89R10
- ASTM (2011a). *E3-11 Standard guide for preparation of metallographic specimens*. ASTM. 10.1520/E0003-11
- ASTM (2011b). *G5-94 Standard reference test method for making potentiostatic and potentiodynamic anodic polarization measurements*. ASTM. 10.1520/G0005-94R11E01
- ASTM (2015). *G106-89 Standard practice for verification of algorithm and equipment for electrochemical impedance measurements*. ASTM. 10.1520/G0106-89R15
- Borgioli, F., Galvanetto, E., and Bacci, T. (2019). Surface modification of austenitic stainless steel by means of low pressure glow-discharge treatments with nitrogen. *Coatings*, 9(10), 604. 10.3390/coatings9100604
- Bravo, E. and Vieira I. (2015). Influence of cerium ions and shelf-life of hybrid solution as pre-treatment for AA 2024 aluminium alloy on its anticorrosion performance. *Surface and Interface Analysis*, 48(8), 809-817. 10.1002/sia.5901
- Dearnaley, G. (1969). Ion Bombardment and implantation. *Reports on Progress in Physics*, 32(2), 405-491. 10.1088/0034-4885/32/2/301
- Dugar-Zhabon, V. D., Castro, B. J., Dulce Moreno, H. J., and Tsygankov P. A. (1999). Device JUPITER for ion implantation. *Revista Colombiana de Física*, 31(2), 181-184.
- Dugar-Zhabon, V. D., Dulce Moreno, J., and Tsygankov, P. A. (2002). High voltage pulse discharge for ion treatment of metals. *Review of Scientific Instruments*, 73, 828. 10.1063/1.1429785
- Fossati A., Borgioli, F., Galvanetto, E., and Bacci, T. (2006). Glow-discharge nitriding of AISI 316L austenitic stainless steel: influence of treatment time. *Surface & Coatings Technology*, 200(11), 3511-3517. 10.1016/j.surfcoat.2004.10.122
- Hannani, A. and Kermiche, F. (1998). The Electrochemical Behaviour of AISI 304 Stainless Steel Following Surface Modification by Ion Implantation. *Transactions of the IMF*, 76(3), 114-116, 10.1080/00202967.1998.11871208
- Jiménez-Morales, A., Galván J. C., Rodríguez R., and de Damborenea J. J. (1997). Electrochemical study of the corrosion behaviour of copper surfaces modified by nitrogen ion implantation. *Journal of Applied Electrochemistry*, 27, 550-557. 10.1023/A:1018446628256
- Leitao, E., Silva, R. A., and Barbosa, M. A. (1997). Electrochemical impedance spectroscopy of nitrogen- and carbon-sputter coated 316 L stainless steel. *Corrosion Science*, 39, 333-338. 10.1016/S0010-938X(97)83349-5
- Maleki-Ghaleh, J., Khalil-Allafi, M., Sadeghpour-Motlagh, M. S., Shakeri, S., Masoudfar, A., Farrokhi, Y., Beygi Khosrowshahi, A., Nadernezhad, M. H., Siadati, M.H., Javidi, M., and Shakiba, M. (2014). Effect of surface modification by nitrogen ion implantation on the electrochemical and cellular behaviors of super-elastic NiTi shape memory alloy. *Journal of Materials Science: Materials in Medicine*, 25(12), 2605-2617, 10.1007/s10856-014-5283-4
- Martínez-Orellana L., Pérez, F., and Gómez, C. (2005). The effect of nitrogen ion implantation on the corrosion behaviour of stainless steels in chloride media. *Surface and Coatings Technology*, 200(5-6), 1609-1615. 10.1016/j.surfcoat.2005.08.034
- Muthukumar, V., Selladura, V., Nandhakumar, S., and Senthilkumar, M. (2010). Experimental investigation on corrosion and hardness of ion implanted AISI 316L stainless steel. *Materials and Design*, 31(6), 2813-2817. 10.1016/j.matdes.2010.01.007
- National Research Council (1979). *Ion implantation as a new surface treatment technology*. The National Academies Press. 10.17226/19823
- Nunura, C. and Lecaros, C. (2015). Caracterización del acero inoxidable AISI 420 y los efectos de la presencia de carburos de cromo en la estructura martensítica. *Revista I+i, Investigación Aplicada e Innovación*, 9, 1-10. <https://www.tecsup.edu.pe/sites/default/files/page/file/revista/Volumen-9/Art-1.pdf>
- Olaya, J. J., Piratoba, U., and Rodil S. E. (2011). Resistencia a la corrosión de recubrimientos de CRN depositados por PVD con UBM: tecnología eficiente y ambientalmente limpia. *Revista Latinoamericana de Metalurgia y Materiales*, 31(1), 44-51. <https://www.rlmm.org/ojs/index.php/rlmm/article/viewFile/132/101>

- Padhy, N., Ningshen, S., Panigrahi, B. K., and Kamachi M. (2010). Corrosion behaviour of nitrogen ion implanted AISI type 304L stainless steel in nitric acid medium. *Corrosion Science*, 52(1), 104-112. 10.1016/j.corsci.2009.08.042
- Parada, F. F., Tsygankov P., Dougar-Zhabon, V., Peña, D., Coronado, J., Gonzales, J., and Valbuena-Niño E. D. (2019). Morphologic evaluation of silicon surface modified with titanium and titanium+nitrogen. *Acta Microscopica*, 28(2), 39-47. <https://acta-microscopica.org/acta/article/view/529>
- Peña D., Fontalvo P., Estupiñán H., Valbuena-Niño, E.D., and Vesga W. 2009. Evaluación experimental de la resistencia a la corrosión de un acero AISI-SAE 4140 implantado con iones de nitrógeno. *Dyna*, 76(159), 43-52. <https://revistas.unal.edu.co/index.php/dyna/article/view/13039>
- Pereira C., De Souza, F. S., Marin, G., Hickel, S. M., Bindera C., and Nelmo A. (2017). Corrosion resistance of low-carbon steel modified by plasma nitriding and diamond-like carbon. *Diamond & Related Materials*, 80, 54-161. 10.1016/j.diamond.2017.11.001
- Piratoba, U., Camargo, A., and Olaya J. J. (2010). Impedancia Electroquímica - Interpretación de diagramas típicos con circuitos equivalentes. *Dyna*, 77(164), 6975. <https://revistas.unal.edu.co/index.php/dyna/article/view/25578>
- Sanabria, F., Viejo, F., and Valbuena-Niño, E. D. (2019). Performance in saline environment of a carbon steel surface modified by three-dimensional ion implantation. *Journal of Physics: Conference Series*, 1403, 012015. 10.1088/1742-6596/1403/1/012015
- Sanabria, F., Valbuena-Niño, E. D., Rincón, M., Estupiñán, H. A., and Viejo, F. (2020). Surface evaluation of carbon steel doped with nitrogen ions. *Revista UIS Ingenierías*, 19(1), 205-212. 10.18273/revuin.v19n1-2020019
- Sanabria, F., Gil, L., Matos, C., and Valbuena-Niño E.D. (2019). Experimental evaluation on electrochemical corrosion of ion implanted medium carbon steel of titanium and titanium+nitrogen. *Acta microscopica*, 28(2), 72-85.
- Valbuena-Niño, E. D., Dulce, H. J., and Dugar-Zhabon, V. (2010). Characterization of AISI 4140 Steel Implanted by Nitrogen Ions. *Revista Colombiana de Física*, 42(3), 387-392. <http://revcolfis.org/ojs/index.php/rcf/article/view/420329.html>
- Valbuena-Niño, E. D., Dugar-Zhabon, V., Dulce Moreno, H. J., Peña Rodríguez, G., Garnica, H. A., and Tsygankov, P. (2012). Application of electric arc and high voltage simultaneous discharges for advanced superficial treatment of metals. *Revista Iteckne*, 9(1), 14-20.
- Valbuena-Niño E. D., Gil L., Hernández L., Barba-Ortega J. J., and Dougar-Zhabon V. (2016). Characterization of the alloy steel modified superficially with ions of titanium and nitrogen. *CT&F- Ciencia, Tecnología y Futuro*, 6(3), 135-146. 10.29047/01225383.14
- Valbuena-Niño, E. D., Gil, L., Hernández, L., and Sanabria, F. (2020). Corrosion resistance of a carbon-steel surface modified by three-dimensional ion implantation and electric arc. *Advances in Materials Research*, 9(1), 1-14. 10.12989/amr.2020.9.1.001
- Valbuena-Niño E. D., Peña D., Salinas D. V., and Chinchilla L. F. (2011). Modificación Superficial de un Acero AISI SAE 1045 mediante la implantación de iones de nitrógeno y titanio. *Revista Iteckne*, 8(1), 31-36. 10.15332/iteckne.v8i1.259
- Vasilescu, C., Drob, S. I., Calderón, J. M., Osiceanu, P., Popa, M. Vasilescu, E., and Marcu, M. (2015). Long-term corrosion resistance of new Ti-Ta-Zr alloy in simulated physiological fluids by electrochemical and surface analysis methods. *Corrosion Science*, 93, 310-323. 10.1016/j.corsci.2015.01.038
- Vladmir, I. K. and Tsygankov, P. A. (1997). The use of a high voltage discharge at low pressure for 3D ion implantation. *Surface and Coatings Technology*, 96(1), 68-74. 10.1016/S0257-8972(97)00117-5
- Voort, V., Lucas, G. M., and Manilova, E. P. (2004). Metallography and microstructures of stainless steels and maraging steels. *ASM Handbook: Metallography and Microstructures, International*, 9, 670-700. 10.31399/asm.hb.v09.a0003767
- Walsh, F. C., Ponce de León, C., Kerr, C., Court, S., and Barker, B. D. (2008). Electrochemical characterisation of the porosity and corrosion resistance of electrochemically deposited metal coatings. *Surface & Coatings Technology*, 202(21), 5092-5102. 10.1016/j.surfcoat.2008.05.008
- Was, G. S. (1990). Ion beam modification of metals: Compositional and microstructural changes. *Progress in Surface Science*, 32(3-4), 211-332. 10.1016/0079-6816(89)90005-1

Comparison of Treatments by Mercerization and Plasma Glow Discharge on Residues of the Amazon Chestnut Shell (*Bertholletia Excelsa*)

Comparación de tratamientos por mercerización y descarga intensa de plasma sobre residuos de la cáscara de castaña amazónica (*Bertholletia excelsa*)

Ximena Zapata-Londoño¹, James Janderson Rosero-Romo², Hugo Armando Estupiñán-Durán³

ABSTRACT

The chestnut shell from the Amazon region shared between Colombia, Brazil, and Perú is an abundant residue of the walnut used for obtaining food and cosmetic products. This residue is not yet usable due to the lack of knowledge of its properties and the environmental impact generated by its treatment through methods such as mercerization. This work presents the results of the characterization of Amazon chestnut shell residues treated by two methods, mercerization with NaOH solution and intense plasma discharge (Glow Discharge Plasma), in a reactor with argon gas in a 0,3 bar vacuum and discharge conditions of 80 mA and 600 s. The microstructural, morphological, topographic, and nanomechanical changes of the chestnut residues without treatment and with the two proposed treatments were evaluated by means of the μ Raman, scanning electron microscopy, and atomic force microscopy techniques. The results showed the effectiveness of the plasma method over the mercerization method at obtaining more crystalline cellulose structures due to the reduction of hemicellulose, lignin, and the aqueous phase of walnut shell waste.

Keywords: Amazonian chestnut, *Bertholletia excelsa*, cellulose, plasma glow discharge

RESUMEN

La cáscara de castaña proveniente de la región amazónica, compartida entre Colombia, Brasil y Perú, es un residuo abundante de la nuez empleada en la obtención de productos alimenticios y cosméticos. Este residuo no es utilizable por la falta de conocimiento de sus propiedades y del impacto ambiental generado por su tratamiento por métodos como la mercerización. En este trabajo se muestran los resultados de la caracterización de los residuos de cáscara de castaña amazónica tratados por dos métodos, mercerización con solución de NaOH y descarga intensa de plasma (*Glow Discharge Plasma*), en un reactor con gas de argón en un vacío de 0,3 bar y condiciones de descarga de 80 mA y 600 s. Los cambios microestructurales, morfológicos, topográficos y nanomecánicos de los residuos de castaña sin tratamiento y con los dos tratamientos propuestos se evaluaron mediante las técnicas de μ Raman, microscopía electrónica de barrido y microscopía de fuerza atómica. Los resultados mostraron la efectividad del método por plasma, por encima del método de mercerización, para la obtención de estructuras más cristalinas de celulosa debido a la reducción de la hemicelulosa, la lignina y la fase acuosa de los desechos de cáscara de nuez.

Palabras clave: castaña amazónica, *Bertholletia excelsa*, celulosa, descarga intensa de plasma

Received: April 27th, 2020

Accepted: May 4th, 2021

Introduction

Generating agricultural waste is inevitable, since a large amount of it can result from the harvest in the early stages of the food production chain, which causes environmental and economic problems in cultivation areas. For example, one of the main economic activities in the Brazilian Amazon region is the Brazilian nut, whose shelling stage is a process that generates large amounts of waste, representing 90% by volume of the chestnut crops (Cardozo *et al.*, 2014; de Souza, E. S., *et al.*, 2019). This product is part of the so-called 'dried fruits', which provide important nutritional benefits due to their high content of proteins, carbohydrates, unsaturated lipids, essential vitamins, and minerals (ARS-US, 2019). However, Brazilian nut harvesting maintains a constant demand in the international market.

Bertholletia excelsa is the scientific name by which this walnut species is known, according to its taxonomy and ecology.

¹Biological Engineering Student, Universidad Nacional de Colombia, Medellín, Colombia. Email: xzapatal@unal.edu.co

²Physical Engineer, Universidad Nacional de Colombia, Medellín, Colombia. M.Eng. in Engineering, Materials and processes, Universidad Nacional de Colombia, Medellín, Colombia. Email: jjroseror@unal.edu.co

³Metallurgical Engineer, Universidad Industrial de Santander, Colombia. M.Eng. in Engineering, Universidad Industrial de Santander, Colombia. Ph.D. in Chemical Engineering, Affiliation: Associate Professor, Universidad Nacional de Colombia, Medellín, Colombia. Email: haestupinand@unal.edu.co

How to cite: Zapata-Londoño, X., Rosero-Romo, J. J., and Estupiñán-Durán, H. A. (2022). Comparison of Treatments by Mercerization and Plasma Glow Discharge on Residues of the Amazon Chestnut Shell (*Bertholletia Excelsa*). *Ingeniería e Investigación*, 42(1), e86698. 10.15446/ing.investig.v42n1.86698



Attribution 4.0 International (CC BY 4.0) Share - Adapt

It belongs to the *Lecythidaceae* family, found mainly in the Brazilian Amazon and several South American countries such as French Guyana, Suriname, Bolivia, Venezuela, Perú, and Colombia, due to the fact that its growth is favored by sandy or clayey soils with good drainage. Furthermore, it is an endemic species, and it is impossible to domesticate, since it forms a natural balance dependent on rodents and specific organisms for pollination (Melo *et al.*, 2018). Additionally, this species is representative of the Amazonian tropical forest, not only for its economic and environmental importance, but also for its size (up to 50 m), with a trunk that reaches 2 m in diameter (Salo *et al.*, 2013). Its fruit is extremely hard, with a shape similar to that of coconut, and it can weigh up to 2 kg with 12 to 25 nuts inside, each with its own shell (Bonelli *et al.*, 2001).

The Brazilian nut shell is mainly composed of cellulose, lignin, and hemicellulose, so a convenient option to reduce the impact of generating unusable waste would be using it as a source for obtaining fibrils and/or cellulose nanocrystals, which is especially important for the multiple applications it can have in the paper, textile, food, and nanotechnology industries, given its use in the manufacture of bio-nanocomposites, pharmaceuticals, biomedical implants, medicines, among others; it is classified as a non-toxic, highly crystalline, hydrophilic material with outstanding mechanical properties, especially due to its high rigidity. (Naduparambath *et al.*, 2018; de Souza, A. G. *et al.*, 2019).

To produce cellulose from biowaste, it is necessary to eliminate hemicellulose, lignin, and other components present in the lignocellulosic material that are rigidly associated through non-covalent bonds and covalent cross linkages (Tezcan and Atici, 2017). Figure 1 shows the molecular scheme of a lignocellulosic biomass, where hemicellulose is a carbohydrate polymer in the form of a network that covers the cellulose, and lignin is a polymer with an aromatic structure of a hydrophobic nature located between cellulose and hemicellulose fibers (Jagtap *et al.*, 2018; Sun, *et al.*, 2016; Álvarez-Rodríguez *et al.*, 2012). Current methods for obtaining cellulose are based on delignifying, that is, eliminating lignin through chemical pretreatments such as acid hydrolysis, basic hydrolysis, high pressure steam, among others (de Souza E. S., *et al.*, 2019).

Basic hydrolysis is a very common method, also known as the 'mercerization method', used to remove lignin from plant fiber waste. During this process, lignin is generally reduced by means of diluted NaOH, causing the separation between the structural links of lignin and the carbohydrates found on the external surface of the biomass, given the increase in its internal surface area (swelling) (Jaramillo-Quiceno, 2016; Rosa *et al.*, 2010). One of the advantages of this method is the high efficiency in the solubilization of lignin. However, its treatment conditions imply the use of very expensive industrial equipment, as well as environmental and human health problems due to the use of chemical products (Tezcan and Atici, 2017).

Glow Discharge Plasma (GDP) is a new method for the surface treatment of materials. It is economic and friendly

to the environment, and it allows transforming the surface properties and sometimes of the interior mass of metals, polymers, elastomers, ceramics, etc. Surface cleaning, etching, crosslinking, and changes in the chemical structure are some of the most important modifications reported in materials treated with this technique (Vacková *et al.*, 2019). Its operation consists of introducing a sample into a vacuum chamber under the action of a high-energy ionized gas (plasma) produced by an electric field within the chamber. The sample of interest interacts with cold ions, high-energy electrons, free radicals, and ultraviolet radiation, thus generating changes in their properties. These modifications depend on the working parameters of the plasma equipment: voltage, type of gas used, pressure, and the polarity of the sample versus the polarity of the equipment. In a polymer, for example, when the electrons collide with the surface, a break in the bonds and the formation of different molecular structures take place (Tsai *et al.*, 2010). Different industries all over the world are planning to incorporate the modification of the surface properties of many materials into their production lines. This includes textiles, polymeric fibers, food, packaging, and other materials of an inorganic and organic nature. Therefore, the study of the transformation of the properties of plant waste is a great opportunity to explore a wide range of interesting applications.

Studying the impact of technologies for the treatment of these new materials, specifically in the modification of vegetable fibers from agro-industrial waste, is one of the objectives of this research, as well as presenting the comparative results obtained from the treatment by intense plasma discharge and the treatment by mercerization of residues of chestnut walnut shell fibers, with respect to changes in morphology, microstructure, and mechanical behavior.

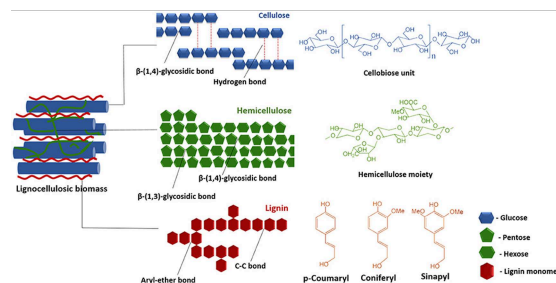


Figure 1. Molecular scheme of lignocellulosic biomass.

Experimental section

Materials and methods

The main objective of the methodological development proposed in this work was to prepare a useful residue extracted from the shell of the Amazonian chestnut using plasma glow discharge and mercerization treatments to compare the stiffness, morphological, topographic, and microstructural changes generated in the treated residues. To this effect, the collection and supply of seeds of the chestnut (*Bertholletia excelsa*) was carried out by residents of the jungle near the city of Leticia, located in the Colombian Amazon region.

These seeds, approximately 4 to 5 cm in diameter, were washed with distilled water and simultaneously brushed to remove any adhering organic residue, before manually separating the shell and the fruit from the seed. This procedure was performed with a hammer, with extreme caution to avoid mixing the fruit of the walnut with the macerated shell. The residues obtained were reduced in size using a mortar and then separated by means of granulometric sieves with a 106-micron mesh, thus obtaining three triplicate samples of approximately 0,5 g each for study. A group of three of these samples was labeled as 'untreated', and the other two groups of three samples were marked as 'mercerized' and 'plasma', respectively.

For the mercerization process of the walnut shell residues, NaOH solution was used. The variables established as preliminary control were NaOH concentration, temperature, exposure time, and fiber weight to NaOH solution ratio. Then, in the main experimental phase, these variables were assumed to be constant, according to previous works (Jaramillo-Quiceno, 2016). For this, 0,5 g of sample were treated at a concentration of 4% NaOH, a temperature of 40 °C for 2 h, and a fiber: solution ratio of 1:15. After this step, the sample was washed and filtered with 1% acetic acid in solution and then rinsed with distilled water to remove unreacted NaOH residues and water-soluble extracts. After this alkaline treatment, the fibers were dried in two stages, the first for 24 hours at room temperature, and the second at 70 °C for 48 h in a drying oven to remove as much moisture as possible.

A Quorum Technologies Q150R sputtering reactor, adapted for the GDP process, was used on the crushed walnut shell samples, with an atmosphere of argon ionizing gas at a vacuum pressure of 0,3 bar and additional operating conditions of 80 mA, under positive polarity conditions in the sample holder and 600 s of processing time.

Raman spectra of the shell samples with and without their corresponding treatments were obtained with a LabRam HR Evolution Horiba Scientific micro-Raman-Confocal spectrometer coupled with an Olympus BX41 light microscope with a 100X objective for the qualitative analysis of chemical structures. To this effect, 0,15 g of each sample were manually compacted to eliminate dispersions and placed on a glass slide. Scans were performed in a range of 50 cm^{-1} to 3 500 cm^{-1} with a 785 nm laser and an acquisition time of 6 s with 12 accumulations. The software used to determine the bands of interest and the corresponding processing of the spectra obtained was LabSpace6, along with its database, while also processing the spectra acquired with the baseline and the univariate method with Lorentian adjustment, in order to obtain intensity values with greater precision.

Images were obtained from 500X to 2000X with a SEM EVO MA10 Carl Zeiss scanning electron microscope operating at a voltage of 5 kV and a working distance of 8,5 mm. This allowed analyzing and comparing the morphology of chestnut shell residues with and without the mercerization and plasma treatments. The observed samples were pre-coated with a thin layer of 5 nm gold (measured with a piezoelectric device

conditioned in sputtering equipment), as is recommended for observing non-conductive samples in SEM.

Using the AFM Park Systems NX10 atomic force microscope in areas of 5 x 5 μm and 256 x 256 pixels, topography, dimensional distribution, and stiffness measurements of the treated and untreated chestnut shell residues were performed on the Pint Point scanning mode, with a tip on cantilever (reference NSC14 with a force constant of 5 N/m and a frequency of 160 KHz).

Results and discussion

The images of the untreated seeds and a scheme with the different stages of treatment are shown in Figure 2.

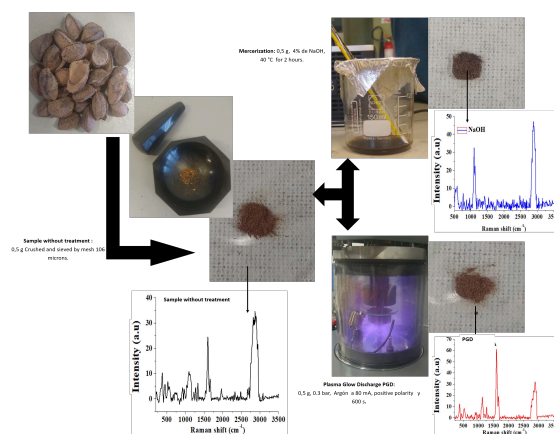


Figure 2. Chestnut husk treatments: a) Crushed and sieved, b) Mercerization, c) Plasma.

The untreated chestnut shell shows a brown color, which manifests itself in the aqueous solution resulting from the mercerization treatment with NaOH due to a partial elimination of lignin (Rosa *et al.*, 2010). This color change did not occur in the chestnut shell samples treated with discharge plasma.

Crystallinity in cellulose has an important effect on the physical, mechanical, and chemical properties of the fibers and microfibrils that constitute it. Similar works have found that a higher crystallinity increases tensile strength and gives greater dimensional stability and density to the fiber while decreasing properties such as chemical reactivity and swelling (Jaramillo-Quiceno, 2016; López-Durán *et al.*, 2018; Kathirselvam *et al.*, 2019). The Raman spectra of the fibers processed by mercerization and plasma, as well as of those unprocessed, are shown in Figures 3a, b, c, and d, where the variations in the intensity of the main bands represent, among other characteristics, changes in crystallinity and the reduction of lignocellulose from the residues of the Amazonian chestnut shell due to the treatments proposed in this research.

In Figure 3a, the predominant bands in the spectral region between 1 525 cm^{-1} and 1 700 cm^{-1} are presented, thus representing the aryl stretching vibration, which is symmetric and mainly associated with lignin; as well as a 1 599 cm^{-1} band whose attenuation indicates the delignification of the

fiber of shell residues from mercerization (Gierlinger *et al.*, 2013). In the Raman spectrum of plasma-treated fibers, the last band does not completely disappear; according to Segmehl *et al.* (2019), the typical distribution of lignin between hemicellulose and cellulose fibers is not uniform and, therefore, the location of the analyzed region is an important factor because there can be significant variations in the collected Raman signal. Taking this effect into account, the presented spectrum accounts for the average of several acquired. The bands of the spectra of the different analyzed samples located between 2 862 and 2 882 cm^{-1} represent the amorphous phase of cellulose, generally associated with the aqueous phase present in the residues. These bands decrease in intensity in the treated samples, mainly in the plasma-treated one. Table 1 shows the Raman band assignments for the Amazonian chestnut shell (*Bertholletia excelsa*).

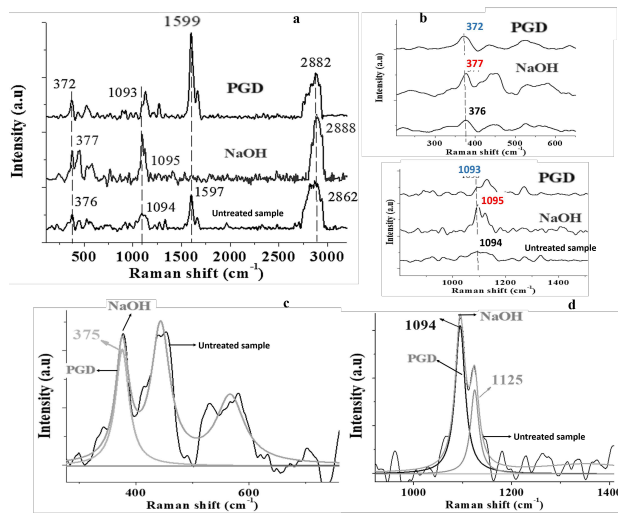


Figure 3. Raman spectra and Lorentzian adjustment: a) Raman spectra of chestnut fibers with and without mercerization and plasma treatments; b) Bands of interest for the analysis and adjustment to calculate the percentage of crystallinity; c-d) Lorentzian adjustment for bands 375 cm^{-1} and 1 094 cm^{-1} .

Figure 3b shows the bands of the Raman spectra representing the loss of cellulose in the untreated walnut shell fibers at 374 and 1 096 cm^{-1} , those treated by mercerization at 377 and 1 095 cm^{-1} , and those plasma-treated at 372 and 1 093 cm^{-1} . Figures 3c and d show spectra with these bands of interest with a Lorentzian-type fit. In Figure 3b, the Raman bands between 1 096 and 1 122 cm^{-1} are associated with the stretching of the typical glycosidic bond of cellulose. The spectra with Lorentzian analysis in Figure 3d show the definition of the bands at 1 094, 1 095, and 1 125 cm^{-1} , which represent partial and non-total loss of cellulose after the mercerization and plasma treatments. The transformation from type I to type II cellulose is generally related to the variation of the band at 380 cm^{-1} , according to studies carried out on fibers treated by mercerization with NaOH (Segmehl *et al.*, 2019). However, in this study, the position of this band for the three cases, 376, 377, and 372 cm^{-1} is relatively similar, although modifications to the bandwidth

are observed due to the defects induced from the treatments on the walnut shell fibers.

Table 1. Raman band assignments for Amazonian chestnut shell (*Bertholletia excelsa*) samples

Chemical species	Raman Shift (cm^{-1})	Band assignment
Lignin	1 599, 1 597	Aryl ring stretching, symmetric
Cellulose	372, 377, 376	β -D-glucosides
	1 093, 1 095, 1 094	C-O-C stretching, asymmetric
	1 122, 1 125	C-O-C stretching, asymmetric
Hemicellulose	2 882, 2 888, 2 862	C-H stretching

Source: Authors

Considering that the changes in cellulose crystallinity are attributed to the degradation of lignocellulose and hemicellulose, a method has been proposed to quantitatively determine these changes based on the ratio of the intensities of the bands at 380 and 1 096 cm^{-1} (I_{380}/I_{1096}) and a data treatment with univariate analysis to solve problems involving the presence of fluorescence in the spectra (Agarwal *et al.*, 2010; Agarwal *et al.*, 2013). Similar works to determine the crystallinity of cellulose fibers have used X-ray diffraction patterns, with discrepancies in the reliability of the results obtained when varying the size of the fibers (Carrión-Prieto *et al.*, 2019). Contrary to the spectra obtained in this study, due to the interaction of the signal that relates hemicellulose and pectin, a Raman dispersion can be produced, leading to an imprecise measurement of cellulose crystallinity (Anderson *et al.*, 2003). According to this method, to determine the percentage of crystallinity in the walnut shell cellulose fibers, four Raman spectra have been processed for each treatment for their respective calibration, thus obtaining values of I_{375}/I_{1094} . In this sense, Equation (1) has been used to obtain the percentage of crystallinity (X_{Raman}) of the samples not treated and treated by GDP and mercerization.

$$X_{\text{Raman}} = \frac{\left(\frac{I_{375}}{I_{1094}}\right) - 0,0375}{0,0214} \times 100 \quad (1)$$

The results of this analysis are presented in Table 2.

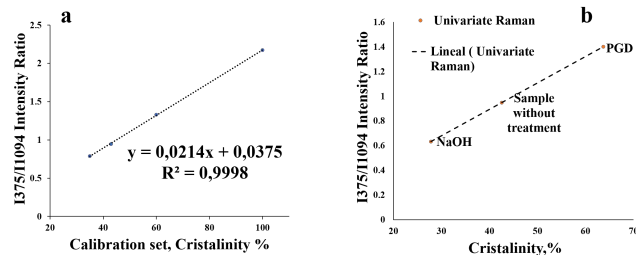
According to Table 2, the 1,5 value of I_{375}/I_{1094} reported for the sample treated by GDP (I_{372}/I_{1095}) represents the highest value of cellulose crystallinity with respect to the values of 0,62 and 0,94 reported for the samples treated by mercerization and without treatment, respectively. The presence of the Raman spectral band at 1 599 cm^{-1} corresponding to the structural vibration of lignocellulose in untreated and plasma-treated walnut shell microfibers, which does not appear in the sample treated by mercerization, affects the value of the intensity of the band at 1 094 cm^{-1} , whose value is higher in the sample treated by mercerization. Figure 4 shows the calibration graph of the four spectra taken in each sample, as well as the graph that relates the percentages of crystallinity vs. the calculated I_{375}/I_{1094} ratio.

According to the graph in Figure 4b, shown in ascending order by the degree of crystallinity, the walnut shell fibers treated by mercerization had a value of 27%, 42% for the sample

Table 2. Raman intensity values and I_{375}/I_{1094} ratio for the calculation of the X_{Raman} crystallinity factor

SAMPLE	Raman Shift (cm^{-1})	Intensity (a.u)	I_{375}/I_{1094}	X_{Raman} (%)
Treated with NaOH	377, 1 095	20, 32	0,62	27,82
Treated with GDP	372, 1 095	12, 8	1,5	63,71
Without treatment	376, 1 093	10, 25	0,94	42,55

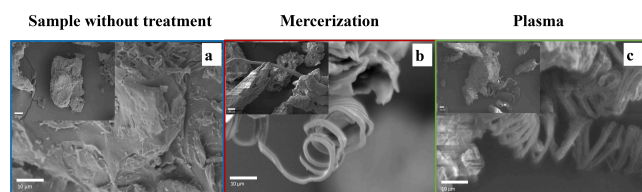
Source: Authors

**Figure 4.** a) Graph showing the relationship between the crystallinity of the calibration set versus the Raman intensity ratio I_{375}/I_{1094} ; b) Graph that relates the crystallinity of each sample with the Raman intensities I_{375}/I_{1094} with univariate analysis.

without treatment, and 64% for the fiber treated by GDP. These values, as well as the I_{375}/I_{1094} ratio, probably show some dispersion due to the presence of lignocellulose, which especially affects the band associated with microcrystalline cellulose at 1095 cm^{-1} . This band has been used for the study of mechanical properties in vegetable fibers, specifically for changes in viscoelastic properties (Eichhorn and Young, 2001).

Morphological description of the fibers by Scanning Electron Microscopy (SEM)

Figure 5 shows the SEM images of the fibers with and without the treatments. The surfaces of the shell residues have rough and porous shapes, thus evidencing the presence of amorphous regions associated with morphologies other than cellulose, such as lignin and hemicellulose (Figure 5a and b). In the fibers treated by that mercerization and GDP, the size of the cellulose microfibrils was identified between $1,5$ and $2,5 \mu\text{m}$.

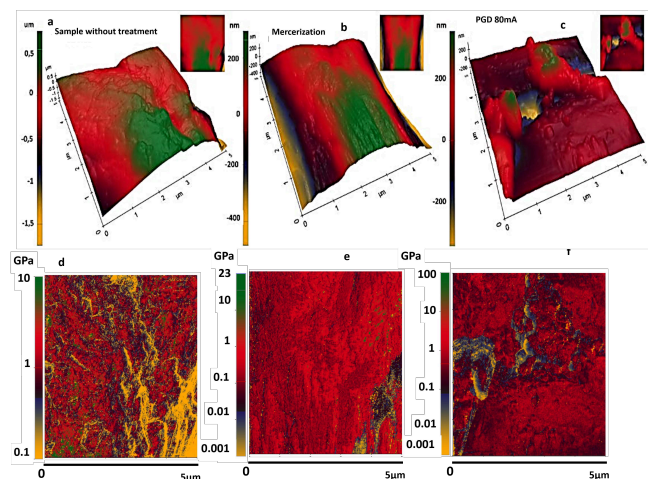
**Figure 5.** Morphological analysis: a) Image of the sample without treatment; b) Chestnut husk fibers with mercerization treatment in NaOH; c) Chestnut fibers with 80 mA plasma treatment.

Likewise, Rosa *et al.* (2010), in their research on coconut shells, related what was observed in SEM images with the partial removal of impurities (lignin, hemicellulose, and other compounds present in the shell) based on partial

fibrillation, unlike the untreated sample. Results obtained by the μRaman Spectroscopy technique of the plasma-treated samples are characterized by the presence of bands associated with cellulose, which are more defined than the bands of the samples without treatment. However, in both the mercerization and plasma treatment, they showed a level of partial defibrillation with a still compact morphology, similar to the morphology of the samples without treatment (according to the comparison in Figure 5a, b, and c), thus corroborating the results showing the Raman bands associated with lignin. In addition to this comparative analysis, it should be noted that the chestnut walnut shell sample with the highest defibrillation was the plasma-treated one, where long, continuous, spirally wound shapes of fibers of approximately $2,5 \mu\text{m}$ of diameter were observed.

Atomic Force Microscope (AFM)

Figure 6a shows the topographic characteristics of a walnut shell sample without any treatment, and Figures 6b and c, the topography images of the samples treated by mercerization and plasma, respectively. From this characterization, roughness measurements in $R_a (\mu\text{m})$ were obtained, observing a decrease in this value for the samples treated by mercerization and by plasma in their order.

**Figure 6.** AFM images of topography (3D) and stiffness (2D): a) untreated sample topography, b) mercerization-treated sample topography, c) plasma-treated sample topography, d) Stiffness image for untreated sample, e) Stiffness image for sample treated by mercerization, f) Stiffness image for sample treated by plasma.

This aspect is associated with the effect of mercerization and plasma treatment on the removal of cementitious material from the walnut shell or the structure of its first amorphous region, which is mainly composed of hemicellulose and lignin, which corroborates the results obtained through Raman and SEM imaging. The decrease in the roughness of the surfaces of the walnut shells after plasma treatment is caused by the breakdown of the amorphous structures of hemicellulose and lignin that are present in the primary layer of microfibrils, thus exposing a secondary layer rich in cellulose crystalline

and with a smooth topography. Table 3 shows the values of roughness R_a (μm) and stiffness (GPa) obtained.

Table 3. Roughness R_a (μm) and Stiffness (GPa) values for chestnut nut fibers without treatment and with treatment

SAMPLE	R_a (μm)	Stiffness (GPa)
Treated with NaOH	$0,137 \pm 0,013$	$11,55 \pm 0,2$
Treated with GDP	$0,071 \pm 0,01$	$88,4 \pm 0,2$
Without treatment	$0,193 \pm 0,010$	$5,94 \pm 0,3$

Source: Authors

Figures 6d, e, and f refer to the images acquired by the AFM's Pin-Point mode, showing the variation of the stiffness on the surface ($5 \times 5 \mu\text{m}$) of the walnut shell residues. In the gray bar, the different color tones ranging from light gray, medium light gray, medium dark gray, and dark gray indicate the variation of stiffness in the range of 0,001 to 100 GPa. Medium dark gray and dark gray represent the areas with the highest stiffness distribution in the walnut shell residues and the most representative of the physical-mechanical changes manifested from the treatments developed in this research. In the untreated walnut shell samples, this zone appears between 0,7 and 7 GPa, with the notable presence of less rigid zones (between 0,1 and 0,7 GPa) in a light gray color tone. In Figure 6e (a sample treated by mercerization), the stiffer zones appear between 0,05 and 8 GPa, with a small distribution of less rigid structures between 0,001 and 0,3 GPa (light gray color tone). For the plasma-treated walnut shell sample shown in Figure 6f, values between 0,09 and 35 GPa represent areas of higher rigidity, and those between 0,001 and 0,09 GPa correspond to less rigid areas.

Treatment processes in vegetable fibers, especially mercerization, generally produce lignin and hemicellulose removal effects on the fibers (Cheng and Wang, 2008; Cousins, 1978). While comparing the stiffness results of the different treated and untreated walnut shell samples, it was observed that the most notable changes occurred in the GDP-treated samples. From the process by plasma in vegetable fibers, it is known that the decrease in cellulose, hemicellulose, and lignin is caused by the breakdown of the glucoside bonds of cellulose, of the sugars present in the structure of hemicellulose, and the carboxylic and hydroxyls bonds in cellulose, thus generating a molecular restructuring of the carbon covalent bonds of the fibers with respect to oxygen ions. This causes important changes in the stiffness of the treated structures. Several studies have reported that the increase in stiffness is associated with a more crystalline structuring of cellulose microfibrils, which is consistent with the results obtained by AFM imaging, the morphological and structural changes observed in the SEM characterization, and the analysis of the spectral bands obtained by Raman (Marcuello *et al.*, 2019).

In the third column of Table 3, the stiffness values obtained by analysis in the AFM XEI software are shown. This procedure consists of processing the images acquired and shown in Figure 6d-f to obtain an arithmetic average in GPa of the selected region. A higher average stiffness value was found

in the plasma-treated samples, which matches the values analyzed in the gray tone bands of their respective images. An important aspect to consider when processing the fibers with plasma is the drastic decrease in the humidity of the fibers due to the vacuum of the procedure. This reduces their viscoelastic properties, with the obvious consequence of increasing the rigidity of the walnut shell. This behavior was also observed in the samples treated by mercerization, which presented a stiffness value of twice that of the samples without treatment and almost eight times less than that of the samples treated with plasma. In general terms, the increase in the level of crystallinity and the stiffness of the walnut shell fibers is a consequence of the covalent molecular restructuring of the carbon and oxygen bonds of the fibers, in addition to the decrease in the aqueous phase (Marcuello *et al.*, 2019).

Conclusions

Both the mercerization and plasma treatment on the Amazonian chestnut walnut shell generated the release of agglomerated cellulose microfibrils in spirals with diameters between 1,5 and 2,5 μm , according to the SEM image analysis. The Raman spectra for both treatments used in this research showed bands associated with the presence of cellulose, with the disappearance of the 1599 cm^{-1} band related to lignin degradation, with a greater effect in the treatment by mercerization than by plasma.

Additionally, the calculation of the crystallinity index proposed in this work with the relation of intensities associated with cellulose showed a significant increase in crystallinity for plasma-treated samples compared to the untreated samples, as well as a decrease in crystallinity in the sample treated by mercerization, which indicates a transformation effect based on the breakdown and covalent restructuring of carbon-oxygen bonds in the fibers treated by plasma, and a structural breakdown effect with a low level of reconstitution for the mercerization treatment.

In addition to this, the plasma treatment decreased the aqueous phase associated with cellulose, hemicellulose, and amorphous lignin, thus affecting the original viscoelastic properties of the chestnut shell residues and increasing their rigidity, as evidenced in the results obtained by AFM on the Pin-Point itinerant contact mode. However, an important effect must be added to the increase in the rigidity of the shell, based on the restructuring of the carbon-oxygen bonds that occurs after the removal of the first amorphous wall of hemicellulose and lignin, which exposes a second wall composed of crystalline cellulose, partially free of these amorphous substructures. This was an important factor for the decrease in the roughness of the structure treated by plasma.

References

- Agarwal, U., Reiner, R. S., and Ralph, S. A. (2010). Cellulose I crystallinity determination using FT-Raman spectroscopy: univariate and multivariate methods. *Cellulose*, 17, 721-733. 10.1007/s10570-010-9420-z
- Agarwal, U. P., Reiner, R. R., Ralph, S. A., Forest, A., Gi, O., and Drive, P. (2013). Estimation of Cellulose Crystallinity of Lignocelluloses Using Near-IR. *Journal of Agricultural and Food Chemistry*, 61, 103-113. 10.1021/jf304465k
- Bonelli, P., Della Rocca, P., Cerrella, E., and Cukierman, A. (2001). Effect of pyrolysis temperature on composition, surface properties and thermal degradation rates of Brazil Nut shells. *Bioresource Technology*, 76(1), 15-22. 10.1016/S0960-8524(00)00085-7
- Álvarez Rodríguez, A., Pizarro-García, C., and Folgueras-Díaz, M.-B. (2012). Caracterización química de biomasa y su relación con el poder calorífico. *Repositorio Institucional de La Universidad de Oviedo*, 1-12. https://digibuo.uniovi.es/dspace/bitstream/handle/10651/17777/TFM_Ana_AlvarezProteg.pdf;jsessionid=61CEC16628EFBE55B4399447CD243E32?sequence=6
- Cardozo, E., Erlich, C., Alejo, L., and Fransson, T. H. (2014). Combustion of agricultural residues: An experimental study for small-scale applications. *Fuel*, 115, 778-787. 10.1016/J.FUEL.2013.07.054
- Cheng, Q. and Wang, S. (2008). A method for testing the elastic modulus of single cellulose fibrils via atomic force microscopy. *Composites Part A*, 39(12), 1838-1843. 10.1016/j.compositesa.2008.09.007
- Cousins, W. J. (1978). Young's modulus of hemicellulose as related to moisture content. *Wood Science and Technology*, 12(3), 161-167. 10.1007/BF00372862
- Eichhorn, S. J. and Young, R. J. (2001). The Young's modulus of a microcrystalline cellulose. *Cellulose*, 8, 197-207. 10.1023/A:1013181804540
- Hepworth, D. and Bruce, D. (2000). The Mechanical Properties of a Composite Manufactured from Non-Fibrous Vegetable Tissue and PVA. *Composites Part A: Applied Science and Manufacturing*, 31(3), 283-285. 10.1016/S1359-835X(99)00100-1
- Gierlinger, N., Keplinger, T., Harrington, M., and Schwanninger, M. (2013). *Raman Imaging of Lignocellulosic Feedstock*. IntechOpen. 10.5772/50878
- Baruah, J., Nath, B. K., Sharma, R., Kumar, S., Deka, R. C., Baruah, D. C., and Kalita, E. (2018). Recent Trends in the Pretreatment of Lignocellulosic Biomass for Value-Added Products. *Frontiers in Energy Research*, 6, 141. 10.3389/fenrg.2018.00141
- Jaramillo-Quiceno, N. (2016). *Efecto del proceso de mercerización en el comportamiento de la fibra de hoja de piña (FHP) como refuerzo en una matriz de polipropileno*. <https://www.semanticscholar.org/paper/Efecto-del-proceso-de-mercerizaci%C3%B3n-en-el-de-la-de-Quiceno/13945ae8739e1372c068a89d71cd96e6d9a896ac>
- Kathirselvam, M., Kumaravel, A., Arthanarieswaran, V. P., and Saravanakumar, S. S. (2019). Isolation and characterization of cellulose fibers from *Thespesia populnea* barks: A study on physicochemical and structural properties. *International Journal of Biological Macromolecules*, 129, 396-406. 10.1016/j.ijbiomac.2019.02.044
- López-Durán, V., Larsson, P. A., and Wågberg, L. (2018). Chemical modification of cellulose-rich fibres to clarify the influence of the chemical structure on the physical and mechanical properties of cellulose fibres and thereof made sheets. *Carbohydrate Polymers*, 182, 1-7. 10.1016/j.carbpol.2017.11.006
- Marcuello, C., Foulon, L., Chabbert, B., Aguié-béghin, V., and Molinari, M. (2019). Young's modulus of lignocellulosic polymers and their adhesion with. *International Journal of Biological Macromolecules*, 147, 1064-1075. 10.1016/j.ijbiomac.2019.10.074
- Melo, V. F., Batista, A. H., Barbosa, J. Z., Barbeiro, L., Gomes, R., and Dutra, M. T. M. (2018). Soil quality and reforestation of the Brazil nut tree (*Bertholletia excelsa* Bonpl.) after laterite-type bauxite mining in the Brazilian Amazon forest. *Ecological Engineering*, 125, 111-118. 10.1016/j.ecoleng.2018.10.016
- Naduparambath, S., Jinitha, T. V., Shaniba, V., Serejith, M. P., Balan, A. K., and Purushothaman, E. (2018). Isolation and characterization of cellulose nanocrystals from sago seed shells. *Carbohydrate Polymers*, 180, 13-20. 10.1016/J.CARBPOL.2017.09.088
- Carrión-Prieto, P., Martín-Ramos, P., Hernández-Navarro, S., Sánchez-Sastre, L. F., Marcos-Robles, J. L., and Martín-Gil, J. (2019). Crystallinity of cellulose microfibrils derived from *Cistus ladanifer* and *Erica arborea* shrubs. *Maderas. Ciencia y tecnología*, 21(4), 447-456. 10.4067/S0718-221X2019005000402
- Rodríguez-Álvarez, A., Pizarro, C., and Folgueras, M. (2012). Caracterización Química De Biomasa Y Su Relación. *Universidad de Oviedo*. https://digibuo.uniovi.es/dspace/bitstream/handle/10651/17777/TFM_Ana_AlvarezProteg.pdf;jsessionid=61CEC16628EFBE55B4399447CD243E32?sequence=6
- Rosa, M. F., Medeiros, E. S., Malmonge, J. A., Gregorski, K. S., Wood, D. F., Mattoso, L. H. C., Glenn, G., Orts, W. J., and Imam, S. H. (2010). Cellulose nanowhiskers from coconut husk fibers: Effect of preparation conditions on their thermal and morphological behavior. *Carbohydrate Polymers*, 81(1), 83-92. 10.1016/j.carbpol.2010.01.059
- Salo, M., Sirén, A., and Kalliola, R. (2013). Collect Locally, Eat Globally – The Journey of the Brazil nut. *Diagnosing Wild Species Harvest*, 2013, 143-160. 10.1016/B978-0-12-397204-0.00008-5
- Segmehl, J. S., Keplinger, T., Krasnobaev, A., Berg, J. K., Willa, C., and Burgert, I. (2019). Facilitated delignification in CAD deficient transgenic poplar studied by confocal Raman spectroscopy imaging. *Spectrochimica Acta Part A: Molecular and Biomolecular Spectroscopy*, 206, 177-184. 10.1016/j.saa.2018.07.080

- de Souza, A. G., Rocha, D. B., Kano, F. S., and Rosa, D. d. S. (2019). Valorization of industrial paper waste by isolating cellulose nanostructures with different pretreatment methods. *Resources, Conservation and Recycling*, 143, 133-142. 10.1016/j.RESCONREC.2018.12.031
- de Souza, E. S., Dias, Y. N., da Costa, H. S. C., Pinto, D. A., de Oliveira, D. M., de Souza Falção, N. P., Texeira, R. A., and Fernandes, A. R. (2019). Organic residues and biochar to immobilize potentially toxic elements in soil from a gold mine in the Amazon. *Ecotoxicology and Environmental Safety*, 169, 425-434. 10.1016/j.ECOENV.2018.11.032
- Sun, S., Sun, S., Cao, X., and Sun, R. (2016 delete that). The role of pretreatment in improving the enzymatic hydrolysis of lignocellulosic materials. *Bioresource Technology*, 199, 49-58. 10.1016/j.biortech.2015.08.061
- Tezcan, E. and Atici, O. G. (2017). A new method for recovery of cellulose from lignocellulosic bio-waste: Pile processing. *Waste Management*, 70, 181-188. 10.1016/J.WASMAN.2017.09.017
- Tsai, G., Montero, J., Calle, W., Quinde, M., and Sarmiento, P. (2010). Plasma: una tecnología de gran potencial para la industria y la ciencia. *Ingenius*, 4, 66-72. 10.17163/ings.n4.2010.07
- U.S. Department of Agriculture (2010). *National Nutrient Database for Standard Reference, Food, nut and seed products Group: 12*. <https://fdc.nal.usda.gov/ndb/search/list%20United>
- U.S. Department of Agriculture, Agricultural Research Service (ARS-US) (2019). *Food Data Central*. <https://fdc.nal.usda.gov>
- Vacková, T., Špatenka, P., and Balakrishna, S. (2019). Plasma Treatment of Powders and Fibers. In Thomas, S., Mozetič, M., Cvelbar, U., Špatenka, P., and Praveen, K. M. (Eds.) *Non-Thermal Plasma Technology for Polymeric Materials* (pp. 193-210). Elsevier. 10.1016/b978-0-12-813152-7.00007-x

COVID-19 Diagnosis with Deep Learning

Diagnóstico de COVID-19 con *Deep Learning*

Hatice Catal Reis ¹

ABSTRACT

The coronavirus disease 2019 (COVID-19) is fatal and spreading rapidly. Early detection and diagnosis of the COVID-19 infection will prevent rapid spread. This study aims to automatically detect COVID-19 through a chest computed tomography (CT) dataset. The standard models for automatic COVID-19 detection using raw chest CT images are presented. This study uses convolutional neural network (CNN), Zeiler and Fergus network (ZFNet), and dense convolutional network-121 (DenseNet121) architectures of deep convolutional neural network models. The proposed models are presented to provide accurate diagnosis for binary classification. The datasets were obtained from a public database. This retrospective study included 757 chest CT images (360 confirmed COVID-19 and 397 non-COVID-19 chest CT images). The algorithms were coded using the Python programming language. The performance metrics used were accuracy, precision, recall, F1-score, and ROC-AUC. Comparative analyses are presented between the three models by considering hyper-parameter factors to find the best model. We obtained the best performance, with an accuracy of 94,7%, a recall of 90%, a precision of 100%, and an F1-score of 94,7% from the CNN model. As a result, the CNN algorithm is more accurate and precise than the ZFNet and DenseNet121 models. This study can present a second point of view to medical staff.

Keywords: COVID-19, deep learning, convolutional neural network, Zeiler and Fergus network, dense convolutional network-121

RESUMEN

La enfermedad del coronavirus 2019 (COVID-19) es fatal y se está propagando rápidamente. La detección y el diagnóstico tempranos de la infección por COVID-19 evitarán la propagación rápida. Este estudio tiene como objetivo detectar COVID-19 automáticamente a partir del conjunto de datos de tomografía computarizada de tórax (TC). Se presentan los modelos estándar para la detección automática de COVID-19 utilizando imágenes de TC de tórax sin procesar. El estudio consta de arquitecturas de red neuronal convolucional (CNN), red Zeiler y Fergus (ZFNet) y red convolucional densa-121 (DenseNet121) de modelos de redes neuronales convolucionales profundas. Los modelos propuestos se presentan para proporcionar diagnósticos precisos para clasificación binaria. Los conjuntos de datos se obtuvieron de una base de datos pública. Este estudio retrospectivo incluyó 757 imágenes de TC de tórax (360 imágenes de TC de tórax COVID-19 confirmadas y 397 imágenes no COVID-19). Los algoritmos se codificaron utilizando el lenguaje de programación Python. Los parámetros de desempeño que se utilizaron fueron exactitud, precisión, recuperación, puntaje-F1 y ROC-AUC. Se presentan análisis comparativos entre los tres modelos considerando factores de hiperparámetros para encontrar el mejor modelo. Obtuvimos el mejor rendimiento, con exactitud del 94,7 %, recuperación del 90 %, precisión del 100 % y puntuación-F1 del 94,7 % del modelo de CNN. Como resultado, el algoritmo de CNN es más exacto y preciso que los modelos ZFNet y DenseNet121. Este estudio puede presentar un segundo punto de vista al personal médico.

Palabras clave: COVID-19, deep learning, red neuronal convolucional, red Zeiler y Fergus, red convolucional densa-121

Received: July 2nd, 2020

Accepted: April 20th, 2021

Introduction

Machine-learning (ML) techniques have been used in medical imaging and infectious disease diagnosis (Lundervold and Lundervold, 2019; Chen *et al.*, 2016; Ardabili *et al.*, 2020). The coronavirus disease 2019 (COVID-19), which started to spread from Wuhan (China), as of the end of December 2019 (Zhu *et al.*, 2020; Huang *et al.*, 2020), has affected the whole world. According to the updated data, there have been more than 134 957 021 confirmed cases and 2 918 752 confirmed deaths because of COVID-19 in 223 countries as of 11 April 2021 (WHO, 2021). Coronaviruses (CoVs) are related to zoonotic viruses that can cause disease in mammal or bird species (Tezer and Bedir Demirdag, 2020). Various medical approaches are available to diagnose and detect COVID-19 in patients, such as the transcription-polymerase chain reaction (RT-PCR) test kits (Ai *et al.*, 2020) and chest

computed tomography (CT) images. Chest CT scans have played a vital role in diagnosis during this pandemic (Akca *et al.*, 2020; Bao *et al.*, 2020; Chung *et al.*, 2020; Lei *et al.*, 2020). Early detection, diagnosis, isolation, and treatment are critical to preventing further spread of the disease (Guner *et al.*, 2020). In some cases, real-time polymerase chain reactions can give incorrect or inadequate information (Ai *et al.*, 2020). It is critical to develop cost-effective and accurate

¹Ph.D. in Geomatics Engineering, Yildiz Technical University, Turkey. Affiliation: Assistant Professor, Department of Geomatics Engineering, Gumushane University, Gumushane, Turkey. E-mail: hatice.catal@yahoo.com.tr

How to cite: Catal Reis, H. (2022). COVID-19 Diagnosis with Deep Learning. *Ingeniería e Investigación*, 42(1), e88825. 10.15446/ing.investig.v42n1.88825



Attribution 4.0 International (CC BY 4.0) Share - Adapt

detection methods that all countries can benefit from. Deep learning (DL) is a part of machine learning (Deng, 2014). Recently, this technique has shown effective performance in the field of medical image processing. DL-based research has been presented for the detection of COVID-19. This includes artificial neural networks (ANN), convolutional neural networks (CNN), recurrent neural networks (RNN, a hybrid classifier architecture) (Goreke *et al.*, 2021); ResNet50, InceptionV3, and InceptionResNetV2 (Narin *et al.*, 2020); nCOVnet (Panwar *et al.*, 2020); DarkCovidNet (Ozturk *et al.*, 2020); VGG-19 (Ioannis and Bessiana, 2020); COVID-NET (Wang and Wong, 2020); and Xception and ResNeXt (Jain *et al.*, 2021) models using X-ray images. At the same time, studies that detect COVID-19 using CT images have been presented in the literature. AlexNet, VGG-16, VGG-19, SqueezeNet, GoogLeNet (Ardakani *et al.*, 2020), ResNet-50 as a specific model (Li *et al.*, 2020), DenseNet (Yang *et al.*, 2020), and DenseNet201 (Jaiswal *et al.*, 2020) algorithms have used CT images for COVID-19 detection and diagnosis. Although there are studies on the subject, there is still insufficient literature. Deep learning algorithms can help develop a new useful diagnosis and management system for COVID-19 cases. In this study, we have proposed three models for an automatic prediction of COVID-19 using DL-based using chest CT images. The proposed models have an end-to-end architecture that uses feature extraction methods and raw chest-CT images for analysis. These models are a customized CNN, ZFNet, and DenseNet121. We reached this accuracy by means of a large-size dataset and multi-layer models. Along with the customized CNN model, we proposed a small-size nonstandard dataset.

Radiologists have to be pioneers in medical imaging and interpretation during the COVID-19 pandemic, but the medical staff are currently under heavy workloads. Therefore, DL-based approaches can help contribute to the medical system and offer a secondary perspective.

This study is organized as follows: in section 2 (Materials and methods), we give a short overview of the literature in deep learning and the proposed models; we describe how we obtained the dataset, and we present architecture charts and plots. Then, we provide a statistical analysis. In section 3 (Results), we show the results of the experiment. After that, we discuss and interpret the obtained results and conclusions.

Materials and methods

In this section, we define the dataset used in the study for DL. The second part is followed by the proposed CNN, ZFNet, and DenseNet121. It compares the performance of these three models. We built DL-based platforms for automatic detection and prediction of COVID-19 (Figure 1).

Deep learning is a subclass of machine learning and is the most popular approach in artificial intelligence applications (LeCun *et al.*, 2015). DL is a method that imitates the human brain in the use of information and aims for new approaches in complex data solutions. The most important feature that distinguishes deep learning from traditional neural networks

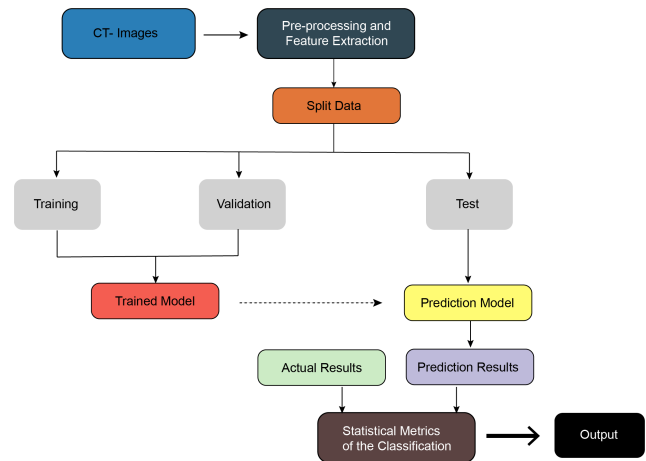


Figure 1. A schematic presentation of the study.

Source: Author

is that it has more than one hidden layer (Sejnowski and Tesauro, 1989). Generally, the architecture of convolutional neural networks consists of input, convolution, pooling, convolution, pooling, fully connected, fully connected, and output prediction (Pouyanfar *et al.*, 2018).

The data were downloaded and used from the GitHub public database. The COVID-CT-Dataset has 360 CT images containing clinical findings of COVID-19 from 216 patients and 397 non-COVID-19 CT images (Github/UCSD-AI4H, 2020). No human and no animal rights were violated. The research was performed according to the principles of the Declaration of Helsinki. We used the Keras deep learning library with the TensorFlow backend to implement deep learning models (Figure 3). This study was done on a personal laptop equipped with an Intel i5 processor, 6 GB of RAM, and a GTX 940MX NVidia GPU with 2GB of VRAM. Table 1 shows the DL methods used and statistics of the dataset for chest CT images.

Table 1. Statistics of the dataset

Models	Target	Training	Validation	Test	T
	images				
CNN	Covid-19	321	19	20	360
	Non-Covid-19	360	19	18	397
	Total	681	38	38	757
ZFNet	Covid-19	324	17	19	360
	Non-Covid-19	357	21	19	397
	Total	681	38	38	757
DenseNet121	Covid-19	325	18	17	360
	Non-Covid-19	356	20	21	397
	Total	681	38	38	757

Source: Author

A chest CT dataset was used (Figure 2), which was obtained with different techniques and did not have standard features. Therefore, all images were pre-processed.

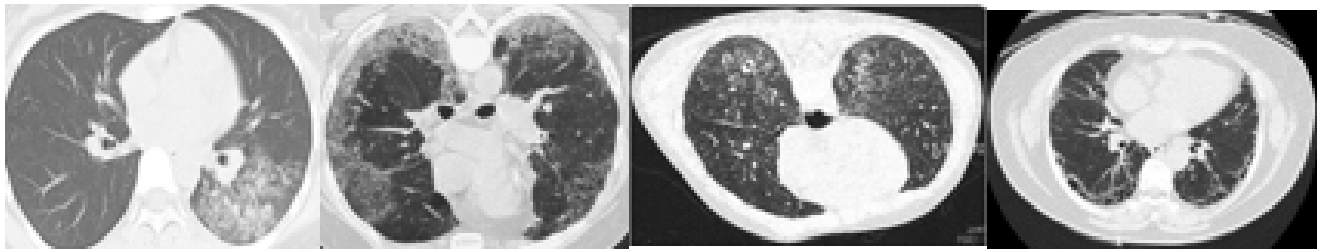


Figure 2. Raw chest CT image samples.

Source: Author

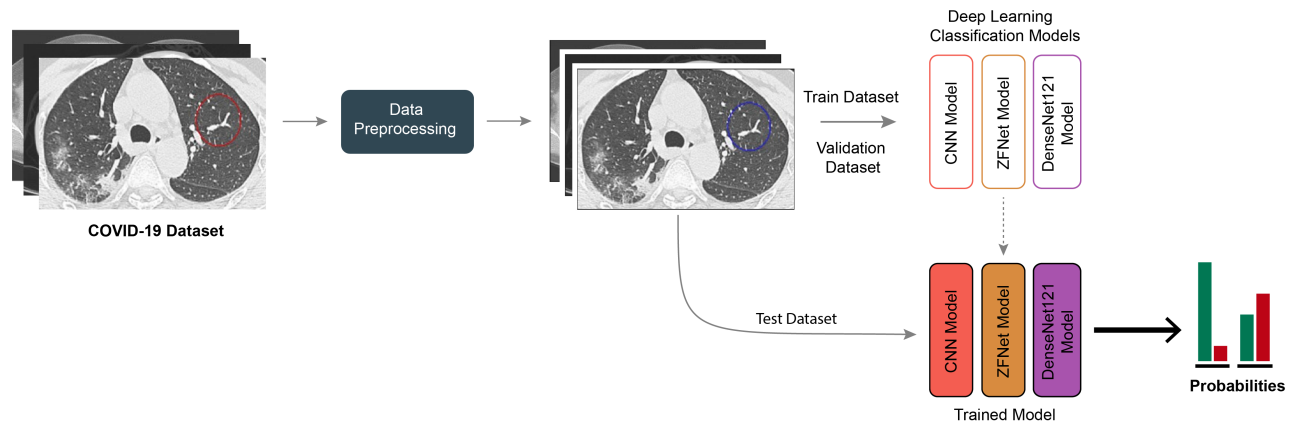


Figure 3. Deep learning algorithm framework.

Source: Author

Problem solving with the help of deep learning is equivalent to optimally designing a multi-layered network structure. The raw CT dataset and 100 epochs were used as the input layer in our study (Figures 4 to 6). BatchNormalization caused the model to learn better during training, and it also positively affected the stability of the network.

CNNs have been used in imaging-based classification in various medical areas (Lakhani and Sundaram, 2017; Esteva *et al.*, 2017). They have been significantly practiced in medical image processing to develop health research (Choe *et al.*, 2019). CNNs are a kind of artificial neural network with multiple layers contributing to high accuracy and cost reduction in its large datasets (Panwar *et al.*, 2020). The customized CNN's architecture contains 3 layers instead of 2 in the 2-3-4 layers (Figure 4). Therefore, we increased the model's performance in terms of accuracy.

Performance measures

This study used the receiver operating characteristic (ROC) curve to evaluate classifier output quality. ROC curve analysis is generally used in medical studies for evaluating the diagnostic accuracy of a continuous class (Kamarudin *et al.*, 2017). The confusion matrix is based on four parameters, identified as True Positive (TP), False Positive (FP), False Negative (FN), and True Negative (TN), as shown in Table 2. Accuracy, precision, recall, F1-score, and ROC-AUC metrics were used for performance measurement (Togacar *et al.*, 2020).

Table 2. Confusion matrix

	Predicted Positive	Predicted Negative
Actual Positive	True Positive (TP)	False Negative (FN)
Actual Negative	False Positive (FP)	True Negative (TN)

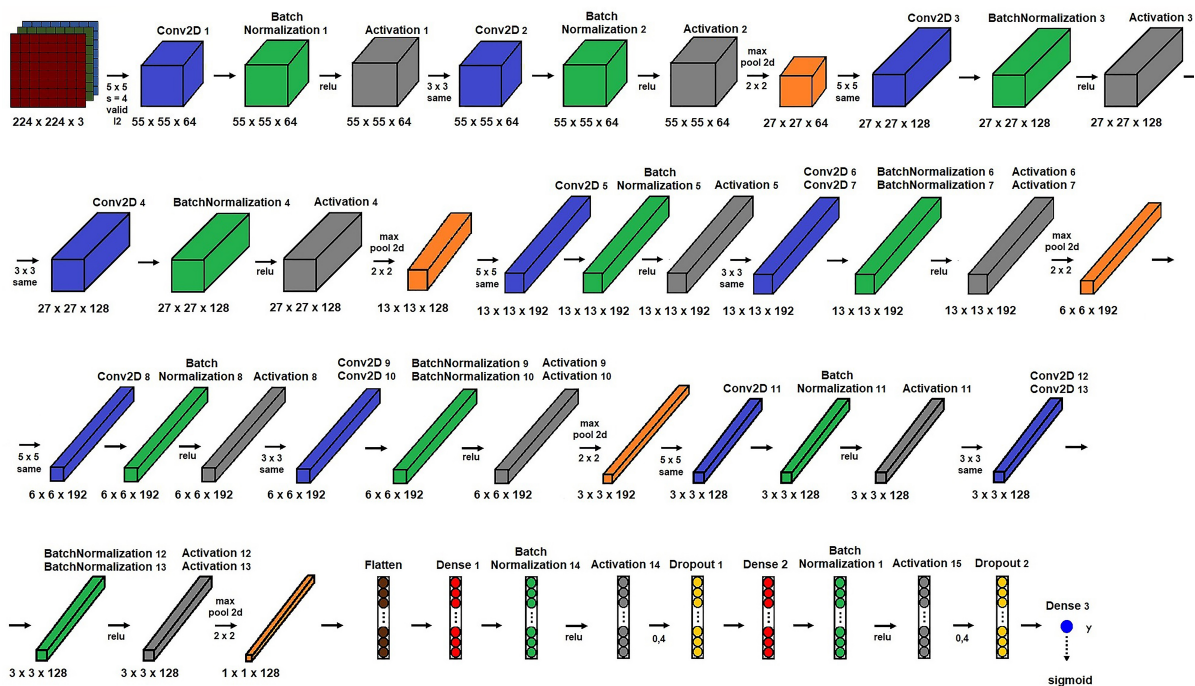
Source: Author

$$\text{Precision} = \frac{(TP)}{(TP + FP)} \quad (1)$$

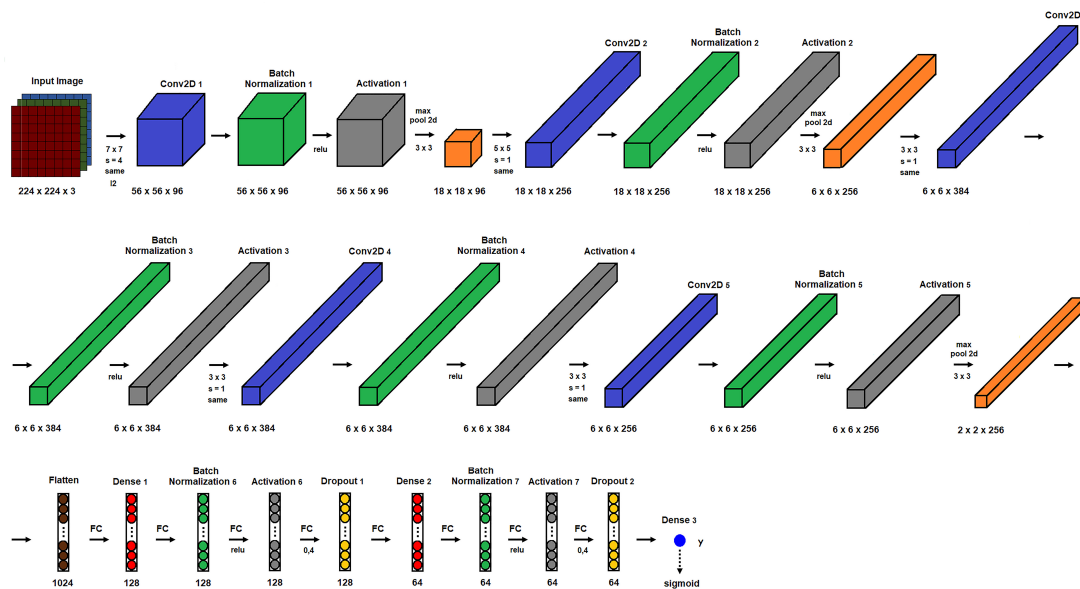
$$\text{Recall} = \frac{(TP)}{(TP + FN)} \quad (2)$$

$$\text{F1 - Score} = \frac{2 (\text{Recall} * \text{Precision})}{(\text{Recall} + \text{Precision})} \quad (3)$$

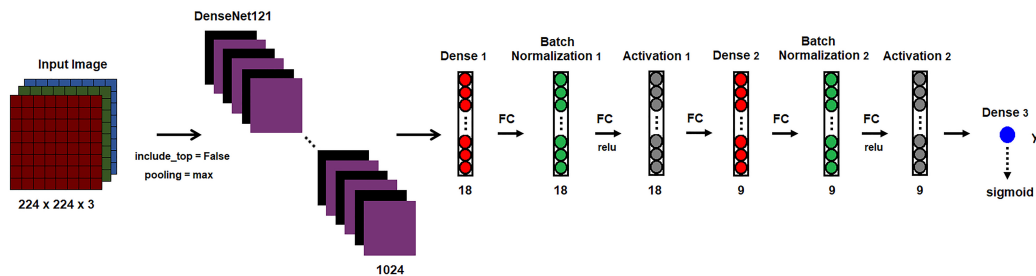
$$\text{Accuracy} = \frac{(TP + TN)}{(TP + TN + FP + FN)} \quad (4)$$



Source: Author



Source: Author



Source: Author

Experimental results

We used CNN, ZFNet, and DenseNet121 DL algorithms to detect COVID-19 for training, validation, and testing purposes. Visual performance plots are given in Figures 7 to 9, and the evaluation results of the methods are shown in Table 3.

Table 3. Comparative results of models

Models	Accuracy	Precision	Recall	F1-score	ROC-AUC
Customized-CNN	0,947	1,000	0,900	0,947	0,950
CNN	0,947	0,944	0,904	0,944	0,940
ZFNet	0,868	0,850	0,895	0,872	0,868
DenseNet121	0,842	0,867	0,765	0,813	0,835

Source: Author

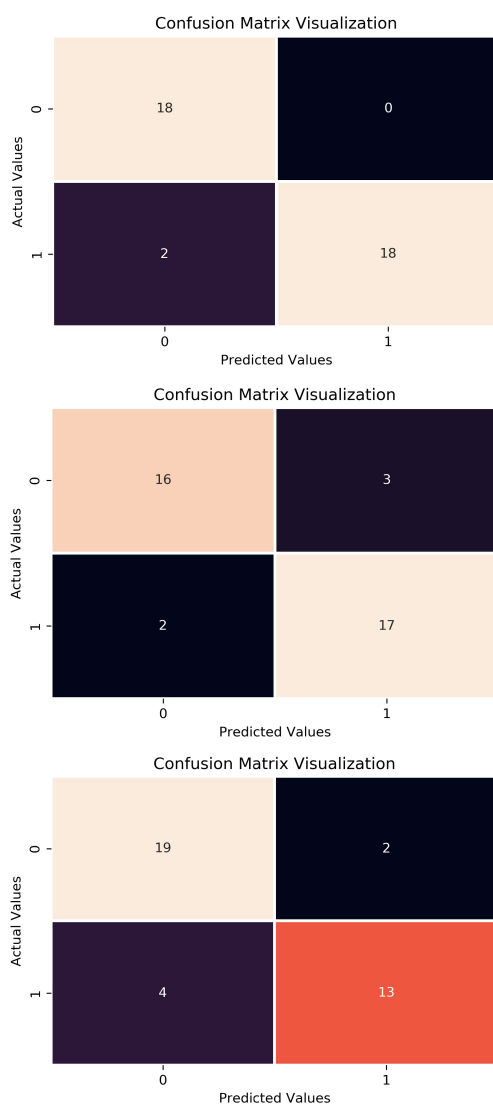


Figure 7. Confusion matrix visualization: (top) CNN, (middle) ZFNet, (bottom) DenseNet121.

Source: Author

We obtained the best performance with the customized CNN model, with an accuracy of 94,7%, a recall of 90%, a precision

of 100%, and an F1-score of 94,7%. The lowest performance values were obtained by DenseNet121 with an accuracy of 84,2%, a recall of 76,5%, a precision of 85%, and an F1-score of 81,2%. The confusion matrix for the detection of COVID-19 obtained from the study is given in Figure 7. Accuracy, precision, recall, F1-score, and ROC-AUC were used for performance evaluation (Table 3).

The loss function layer is used to calculate the expected results predicted by the vital features (Sriporn *et al.*, 2020) (Figure 8).

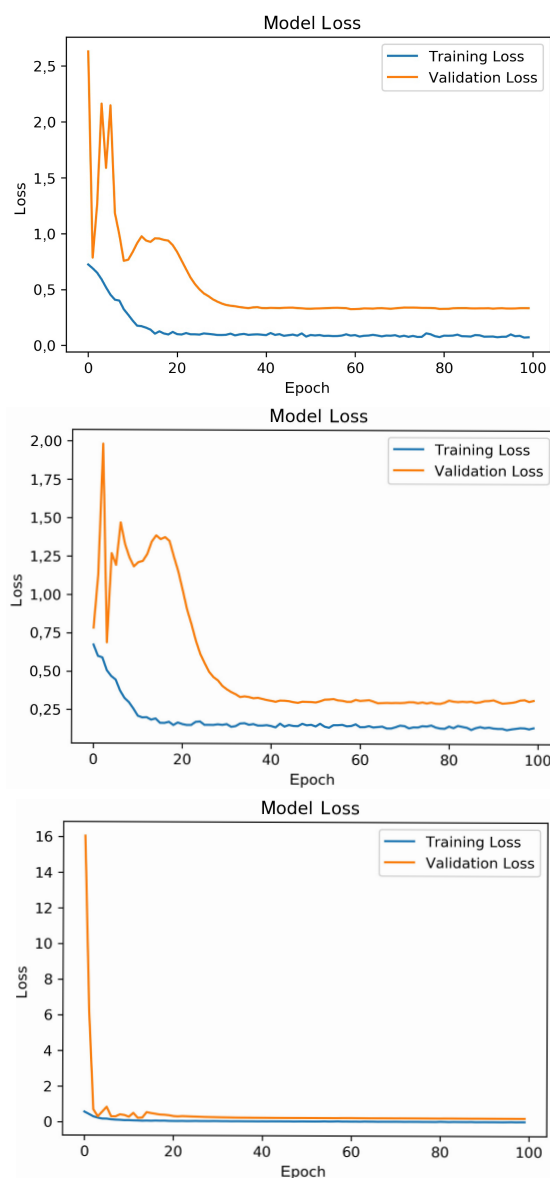


Figure 8. Training loss and validation loss values for CNN (top), ZFNet (middle), DenseNet121 (bottom).

Source: Author

According to the results of the ROC curve (Figure 9), we obtained the best result from the CNN model with 95%, the second best result from the ZFNet model with 86,8%, and the lowest result with the DenseNet121 model (83,5%).

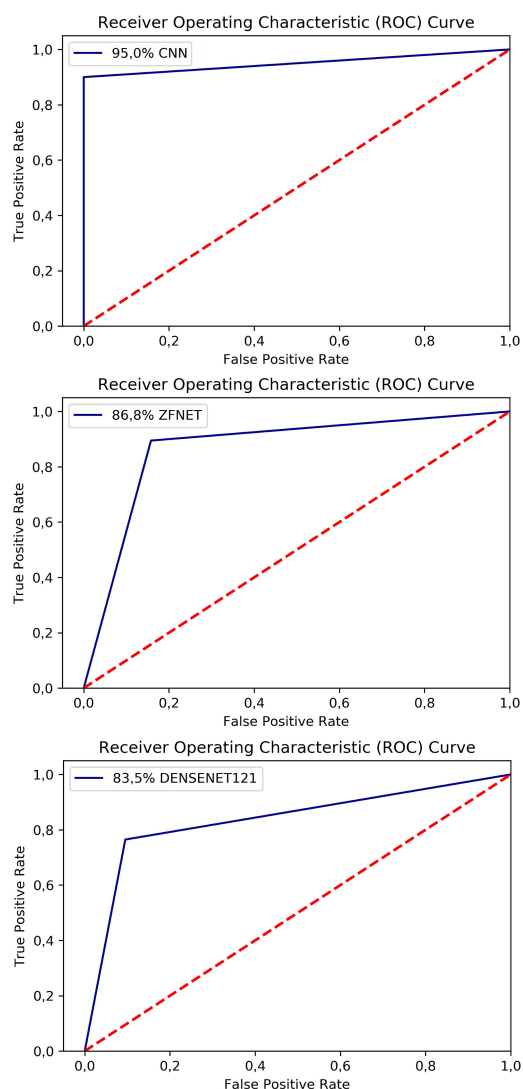


Figure 9. ROC curve obtained for customized CNN (top), ZFNet (middle), (bottom) DenseNet121Algorithm.

Source: Author

Conclusions

In this study, we focused on the detection and prediction of COVID-19 using chest CT imaging. As a result, the CNN algorithm gave more satisfactory and higher accuracy than ZFNet and DenseNet121. The additional layers we applied for the CNN model increased the study's performance (while the standard CNN ROC-AUC value was 94%, it increased to 95% with the customized method). We presented a different perspective to the standard CNN approach. According to the results, the customized CNN model can be used to automatically predict the COVID-19 disease.

A major limitation of this study is the use of a limited number of COVID-19 chest CT images; it can offer radiologists and medical staff a second perspective. COVID-19 diagnosis performed using DL-based algorithms can help medical staff with reporting and interpreting. In future work, studies with more datasets and different machine learning methods will be presented.

Conflict of interest disclosure

The author hereby declares that there is no conflict of interest.

Acknowledgments

We would like to thank Veysel Turk and Serhat Kaya for their technical contribution.

References

- Ai, T., Yang, Z., Hou, H., Zhan, C., Chen, C., Lv, W., Tao, Q., Sun, Ziyong, and Xia, L. (2020). Correlation of chest CT and RT-PCR testing in coronavirus disease 2019 (COVID-19) in China: a report of 1014 cases. *Radiology*, 296(2), E32-E40. 10.1148/radiol.2020200642
- Akcaay, S., Ozlu, T., and Yilmaz, A. (2020). Radiological approaches to COVID-19 pneumonia. *Turkish Journal of Medical Sciences*, 50(SI-1), 604-610. 10.3906/sag-2004-160
- Ardabili, S., Mosavi, A., Ghamisi, P., Ferdinand, F., Varkonyi-Koczy, A. R., and Reuter, U. R. (2020). COVID-19 outbreak prediction with machine learning. *Algorithms*, 13(10), 249. 0.3390/a13100249
- Ardakani, A. A., Kanafi, A. R., Acharya, U. R., Khadem, N., and Mohammadi, A. (2020). Application of deep learning technique to manage COVID-19 in routine clinical practice using CT images: results of 10 convolutional neural networks. *Computers in Biology and Medicine*, 121, 103795. 10.1016/j.compbimed.2020.103795
- Bao, C., Liu, X., Zhang, H., Li, Y., and Liu, J. (2020). Coronavirus disease 2019 (COVID-19) CT findings: A systematic review and meta-analysis. *Journal of the American College of Radiology*, 17(6), 701-709. 10.1016/j.jacr.2020.03.006
- Chen, X., Wang, Z. J., and McKeown, M. (2016). Joint blind source separation for neurophysiological data analysis: multiset and multimodal methods. *IEEE Signal Processing Magazine*, 33(3), 86-107. 10.1109/MSP.2016.2521870
- Choe, J., Lee, S. M., Do, K.-H., Lee, G., Lee, J.-G., Lee, S. M., and Deo, J. B. (2019). Deep learning-based image conversion of CT reconstruction kernels improves radionics reproducibility for pulmonary nodules or masses. *Radiology*, 292(2), 365-373. 10.1148/radiol.2019181960
- Chung, M., Bernheim, A., Mei, X., Zhang, N., Huang, M., Zeng, X., Cui, J., Yang, Y., Fayad, Z. A., Jacobi, A., Li, K., Li, S., and Shan, H. (2020). CT imaging features of 2019 novel coronavirus (2019-ncov). *Radiology*, 295, 202-207. 10.1148/radiol.2020200230
- Deng, L. (2014). A tutorial survey of architectures, algorithms, and applications for deep learning. *APSIPA Transactions on Signal and Information Processing*, 3, 1-29. 10.1017/at-sip.2013.9
- Esteva, A., Kuprel, B., Novoa, R. A., Ko, J., Swetter, S. M., Blau, H. M., and Thrun, S. (2017). Dermatologist-level classification of skin cancer with deep neural networks. *Nature*, 542, 115-118. 10.1038/nature21056

- GitHub/UCSD-AI4H. (2020, April 20). COVID CT. <https://github.com/UCSD-AI4H/COVID-CT>
- Goreke, V., Sari, V., and Kockanat, S. (2021). A novel classifier architecture based on deep neural network for COVID-19 detection using laboratory findings. *Applied Soft Computing Journal*, 106, 107329. 10.1016/j.asoc.2021.107329
- Guner, R., Hasanoglu, I., and Aktas, F. (2020). COVID-19: Prevention and control measures in community. *Turkish Journal of Medical Sciences*, 50(S1-1), 571-577. 10.3906/sag-2004-146
- Huang, C., Wang, Y., Li, X., Ren, L., Zhao, J., Hu, Y., Zhang, L., Fan, G., Xu, J., Gu, X., Cheng, Z., Yu, T., Xia, J., Wei, Y., Wu, W., Xie, X., Yin, W., Li, H., Liu, M. . . . Cao, B. (2020). Clinical features of patients infected with 2019 novel coronavirus in Wuhan, China. *The Lancet*, 395(10223), 497-506. 10.1016/S0140-6736(20)30183-5
- Ioannis, D. A. and Bessiana, B. (2020). COVID-19: Automatic Detection from X-Ray Images Utilizing Transfer Learning with Convolutional Neural Networks. <https://arxiv.org/ftp/arxiv/papers/2003/2003.11617.pdf>
- Jain, R., Gupta, M., Taneja, S., and Hemanth, D. J. (2021). Deep learning based detection and analysis of COVID-19 on chest X-ray images. *Applied Intelligence*, 51, 1690-1700. 10.1007/s10489-020-01902-1
- Jaiswal, A., Gianchandani, N., Singh, D., Kumar, V., and Kaur, M. (2020). Classification of the COVID-19 infected patients using DenseNet201 based deep transfer learning. *Journal of Biomolecular Structure and Dynamics*, 38, 1-8. 10.1080/07391102.2020.1788642
- Kamarudin, A. N., Cox, T., and Kolamunnage-Dona, R. (2017). Time-dependent ROC curve analysis in medical research: current methods and applications. *BMC Medical Research Methodology*, 17(1), 53. 10.1186/s12874-017-0332-6
- Lakhani, P. and Sundaram, B. (2017). Deep learning at chest radiography: automated classification of pulmonary tuberculosis by using convolutional neural networks. *Radiology*, 284(2), 574-582. 10.1148/radiol.2017162326
- LeCun, Y., Bengio, Y., and Hinton, G. (2015). Deep learning. *Nature*, 521, 436-444. 10.1038/nature14539
- Lei, J., Li, J., Li, X., and Qi, X. (2020). CT imaging of the 2019 novel coronavirus (2019-ncov) pneumonia. *Radiology*, 295(1), 18. 10.1148/radiol.2020200236
- Li, L., Qin, L., Xu, Z., Yin, Y., Wang, X., Kong, B., Bai, J., Lu, Y., Fang, Z., Song, Q., Cao, K., Liu, D., Wang, G., Xu, Q., Fang, X. Zhang, S., Xia, J., and Xia, J. (2020). Artificial intelligence distinguishes COVID-19 from community acquired pneumonia on chest CT. *Radiology*, 296(2). 10.1148/radiol.2020200905
- Lundervold, A. S. and Lundervold, A. (2019). An overview of deep learning in medical imaging focusing on MRI. *Zeitschrift für Medizinische Physik*, 29(2), 102-127. 10.1016/j.zemedi.2018.11.002
- Narin, A., Kaya, C., and Pamuk, Z. (2020). Automatic Detection of Coronavirus Disease (COVID- 19) Using X-Ray Images and Deep Convolutional Neural Networks. <https://arxiv.org/ftp/arxiv/papers/2003/2003.10849.pdf>
- Ozturk, T., Talo, M., Yildirim, E. A., Baloglu, U. B., Yildirim, O., and Acharya, U. J. (2020). Automated detection of COVID-19 cases using deep neural networks with X-ray images. *Computers in Biology and Medicine*, 121, 103792. 10.1016/j.combiomed.2020.103792
- Panwar, H., Gupta, P. K., Siddiqui, M. K., Morales-Menendez, R., and Singh, V. (2020). Application of deep learning for fast detection of COVID-19 in X-Rays using nCOVnet. *Chaos, Solitons and Fractals*, 138, 109944. 10.1016/j.chaos.2020.109944
- Pouyanfar, S., Sadiq, S., Yan, Y., Tian, H., Tao, Y., Presa-Reyes, M., Shyu, M.-L., Chen, S.-C., and Iyengar, S. S. (2018). A survey on deep learning: Algorithms, techniques, and applications. *ACM Computing Surveys*, 51(5), 92. 10.1145/3234150
- Sejnowski, T. and Tesauero, G. (1989). The Hebbian rule for synaptic plasticity algorithms and implementations. In J. H. Byrne and W. O. Berry (Eds.). *Neural models of plasticity* (pp. 94-103). California Academic Press.
- Sriporn, K., Tsai, C. F., Tsai, C. E., and Wang, P. (2020). Analyzing lung disease using highly effective deep learning techniques. *Healthcare*, 8(107), 1-21. 10.3390/healthcare8020107
- Tezer, H. and Bedir Demirdag, T. (2020). Novel coronavirus disease (COVID-19) in children. *Turkish Journal of Medical Sciences*, 50(SI-1), 592-603. 10.3906/sag-2004-174
- Togacar, M., Ergen, B., and Comert, Z. (2020). BrainMRNet: Brain tumor detection using magnetic resonance images with a novel convolutional neural network model. *Medical Hypotheses*, 134, 109531. 10.1016/j.mehy.2019.109531
- Wang, L. and Wong, A. (2020). COVID-Net: A Tailored Deep Convolutional Neural Network Design for Detection of COVID-19 Cases from Chest Radiography Images. <https://arxiv.org/pdf/2003.09871.pdf>
- World Health Organization (WHO) (2021, April 11). *World Health Organization*. <https://www.who.int/emergencies/diseases/novel-coronavirus-2019>
- Yang, S., Jiang, L., Cao, Z., Wang, L., Cao, J., Feng, R., Zhang, Z., Xue, X., Shi, Y., and Shan, F. (2020). Deep learning for detecting corona virus disease 2019 (COVID-19) on high-resolution computed tomography: a pilot study. *Annals of Translational Medicine*, 8(7), 50. 10.21037/atm.2020.03.132
- Zhu, N., Zhang, D., Wang, W. J., Li, X., Yang, B., Song, J., Zhao, X., Huang, B., Shi, W., Lu, R., Niu, P., Zhan, F., Ma, X., Wang, D., Xu, W., Wu, G., Gao, G. F., and Tan, W. (2020). A novel coronavirus from patients with pneumonia in China, 2019. *The New England Journal of Medicine*, 382(8), 727-733. 10.1056/NEJMoa2001017

Appendix

Table A1. Parameters of the customized CNN model for binary classification

Layers	Feature Map	Size	Kernel Size	Activation Function
Input	Image	1	224 x 224 x 3	-
1	Conv2D	64	5 x 5 x 64	relu
2	Conv2D	64	5 x 5 x 64	relu
	MaxPooling2D	64	2 x 2	-
3	Conv2D	128	27 x 27 x 128	relu
4	Conv2D	128	27 x 2 x 128	relu
	MaxPooling2D	128	13 x 13 x 128	-
5	Conv2D	192	13 x 13 x 192	relu
6	2 x Conv2D	192	13 x 13 x 192	relu
	MaxPooling2D	192	6 x 6 x 192	-
8	Conv2D	192	6 x 6 x 192	relu
9	2 x Conv2D	192	3 x 3 x 192	relu
	MaxPooling2D	192	3 x 3 x 192	-
11	Conv2D	128	3 x 3 x 128	relu
12	2 x Conv2D	128	3 x 3 x 128	relu
	MaxPooling2D	128	1 x 1 x 128	-
14	FC	-	128	relu
15	FC	-	64	relu
Output	FC	-	1	sigmoid

Source: Author

Table A2. Parameters of the ZFNet model for binary classification

Layers	Feature Map	Size	Kernel Size	Activation Function
Input	Image	1	224 x 224 x 3	-
1	Conv2D	96	56 x 56 x 96	relu
	MaxPooling2D	96	18 x 18 x 96	-
2	Conv2D	256	18 x 18 x 256	relu
	MaxPooling2D	256	6 x 6 x 256	-
3	Conv2D	384	6 x 6 x 384	relu
4	Conv2D	384	6 x 6 x 384	relu
5	Conv2D	256	6 x 6 x 256	relu
	MaxPooling2D	256	2 x 2 x 256	-
6	FC	-	128	relu
7	FC	-	64	relu
Output	FC	-	1	sigmoid

Source: Author

Table A3. Parameters of the DenseNet121 model for binary classification

Layers	Size	Activation Function
Input	Image	224 x 224 x 3
1	DenseNet121	1 024
2	FC	18
3	FC	9
Output	FC	1

Source: Author

Detection of COVID-19 and Other Pneumonia Cases using Convolutional Neural Networks and X-ray Images

Detección de COVID-19 y otros casos de neumonía utilizando redes neuronales convolucionales e imágenes de rayos-X

Carlos Eduardo Belman-López¹

ABSTRACT

Given that it is fundamental to detect positive COVID-19 cases and treat affected patients quickly to mitigate the impact of the virus, X-ray images have been subjected to research regarding COVID-19, together with deep learning models, eliminating disadvantages such as the scarcity of RT-PCR test kits, their elevated costs, and the long wait for results. The contribution of this paper is to present new models for detecting COVID-19 and other cases of pneumonia using chest X-ray images and convolutional neural networks, thus providing accurate diagnostics in binary and 4-classes classification scenarios. Classification accuracy was improved, and overfitting was prevented by following 2 actions: (1) increasing the data set size while the classification scenarios were balanced; and (2) adding regularization techniques and performing hyperparameter optimization. Additionally, the network capacity and size in the models were reduced as much as possible, making the final models a perfect option to be deployed locally on devices with limited capacities and without the need for Internet access. The impact of key hyperparameters was tested using modern deep learning packages. The final models obtained a classification accuracy of 99,17 and 94,03% for the binary and categorical scenarios, respectively, achieving superior performance compared to other studies in the literature, and requiring a significantly lower number of parameters. The models can also be placed on a digital platform to provide instantaneous diagnostics and surpass the shortage of experts and radiologists.

Keywords: coronavirus, COVID-19, convolutional neural networks, deep learning, chest X-ray images, pneumonia

RESUMEN

Dado que es esencial detectar los casos positivos y tratar a los pacientes afectados rápidamente para mitigar el impacto del COVID-19, los rayos-X han sido investigados para la detección del virus, en conjunto con modelos de aprendizaje profundo, eliminando desventajas como la escasez de kits de prueba RT-PCR, sus elevados costos y la larga espera por los resultados. La contribución de este estudio es presentar nuevos modelos para detectar COVID-19 y otros casos de neumonía utilizando imágenes de rayos-X y redes neuronales convolucionales, proporcionando diagnósticos precisos escenarios de clasificación binaria y categórica. La precisión en la clasificación fue mejorada y el sobreajuste fue evitado mediante 2 acciones: (1) aumentando el tamaño del conjunto de datos, al mismo tiempo que los escenarios de clasificación fueron balanceados; y (2) agregando técnicas de regularización y optimizando los hiperparámetros. Adicionalmente, la capacidad y tamaño de los modelos fueron reducidos tanto como fue posible, convirtiendo a los modelos finales en una opción perfecta para ser desplegados localmente en dispositivos con capacidades limitadas y sin necesidad de acceso a Internet. El impacto de hiperparámetros clave fue puesto a prueba utilizando paquetes modernos de aprendizaje profundo. Los modelos finales obtuvieron una precisión de 99,17 y 94,03 % para los escenarios binario y categórico respectivamente, logrando un rendimiento superior en comparación con otras propuestas en la literatura y utilizando un número significativamente menor de parámetros. Los modelos también pueden ser colocados sobre una plataforma digital para proporcionar diagnósticos al instante y superar la escasez de expertos y radiólogos.

Palabras clave: coronavirus, COVID-19, redes neuronales convolucionales, aprendizaje profundo, imágenes rayos-X de tórax, neumonía

Received: September 1st, 2020

Accepted: May 25th, 2021

Introduction

On December 31, 2019, the World Health Organization issued a warning about several cases of a respiratory illness emerging from the city of Wuhan, in the Hubei province of China, with clinical manifestations similar to viral pneumonia and symptoms such as coughing, fever, and dyspnea. This newly discovered virus was named COVID-19, and it is caused by the SARS-CoV-2 virus (Chung *et al.*, 2020).

Most people who are infected with COVID-19 experience a mild to moderate respiratory illness and may recover without

¹ Computer Systems Engineer and M.Sc. in Industrial Engineering, Tecnológico Nacional de México en Celaya. Affiliation: Ph.D. Student, Tecnológico Nacional de México en Celaya. E-mail: carlosbelman@gmail.com

How to cite: Belman-López C. E. (2022). Detection of COVID-19 and Other Pneumonia Cases Using Convolutional Neural Networks and X-ray Images. *Ingeniería e Investigación*, 42(1), e90289. 10.15446/ing.investig.v42n1.90289



Attribution 4.0 International (CC BY 4.0) Share - Adapt

requiring special treatment. Older people, and those with underlying medical problems such as cardiovascular disease, diabetes, chronic respiratory disease, and cancer are more likely to develop serious complications. An efficient way to prevent and reduce infections is by quickly detecting positive COVID-19 cases, isolating patients, and starting their treatment as soon as possible. COVID-19 spreads primarily through droplets of saliva or discharge from the nose when an infected person coughs or sneezes. There are currently no specific treatments for COVID-19 (WHO, 2020) and, as the global pandemic progresses, scientists from a wide variety of specialties play pivotal roles in developing new diagnostic, forecasting, and modeling methods. For example, Sun and Wang (2020) developed a mathematical model to characterize imported and asymptomatic patients without strict a 'quarantine', which was useful in modeling the COVID-19 epidemic. Boccaletti *et al.* (2020) presented an evolutionary modeling of COVID-19 using mathematical models and deep learning approaches. However, regarding diagnostic and detection methods, much of the current literature has focused on radiology techniques such as portable chest radiography (X-rays) and computed tomography (CT) scans (Chung *et al.*, 2020; Zhou *et al.*, 2020). For instance, Wang *et al.* (2021) used CT images and pre-trained deep learning models together with discriminant correlation analysis to classify COVID-19, pneumonia, tuberculosis, and healthy cases. Zhang *et al.* (2021) used 18-way data augmentation, a convolutional block attention module, and CT images to diagnose COVID-19 and healthy cases. However, due to infection issues related to transporting patients to CT suites, inefficiencies in CT room decontamination, and the lack of CT equipment in some parts of the world, X-rays will likely be the most common way to identify and follow up lung abnormalities including COVID-19. Additionally, depending on the air exchange rates, CT rooms may be unavailable for approximately one hour after imaging infected patients (ACR, 2020). Therefore, chest X-ray utilization for early COVID-19 detection plays a key role in areas all over the world with limited access to reliable RT-PCR (reverse transcription polymerase chain reaction) tests for COVID-19 (Jacobi *et al.*, 2020).

Furthermore, Artificial Intelligence (AI) methods are among the most widely used tools in the fight against the COVID-19 pandemic. Castillo and Melin (2020) proposed a model for forecasting confirmed cases and deaths in different countries based on their corresponding time series using a hybrid fuzzy-fractal approach. Particularly in the case of Mexico, Melin *et al.* (2020) forecasted the COVID-19 time series at the state and national levels with a multiple ensemble neural network model with fuzzy response aggregation. Castillo and Melin (2021) proposed a hybrid intelligent fuzzy fractal approach for classifying countries based on a mixture of fractal theoretical concepts and fuzzy logic to achieve an accurate classification of countries based on the complexity of their COVID-19 time series.

As of March 2021, 127 349 248 confirmed cases of COVID-19, including 2 787 593 deaths have been reported worldwide (WHO, 2021), and the numbers keep increasing. Therefore,

it is critical to detect cases of COVID-19 as soon as possible in order to prevent the further spread of this pandemic, as well as to instantly treat affected patients. The need for auxiliary diagnostic tools has increased, and recent findings obtained using radiology techniques suggest that X-ray images contain significant information about COVID-19 infections. AI methods coupled with radiology techniques can be helpful for the accurate detection of this disease and can also help overcome the shortage of radiologists and experts in remote places (Ozturk *et al.*, 2020).

AI methods, especially machine learning (Raschka and Mirjalili, 2017; SAS Institute Inc., 2018) and deep learning approaches (Beysolow II, 2017; Chen and Lin, 2014; James *et al.*, 2013) have been successfully applied in various areas such as IoT (Yang *et al.*, 2019), manufacturing (Lee *et al.*, 2015), computer vision (Rosebrock, 2017), autonomous vehicles (Nguyen *et al.*, 2018), natural language processing (Zhou *et al.*, 2020), robotics, education (Picciano, 2012) and healthcare (Rong *et al.*, 2020).

In healthcare, machine learning and deep learning techniques such as linear discriminant analysis, support vector machines, and feed forward neural networks have been used in several classification problems like lung disease classification (Varela-Santos and Melin, 2020), efficient segmentations of cardiac sound signals (Patidar and Pachori, 2013), classification of motor imagery electroencephalogram signals for enhancing brain-computer interfaces (Gaur *et al.*, 2015), and the classification of normal and epileptic seizure electroencephalogram signals (Pachori *et al.*, 2015). However, convolutional neural networks (CNNs) are the state-of-art method when it comes to image classification (Chollet, 2018) and provide better results in non-linear problems with highly dimensional spaces. CNNs have been used for signal and biomedical image processing (Wang *et al.*, 2018), for classifying multidimensional and thermal images, and for image segmentation (Fasihi and Mikhael, 2016).

CNNs have several characteristics that justify their status as an AI and image processing tool. According to Chollet (2018), these characteristics are simplicity, scalability, and versatility. Simplicity refers to the fact that CNNs remove the need for feature engineering, replacing complex and heavy pipelines with simple and end-to-end trainable models. CNNs are scalable because they are highly suitable for parallelization on GPUs or TPUs. Additionally, CNNs can be trained by iterating over large or small batches of data, allowing them to be trained on datasets of arbitrary size. Versatility and reusability are regarded as features because, unlike many prior machine-learning approaches, CNNs can be trained on additional data without restarting from scratch, thus making them viable for continuous learning. Furthermore, trained CNNs are reusable, for example, CNNs trained for image classification can be dropped into a video processing pipeline. This allows reinvesting and reusing previous work into increasingly complex and powerful models. Additionally, new techniques and researches have recently emerged to further improve the performance of CNNs, such as the novel convolutional block attention module (Zhang *et al.*, 2021), data augmentation techniques, new architectures and

pre-trained models (He *et al.*, 2016; Nayak *et al.*, 2021), optimization algorithms (Kingma and Ba, 2014), activation functions (Pedamonti, 2018), regularization techniques such as dropout (Srivastava *et al.*, 2014) and batch normalization (Chen *et al.*, 2019), among others.

Finally, CNNs may be deployed into devices with limited capacities when their size is appropriate, so that untrained personal use these devices to diagnose many kinds of illnesses in undeveloped areas (Rong *et al.*, 2020).

Recently, radiology images (X-ray images) in conjunction with deep learning methods (such as CNNs) have been investigated for COVID-19 detection in order to eliminate disadvantages such as the insufficient number of RT-PCR test kits, testing costs, and the long wait for results.

Wang *et al.* (2020) used traditional neural networks with transfer learning from ImageNet database (Liu and Deng, 2015) to obtain a 93,3% accuracy in classifying 3 classes (COVID-19, normal, and pneumonia). Ioannis *et al.* (2020) developed a deep learning model using 224 confirmed COVID-19 images. Their model obtained 98,75 and 93,48% accuracy in classifying 2 and 3 classes, respectively. Sethy *et al.* (2020) obtained a 95,3% accuracy using 50 chest X-ray images (25 COVID-19 + 25 Non-COVID) in conjunction with a ResNet50 (He *et al.*, 2016) pre-trained model and SVM. Ozturk *et al.* (2020) proposed a deep neural network using 17 convolutional layers, obtaining 98,08 and only 87,02% of accuracy in classifying 2 and 3 classes, respectively. Narin *et al.* (2020) obtained a 98% of accuracy using 100 chest X-ray images (50 COVID-19 + 50 Non-COVID) in conjunction with the ResNet50 (He *et al.*, 2016) pre-trained model. Mahmud *et al.* (2020) used a multi-dilation convolutional neural network for automatic COVID-19 detection, achieving 97,4% and 90,3% of accuracy in classifying 2 (COVID-19 and Non-COVID-19) and 4 classes (COVID-19, normal, viral pneumonia, and bacterial pneumonia), respectively. Loey *et al.* (2020) used a detection model based on GAN and transfer learning to obtain 80,6, 85,2, and 99,99% for four (COVID-19, normal, viral pneumonia, and bacterial pneumonia), three (COVID-19, normal and bacterial pneumonia) and two classes (COVID-19 and normal), respectively. Nayak *et al.* (2021) evaluated the effectiveness of eight pre-trained CNN models such as AlexNet, VGG-16, GoogleNet, MobileNet-V2, SqueezeNet, ResNet-34, ResNet-50, and Inception-V3 for classification two classes (COVID-19 and normal). Varela-Santos and Melin (2021) compared traditional neural networks, feature based traditional neural networks, CNNs, support vector machines (SVM), and k-nearest neighbors to predict 2, 3, and 6 output classes, obtaining as high as 88,54% when more than 3 outputs classes were present in the data set. Chaudhary and Pachori (2020) used the Fourier-Bessel series expansion-based dyadic decomposition method to decompose an X-ray image into sub-band images that are fed into a ResNet50 pre-trained model, where ensemble CNN features are finally fed to the softmax classifier. In the study, 750 images were used (250 for pneumonia, 250 for COVID-19, and 250 for normal).

In most of these cases, the obtained results are biased and overfitted due to a huge network capacity (specially in transfer

learning approaches) compared with the small number of COVID-19 images. Also, the classification scenarios are limited to only 2 or 3 classes. It should be highlighted that the larger networks will likely overfit, while simpler models are less likely to do so.

In turn, approaches based on transfer learning (Chollet 2017; Szegedy *et al.*, 2016) used pre-trained models in datasets scarcely related to X-ray images and would have to go through a heavy fine-tuning phase to adjust the abstract representations in the models to make them relevant for the problem at hand. However, they would end up with an excess capacity compared to the dataset size. Additionally, another drawback for transfer learning approaches is that they result in very big and heavy models, thus making it difficult to deploy them on devices with limited capacities, or acquiring Internet access if these large models are deployed in the cloud, which is not always possible in remote or poor regions.

For these reasons, the contribution of this paper is:

- To present new models for detecting COVID-19 and other pneumonia cases using chest X-ray images and CNNs. The proposed models were developed to provide accurate diagnostics in more output classes than previous studies, covering two scenarios: binary classification (COVID-19 vs. Non-COVID) and 4-classes classification (COVID-19 vs. Normal vs. Bacterial Pneumonia vs. Viral Pneumonia). Figure 1 illustrates samples of images used for this study.

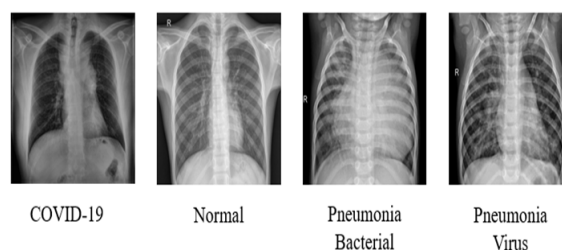


Figure 1. Samples of the involved categories.

Source: Authors

- To improve accuracy in the results and prevent overfitting by following 2 actions: (1) increasing the data set size (considering more data repositories and using data augmentation techniques) while classification scenarios are balanced; and (2) adding regularization techniques such as dropout and performing automated hyperparameter optimization.
- To reduce the employed network capacity and size as much as possible, thus making the final models an option to be deployed locally on devices with limited capacities and without the need for Internet access.

The impact of key hyperparameters such as batch size, learning rate, number of epochs, image resolution, activation function, number of convolutional layers, the size for each

layer, and neurons in the dense layer was extensively experimented on using modern deep learning packages such as Hyperas and Hyperopt (Pumperla, 2021; Bergstra, 2021). The final proposed models achieved superior performance and required a significantly lower number of parameters compared to other studies in the literature.

Materials and Methods

In this study, new models for detecting COVID-19 and other pneumonia cases using CNNs and X-ray images are presented. Figure 2 shows the general method used to obtain the proposed models. In general, the method consists of the following phases: consolidating the data set, preprocessing (which includes normalization and image augmentation), and experimentation and automated hyperparameter optimization.

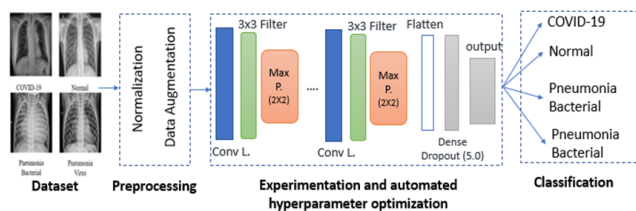


Figure 2. General method used to obtain the proposed CNNs.

Source: Authors

Data set

The main challenge when applying deep learning approaches is to collect an adequate number of samples for effective training. The literature referenced in the Introduction section reveals that the earlier models are validated using a fewer number of samples, and the data in most cases is imbalanced (Nayak *et al.*, 2021).

One of the goals of this research is to improve the accuracy and prevent overfitting by increasing the data set size, considering more data repositories and using data augmentation techniques while the classification scenarios are balanced.

For the COVID-19 class, 489 images were obtained from ISMIR (2020) and Cohen *et al.* (2020); 35 images were obtained from Chung (2020b), and 56 images were obtained from Chung (2020a). For the Non-COVID-19 class (Normal/Bacterial Pneumonia/Viral Pneumonia), 2 940 images were obtained from Kaggle Inc. (2020).

The number of images for each category is presented in Table 1. In order to avoid the issue with unbalanced data, 400 X-ray images belonging to the COVID-19 category were increased to 800 via image augmentation. This process consisted of rotating each image once in an angle between 0 and 360 degrees. Both scenarios balanced the number of images according to the available images in the COVID-19 category.

For this reason, the binary classification scenario analyzed a total of 1 960 images, 980 belonging to the COVID-19 class

and 980 belonging to the Non-COVID-19 (Normal/Bacterial Pneumonia /Viral Pneumonia) class. Finally, the categorical scenario (4 classes) analyzed a total of 3 829 images, 980 for each category involved.

Table 1. Number of images for each category in the different scenarios

Scenario	Dataset	COVID-19	Non-COVID		
			Normal	Bacterial Pneumonia	Viral Pneumonia
Binary classification (1 960 total images)	Training	400 images increased to 800 by image augmentation	266	267	266
	Testing	180	60	60	60
	Total	980		980	
Categorical classification (4 classes and 3 920 total images)	Training	400 images increased to 800 by image augmentation	800	800	800
	Testing	180	180	180	180
	Total	980	980	980	980

Source: Authors

Experimental setup

The CNNs were developed using Python (Python Software Foundation, 2020) in conjunction with the TensorFlow (Abadi *et al.*, 2015) and Keras (Chollet, 2015) libraries. Training and experiments were conducted on a computer equipped with an Intel Core i5-6200U processor (@ 2,40 GHz), 16 GB of RAM, 222 GB HDD, and Windows 10.

Preprocessing

Data preprocessing aims to make available raw data more suitable for neural networks (Chollet, 2018). Therefore, the collected X-ray images were preprocessed to make the training process faster and easier to implement. The images were reshaped to uniform sizes followed by value normalization (VN), which consisted of dividing the values by 255 and casting them to float type so that inputs are floating point values in the 0-1 range before processing.

Training parameters

The CNNs were trained with a backpropagation algorithm (Duchi *et al.*, 2011) to minimize the cross-entropy loss function (binary cross-entropy for the binary scenario and categorical for the 4-classes scenario) with dropout set to 0,5 to reduce overfitting and weights updated by using the Adam optimizer (Kingma and Ba, 2014).

Each convolution layer utilized a 3×3 filter and an activation function after each convolution for non-linear activation, followed by a max pooling layer with 2×2 window and no stride (stride 1). The steps per epoch were calculated by dividing the total training sample between the corresponding batch size, and the validation steps were calculated dividing the total validation sample between the testing batch size (set to 20). Accuracy was the metric used for monitoring the training and testing phases. For the

categorical scenario, softmax activation was used to produce a probability distribution over the four categories in the output layer, while sigmoid activation was used for the binary scenario to normalize the probability prediction in the output layer. A dense layer was utilized before the output layer.

Experimentation and hyperparameters optimization

In addition to the training parameters selected in the previous section, the impact of key hyperparameters such as batch size, learning rate, number of epochs, image resolution, activation function, number of convolutional layers, the size for each layer, and neurons in the dense layer were tested.

The optimization of these hyperparameters is a difficult part that usually requires a lot of effort, time, computational resources, and extensive experimentation. But through modern deep learning packages on Python such as Hyperas (Pumperla, 2021) and Hyperopt (Bergstra, 2021), extensive experimentation and hyperparameters optimization are automated, evaluating all the options for each hyperparameter in just one execution per scenario, and automatically selecting the combination that provides the best accuracy. Just as an example, to test different values for the batch size, the code `batch_size = {{choice([20,32,40])}}` can be used, and these different options will be tested in the same training execution.

According to Mahmud *et al.* (2020), models that analyze COVID-19 images with a 256×256 resolution yield good results. Therefore, imaging was carried out in 256×256 and 200×200 resolutions (this second resolution reduces the number of trainable parameters in the models). Both of these allowed a maximum of 6 convolutional layers, so 3, 4, 5 and 6 layers were tested during 60 epochs, analyzing the accuracy, network capacity (total trainable parameters), and overfit. The tested activation functions were relu, elu, and leaky relu. The depth of the feature maps was progressively increased in the network (from 32 to 256), whereas the size of the feature maps decreased (for instance, from 198×198 to 1×1 when a 200×200 resolution was used). Table 2 shows a summary of the different choices tested for each hyperparameter, and Table 3 shows the best models, their accuracy, number of trainable parameters, and their selected hyperparameters after experimentation. The models were validated through cross-validation, confusion matrix and precision, recall, and F1-score values.

Table 2. Hyperparameters experimented in the two scenarios (binary and categorical)

Learning rate	Resolution	Act.	Batch size	Epochs	Layers	Size per layer	Neurons in dense layer
1e-01	256×256	Relu	20	1-60	3 to 6	32	256
1e-02	200×200	Elu	32			64	512
1e-03		Leaky	40			128	1 024
		Relu				256	

Source: Authors

Table 3. Best models and their numbers of trainable parameters and selected hyperparameters

Best model	Trainable Parameters	Resolution	Act.	Conv. Layers	Accuracy	Dense Layer
4-classes	1 328 900	200	Relu	32-64-64-128-128	94,03	512
Binary	355 108	200	Relu	32-32-64-64-128-128	99,17	512

Source: Authors

Results and discussion

This study presents new CNN models for detecting COVID-19 and other pneumonia cases using X-ray images in two different scenarios. These scenarios are binary classification (COVID-19 vs. Non-COVID) and 4-classes classification (COVID-19 vs. Normal vs. Bacterial Pneumonia vs. Viral Pneumonia). In both cases, a larger number of COVID-19 images was obtained to train and test the models. The classification problems were also balanced, dropout was used for regularization, and a balance was found between too much capacity and not enough network capacity through extensive experimentation. Additionally, extensive experimentation and hyperparameter optimization were automated using modern deep learning packages, and the impact of key hyperparameters was evaluated, such as batch size, learning rate, number of epochs, image resolution, activation function, number of convolutional layers, the size for each layer, and neurons in the dense layer.

Transfer learning approaches such as the one by Wang *et al.* (2020) obtained a 93,3% accuracy in classifying 3 classes using a pre-trained model based on ImageNet and 11,75 million parameters. Sethy *et al.* (2020) obtained a 95,3% accuracy using only 50 chest X-ray images and 24,97 million parameters (ResNet50 + SVM). Narin *et al.* (2020) obtained a 98% accuracy using only 100 chest X-ray images and 24,97 million parameters (ResNet50). Loey *et al.* (2020) obtained only 80,6 and 99,99% for 4 and 2 classes using detection models based on GAN, transfer learning and 61 million parameters. Nayak *et al.* (2021) obtained a 98,33% accuracy in classifying 2 classes using ResNet-34 and 21,8 million of parameters. Ioannis *et al.* (2020) obtained 98,75 and 93,48% accuracy in classifying 2 and 3 classes, respectively, using 224 COVID-19 images, a deep learning model based on VGG-19 network, and 20,37 million parameters. Chaudhary and Pachori (2020) obtained a 98,3% accuracy classifying 3 classes using 750 total images but without specifying the network capacity, trainable parameters, or computational complexity for the final model.

In all these cases, the obtained results are biased and overfitted due to the huge network capacity (million parameters) compared with the small number of COVID-19 images. Moreover, scenarios are limited to only 2 or 3 classes. In turn, the pre-trained models are little related to X-ray images and had to go through a heavy fine-tuning phase to adjust the models to make them relevant for the problem at hand, but this resulted in models with excess

capacity compared to sample size. Another drawback of these approaches is that they end up in very big and heavy models, thus making it difficult to deploy them on devices with limited capacities. People may also require Internet access to large models deployed in the cloud, which is not always possible in remote or poor regions.

Other approaches that do not use transfer learning such as Ozturk *et al.* (2020) obtained 98,08 and only 87,02% in classifying 2 and 3 classes using 17 convolutional layers and 1 164 million parameters. Mahmud *et al.* (2020) achieved 97,4 and 90,3% classifying 2 (COVID-19 and Non-COVID-19) and 4 classes (COVID-19, normal, viral pneumonia, and bacterial pneumonia), using a multi-dilation convolutional neural network. Varela-Santos and Melin (2021) compared traditional neural networks, feature based traditional neural networks, CNNs, support vector machines (SVM), and k-nearest neighbors for predicting 2, 3, and 6 output classes, obtaining at most 88,54% when more than 3 outputs classes were present in the data set. Additionally, it is not clear if some method is better than the others, and the network capacity or trainable parameters for these models are not specified.

Most of the previous studies have only used between 25 and 224 COVID-19 images, for analyzing just 2 or 3 categories. Furthermore, the hyperparameter optimization process is not performed in an exhaustive and automated way as this research does. Additionally, only Mahmud *et al.* (2020), Loey *et al.* (2020), and Santos and Melin (2021) analyzed 4 categories, obtaining an accuracy of 90,3, 80,6, and 88,54%, respectively, which can be clearly improved. In this research, 980 COVID-19 images were used (580 increased to 980 by image augmentation to avoid the unbalanced data problem) and a total of 1 960 and 3 920 images for each classification scenario, respectively, which is a significantly higher number of images. Furthermore, the network capacity for the binary scenario was adjusted to only 353 569 parameters, while the accuracy was increased to 99,17%, and, for the categorical scenario (4 classes involved), the network capacity was adjusted to only 1 328 900 parameters, while the accuracy was increased to 94,01%.

Extensive experimentation and hyperparameter optimization were automated, evaluating an appropriate set of options for each hyperparameter in just one execution per scenario and automatically selecting the combination that provided the best accuracy. The proposed models obtained superior performance, analyzed a larger number of classes, and required a significantly lower number of parameters compared to other studies in the literature (Table 4).

With these network sizes (number of parameters), the models are a perfect choice to be deployed locally on devices with limited capacities and without the need for Internet access. The resolution used in both cases was 200x200. For an analysis of each model, the categorical and binary confusion matrix were provided in Figures 3a and 3b, respectively, and precision, sensitivity/recall, and F1-score values are shown in Table 5. The details for the final proposed models are given in Tables 6 and 7.

The proposed models can be used for the diagnosis of COVID-19 in just a couple of seconds. These can also be widely applied because X-ray techniques are preferred to CT because they are more accessible, cheaper, and widely applied in health centers. Patients diagnosed as positive by the models can be addressed to advanced health centers for confirmation, initiating a treatment immediately. COVID-19 public images are still limited, which, in turn, is a limitation in this study; a greater number of images could help to increase the performance, especially in the categorical scenario.

Table 4. Comparison of the proposed COVID-19 diagnostic models with previous works in the literature

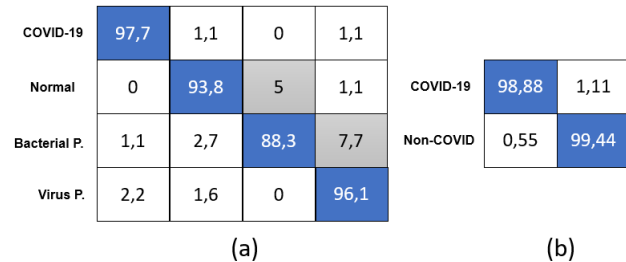
Reference	Number of images	Architecture/ parameters	Acc (%) (binary)	Acc (%) (Cat.)
Sethy <i>et al.</i> (2020)	25 COVID-19 + 25 Non-COVID	ReNet-50 / SVM 24,97 Million	95,38	
Narin <i>et al.</i> (2020)	50 COVID-19 + 50 Non-COVID	ResNet-50 24,97 Million	98	
Loey <i>et al.</i> (2020)	69 COVID-19 + 70 Normal	Alexnet / GAN 61 Million Googlenet / GAN	99	80,6 (4 classes)
	69 COVID-19 + 79 Normal + 79 Viral Pneumonia + 79 Bac. Pneumonia			
Ozturk <i>et al.</i> (2020)	125 COVID-19 + 500 Normal	DarkCovidNet / 1 164 434	98,08	87,02 (3 classes)
	125 COVID-19 + 500 Pneumonia + 500 Normal			
Ioannis <i>et al.</i> (2020)	224 COVID-19 + 700 Pneumonia + 504 Normal	VGG-19/20,37 Million		93,48 (3 classes)
Wang <i>et al.</i> (2020)	358 COVID-19 + 5 538 Pneumonia + 8 066 Normal	COVID-Net/11,75 million		93,3 (3 classes)
Mahmud <i>et al.</i> (2020)	305 COVID-19 + 305 Normal	Multi-resolution CovXNet	97,4	90,3 (4 classes)
	305 COVID-19 + 305 Normal + 305 Viral Pneumonia + 305 Bac. Pneumonia			
Nayak <i>et al.</i> (2021)	203 COVID-19 + 203 Normal	ResNet34 / 21,8 million	98,33	
Chaudhary and Pachori (2020)	250 COVID-19 + 250 Pneumonia + 250 Normal	FBD Method + ResNet50		98,6 (3 classes)
Santos and Melin (2021)	158 distributed images in 6 classes	Feature based traditional neural networks		88,54 (6 classes)
This proposal	980 COVID-19 + 980 Non-COVID	Convolutional Neural Networks 355 108 / 1 328 900	99,17	94,03 (4 classes)
	980 COVID-19 + 980 Normal + 980 Viral Pneumonia + 980 Bacterial Pneumonia			

Source: Authors

Table 5. Precision, recall/sensitivity, and F1-score values obtained for each model

	Class	Performance Metrics (%)			
		Precision	Recall	F1-score	Accuracy
Binary Scenario	COVID-19	0,99	0,99	0,99	99,17
	Non-COVID	0,99	0,99	0,99	
Categorical Scenario	COVID-19	0,97	0,98	0,97	94,03
	Normal	0,94	0,94	0,94	
	Bacterial P.	0,95	0,88	0,91	
	Virus P.	0,91	0,96	0,93	

Source: Authors

**Figure 3.** Categorical (a) and binary confusion matrix (b).

Source: Authors

Table 6. The layers and parameters of the proposed model in the binary scenario

Number of Layer	Layer Type	Output Shape	Parameters
1	Conv2D	(198, 198, 32)	896
2	MaxPooling2D	(99, 99, 32)	0
3	Conv2D	(97, 97, 32)	9248
4	MaxPooling2D	(48, 48, 32)	0
5	Conv2D	(46, 46, 64)	18 496
6	MaxPooling2D	(23, 23, 64)	0
7	Conv2D	(21, 21, 64)	36 928
8	MaxPooling2D	(10, 10, 64)	0
9	Conv2D	(8, 8, 128)	73 856
10	MaxPooling2D	(4, 4, 128)	0
11	Conv2D	(2, 2, 128)	147 584
12	MaxPooling2D	(1, 1, 128)	0
13	Flatten	(128)	0
14	Dropout	(128)	0
15	Dense	(512)	66 048
16	Dense	(1)	513
Total trainable parameters: 353 569			

Source: Authors

Conclusions and future work

Deep learning deals with more complex and extensive data sets for which classical machine learning and statistical techniques such as Bayesian analysis and support vector machines, among others, would be impractical. Deep learning has interesting applications in healthcare areas, such as biomedicine, disease diagnostics, living assistance, biomedical information processing, among others. It has

Table 7. The layers and parameters of the proposed model in the categorical scenario

Number of Layer	Layer Type	Output Shape	Parameters
1	Conv2D	(198, 198, 32)	896
2	MaxPooling2D	(99, 99, 32)	0
3	Conv2D	(97, 97, 64)	18 496
4	MaxPooling2D	(48, 48, 64)	0
5	Conv2D	(46, 46, 64)	36 928
6	MaxPooling2D	(23, 23, 64)	0
7	Conv2D	(21, 21, 128)	73 856
8	MaxPooling2D	(10, 10, 128)	0
9	Conv2D	(8, 8, 128)	147 584
10	MaxPooling2D	(4, 4, 128)	0
13	Flatten	(2048)	0
14	Dropout	(2048)	0
15	Dense	(512)	1 049 088
16	Dense	(1)	2 052
Total trainable parameters: 1 328 900			

Source: Authors

also achieved outstanding results solving problem such as image classification, speech recognition, autonomous driving, text-to-speech conversion, language translation, targeted advertising, or natural language processing. When enough labeled data is available to solve the problem, supervised learning can achieve very good performance on many tasks, for example, in image processing. For other problems, where there is insufficient labeled data, there are various deep learning techniques to enhance the model performance, such as semi-supervised and unsupervised learning with unlabeled data or transfer learning approaches using pre-trained models. A disadvantage of transfer learning approaches is that they end up in very big and heavy models, thus making it difficult to deploy them on devices with limited capacities. They may also require Internet access when they are deployed in the cloud, which is not always possible in remote or poor regions. This study presents new models for COVID-19 detection and other pneumonia cases using CNNs and X-ray images. CNNs are the state-of-art methods when it comes to image classification, and they provide better results in non-linear problems with highly dimensional spaces. The proposed CNN models were developed to provide accurate diagnostics in more output classes, while the accuracy was increased in comparison with previous studies. The proposed models prevented overfitting by following 2 actions: (1) increasing the data set size (considering more data repositories and using data augmentation techniques) while classification scenarios are balanced, (2) adding regularization techniques such as dropout and performing hyperparameter optimization.

The impact of key hyperparameters such as batch size, learning rate, number of epochs, image resolution, activation function, number of convolutional layers, the size for each layer, and neurons in the dense layer were tested. Hyperparameter optimization is a difficult part that usually requires a lot of effort, time, computational resources, and extensive experimentations. However, by using modern deep

learning packages such as Hyperas and Hyperopt, extensive experimentation and hyperparameters optimization are automated, evaluating all the options for each hyperparameter in just one execution for each scenario. In previous research, the obtained results are biased and overfitted due to the huge network capacity compared with the small number of COVID-19 images, and hyperparameter optimization is done weakly and manually in just a few hyperparameters. It should be highlighted that larger networks will likely overfit, while simpler models are less likely to overfit than complex ones. The proposed models provided a satisfactory accuracy of 99,17% for binary classification (COVID-19 and Non-COVID) and 94,03% for 4-classes classification (COVID-19 vs. Normal vs. Bacterial Pneumonia vs. Viral Pneumonia), obtaining superior performance compared to other studies in the literature. Finally, the proposed models reduced the network capacity and size as much as possible, thus making the final models an option to be deployed locally on devices with limited capacities and without the need for Internet access. The developed models (available at <https://github.com/carlosbelman/COVID-19-Automated-Detection-Models/>) can also be deployed on a digital platform to provide immediate diagnostics.

In the future, the proposed models can be extended by incorporating more output categories and validating them by using more images. As the models were developed using Python and TensorFlow, the next step will be to deploy these models in devices with limited capacities, using Android and TensorFlow Lite, or through hybrid mobile applications using platforms such as Ionic and TensorFlow JS. In this way, the models can be deployed locally, fully automating the process of detection, and they will not require Internet access in the future, thus providing diagnosis in a few seconds, helping affected people and health centers immediately, or making them usable in remote regions affected by COVID-19 to overcome the lack of radiologists and experts.

Acknowledgements

The author would like to thank the Mexican Council of Science and Technology (CONACYT – Consejo Nacional de Ciencia y Tecnología) for financing this research by awarding a scholarship for postgraduate studies (under CVU 773443).

References

- Abadi, M., Agarwal, A., Barham, P., and Brevdo, E. (2015). *TensorFlow: Large-Scale Machine Learning on Heterogeneous Systems*. <https://www.tensorflow.org/>
- American College of Radiology (ACR) (2020, March 11). *ACR Recommendations for the use of Chest Radiography and Computed Tomography (CT) for Suspected COVID-19 Infection*. <https://www.acr.org/Advocacy-and-Economics/ACR-Position-Statements/Recommendations-for-Chest-Radiography-and-CT-for-Suspected-COVID19-Infection>
- Bergstra, J. (2021). *hyperopt PyPI*. <https://pypi.org/project/hyperopt/>
- Beysolow II, T. (2017). *Introduction to Deep Learning Using R - A Step-by-Step Guide to Learning and Implementing Deep Learning Models Using R*. Apress.
- Boccaletti, S., Ditto, W., Mindlin, G., and Atangana, A. (2020). Modeling and forecasting of epidemic spreading: The case of Covid-19 and beyond. *Chaos, Solitons and Fractals*, 135, 109794. 10.1016/j.chaos.2020.109794
- Castillo, O. and Melin, P. (2020). Forecasting of COVID-19 time series for countries in the world based on a hybrid approach combining the fractal dimension and fuzzy logic. *Chaos, Solitons and Fractals*, 140, 11024. 10.1016/j.chaos.2020.110242
- Castillo, O. and Melin, P. (2021). A Novel Method for a COVID-19 Classification of Countries Based on an Intelligent Fuzzy Fractal Approach. *Healthcare*, 9(2), 196. 10.3390/healthcare9020196
- Chaudhary, P. K. and Pachori, R. B. (2020). Automatic diagnosis of COVID-19 and pneumonia using FBD method. In IEEE (Eds.) *International Conference on Bioinformatics and Biomedicine (BIBM)* (pp. 1-7). IEEE. 10.1109/BIBM49941.2020.9313252
- Chen, G., Chen, P., Shi, Y., Hsieh, C.-Y., Liao, B., and Zhang, S. (2019). *Rethinking the Usage of Batch Normalization and Dropout in the Training of Deep Neural Networks*. arxiv preprint. <https://arxiv.org/abs/1905.05928>
- Chen, X.-W. And Lin, X. (2014). Big Data Deep Learning: Challenges and Perspectives. *IEEE Access*, 2, 514-525. 10.1109/ACCESS.2014.2325029
- Chollet, F. (2015). *Keras*. <https://keras.io>
- Chollet, F. (2017). Xception: Deep Learning with Depthwise Separable Convolutions. In IEEE (Eds.) *Proceedings of the 2017 IEEE Conference on Computer Vision and Pattern Recognition (CVPR)* (pp. 1800-1807). IEEE. 10.1109/CVPR.2017.195
- Chollet, F. (2018). *Deep Learning with Python*. Manning Publications Co.
- Chung, M., Bernheim, A., Mei, X., Zhang, N., Huang, M., Zeng, X., Cui, J., Xu, W., Yang, Y. Fayad, Z. A., Jacobi, A., Li, K., Li, S, and Shang, H. (2020). CT Imaging Features of 2019 Novel Coronavirus (2019-nCoV). *Radiology*, 295(1), 202-207. 10.1148/radiol.2020200230
- Chung, A. (2020a). *Actualmed COVID-19 chest x-ray data initiative*. <https://github.com/agchung/Actualmed-COVID-chestxray-dataset>
- Chung, A. (2020b). *Figure 1 COVID-19 Chest X-Ray Dataset Initiative*. <https://github.com/agchung/Figure1-COVID-chestxray-dataset>
- Duchi, J., Hazan, E., and Singer, Y. (2011). Adaptive subgradient methods for online learning and stochastic optimization. *Journal of Machine Learning Research*, 12(61), 2121-2159.
- Fasihi, M. and Mikhael, W. (2016). Overview of current biomedical image segmentation methods [Conference presentation]. *International Conference on Computational Science and Computational Intelligence*, Las Vegas, NV, United States of America. 10.1109/SCI.2016.0156

- Gaur, P., Pachori, B. R., Wang, H., and Prasad, G. (2015). An Empirical Mode Decomposition Based Filtering Method for Classification of Motor-Imagery EEG Signals for Enhancing Brain-Computer Interface. In IEEE (Eds.) *International Joint Conference on Neural Networks (IJCNN)* (pp. 1-7). IEEE. 10.1109/IJCNN.2015.7280754
- He, K., Zhang, X., Ren, S., and Sun, J. (2016). Deep Residual Learning for Image Recognition. In IEEE (Eds.) *Proceedings of the 2016 IEEE Conference on Computer Vision and Pattern Recognition (CVPR)* (pp. 770-778). IEEE.
- Italian Society of Medical and Interventional Radiology (ISMIR) (2020). *COVID-19 DATABASE*. <https://www.sirm.org/en/category/articles/covid-19-database/>
- Jacobi, A., Chung, M., Bernheim, A., and Eber, C. (2020). Portable chest X-ray in coronavirus disease-19 (COVID-19): A pictorial review. *Clinical Imaging*, 64, 35-42. 10.1016/j.clinimag.2020.04.001
- James, G., Witten, D., Hastie, T., and Tibshirani, R. (2013). *An Introduction to Statistical Learning with Applications in R*. Springer.
- Kaggle Inc. (2020). *Chest X-Ray Images (Pneumonia)*. <https://www.kaggle.com/paultimothymooney/chest-xray-pneumonia>
- Kingma, D. and Ba, J. (2014). *Adam: a method for stochastic optimization*. *arXiv preprint*. <https://arxiv.org/abs/1412.6980v5>
- Lee, J., Bagheri, B., and Kao, H.-A. (2014). A Cyber-Physical Systems architecture for Industry 4.0-based manufacturing systems. *Manufacturing Letters*, 3, 18-23. 10.1016/j.mfglet.2014.12.001
- Liu, S. and Deng, W. (2015). Very deep convolutional neural network based image classification using small training sample size. In IEEE (Eds.) *Proceedings of the 2015 3rd IAPR Asian Conference on Pattern Recognition (ACPR)* (pp. 730-734). IEEE. 10.1109/ACPR.2015.7486599
- Melin, P., Monica, J., Sanchez, D., and Castillo, O. (2020). Multiple Ensemble Neural Network Models with Fuzzy Response Aggregation for Predicting COVID-19 Time Series: The Case of Mexico. *Healthcare*, 8(2), 181. 10.3390/healthcare8020181
- Nayak, S. R., Nayak, D. R., Sinha, U., Arora, V., and Pachori, R. B. (2021). Application of deep learning techniques for detection of COVID-19 cases using chest X-ray images: A comprehensive study. *Biomedical Signal Processing and Control*, 64, 102365. 10.1016/j.bspc.2020.102365
- Nguyen, H., Kieu, L., Wen, T., and Cai, C. (2018). Deep learning methods in transportation domain: a review. *IET Intelligent Transport Systems*, 12(9), 998-1004. 10.1049/iet-its.2018.0064
- Ozturk, T., Talo, M., Yildirim, E., Baloglu, U., and Yildirim, O. (2020). Automated detection of COVID-19 cases using deep neural networks with X-ray images. *Computers in Biology and Medicine*, 121, 103792. 10.1016/j.compbiomed.2020.103792
- Pachori, R., Sharma, R., and Patidar, S. (2015). Classification of Normal and Epileptic Seizure EEG Signals Based on Empirical Mode Decomposition. In Zhu, Q. and Azar, A. (Eds.). *Complex System Modelling and Control Through Intelligent Soft Computations* (pp. 367-388). Springer. 10.1007/978-3-319-12883-2_13
- Patidar, S. and Pachori, R. B. (2013). Segmentation of cardiac sound signals by removing murmurs using constrained tunable-Q wavelet transform. *Biomedical Signal Processing and Control*, 8(6), 559-567. 10.1016/j.bspc.2013.05.004
- Pedamonti, D. (2018). *Comparison of non-linear activation functions for deep neural networks on MNIST classification task*. *arXiv preprint*. <https://arxiv.org/abs/1804.02763v1>
- Picciano, A. (2012). The Evolution of Big Data and Learning Analytics in American Higher Education. *Journal of Asynchronous Learning Networks*, 16(3), 9-20. 10.24059/olj.v16i3.267
- Pumperla, M. (2021). *hyperas PyPI*. <https://pypi.org/project/hyperas/>
- Python Software Foundation. (2020). *Python*. <https://www.python.org/>
- Raschka, S. and Mirjalili, V. (2017). *Python Machine Learning*. Packt Publishing.
- Rong, G., Mendez, A., Assi, E., Zhao, B., and Sawan, M. (2020). Artificial Intelligence in Healthcare: Review and Prediction Case Studies. *Engineering*, 6(3), 291-301. 10.1016/j.eng.2019.08.015
- Rosebrock, A. (2017). *Deep Learning for Computer Vision with Python*. PyImageSearch.
- SAS Institute Inc. (2018, May 9). *Machine Learning: What it is and why it matters* | SAS. https://www.sas.com/en_us/insights/analytics/machine-learning.html#machine-learning-importance
- Srivastava, N., Hinton, G., Krizhevsky, A., Sutskever, I., and Salakhutdinov, R. (2014). Dropout: A Simple Way to Prevent Neural Networks from Overfitting. *Journal of Machine Learning Research*, 15(56), 1929-1958.
- Sun, T. and Wang, Y. (2020). Modeling COVID-19 epidemic in Heilongjiang province, China. *Chaos, Solitons and Fractals*, 138, 109949. 10.1016/j.chaos.2020.109949
- Szegedy, C., Vanhoucke, V., and Ioffe, S. J. (2016). Rethinking the inception architecture for computer vision. In IEEE (Eds.) *Proceedings of the IEEE Conference on Computer Vision and Pattern Recognition* (pp. 2818-2826). IEEE. 10.1109/CVPR.2016.308
- Varela-Santos, S. and Melin, P. (2020). A new modular neural network approach with fuzzy response integration for lung disease classification based on multiple objective feature optimization in chest X-ray images. *Expert Systems with Applications*, 168, 114361. 10.1016/j.eswa.2020.114361
- Varela-Santos, S. and Melin, P. (2021). A new approach for classifying coronavirus COVID-19 based on its manifestation on chest X-rays using texture features and neural networks. *Information Sciences*, 545, 403-414. 10.1016/j.ins.2020.09.041

- Wang, J., Ma, Y., Zhang, L., Gao, R., and Wu, D. (2018). Deep learning for smart manufacturing: Methods and applications. *Journal of Manufacturing Systems*, 48C, 144-156. 10.1016/j.jmsy.2018.01.003
- Wang, S.-H., Nayak, D. R., Guttery, D., Zhang, X., and Zhang, Y.-D. (2021). COVID-19 classification by CCSHNet with deep fusion using transfer learning and discriminant correlation analysis. *Information Fusion*, 68, 131-148. 10.1016/j.inffus.2020.11.005
- World Health Organization (WHO) (2021, March 30). *WHO Coronavirus (COVID-19) Dashboard*. <https://covid19.who.int/>
- World Health Organization (WHO) (2020). *Coronavirus*. https://www.who.int/health-topics/coronavirus#tab=tab_1
- Yang, H., Kumara, S., Bukkapatnam, S., and Tsung, F. (2019). The Internet of Things for Smart Manufacturing: A Review. *IJSE Transactions*, 51(11), 1190-1216. 10.1080/24725854.2018.1555383
- Zhang, Y., Zhang, X., and Zhu, W. (2021). ANC: Attention Network for COVID-19 Explainable Diagnosis Based on Convolutional Block Attention Module. *Computer Modeling in Engineering & Sciences*, 127(3), 1037-1058. 10.32604/cmescs.2021.015807
- Zhou, M., Duan, N., Liu, S., and Shum, H.-Y. (2020). Progress in Neural NLP: Modeling, Learning, and Reasoning. *Engineering*, 6(3), 275-290. 10.1016/j.eng.2019.12.014
- Zhou, S., Wang, Y., Zhu, T., and Xia, L. (2020). CT features of coronavirus disease 2019 (COVID-19). *American Journal of Roentgenology*, 214(6), 1287-1294. 10.2214/AJR.20.22975

Design and Implementation of Network Monitoring System for Campus Infrastructure Using Software Agents

Diseño e implementación de un sistema de monitoreo de red para infraestructura de campus usando agentes de software

Rodrigo I. Espinel-Villalobos¹, Erick Ardila-Triana², Henry Zarate-Ceballos³, and Jorge E. Ortiz-Triviño⁴

ABSTRACT

In network management and monitoring systems, or Network Management Stations (NMS), the Simple Network monitoring Protocol (SNMP) is normally used, with which it is possible to obtain information on the behavior, the values of the variables, and the status of the network architecture. However, for large corporate networks, the protocol can present latency in data collection and processing, thus making real-time monitoring difficult. This article proposes a multi-agent system based on layers, with three types of agents. This includes the collector agent, which uses a Management Information Base (MIB) value to collect information from the network equipment, an input table of information from the network devices for the consolidator agent to process the collected data and leave it in a consumable format, and its subsequent representation by the application agent as a web service, in this case, as a heat map.

Keywords: distributed systems, multi-agent system, network monitoring, parallelization, SNMP

RESUMEN

En los sistemas de administración y monitoreo de redes o *Network Management Stations* (NMS), normalmente se utiliza el protocolo *Simple Network Monitoring Protocol* (SNMP), con el cual es posible obtener información sobre el comportamiento, los valores de las variables y el estado de la arquitectura de red. Sin embargo, para las grandes redes corporativas, el protocolo puede presentar latencia en la recopilación y el procesamiento de datos, lo que dificulta el monitoreo en tiempo real. Este artículo propone un sistema multi-agente basado en capas con tres tipos de agentes. Esto incluye el agente recolector que utiliza un valor MIB (Management Information Base) para recolectar información de los equipos de red, una tabla de entrada de información de los dispositivos de red para que el agente consolidador realice el procesamiento de los datos recolectada y los deje en un formato consumible y su subsiguiente representación por parte del agente de aplicación como un servicio web, en este caso como un mapa de calor.

Palabras clave: sistemas distribuidos, sistema multi-agente, monitoreo de redes, paralelización, SNMP

Received: May 29th, 2020

Accepted: June 2nd, 2021

Introduction

Today's networks are dynamic, and numerous transactions per second between different clients, applications, sensors, and devices are needed to deploy new services, which consumes the information generated throughout the network ecosystem. Traditional communication between network devices (Core and End Users) generates transactions in traffic control. In most cases, the Simple Network Monitoring Protocol (SNMP) is used to analyze traffic, with the purpose of allowing the administrators to change and monitor the state of devices that support the protocol, for instance, by shutting down an interface, checking the users on a Vlan, counting the users' sessions, etc. (Stallings, 1998; Gonçalves *et al.*, 2012). The SNMP has two types of entities: managers and agents. Managers work in Network Management Stations (NMS) and receive messages and traps from SNMP agents. SNMP agents, in turn, provide management information to the NMS. The agent is software-executed on a network device and incorporated into the operative system by the user-administrator. The SNMP protocol uses a hierarchical structure called Man-

agement Information Base (MIB). This structure is a database of managed objects containing information about the devices and the network. The MIB has two types of objects: scalar

¹Systems Engineer, Universidad Nacional de Colombia, Colombia. M.Sc. in Cybersecurity, INSA Centre Val de Loire. Affiliation: Researcher, Universidad Nacional de Colombia, Colombia. E-mail: riespinelv@unal.edu.co

²Systems Engineer, Universidad Nacional de Colombia, Colombia. M.Sc. in Telecommunications Engineering, Universidad Nacional de Colombia, Colombia. Affiliation: Chief of Communications Networks, Universidad Nacional de Colombia, Colombia. E-mail: eardilat@unal.edu.co

³Electronic Engineer, Universidad Central, Colombia. Ph.D. in Computer Science, Universidad Nacional de Colombia, Colombia. Affiliation: Researcher, Universidad Nacional de Colombia, Colombia. E-mail: hzaratec@unal.edu.co

⁴Systems Engineer, Universidad Nacional de Colombia, Colombia. Ph.D. in Computer Science, Universidad Nacional de Colombia, Colombia. Affiliation: Associate Professor, Universidad Nacional de Colombia, Colombia. E-mail: jeortizt@unal.edu.co

How to cite: Espinel, R., Ardila-Triana, E., Zárate, H., and Ortiz, J. E. (2022). Design and Implementation of Network Monitoring System for Campus Infrastructure Using Software Agents. *Ingeniería e Investigación*, 42(1), e87564. <https://doi.org/10.15446/ing.investig.v42n1.87564>



Attribution 4.0 International (CC BY 4.0) Share - Adapt

and tabular. These are useful to present the NMS information. The Object Identifier (OID) is organized in a tree-like hierarchy as a set of integers separated by dots, with the purpose of instantiating objects with a unique ID, for instance, devices and their function (router, switch), interface name, interface state, and so on (Kaushik, 2010). SNMP's modularity helps it evolve through three major versions and find widespread use and acceptance. The IETF recognizes SNMP version 3, defined by RFC 3411 and RFC 3418, as the current standard version of SNMP. The IETF has designated SNMPv3 as a full Internet standard, the highest level of maturity for an RFC. In practice, SNMP implementations often support multiple versions: typically, SNMPv1, SNMPv2c, and SNMPv3. SNMP is a useful and versatile protocol that can work with other network information data sets, neural networks, machine learning systems, multi agent systems, or other monitoring platforms. For instance, in Sánchez *et al.* (2013) machine learning uses clustering and visualization techniques to identify and locate anomalous SNMP situations, and thus get an idea of network performance. Other approaches are focused on information security and cybersecurity to detect network attacks based on machine learning and event correlation (Hwoij *et al.*, 2020; Al-Naymat *et al.*, 2019).

Our approach is a campus network testbed based on a multi-agent system with mobile agents to monitor and present the location of users on a campus network via the SNMP protocol. The proposed model has three types of agents, *i*) the collector agent, *ii*) the consolidator agent, and *iii*) the painter agent.

This paper is organized as follows: the Methodology section shows the process used to design and implement the model; the Related Work section presents a review of existing solutions similar to our proposal; the Framework Architecture section introduces the reference models adopted in the debate for the system architecture and describes its components; the Use case section explains the implementation and its scope; the Results section describes the implemented prototype and the experimental demonstration of the proposed solution, showing its effectiveness; and, finally, the conclusions are presented in the Conclusions section, along with future work.

Methodology

Based on previous applications used on the university campus to measure the number of users per building, a new model is proposed that incorporates a multi-agent architecture to optimize data collection times on the network. A multi-agent model with SNMP was designed, developed, and implemented to allow comparative measurements between the two systems, as well as to verify the change in collection response times. The procedure is classified in three stages: (I) a description of the multi-agent architecture and the different layers and agents of the proposed model; (II) a description of the implementation and scope of the model; (III) an analysis of results and proposals for improvement.

Related Work

System monitoring and detection through the SNMP protocol with *snmpwalk* command routines are a solution to monitor and collect information about the network. However, this approach has huge response times, and it decreases the device's performance by consuming computing resources such as CPU and memory while querying on the MIB. The model presented by Brattstorm and Morreale (2017) uses metrics, collection, storage, presentation, and alerting to notify the system or device administrator or central control process of abnormal system or device behavior, where presentation is the way of displaying control data and issuing alerts. Another approach is proposed by Affandi *et al.* (2015) with a network mapping tool that sends early warnings via Short Message Service (SMS). The process starts with network mapping using the SNMP agent on all network interfaces. The information contained in the agents is retrieved and processed as Transport Control Protocol (TCP) traffic. Finally, a monitoring system checks TCP traffic and the use of computing resources. This process allows the bandwidth and resources optimization to manage the emergency systems and control some variables via SNMP agents.

An implementation to monitor networks and systems is proposed by some authors with a generic matrix grammar (Min, 2011; García *et al.*, 2014). This framework uses some protocols to display and monitor the system, such as Windows Management Instrumentation (WMI), Computer Integrated Manufacturing (CIM), and SNMP to remotely collect and manage NMS data. The authors propose a monitoring automation engine with a matrix analyzer into the multi-agent-based solution. Additionally, the most widely used monitoring information systems use a traditional *snmpwalk* command to enable system integration with any management tool with SNMP support such as Nagios (Barth, 2008), SNMP MIB Browser Android Tool (Hidalgo and Gamess, 2014), and Manage Engine MIB Browser Free Tool (Free SNMP Walk Tool for Windows and Linux, n.d.). A layered approach is introduced by Wan *et al.* In this paper, a smart emergency system is proposed. This model collects data from urban areas, and its most important task is to detect an emergency and handle it in a timely fashion to ensure protect human integrity and the continuous operation of critic infrastructures.

Other authors have developed SNMP and multi-agent systems (Barruio *et al.*, 2017; Moreira *et al.*, 2016; Torre and Yucelen, 2018). The first model is a proposal for a mechanism to provide flexibility and dynamism using virtual agent organizations (VO) embedded in different wireless sensors, which are embedded in devices with limited computational resources. The PANGAEA framework incorporates features to the wireless sensor network such as adaptability, reorganization and learning capabilities, its agents have a control role in automatically collecting and processing information. This approach allows using the MAS as a virtual organization to define the structure, roles, and hierarchies, thus regulating the interaction and communications between agents and network devices via SNMP and MIB analysis. The second approach uses the SNMP protocol to manage ubiquitous

systems through behavior graphs and a metric called the expected behavior representation (GoES). This method allows the link between SNMP agents and commercial off-the-shelf systems (COTS). The approach consists of characterizing the context of devices and testing whether they are able to understand what other systems are doing by monitoring their state. Finally, the approach with mobile agents described by Madi and Alkasasbeh (2019) is a simulation with a Omnet++ network simulator that aims to use the mobile agent on the network with different amounts of nodes (5, 10, 15, 20, and 30 nodes in the proposed scenario). The objective is to probe an algorithm to improve SNMP queries using two type of agents: link and data agents. The link agent is responsible for discovering the network and storing the connected nodes in the home server. The data agent is responsible for data retrieval.

Another approach focused on the choice of a methodology to design and implement multi-agent systems to design the monitoring system, as shown in Lin and Jiang (2014), to introduce the design steps and organizational methods such as GAIA and Ingenia. Based on the methodological approach, Isaza *et al.* used JADE as a multi-agent framework and the GAIA methodology to monitor 32 personal computers.

There are models without the SNMP protocol to monitor university campus networks with specific architectures, as is the case of lot, deployed as a platform to characterize energy consumption (Moura *et al.*, 2021) in order to manage electrical resources or electrical grids (Chiadone *et al.*, 2019). Another approach used to monitor networks includes Software Defined Networks (SDN) techniques to monitor traffic flows on lot devices. These models need two psychic channels to monitor the network: the data plane and the control plane (Pashamoktari *et al.*, 2020).

Finally, network monitoring has evolved into the field of cybersecurity as a monitoring system on a campus and industry infrastructure to identify and mitigate potential vulnerabilities (Laštovička *et al.*, 2020), in addition to analyzing the network flow with recurring neural networks (Yang *et al.*, 2020), wireless analysis (Jin *et al.*, 2019; Allahham and Rahman, 2018), or risk assessment (Awang *et al.*, 2020).

Our approach is an intermediate model proposed to monitor campus network core devices (routers, switches, and manageable network devices) and as a possible platform to deploy some monitoring systems for other variables taken from sensors, personal computers, or other linked devices within the campus network.

Framework Architecture

Our approach contemplates a three-layer architecture as shown in Figure 1 with mobile agents and a dispersion strategy to scan the campus network. Each of these layers has a specific task to accomplish an objective and finally obtain the number of users present in the network as a heat map. All the services are deployed on an virtual server on the private cloud infrastructure of the University.

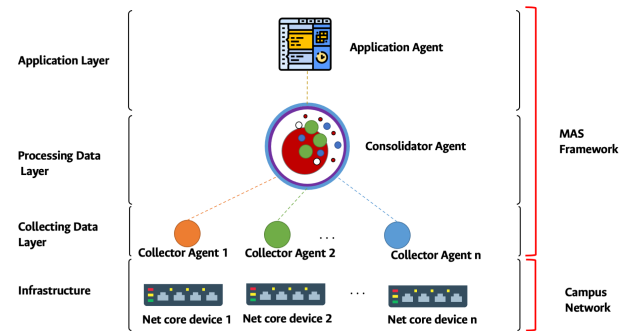


Figure 1. Proposed multi-agent system architecture.

Source: Authors

Data collection layer: It is the bottom layer that establishes communication with the SNMP agents using the Pysnmp library to make the query with the OID code on the MIB. It contains the collector agents (mobile agent).

Data processing layer: It is the intermediate layer that consolidates all the data obtained from all the collecting agents. It is also tasked with deploying and organizing the collecting agents. It summarizes, analyzes, and draws statistics from the data obtained.

Application layer: Its is the top layer that displays the collected information. It contains the application agent that creates the different web files to present data in the form of a heat map. Furthermore, all the data obtained from the preceding layers are also available in tables for ease of use and analysis.

PySNMP library

The library that has been used for our implementation is PySNMP (PySNMP 4.4.12, n.d), a free and open source implementation of the v1/v2c/v3 SNMP engine that is distributed under a 2-clause BSD license. It manages different layers as an evolution of SNMP We have used only the first layer of Pysnm2 in the implementation (Figure 2). This layer covers a basic and low-level protocol scope (SNMP v1/v2) in order to make a simple implementation and use all the power of the SNMP API to use the core functions of the SNMP protocol. Figure 2 shows the modular architecture of the library. Not all functionalities have been used in this work, but it can provide a handful of easy to use tools.

A brief description of the library is presented below:

- **SNMP engine:** it is a central object that controls the other components of the SNMP system.
- **Transport subsystem:** it is used to send SNMP messages and accept them from the network. The I/O subsystem consists of an abstract dispatcher and one or more abstract transport classes.
- **Message and PDU dispatcher:** its main responsibilities include dispatching PDUs from SNMP applications through various subsystems, all the way down to the transport dispatcher, as well as passing SNMP messages from the network up to SNMP applications.

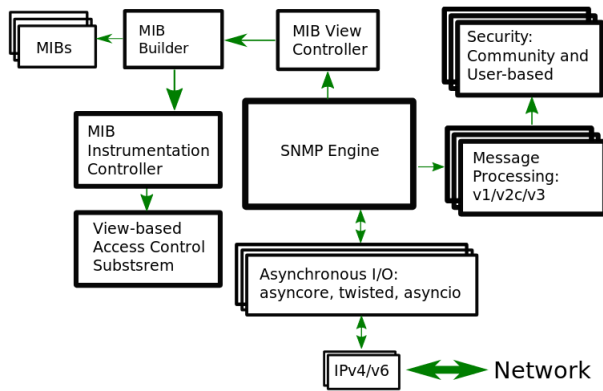


Figure 2. PySNMP library.

Source: Authors

- **Message Security Modules:** it performs message authentication and/or encryption. At the time of this writing, the User-Based (for v3) and Community (for v1/2c) modules are implemented in PySNMP. All security modules share the standard API used by the message processing subsystem.
- **Message processing modules:** it handles message-level protocol operations for current and possibly future versions of the SNMP protocol. Most importantly, they include message parsing/building and possibly invoke security services when required.
- **MIB modules:** used by the SNMP engine to maintain its configuration and operational statistics.

Data collection layer-collector agent

The collector agent has only one task: to communicate with an SNMP agent. These agents receive all the information needed from the preceding layers: the SNMP community name and the node target. The work of these agents is entirely reactive, as they only respond to the demands of the second layer. They manage errors that can be generated during SNMP communication and report them to the next layer; the algorithm overview is shown in Algorithm 1. In order to get the expected values, some parameters are needed to identify certain core switches in the network. Some of the given parameters are switch number, rack number, telecommunications enclosure room ID and its respective floor number, and building number of the university campus to which the device belongs (according to the building nomenclature). All these fields have three descriptive characters.

As shown in Algorithm 1, the work of each collector agent requires parameters such as lan, network scope, and SNMP community. The algorithm starts with a loop for every vlan on the switch. Each vlan is isolated from the others and, to make a more realistic measurement, all available vlans must be analyzed. Each of these changes the SNMP community, as a complement to SNMP validation. As a result, this validation is as follows: `SNMPCommunity@VLAN_NUMBER`. Communication problems may occur. Each SNMP request

that files are logged along with the switch IP address and the associated vlan. Once the work is finished, the agent moves on, and the result is taken by the consolidator agent.

Algorithm 1 Collector Agent

Require: IP Address - SNMP community - Vlans - Log File

```

Move
for Every Vlan do
    Create connexion SNMP
    Manipulate SNMP Response
    Report missed calls
end for
return Number of users

```

Listing 1: SNMP request

```

1 error_indication, error_status, error_index, var_bind_table =
  cmd_gen.nextCmd(cmdgen.CommunityData('{}@{}'.format(
    community_name, str(vlan))), cmdgen.UdpTransportTarget(
    (target, 161), timeout=1, retries=1),
    1.3.6.1.2.1.17.4.3.1.2')

```

The nextCmd method provided by the Pysnmp library allows to perform a snmpwalk operation by iterating over the MIB with `OID 1.3.6.1.2.1.17.4.3.1.2`. The `"dot1dTpFdbPort"` allows reading a table with the MAC addresses that have been seen through a given port. As we make use of an SNMP walk operation, we do not need to specify a port, but we go through all possible ports to get an accurate measurement.

Consolidation layer-consolidator agent

Agents in this layer are tasked with getting all the network devices to be scanned and deploying collector agents. This implementation, as shown in Algorithm 2, considers a pool of threads, each collector agent will manage its own thread, and the consolidator agent is responsible for synchronizing and managing the threads. The consolidator agent will call each agent, assign them a target and manage their response. The target is an IP address of the network devices. Each one of these threads has an independent execution. Communication between these execution time agents is asynchronous; hence, we can make use of distributed parallel processing at jobs (mobile agents), thus reducing network delay and execution time. When the collector agent completes its work, the consolidator agent has to examine the data. In this step, the consolidator agent logs some information in terms of performance or errors, with the objective of making statistics. Therefore, the data is sent to the presentation layer. The logic of this agent is presented as follows.

This agent receives information from the presentation layer as the SNMP community and the name of the file source. These parameters are given to the collector agents to accomplish their tasks. Here the input file is analyzed with a mapping between physical buildings, IP references and vlans. For each physical building, a log file is created with a pool of threads. Each thread is going to point to a network device in that building. After the execution of the mobile agents' collection is done, the results are logged and added to the statistics. The final data is exposed to the presentation layer. The input file is represented as follows:

Algorithm 2 Consolidator Agent

Require: List IP Addresses - List Vlans - SNMP Community

```

for IP address in list do
    Create thread
    Call Agent Collector
    Collect result
end for
Sum up results
Get statistics
return

```

- **Physical section:** Section code and name, switches in this section together with uplink port
- **Mapping:** Buildings names and codes, network device count, number of buildings
- **List of vlans:** Name, range IP.

Listing 2: SNMP request

```

1 for building in data:
2     with open(file_name, "a") as log_file:
3         log_file.write("Building: {} \n".format(building))
4     result = []
5     args = [[self.community_name, x, list_vlans, file_name,
6             ↪ faults]
7     for x in data[building]]
8     with mp.Pool() as pool:
9         for i in pool.imap_unordered(Collector.get_users,
10                                     ↪ args):
11             result.append(i)

```

In this part of the code, we iterate over the list of buildings, logging the obtained data. In line 7, a pool of collector agents are called. This call acts asynchronously using all the processors available in the machine through the PySNMP library. In line 8, the call to the collector mobile agents is made along with the information related to the device managed by SNMP.

Application layer-application agent

This layer is responsible for initializing the system and displaying the results, as shown in Algorithm 3. During the initialization, the consolidation agents are called and assigned their tasks. Once all the underlying layers (collection and consolidation) have finished their work, they send the results to the presentation layer, where they are computed, and a HTML file is created. This file contains the HTML code necessary to display a heat map, helped by the *OpenLayers* open source technology. To complete the map, the application agent takes the coordinates and publishes the information as a web server. Thus, all the University's buildings can be appropriately named and pointed in this map. These coordinates were taken in the geodetic coordinate system 'EPSG:4326' in order to make the data available for future use. Styles and actions modules (javascript) were created with a user-centered design approach. The web module is done, and a python script is responsible of serving web files to make them available over the network. The result is shown in Figure 6. The gradient color has a variation from 0 to 1 according to the *OpenLayers* specification. The weight of

each point on the map is calculated between the number of users present in the whole building versus the total number of people in the university, with red being the closest to 1, turning greener the farther away they are.

Algorithm 3 Presentation Agent

Require: Coordinates file, SNMP Community, Input File

```

Get Input parameters
Initialize MAS system
Initialize consolidator agent
Get physic coordinates
Get consolidation layer data
Create javascript heat map
Create HTML file

```

Use case

Monitoring a complex system such as a campus network requires mechanisms that efficiently verify the status of users and services on the network. For this experiment, the capacity of the proposed mechanism will be measured by verifying the number of connected users on campus. The empirical experiment was carried out in the facilities of Universidad Nacional de Colombia (Bogotá), which currently has 152 buildings, out of which 129 belong to the faculties, and the remaining 23 correspond to cultural and extension centers located at different points of the city. These facilities have an average of more than 40 000 end users, including undergraduate, postgraduate and extension students, professors, administrative staff, and the general public. At the data network level, there are 73 buildings interconnected to the wired network (optical fiber and ethernet), which have approximately 30 000 structured cabling points, and are distributed in 210 telecommunications enclosures. There are 620 network core devices (switches and routers), which provide approximately 15 000 wired network connections. The university has network management and monitoring systems, such as HP Network Node Manager and Cisco Prime, which are used to monitor network problems such as equipment failures, network loops, or resource saturation (memory, processor, or channel bandwidth) on network equipment. The information provided by these systems is consolidated, which includes the total number of connected users or the distribution of users per vlan. However, obtaining particular information as to how many users are connected in a building or on a specific floor is not possible in real time, so other systems are required to analyze the data, and more processing time is spent. With SNMP, it is possible to consult the network from the core equipment network by analyzing the information of the connected users with an SNMP walk agent. However, the time consumption and processing are too high for the network's monitoring needs.

To monitor and manage the quantity of users in a specific building or floor, the consolidator agent sends the collector agents from the server located in the main data center and checks the network management devices in each building. The second phase is to analyze the information from the collector agents and create the tables and data useful to

publish them on the web server, which managed by the application agent.

As shown in Figure 3, the experiment was deployed on Vmware vsphere 6.5, on a virtual server with 4 vcores (Physical core Intel(R) Xeon(R) CPU E5-2699 v3 @ 2.30GHz), 16 GB RAM, and 100 GB of storage. The operative system was Centos 7. The server works as a web server managed by the application agent; the MAS deployed on python uses the specific agent roles to first send the collector agents as a thread on the network. In some cases, the agent can be deployed and cloned on the server or embedded devices near the net device to collect the information. Mobility is limited, and it is possible to an ambient as a destination with an exposed port (the collector agent needs to know the route). Next, the collector agents return to the server or send the information collected from the net core device, i.e. the query on the MIB. The information is analyzed by the consolidator agent, and it creates information files to present on the application layer as a heat map and information table on the web server.

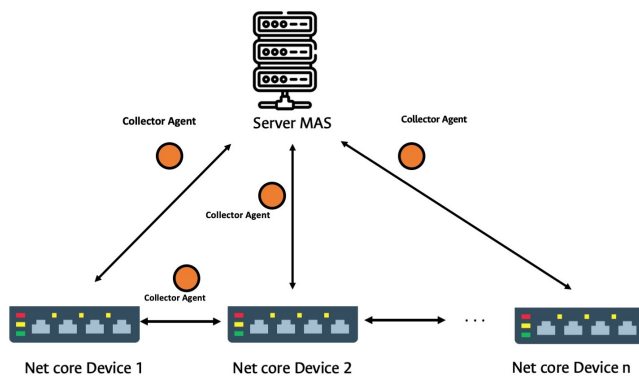


Figure 3. Infrastructure model.

Source: Authors

Results

The results of this empirical approach presented below are not comparable with other schemes proposed in the literature, such as those presented by Isaza *et al.* (2007), which are based on simulation environments. In the case of this work, it is an implementation that raises the technical rigor of the unloading of this system as a service without depending on frameworks such as JADE or Pangea, which are limited by the simulation scenario, that is, abstraction at the software level. In our case, the multi-agent system prototype used for network monitoring was implemented and deployed in computer equipment and network devices such as switches or a router.

The data to carry out the experiment was taken from two sources. The first is the legacy system that uses SNMP2 and sequentially goes one device at a time collecting data. The second source is the proposed multi-agent system model, where data are collected in parallel on the device. Measurements were made every hour, running both systems and measuring execution times. The results obtained from

multiple executions for three months of data are represented in graphs to facilitate comprehension.

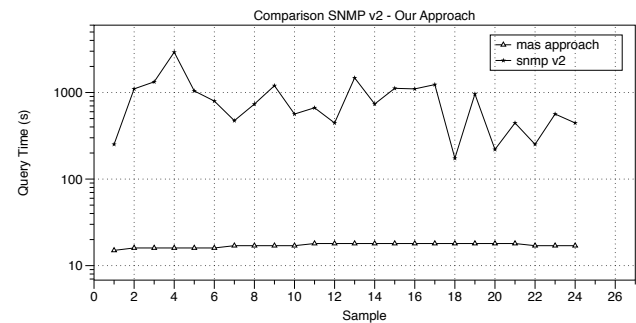


Figure 4. Time reduction; our approach (software agent approach) vs. the traditional mode (SNMP v2).

Source: Authors

In Figure 4, the analyzed data show how time is reduced because of the proposed architecture: a massive amount of agents going through the network with separated zones. Due to the way in which SNMP acts within the network, the time could be extended due to network traffic. This network traffic may cause some SNMP errors that affect the measurements and a certain number of users. Node query time with the traditional SNMP process walk takes more than one hour. In contrast, our approach with a multi-agent system architecture with some mobility reaches averages of 21,83 minutes on the wired campus network (122 network core devices at 73 buildings). During that period, the consolidation process, map creation, and publishing take place.

High traffic on the network and restrictions in the communications channel are some of the factors that make the collection time variable. In this sense, measurements take longer when there are more requests for navigation and service access by users, thus generating an additional load for the agents deployed over all the network devices registered in the system. This non-controllable variable is characterized in Figure 4, where we have the average measurements of the working days of the week. This behavior is close to the self-similar traffic. This sample allows additional management decisions to be made during this period of the day.

Other useful information to characterize user behavior is taken from the collector agents, such as the normal state of the wired network on campus. This information allows determining the amount of users per hour, as shown in Figure 5, with a peak of 6 500 users linked to the network at noon. It was taken on work days in a regular academic semester for three months. This information allows planning of network resources, like switches, vlans, or management systems, infrastructure changes, and new service design. It can also be used to identify anomalous behavior as a security thread.

All types of agents in the model are designed to be customizable, this gives them the ability to make more queries on other specific MIB. This feature allows scaling the solution and taking even more data from the equipment registered in the system, not only the number of users, as seen in Figure 5. The information collected by the system peaks at noon.

This behavior allows characterizing the network and serves as input for a fault detection system or to detect anomalies that can be categorized as cyber-attacks. Finally, the information is displayed on the web server and published on the University's LAN, as shown in Figure 6.

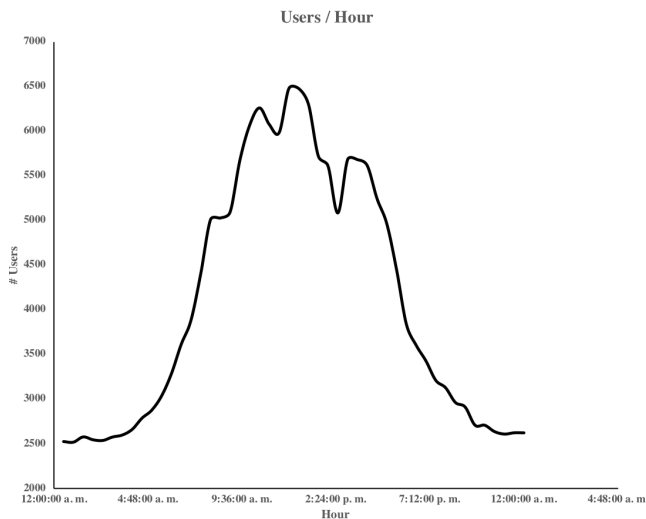


Figure 5. Mean Users campus linked to the network (data from three months).

Source: Authors

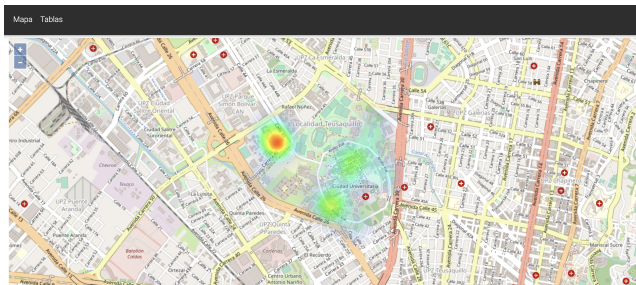


Figure 6. Application Agent (left: heat map; right: user detail table).

Source: Authors

Conclusions

In this work, we used a multi-agent system with some mobility characteristics to determine the number of users on the campus network and the density in specific buildings, reducing the data collection time by one third of the normal time. The agents were used to collect, analyze, and present information about the campus network in less time than traditional SNMP queries.

The obtained results also allow describing user behavior on campus. This information is useful as an input for modelling normal traffic for planning and decision-making for scaling and management of the campus network.

All types of agents in the model are designed to be customizable, this gives them the possibility of making more queries about other specific MIBs. This feature allows scaling the solution and taking even more data from the equipment

registered in the system, not just the number of users. The model would even allow the simultaneous use of several types of collecting agents, each one collecting data for a specific problem to be solved.

We demonstrated the effectiveness of our solution on a case study by implementing the MAS system on a campus network. Our approach allows using other tools apart from the the SNMP protocol for the monitoring or analysis of telecommunications networks. This design based on multiple agents is scalable to allow the incorporation of other protocols in the collection and analysis of the data to convert it into information or present it in the form of a report or graphical interface. It can be used at the level of energy consumption calculation, in a similar way as those presented in the literature (Laštovička *et al.*, 2020; Jin *et al.*, 2019; Allahham and Rahman, 2018), with the great difference of reducing the number of sensors required, that is, the hardware component is reduced through the estimation of energy levels based on theoretical models, and some agent of the developed system is in charge of computing them.

Traditional network management and monitoring schemes made up of the management server and manageable devices, based on the SNMP protocol, have allowed different manufacturers to guarantee a monitoring scheme, offer specialized products, and create their own MIBs. However, as the number of links and core devices within the network grows, latency becomes an additional element that constitutes a limitation for managing these resources, determining the status of the network, and having a complete view of a system. For this reason, the scheme, combined with multiple agents and parallel computing, allows making a network management scheme based on distributed architectures, applications, and algorithms that allow optimizing the use of network protocols, programming language libraries, and operating systems.

This approach increases the impact and reach of these processes, and it is the novelty of this prototype. In the same way, it is not limited or non-scalable like proprietary monitoring platforms such as Nagios or Cisco Monitoring, which only use the SNMP protocol to review records and some states of network devices.

Finally, thanks to the customization capacity of the agents, it is possible to define write-type agents, which would allow the system to modify parameters in the network to improve performance or prevent issues. As for future improvements to the model, focusing on the mobility of the consolidator agent is proposed, thus allowing the coexistence of several of these agents, allowing them in turn to run on different devices in the network. This would facilitate the use of the new capabilities of network equipment that allow running Python on their operating systems, which would most likely further reduce data collection times.

References

- Affandi, A., Riyanto, D., Pratomo, I., and Kusrahardjo, G. (2015). Design and implementation fast response system monitoring server using simple network management protocol

- (snmp). In IEEE (Eds.) *2015 International Seminar on Intelligent Technology and Its Applications (ISITIA)* (pp. 385-390). IEEE. 10.1109/ISITIA.2015.7220011
- Al-Naymat, G., Hambouz, A., and Al-Kasassbeh, M. (2019). Evaluating the impact of feature selection methods on snmp-mib interface parameters to accurately detect network anomalies. In IEEE (Eds.) *2019 IEEE International Symposium on Signal Processing and Information Technology (ISSPIT)* (pp. 1-6). IEEE. 10.1109/ISSPIT47144.2019.9001882
- Allahham, A. A. and Rahman, M. A. (2018). A smart monitoring system for campus using zigbee wireless sensor networks. *International Journal of Software Engineering and Computer Systems (IJSECS)*, 4(1), 1-14. 10.1109/ISSPIT47144.2019.9001882
- Awang, N., Ganthan, A., Samy, L. N., and Hassan, N. H. (2020). A review on risk assessment using risk prediction technique in campus network. *International Journal of Advanced Trends in Computer Science and Engineering*, 9(13), 251-257. 10.30534/ijatcse/2020/3891.32020
- Barriuso, A. L., Villarrubia-González, G., de Paz, J. F., Lozano, A., and Bajo, J. (2018). Combination of multi-agent systems and wireless sensor networks for the monitoring of cattle, *Sensors*, 18(1), 108. 10.3390/s18010108
- Barth, W. (2008). *Nagios: System and network monitoring*. No Starch Press.
- Brattstrom, M. and Morreale, P. (2017). Scalable agentless cloud network monitoring. In IEEE (Eds.) *2017 IEEE 4th International Conference on Cyber Security and Cloud Computing (CSCloud)* (pp. 171-176). IEEE. 10.30534/ijatcse/2020/3891.32020
- Chiandone, M., Dalle Feste, M., Bosich, D. and Sulligoi, G. (2019). Real-time monitoring and control system for trieste university campus electrical distribution grid. In IEEE (Eds.) *2019 IEEE Milan PowerTech* (pp. 1-5). IEEE. 10.30534/ijatcse/2020/3891.32020
- Franco, O. H., Castillo, L. F., Corchado, J. M., and Lopez, C. A. (2007). Multiagent system for software monitoring and users' activities in a network equipment. *Scientia et Technica*, 1(34), 387-393. 10.3390/s140610804
- Free SNMP Walk Tool for Windows and Linux (n.d.). <https://www.manageengine.com/products/mibbrowser-free-tool/>
- Garcia, F. P., Andrade, R., Oliveira, C. T., and de Souza, J. N. (2014). Epmost: An energy-efficient passive monitoring system for wireless sensor networks. *Sensors*, 14(6), 10804-10828. 10.3390/s140610804
- Gonçalves, P., Oliveira, J. L. and Aguiar, R. (2012). A study of encoding overhead in network management protocols. *International Journal of Network Management*, 22(6), 435-450. 10.1002/nem.1801
- Hidalgo, F. and Gamess, E. (2014). Integrating android devices into network management systems based on snmp. *International Journal of Advanced Computer Science and Applications*, 5(5), 1-8. 10.14569/IJACSA.2014.050501
- Hwoij, A., Al-kasassbeh, M., and Al-Fayoumi, M. (2020). *Detecting network anomalies using rule-based machine learning within snmp-mib dataset*. arXiv preprint. <https://arxiv.org/abs/2002.02368>
- Isaza, G., Mejía, M. H., Castillo, L. F., Morales, A., and Duque, N. (2012). Network management using multi-agents system. *ADCAIJ: Advances in Distributed Computing and Artificial Intelligence Journal*, 1(3), 49-54. 10.14201/ADCAIJ20121314954
- Jin, Y., Tomoishi, M., and Yamai, N. (2019). Anomaly detection by monitoring unintended dns traffic on wireless network. In IEEE (Eds.) *2019 IEEE Pacific Rim Conference on Communications, Computers and Signal Processing (PACRIM)* (pp. 1-6). IEEE. 10.1109/PACRIM47961.2019.8985052
- Kaushik, A. (2010). Use of open source technologies for enterprise server monitoring using snmp. *International Journal on Computer Science and Engineering*, 2(7), 2246-2252.
- Laštovička, M., Husák, M., and Sadlek, L. (2020). Network monitoring and enumerating vulnerabilities in large heterogeneous networks. In IEEE (Eds.) *NOMS 2020-2020 IEEE/IFIP Network Operations and Management Symposium* (pp. 1-6). IEEE. 10.1109/NOMS47738.2020.9110394
- Li, X. and Jiang, T. (2014). Design and implementation of the campus network monitoring system. In IEEE (Eds.) *2014 IEEE Workshop on Electronics, Computer and Applications* (pp. 117- 119). IEEE. 10.1109/IWECA.2014.6845571
- Madi, N. and Alkasassbeh, M. (2019). *Collecting mib data from network managed by snmp using multi mobile agents*. arXiv preprint. <https://arxiv.org/abs/1909.02547>
- Min, W. (2011). Distributed network resources monitoring based on multi-agent and matrix grammar. In IEEE (Eds.) *2011 Fourth International Symposium on Parallel Architectures, Algorithms and Programming (PAAP)* (pp. 136-140). IEEE. 10.1109/PAAP.2011.25
- Moreira, R. S., Morla, R. S., Moreira, L. P., and Soares, C. (2016). A behavioral reflective architecture for managing the integration of personal ubicomp systems: automatic snmp-based discovery and management of behavior context in smart-spaces. *Personal and Ubiquitous Computing*, 20(2), 229-243. 10.1109/PAAP.2011.25
- Moura, P., Moreno, J. I., López-López, G., and Álvarez-Campana, M. (2021). Iot platform for energy sustainability in university campuses, *Sensors*, 21(2), 357.
- Pashamokhtari, A., Gharakheili, H. H., and Sivaraman, V. (2020). Progressive monitoring of iot networks using sdn and cost-effective traffic signatures. In IEEE (Eds.) *2020 Workshop on Emerging Technologies for Security in IoT (ETSecIoT)* (pp. 1-6). IEEE. 10.1109/ETSecIoT50046.2020.00005
- Pysnmp 4.4.12 (n.d.). *Pysnmp 4.4.12*. <https://pypi.org/project/pysnmp/>
- Sánchez, R., Herrero, A., and Corchado, E. (2013). Visualization and clustering for snmp intrusion detection. *Cybernetics and Systems*, 44(6-7), 505-532. 10.1080/01969722.2013.803903

- Stallings, W. (1998). *SNMP, SNMPv2, SNMPv3, and RMON 1 and 2*. Addison-Wesley Longman Publishing Co., Inc. 10.1109/COMST.1998.5340405
- Torre, G. D. L. and Yucelen, T. (2018). Adaptive architectures for resilient control of networked multiagent systems in the presence of misbehaving agents. *International Journal of Control*, 91(3), 495-507. 10.1080/00207179.2017.1286040
- Wan, S., Lu, J., Fan, P., and Letaief, K. B. (2017). To smart city: Public safety network design for emergency. *IEEE Access*, 6, 1451-1460. 10.1109/ACCESS.2017.2779137
- Yang, C., Liu, J., Kristiani, E., Liu, M., You, I., and Pau, G. (2020). Netflow monitoring and cyberattack detection using deep learning with ceph. *IEEE Access*, 8, 7842-7850. 10.1109/ACCESS.2019.2963716

Instructions for Authors

Editorial Committee reserves the copyright to printing any material and its total or partial reproduction, as well as the right to accept submitted material or reject it. It also reserves the right to make any editorial modification which it thinks fit. In such event, the author of the submitted material in question will receive the evaluators' recommendations for changes to be made in writing. If an author accepts them, the revised (or rewritten) article must be submitted with the suggested changes having been made by the date fixed by the journal to guarantee its publication in the programmed issue.

The process to be followed for publishing an article in the journal

The article must be uploaded into the journal's OJS website, see the guidelines for article submission in the Authors guide section in our website <http://www.revistas.unal.edu.co/index.php/ingenv/article/view/59291/56815>. Any manuscript must be sent using journal's template (6 pages length max.) and must be accompanied by the license agreement, addressed to the journal's editor, Prof. Andrés Pavas, stating that all authors involved in the work in question agree to it being submitted for consideration in the *Ingeniería e Investigación* journal.

Article and License templates are available on:
<http://www.revistas.unal.edu.co/index.php/ingenv/index>

Once an article has been received by the journal, the corresponding author will be notified by e-mail and the peer-review process will be begun. Following this evaluation, authors will then be informed whether their article has been accepted or not. If accepted, authors must deal with the respective corrections recommended by the evaluators and the Editorial Committee's final decision. If it is to be published.

Content

All articles being considered by the committee for possible publication in the *Ingeniería e Investigación* journal must consist of the following parts:

- Title, abstract and keywords must be written in Spanish and English. The title must clearly explain the contents of the article in question, written in normal title form and be preferably brief. The abstract should contain around 200 words in Spanish and English, as well as including the methods and materials used, results obtained and conclusions drawn.
- An Introduction must be given. It must describe article's general purpose, including its main objective, referring to any previous work and the scope of the current article.
- Conclusions must be drawn. This section must provide the implication of the results found and their relationship to the proposed objective.
- Bibliographical references must be given (an explanation and example of how to set them out is given later on).
- Acknowledgements (Optional). These should be brief and mention any essential support received for carrying out the work being reported.
- Appendix (Optional).

Scientific and technological research articles must also include:

- Experimental development. This must be written giving sufficient details for the subject to be fully understood by readers, including descriptions of any procedures involved.

- Results. These must give a clear explanation and interpretation of the findings. If it is necessary, a brief, focused discussion about how given results can be interpreted.

It is required that the bibliographical references for all articles are included at the end of the article, given in alphabetical order of first authors' surnames and mentioned in the text and, since May 2014, it is asked that the authors use the American Psychological Association (APA) style for citation and references:

- Articles published in journals:

Author, A. A., Author, B. B., & Author, C. C. (year). Article title. Journal Title, volume number(issue number), page numbers.

Del Sasso, L. A., Bey, L. G. & Renzel, D. (1958). Low-scale flight ballistic measurements for guided missiles. *Journal of the Aeronautical Sciences*, 15(10), 605-608

Author, A. A., & Author, B. B. (year). Article title. Journal Title, volume number(issue number), page numbers. Retrieved from <http://www.xxxxxxxxxxxxxxx>

Gaona, P. A. (2014). Information visualization: a proposal to improve search and access digital resources in repositories. *Ingeniería e Investigación*, 34(1), 83-89. Retrieved from <http://www.revistas.unal.edu.co/index.php/ingenv/article/view/39449>

- Books:

Author, A. A. & Author, B. B. (year). Title of work. Location: Publisher.

Turner, M. J., Martin, H. C. & Leible, R. C. (1964). Further development and applications of the stiffness method, *Matrix Methods of Structural Analysis*. New York: the Macmillan Co.

- Conference papers and symposium contributions:

Uribe, J. (1973, September). The effects of fire on the structure of Avianca building, Paper presented at National Seminar concerning Tall Buildings, Bogotá, Colombian School of Engineering.

- Theses or undergraduate projects:

Patton, F. D. (1906). Multiple modes of shear failure in rock-related materials (Ph.D. thesis, University of Illinois).

Further information can be obtained by:

Contacting the Editorial Team (Email: revii_bog@unal.edu.co) or Prof. Andrés Pavas (Editor-in-Chief. Email: fapavasm@unal.edu.co)

The *Ingeniería e Investigación* journal's office is located at: Ciudad Universitaria, Facultad de Ingeniería, Edificio CADE. Telefax: (57-1) 3165000 Ext. 13674. Bogotá - Colombia.